HAL
open science

Investigation of thermal and mechanical behavior of ultra-thin liquids at GHz frequencies

Levgeniia Chaban

To cite this version:

Levgeniia Chaban. Investigation of thermal and mechanical behavior of ultra-thin liquids at GHz frequencies. Materials. Le Mans Université, 2017. English. NNT : 2017LEMA1039 . tel-01816022

HAL Id: tel-01816022

https://theses.hal.science/tel-01816022v1

Submitted on 14 Jun 2018

HAL is a multi-disciplinary open access archive for the deposit and dissemination of scientific research documents, whether they are published or not. The documents may come from teaching and research institutions in France or abroad, or from public or private research centers.

L'archive ouverte pluridisciplinaire **HAL**, est destinée au dépôt et à la diffusion de documents scientifiques de niveau recherche, publiés ou non, émanant des établissements d'enseignement et de recherche français ou étrangers, des laboratoires publics ou privés.

Thèse de Doctorat

Ievgeniia CHABAN

Mémoire présenté en vue de l'obtention du
grade de Docteur de Le Mans Université
sous le sceau de l'Université Bretagne Loire

École doctorale : 3M

Discipline : Sciences des matériaux
Spécialité : Physique
Unité de recherche : *IMMM*

Soutenue le 11 Décembre 2017
Thèse N° : 2017LEMA1039

Investigation of thermal and mechanical behavior of ultra-thin liquids at GHz frequencies

JURY

Rapporteurs :	**Bertrand AUDOIN**, Professeur, Université de Bordeaux **Christ GLORIEUX**, Professeur, Katholieke Universiteit Leuven
Examinateurs :	**Natalia Del FATTI,** Professeur, Université Lyon 1 **Denis MORINEAU**, Directeur de recherche, Université de Rennes 1 **Benjamin CROSS**, Maître de conférence, Université Grenoble Alpes
Directeur de Thèse :	**Thomas PEZERIL**, Chargé de recherche, Le Mans Université
Co-Encadrants de Thèse :	**Rémi BUSSELEZ**, Maître de conférence, Le Mans Université **Vitalyi GUSEV** , Professeur, Le Mans Université

École doctorale 3M: Matière, Molécules et Matériaux
Le Mans, France

THÈSE DE DOCTORAT

Spécialité: "Science des Matériaux"

présentée et soutenue publiquement par

Ievgeniia CHABAN

pour obtenir le grade de docteur

INVESTIGATION DES PROPRIÉTÉS THERMIQUES ET MÉCANIQUES DE LIQUIDES ULTRA-MINCES AUX FRÉQUENCES GHz

---

le 11 décembre 2017

Devant le jury composé de:

B. AUDOIN	Professeur (I2M), Bordeaux	**Rapporteur**
C. GLORIEUX	Professeur (ATF), Leuven, Belgique	**Rapporteur**
N. DEL FATTI	Professeur (ILM), Lyon	**Examinateur**
D. MORINEAU	Directeur de recherche (IPR), Rennes	**Examinateur**
B. CROSS	Maître de conférence (LIPhy), Grenoble	**Examinateur**
T. PEZERIL	Chargé de recherche (IMMM), Le Mans	**Directeur**
R. BUSSELEZ	Maître de conférence (IMMM), Le Mans	**co-Encadrant**
V. GUSEV	Professeur (LAUM),Le Mans	**co-Encadrant**

Abstract

The phenomenon of liquid structuring near interfaces is related to the liquid/interface interaction forces at distances of some molecular dimensions. Despite the fact that this universal structuring effect plays a key role in various fields such as heat transport, particle transport through biological membranes, nanofluidics, microbiology and nanorheology, the experimental investigation of liquid structuring remains challenging.

The aim of this PhD thesis is the experimental study of the structuring/ordering of liquids at nanoscale distances from their interfaces with solids. In this context, we have adapted the experimental technique of picosecond laser ultrasonics to investigate high-frequency longitudinal acoustic properties of ultrathin liquids (glycerol, OMCTS, liquid crystals) confined between solid surfaces of different types. At first, we will present results of time-domain Brillouin scattering (TDBS) used to determine the temperature distribution profile in the investigated liquid volume which can be extrapolated to nanometer dimensions. Results for the evolution of the extracted Brillouin scattering frequencies and attenuation rates recorded at different laser powers give insight to the intrinsic relationship between thermal and mechanical properties of liquids. Second, we will describe our results for the measurements of mechanical properties of ultrathin liquids with a nanometric resolution. Fourier analysis of the recorded TDBS signals for different liquid thicknesses yield the value of the longitudinal speed of sound and attenuation at GHz frequencies. These are compared to the results of separate measurements of bulk liquids at ambient temperature. This novel TDBS experimental scheme is a first step towards the understanding of confined liquids measured by GHz ultrasonic probing.

Keywords: ultrafast phenomena, picosecond laser ultrasonics, liquid confinement, time-resolved spectroscopy, interfacial effects, cumulative heating of liquids

Acknowledgments

Gratitude makes sense of our past, brings peace for today
and creates a vision for tomorrow.

There are so many people met during my "PhD time" who I want to thank. Without all these people none of this would be possible. This time is without a doubt a great step in my professional life.

My biggest recognition is addressed to my supervisors Thomas Pezeril, Rémi Busselez and Vitalyi Gusev. This work could not be done to its fullest without them.

Thomas Pezeril who served as principal investigator, challenged and encouraged me throughout my time spent studying under his supervision. He would have never accepted anything less than my best efforts. All the time we have spent in the laboratory and the discussions we have had were fruitful, productive and sometimes fun because of a clash of our interests. The extensive knowledge, vision, and creative thinking of Thomas Pezeril have been a source of inspiration for me. All my experimental skills gained during this work I got thanks to him. My very first acquaintance with picosecond laser ultrasonics was back in 2014 when I was an intern in his lab. While still being an inexperienced student, he managed to instil in me the love to experiment, to science, and to show that, by labor and effort, one can achieve great results. In times of desperation, he always found the right words to motivate and support me and give faith in science. It was him who introduced to me the Shadok's mottos that later became my mottos. The Shadok's match exactly my life experience as a researcher (see Fig. 1). **"If there is one chance out of a 1000 to succeed, rush failing the 999 first tries"**.

I express my very great appreciation to Rémi Busselez for his valuable and constructive suggestions during the planning and development of this research work.

Les devises Shadok

Expérimentations

Pourqoui faire simple
quand on peut
faire compliqué?!

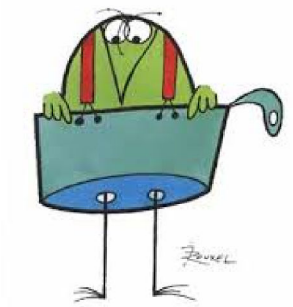

De la notion au concept

La notion de passoir
est independente de
la notion de trou.

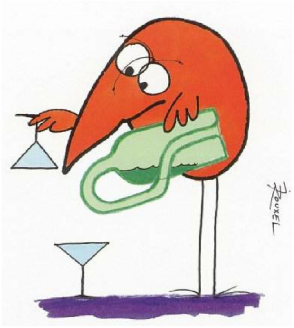

Attitudes réflexives

S'il n'y a pas de solution
c'est qu'il n'y a pas
de problème.

Science expérimentale

En essayant continuellement
on finit par reussir. Donc:
plus ça rate, plus on a
de chance que ça marche.

Observation réfléchie

La plus grave maladie
du cerveau c'est de
réfléchir.

Métacognition

Il faut mieux mobiliser
son intelligence sur des
betises que mobiliser
sa betise sur des choses
intelligentes.

Figure 1. Les Shadoks is an animated television series created by French cartoonist Jacques Rouxel which caused a sensation in France when it was first broadcast in 1968 - 1974.

His willingness to give his time so generously has been very much appreciated. The discussions with him are always motivating, hopeful and inspiring. In moments of hopeless, the discussions with him was encouraging and helped me to believe that everything is not in vain. He is the source of endless great ideas. He always advised me what to improve, what is not worth wasting time, and what to focus on. He showed me the basics of molecular dynamics simulations, which, to my regret, I did not master doing by myself.

I deeply thank Vitalyi Gusev who helped me in theoretical interpretations and comprehension. He made a great contribution to the theoretical explanations in this work. Without his participation in this project many details would have been missed. His boundless mind always has the answers to my questions.

By these few words, I thank for their welcome, also for all the time they have agreed to devote me, for the chance I had to work with them. Sincerely say, it was a big pleasure.

I would like to express my deep gratitude to Lionel Guilmeau for his help in creation and improvement of the sample holder, and in general for his time and interest in my work. He always had time for me and my project and was always ready to come to the rescue. He has got golden hands.

I would like to offer my special thanks to Osamu Matsuda. Actually my first experiments during my internship in 2014 have been done with him. He was an invited researcher at our university and he helped me to figure out the experimental setup. Later, we've met each year and he gave me the necessary advices to make my experiences and our work has been fruitful.

I gratefully acknowledge the contribution of Christoph Klieber to the LabView data acquisition. He made my work thousands of times easier and saved my time. I thank him for LabView program development, for sharing his results and experience with me.

I am especially indebted to Keith A. Nelson for the possibility to work in his group at MIT during one month. This month was very efficient and has brought the important results that allowed to advance the project. For the work in lab I thank also Hyun D. Shin, the PhD student of Keith A. Nelson who shared his experimental setup with me during that time. With Doug we took turns in spending sleepless nights in order to obtain excellent results. He is a skilful and highly competent student.

I gratefully acknowledge the contribution of Mathieu Edely who taught me to use AFM and the equipment of thermal evaporation. I am particularly grateful for the assistance given by Olivier Noël, for his advises and the help in Chromium deposition.

Also thanks to Pascal Ruello for providing me with the temperature controlled stage LinKam which was very useful in the framework with liquid crystals.

I would like also to extend my thanks to my colleagues. Mihn Tran, Viktor Shalagatskyi, Jamal Dabachi, Mariusz Lejman, Valentin Zorgnotti, Tymur Parpiiev, all of them I have met during the PhD and all them influenced me and my work somehow.

I would like to express my sincere appreciation to Aleksandr Alekhin, Yevheniia Chernukha, Rostyslav Danylo, Danylo Babich, Yuliia Pryimak, Oksana Kutova, Yurii Hyrka. I wrote their names in chronological order, because all of them are equally close to me. Everyone supports and emboldens me. Words can sometimes, in moments of grace, attain the quality of deeds. I thank them for the time spent together, for evenings when we were playing the board games.

I would also like to thank all the members of the IMMM laboratory who, through their good humor and their skills, allowed me to work in a pleasant and motivating context. I thank all the students and trainees with whom I have shared these years in joy and good humor.

I would also like to thank the staff of the Collége doctorale and École doctorale for organization, for financial support in conference participation and for enabling the PhD students to follow different courses. Special thanks to Brigitte Chevet for her help during the business trips organization. I wish to acknowledge the financial support provided by Ministry of Education, without this support this work would not be possible.

Of course, there are more sentimental acknowledgments. They are the ones we write to our families, our friends. In everyone's life, at some time, our inner fire goes out. It is then burst into flame by an encounter with another human being. We should all be thankful for those people who rekindle the inner spirit.

Special thanks to my friends Oxana Cherkas, Alexey Los, Ihor Laktionov. During student's life we have experienced many unforgettable moments together. I will never ever forget them and our crazy parties of "Fantastic Four"!!! It was a great time that, unfortunately, will not happen again. I express my appreciation to Alyona Kovdrya and her family for our long-hour skype conversations, for her support in the most difficult times. Thanks to her for always being by my side. The one of the blessings of old friends is that you can afford to be stupid with them.

I would like to express my very great appreciation to my close friends Kristina Zinchenko and Stephen Roille who are very intelligent, talented and young hopeful researchers. Our clumsy singing in karaoke and crazy dances inspired and still inspire

me to develop not only in the scientific field. Despite the distance they are always nearby. I really appreciate it.

Above all I thank my family. My family is my strength. I am what I am thanks to my mother, my step-father, my sister, my little niece. The education I have is thanks to them. My mom has given me everything. Her greatest skill was to encourage me to find my own person and own independence. I appreciate their never-ending love and constant support. Even being so far from me, they always find right words to cheer me up.

Finally, I wish to thank the reviewers and the committee members for their devoted time.

Success is no accident! It is hard work, perseverance, learning, studying, sacrifice and most of all, love of what you are doing or learning to do.

List of acronyms and symbols

Glossary:

AFM	Atomic Force Microscopie
AOM	Acousto-Optical Modulator
AR	Anti - Reflective
BLS	Brillouin Light Scattering
FFT	Fast Fourier Transform
HOPG	Highly Ordered Pyrolytic Graphite
HWP	Half Wave Plate
LC(s)	Liquid crystal(s)
MD	Molecular Dynamics
μSR	Muon Spin Rotation
NI	Nematic-to-Isotropic phase transition
NMR	Nuclear Magnetic resonance
OMCTS	Octamethylcyclotetrasiloxane
PBS	Polarizing Beam Splitter
QWP	Quarter Wave Plate
SFA	Surface Force Apparatus
SHG	Second Harmonic Generation
TTM	Two-Temperature Model
TDBS	Time-Domain Brillouin Scattering
UT3	Ultrasonic Testing Tandem Technique
VUV-FEL	Vacuum UltraViolet Free Electron Laser
8CB	4'-Octyl-4-biphenylcarbonitrile

Frequently used variables and symbols:

T_b	K	Boiling point
T_m	K	Melting point
T_g	K	Glass transition Temperature
ρ	kg· m^{-3}	Density
Z	kg ·m^{-2}·s^{-1}	Acoustic impedance
ξ	m	Absorption depth
λ	m	Optical or acoustic wavelength
ν, ω	Hz	Optical or acostic frequency
C	GHz·ns^{-1}	Linear frequency chirp constant
Γ	s^{-1}	Acoustic attenuation rate
α	m^{-1}	Acoustic attenuation coefficient
c_l	m· s^{-1}	Longitudinal speed of sound
F	mJ· cm^{-2}	Laser fluence
P	mW	Laser power

Table of contents

Abstract **ii**

Acknowledgments **iii**

List of acronyms and symbols **viii**

Overview **xiii**

1 Theoretical considerations onconfinement effects in liquids **1**

1.1 General view on molecular ordering 2

1.2 Principle of liquid structuring under confinement 4

1.2.1 Mechanism of liquid structuring/ordering near the solid surface 5

1.2.2 Conditions for molecular ordering 8

1.3 Properties of confined fluids 10

1.4 Investigation of liquid crystal confinement 11

1.4.1 Brief overview of state of the art 13

1.4.2 Conclusion 16

2 Experimental and instrumental developments **17**

2.1 Picosecond laser ultrasonics 18

2.1.1 Thermo-elastic generation of strain and stress 18

2.1.2 Detection of acoustic waves after propagation through a liquid film 28

2.2 Details of the experimental pump-probe set-up 35

2.2.1 Femtosecond laser system 36

2.2.2 Data acquisition 45

3 Liquid cell **47**
3.1 Sample cell configuration 47
3.2 Choice of materials 48
3.2.1 Generation side substrate: Substrate and transducer film combination 49
3.2.2 The choice of the liquid 49
3.2.3 Detection substrate 53
3.2.4 Impact of the surface roughness on the measurements 54
3.3 Sample cell design and assembly. 55

4 Heating effects **59**
4.1 Nonequilibrium heating of Chromium films by ultrashort laser pulses . 59
4.1.1 Thermal relaxation between electrons and lattice 60
4.1.2 Transient reflectivity of laser excited Chromium films 62
4.1.3 Conclusion 64
4.2 Cumulative laser heating in liquids 65
4.2.1 Temperature dependent measurements for glycerol and OMCTS. Temperature calibration 66
4.2.2 Cumulative thermal heating 71
4.2.3 Conclusion 81

5 Mechanical properties of ultra thin liquids at GHz frequencies. Results and discussions **83**
5.1 Data analysis 83
5.2 Adjustment of the initial liquid film thickness gap 86
5.3 Time domain Brillouin scattering study of glycerol 89
5.3.1 Lateral TDBS measurements on glycerol 89
5.3.2 TDBS piezo measurements of ultrathin glycerol 91
5.4 Time domain Brillouin scattering study of OMCTS 96
5.4.1 Lateral TDBS measurements of OMCTS 96
5.4.2 TDBS piezo measurements of ultrathin OMCTS 100
5.5 Time domain Brillouin scattering study of 8 CB liquid crystals 104
5.5.1 Investigation of 8 CB liquid crystals phase transitions 105
5.6 Lateral TDBS measurements of 8 CB 113
5.7 TDBS piezo measurements of ultrathin 8 CB liquid crystals 115
5.8 Conclusion 119

Conclusions and outlook **121**

Appendix A Liquid crystals **123**

A.1 Classification of Liquid crystals 123

A.2 Distribution functions of molecules by orientation and order parameter 126

A.3 Phase transitions 128

A.3.1 A. Isotropic to nematic phase transition 128

A.3.2 B. Nematic to Smectic A phase transition 129

A.4 Deformation and surface anchoring of nematic LC 131

Appendix B **134**

B.1 Step-by-step procedure of sample mounting 134

B.2 First version of sample configuration 136

B.3 Newton's rings visualization 138

B.4 Interferometric determination of the contact zone from the fs probe reflectivity 141

B.5 Measurements with the Death Star pulse shaper 144

B.6 Optical derivative 146

Appendix C **153**

C.1 Thermal properties 153

C.2 Acoustic properties 154

C.3 Refractive index of studied materials 154

C.4 Temperature dependent parameters of glycerol 155

Bibliography **155**

Overview

Nowadays, one of the rapidly developing domains in science is nanoscience. Nanoscience or, in other words nanotechnology, is the study of structures and materials on the scale of nanometers, e.g. atoms, molecules and objects whose size is on the range of 1-100 nm. Despite its size, there is plethora of effects happening at the nanoscale. It gives the sunset its red color, allows birds to navigate and helps geckos stick to trees. Understanding the nature's nanosecrets can allow us to use them for ourselves.

The ideas and concepts behind nanoscience and nanotechnology started with a talk entitled "There's Plenty of Room at the Bottom" by the physicist Richard Feynman at an American Physical Society meeting at the California Institute of Technology (CalTech) on December 29, 1959 [1], long before the term nanotechnology was used.[1] In this famous lecture, Feynman laid the conceptual foundations for the field of nanothechnology when he imagined a day when things could be miniaturized. He described a process in which scientists would be able to manipulate and control individual atoms and molecules. This was achieved later with the invention of microscopes that involves the ability to see individual atoms and molecules (scanning tunneling microscope (STM) and the atomic force microscope (AFM)). Once scientists got the right tools, the exploration of a strange new world down there started.

Although this area is still new, nanoscale materials were used for centuries. For example, vibrant stained glass windows of Notre Dame Cathedral owed their rich colors to nanoparticles of gold chloride and other metal oxides and chlorides (13th century). Or, a worlwide known Lycurgus Cup (4th century), which shows a different colour depending on whether or not light is passing through it. Colloidal gold and silver in glasses makes it look green when light comes from outside but red when light shines through the inside. For example, as gold gets smaller, it stops looking gold and instead reflects red, purple, blue and finally becomes invisible.

[1] A term of nanothechnology was coined by Norio Taniguchi in 1974.

But nanoworld is not just unusual looking, things behave differently there too. Down at the nanoscale, with the volume reduction, the properties of materials are modified with respect to the bulk. It's important to realize that all materials, including solids, liquids, and gases, show property changes through nanosize regime. As more and more information and interest is accumulating on microscopic, mesoscopic, and nanoscopic (molecular-scale) systems and processes, there is a natural desire to understand and control these phenomena. Even today we can observe how nanoscience has already impacted our lives with innovations as computer hard drives, which store information on magnetic strips that are just 20 nanometers thick, smartphones getting smaller and faster, etc.

A special interest arisen for the investigation of molecular ordering and liquid structuring at nanoscale. Particularly, there has been considerable interest in recent years in the determination of the structure of liquids under confinement. Effects of confinement on liquid structuring is a field that is developing in different systems like water, ionic liquids, liquid crystals and crystalline materials. The properties of nanoconfined liquids were studied over twenty years [2–7] and still, we do not have a full picture of this phenomena, and our knowledge is insufficient and sometimes contradictory. The understanding of this concept will allow to clarify our understanding on the liquid state and the interaction of molecules and particles in liquids at the nanometric level.

The main goal of this PhD project is to get new useful information about liquid structuring/ordering, to understand the fundamental physics of interfacial and confined liquids at the nanoscale.The work in this thesis is focused on the advancement of the ultrafast photoacoustic technique for the viscoelastic measurements of liquids in the GHz frequency range, which remains uncovered by other techniques. The ultimate goal of this PhD project is to probe not only to the mechanical properties of bulk liquids from GHz laser excited ultrasound, but also the mechanical properties of ultrathin liquids. The thesis is organized as follows:

In Chapter 1 we describe in details molecular ordering and liquid structuring under confinement. We introduce some of the basic concepts of ordering in specific complex structures. At the end of the chapter, we present different experimental techniques that have been developed to investigate this problem.

An introduction to the experimental and instrumental developments related to picosecond laser ultrasonics / ultrafast photoacoustics, which can access acoustic frequencies from GHz to even THz, is provided in Chapter 2. In picosecond laser ultrasonics measurements, laser heating of a thin metal transducer film leads to ther-

mal expansion and strain pulse generation. We describe the basic principles of the generation and detection of this strain pulse in our experimental system. The general concepts and details on the detection method of time-domain Brillouin scattering are introduced. The theory of detection in an acousto-optical liquid cavity, which models the liquid sample scheme used in this PhD thesis, is reviewed. In the end, we detail the experimental setup developed during this project to achieve these goals.

Particular attention is paid to the material choice in Chapter 3. We also describe a custom-made liquid sample cell, which is a complex and sophisticated system that gives an access to a wide range of liquid thicknesses, from less than a nanometer up to several hundreds of micrometers. Some notes and remarks on the sample preparation are given at the end of the chapter.

A detailed study of sample cumulative heating caused by laser pump pulses is presented in Chapter 4. The experimental investigations of the laser excitation of chromium transducer films are presented at first. Then we discuss the measurements for glycerol in different sample configurations and OMCTS at different laser powers and temperatures. The study of cumulative heating effect has highlighted the importance of good selection of sample materials.

At the beginning of Chapter 5, we describe the analysis of time-domain Brillouin scattering data, which compares arrival times and amplitudes of strain pulses transmitted through different liquid thicknesses. This allows the extraction of sound velocity and attenuation rates of liquids under study at particular Brillouin frequency. The longitudinal Brillouin scattering data are presented for three different liquids, glycerol, OMCTS and liquid crystal 8 CB, in bulk and ultrathin configurations. If available, the obtained information is compared with information available in the literature.

At the very end of this thesis, in Appendix A, we provide more details on liquid crystals. In Appendix B we review the experimental developments tested during this PhD period. And in Appendix C the reader can find some relevant parameters of the materials.

Chapter 1

Theoretical considerations onconfinement effects in liquids

When we talk about liquid, we always imagine it as a completely random disordered state, which has perfect translational and rotational symmetry. This statement is correct at a high-temperature or low-density limit near the gas-liquid transition. However, under some conditions a local structural ordering in liquid is observed. For example, upon melting of a solid, the existing molecular order does not disappear completely in the liquid state. Such phenomena is known as liquid structuring and molecular ordering in liquids.

Molecular ordering has been studied experimentally, computationally and theoretically for many tens of years. But information on molecular structure, packing arrangement, and inherent disorder is still insufficient and a matter of some controversy. As it was already mentioned, the main manner to investigate the molecular ordering/liquid structuring is the investigation of liquids confined in different geometries. Understanding the dynamics of liquids in confinement continues to be one of the major fundamental issue in the field of nanoscience and remains one in which we still need theoretical frameworks.

In the sections that follow, we get acquainted with some of the basics of molecular ordering, we introduce factors that can impact the liquid structuring and we present the experimental techniques that have been developed to investigate this problem.

1.1 General view on molecular ordering

There are two basic kinds of molecular ordering processes. First, there is the assembly of molecules into clusters or nanoparticles, or even large colloidal aggregates, that occurs spontaneously, which is referred to as self-assembly. Naturally occurring ordering or organization is supposed to be driven by thermodynamics. Amphiphilic molecules are known to spontaneously order at liquid-solid and liquid-air interface, forming well-ordered layers [8]. Or, for example, the first layer of water molecules around a strongly solvated ion are "structured", they are restricted in their positional and orientational order and in their motion. But the effect does not end there; it propagates beyond the first layer, only much more weakly. This is because the water molecules in the first layer interact directly with the charged ion, while those in the second and subsequent layers interact only with other water molecules and only indirectly with the ion. Such molecular ordering is caused by a solute-solvent interaction [9]. Then there are energy-requiring (external field-driven) processes that lead to long-lived metastable or steady-state structures that are not necessarily the thermodynamically most favored structures or true equilibrium state. Such molecular ordering can be driven by the externally applied forces on the system during their preparation such as normal or shear stresses, gravity, and magnetic or electric fields. For example, applying an external magnetic field to magnetic colloidal particles, which tend to associate into linear strings, where all dipoles point in the same direction along the string, will orient these strings along the field. In more concentrated systems the strings associate with one another to form ordered close-packed lattice of magnetic particles.

The "involuntary" ordering of liquid molecules can be caused by various reasons. At least three different types of ordering can be identified: positional ordering into layers, which can be a consequence of liquid/surface interaction, orientational ordering, which affects electrostatic and entropic charge-transfer interactions, and mean density variations near the surfaces, which can give rise to the additional "steric" repulsion between hydrophilic surfaces and a "depletion" attraction between hydrophobic surfaces. Microstructure near the surface and in thin films has played an important role in industrial applications, chemical engineering, and so forth.

What happens with a thin liquid layer deposited on solid surface?

Surface-induced liquid structuring There are many works that evidence that the molecules of the thin liquid on solid surface tend to organise in layer parallel to the solid boundaries [10–14]. The main local density of such liquid oscillates with

distance normal to the boundaries (see below). It has been shown that liquid films can even undergo an abrupt transition from liquid-like to solid-like behavior below a critical thickness corresponding to several molecular layers of the liquid.

The "surface-induced ordering" (oscillatory density profile near the surfaces) has the same physical origin as the oscillations in the radial distribution function of simple liquids. The necessity of these finite-size molecules to organize in a restricted geometry diminishes the number of possible configurations in the liquid state and gives preference to more ordered structures [15]. The tendency of a liquid to organise or, in other words, to structurize at the vicinity of a solid surface is nothing else but a consequence of the interaction between the liquid and the solid surface. Depending on different conditions (the polarity of the interacting surfaces, as example) this interaction can be of different nature, for example dipole-dipole interactions (ion-dipole force, hydrogen bonding), dipole-induced dipole interaction, London interaction etc [6]. For example, the ordering of liquid can be promoted by attractive interactions between an ion and a polar molecule (electrostatic interaction between a positively charged ion and a water molecule in an aqueous environment). Structuration of liquids near their interfaces with solids caused by liquid/solid interactions is known to take place at distances of few molecular dimensions from the interface [13, 16]. Thus the structuration takes place at nanoscale both in liquids composed of relatively small molecules and in liquids composed of relatively large molecules [17, 18]. The shape, the rigidity and symmetry of the molecules affect the structuring. Rigid hard sphere molecules exhibit more short-range order or structure than easily deformable molecules.

Not all liquids become ordered in the vicinity of the surface. This inability can be due to the surfaces, to the liquid, or to both. If the liquid and surface molecules are very different, the surface-induced ordering may not be possible. For example, asymmetric molecules [9, 19, 20] or if the surface is rough or dynamically "labile" (surfaces coated with surfactant monolayers or bilayers), the molecules do not order into discrete layers. The impact of the surfaces is discussed below.

The magnitude and range of molecular ordering in liquids are enhanced additionally by increasing the external pressure and lowering the temperature [9]. The total thickness of the structured liquid can be additionally reduced through squeezing of two parallel solid substrates by approaching one to another, i.e. by nanoconfinement. Nowadays, the study of molecular ordering is a fascinating topic [19, 21–25].

Confinement-induced liquid structuring When a liquid is confined to nanometer scale in a closed system (nano-/mesoporous material [26], squeezing between two

solid surfaces [21]), it exhibits unusual behavior compared to the bulk. The mechanical responses of confined liquids may significantly differ from bulk [27, 28]. The examples of such a system are present in everyday life, the blood moving through our bodies, the lubricant between mechanical parts, the hydraulic or pneumatic braking system in vehicles and much more. When a liquid is confined in an extremely narrow gap, the liquid ordering can be prominent and very interesting effects and new fundamental behavior emerge. There has been considerable interest in recent years in the determination of the structure of liquids adjacent to solid surfaces [19, 21–23, 25, 26, 29]. A large volume of literature shows the impact of the confinement on structure [30–32], on freezing and melting of liquids [26, 31, 33], on the liquid-to-glass transition point T_g [12, 26, 29, 34, 35], dynamic properties [12, 29] any many others properties [27, 28]. The effective shear viscosity is enhanced compared to the bulk, relaxation times are prolonged, and nonlinear responses set in at lower shear rates. These effects are more prominent, the thinner the liquid film. Nonetheless, it should be mentioned that the short-range order in liquid near a surface does not always mean that the liquid is in solid-like state. The fundamental interest in this area is the desire to understand the new physics that occurs due to finite-size effects, surface forces, interfacial, low dimensionality, and/or quenched disorder effects.

During this project, we were working with confined configuration, where a liquid was squeezed between two solid boundaries. We will consider the principle of liquid structuring under our experimental conditions for better understanding and which factors may influence the liquid structuring.

1.2 Principle of liquid structuring under confinement

Liquid confinement happens in many everyday life situations, for example when a miniature sphere falls on a drop of liquid put on a surface. Of course, the liquid squirts out, initially very fast, then slower and slower as the liquid thickness becomes less than the radius of the sphere. Experimentally, it was shown that the film eventually stabilises at a finite thickness of a few molecular diameters [19, 22]. An extraordinarily large pressure is needed to squeeze out the final few layers of liquid between two solid surfaces. But what happens at the molecular level?

1.2.1 Mechanism of liquid structuring/ordering near the solid surface

Let us consider the example depicted in Fig. 1.1 (a, b, c). The liquid is placed in between two flat solid boundaries with smooth surfaces and time by time the force is applied normally to the surfaces to confine the liquid down to the molecular size. The forces in between the solid surfaces and the liquid originates from van der Waals and electrostatic interactions [21]. At the beginning, the molecules are free to move inside the system, they can move, rotate. When the distance between the two solids decreases further and further, the liquid molecules firstly will approach to each other, some of them will escape the system and the remaining molecules will reorganize. At some point, when the distance between two solid substrates is equal to a few molecular layers, the molecules will naturally organize in layers parallel to the solid boundaries and short-range order will appear. When two particles are approaching closer than a few nanometers, continuum theories of attractive Van der Waals and repulsive double-layer forces are no more usable to describe their interaction [21]. It is connected to the fact that the other non-DVLO forces show up. [2] These forces can be monotonically repulsive or attractive, or oscillatory, and can be much stronger at small separations.

The same type of experiments as depicted in Fig. 1.1(a,b,c) have been performed by means of Surface Force Apparatus [22,37,38]. In such experiments, the liquids (cyclohexane, OMCTS) are placed between two flat mica sheets and a force normal to the surfaces is applied gradually in order to confine the liquid. The discovered effect proves liquid ordering under confinement. It was observed that the short-range oscillatory solvation force between two surfaces in a liquid varies between attraction and repulsion with a periodicity equal to some dimension of the confined liquid molecules (Fig. 1.1 (d)). The first predictions of oscillatory force between two smooth walls approaching each other in simple liquid and periodic density variations have been done by [39, 40]. The origin of the oscillatory force is the consequence of a periodic rise in the force necessary to remove each subsequent layer on approaching the surface. Solvation forces arise when the liquid molecules behave differently to those in the bulk liquid, ordering into layers. This force is intimately related to the structure that the confined liquid is forced to adopt under confinement (also known as the density distribution function) and depend not only on the properties of the liquid medium but also on the chemical and physical properties of confining surfaces (see in 1.2.2). Solvation forces can be very

[2] The DLVO theory is named after Boris **D**erjaguin and Lev **L**andau, Evert **V**erwey and Theodoor **O**verbeek. The theory explains the aggregation of aqueous dispersions quantitatively and describes the force between charged surfaces interacting through a liquid medium [36].

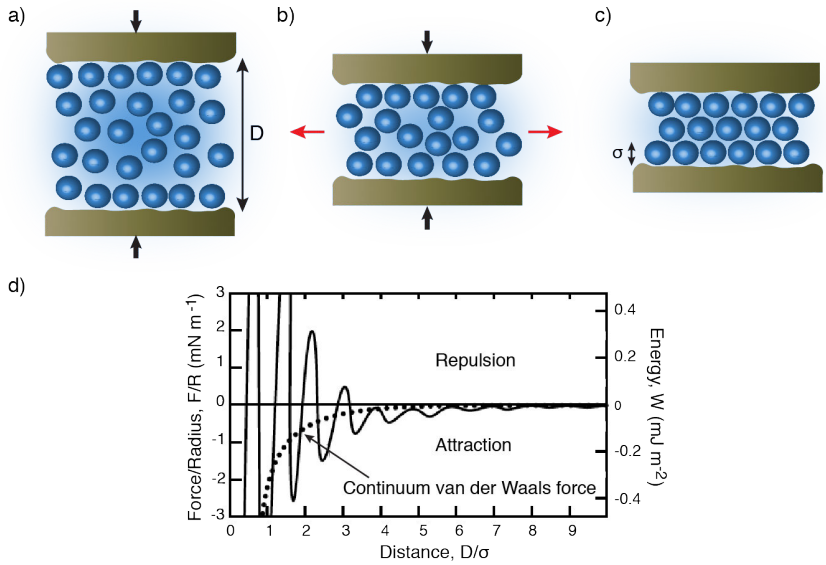

Figure 1.1. A liquid with a mean molecular diameter σ is squeezed between two flat parallel solid substrates. If no forces are applied between the solid boundaries, the liquid is under normal conditions, the molecules can move around the system (a). Once some force is applied normally to the solid boundaries in order to decrease the liquid thickness, some of the molecules will be forced to escape the system since there is no enough room (b). (The black arrows show the applied force, while the red arrows show the "ways of retreat" of liquid molecules). At some point, the molecules will organise into layers parallel to the solid boundaries (c). (d) Measured force F as a function of separation D between two mica sheets immersed in OMCTS. Dotted line: theoretical continuum van der Waals force computed for this system. Experimental data from [22].

strong at short-range, and they are therefore particularly important for determining the magnitude of the adhesion between two surfaces or particles in contact or at their potential minimum.

This effect was also shown theoretically and by computational simulation of the same system [39], the roughness of solid boundaries was considered to be less than the averaged molecular diameter σ (Fig. 1.2). In this case, a density profile for a liquid of spherical particle was considered. The mean local density of the liquid, plotted against the distance between two solid boundaries D, shows that close to the boundaries, the liquid density is vanishingly low because no particle can be located precisely there, but the local density is correspondingly large at a distance of one particle radius removed, while again it reaches a minimum one further particle radius away, and so forth. The constraining effect induced by bringing molecules into close proximity of two solid

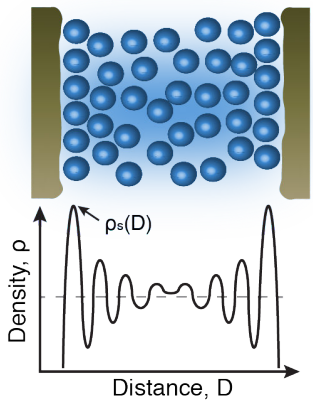

Figure 1.2. Schematic diagram of the local density of a liquid composed of spherical particles, plotted against the distance between two solid boundaries. The tendency to order in layers parallel to the boundaries is indicated by a decaying oscillations with a period of about a particle diameter. This differs from the radial distribution function of a bulk liquid in the sense that degrees of order and disorder parallel to the boundary are possible in bulk.

surfaces dominates over the attractive interactions between the liquid molecules and the solid boundaries, and forces the molecules to order into quasi-discrete layers. The tendency to order in layers parallel to the boundaries is indicated by the decaying oscillations with a period of about a particle diameter. The liquid molecules reorder themselves to accommodate in the gap between the approaching surfaces. The pressure between two surfaces is directly correlated with the density of liquids between these two surfaces. This pressure may be expressed by [6]:

$$P(D) = kT(\rho_s(D) - \rho_s(\infty)) \tag{1.1}$$

where k is the Bolzman constant, T is the absolute temperature of the system, $\rho_s(\infty)$ is the density of the liquid layer adjacent to the surface in case of only one solid surface (i.e. isolated solid-liquid interface), $\rho_s(D)$ is the adjacent layer density in confined configuration. In case of one solid/liquid interface, the density of the liquid layer near the solid surface is less than in case of two boundaries because there is no additional squeezing and the density oscillations across the liquid thickness are weaker. Since the pressure is expressed in terms of density, as a result one gets the oscillating pressure or force between two solid surfaces. This pressure is decreasing with an increase of the distance between two boundaries which is equivalent to a liquid thickness decrease. In case of very small separations, as the last layer of liquid molecules is finally squeezed

out, $\rho(D \to 0) \to 0$ for surface layers and for midplane as well. In this terms the solvation pressure strive for a finite value:

$$P(D \to 0) = -kT\rho(\infty) \tag{1.2}$$

It means that the force at contact point is negative, thus it is attractive or adhesive. The oscillatory force imposes few important conditions on both liquid molecules and solid boundaries. The shape of molecules should not be too irregular and be free to exchange with molecules in the bulk liquid. And the solid boundaries should be smooth or crystalline.

Although the knowledge of liquid structuring is of crucial importance for such fundamental issues as energy and molecular transport across the interfaces, and to such fast developing applications as nanofluidics, our knowledge on liquid structuring at nanoscale is very limited. Knowledge of the parameters of the individual layers as well as of the interactions between the individual layers and between the layers and the solid are very insufficient.

1.2.2 Conditions for molecular ordering

There are different factors that can influence the ordering of liquid molecules. One of the biggest impact comes from the solid surfaces. Whether they are hydrophilic or hydrophobic, smooth or rough, amorphous or crystalline (atomically structured), homogeneous or heterogeneous, natural or patterned, rigid or fluid-like. The quality of the surface greatly affects and can be a hindrance to molecular structuring. In the following we will consider how surface chemistry and roughness can alter the liquid confinement, the issue we face with.

The role of surface roughness in molecule ordering. If two surfaces are smooth at the molecular scale, the liquid molecules tend to organise into layers parallel to the surfaces, but there is no lateral ordering within the layers [41]. Solid surface structure can additionally promote the ordering, if the surface has a periodic lattice structure. Then there will be some epitaxially induced ordering also within the layers. This means that there will be out-of-plane ordering additionally to in-plane ordering, the first referring to the existence of ordered layers, the second referring to the existence of ordering within the layers themselves. Nonetheless, this is an ideal case that never happens in real experimental conditions because no surface is perfectly smooth (flat at the atomic level), and the effects of atomic corrugations are very important when the atomic structure of the surface and the molecules have a comparable size. Thus

the oscillatory force, already mentioned, will depend on the structure of the surface lattices [42]. However, if the two surfaces are randomly rough the oscillatory force will be smoothed out or may disappear altogether and be replaced by a purely monotonic solvation force. The role of the surface roughness is well studied in [43–45]. In [43] the force measurements were carried out with the SFA involving mica surfaces coated with cetyltrimethylammonium bromide (CTAB) and dioctadecyldimethylammonium bromide (DOAB) immersed in octamethylcyclotetrasiloxane (OMCTS). These studies demonstrated how surface roughness influences on oscillatory solvation force, leading to a reduced range of oscillations and even a complete disappearing. In [44, 45] the solvation force dependence on the surface roughness was investigated by Monte Carlo simulations. The same liquid (OMCTS) was placed in a split pore with rough walls. The theoretical calculations showed that the amplitude of the oscillatory force decreases generally with increasing roughness.

To summarize, for the existence of an oscillatory solvation force, the liquid molecules must be able to be correlated over a reasonably long range. This requires that both the liquid molecules and the surfaces possess a high degree of order or symmetry. A surface roughness of only a few angstroms is often sufficient to eliminate any oscillatory component of the force.

Influence of surface chemistry on molecular ordering The existence of oscillatory forces do not require any specific condition on the liquid-solid interactions. However, in case of strong attractive interactions between liquid molecules and solid surfaces (the case of wetting), the molecules close to the solid are more densely packed. As a result, the higher density should increase the repulsive pressure between two confining boundaries, and therefore the oscillations in the force profile as in Fig. 1.1 (c) are shifted toward higher forces with an increasing effect for small distances between solid boundaries. This means that the surface chemistry is critical and control the interaction between liquid molecules and surfaces. If, in contrary, the interaction between liquid molecules is stronger than the interaction between liquid molecules and the solid (non-wetting), then the oscillatory force will be shifted toward negative (attractive) forces with a remaining exponential decay character. According, the surface chemistry should be taken into account while analyzing the molecular ordering and liquid structure near solid/liquid interface. A study, in which the influence of different substrates on the oscillatory forces has been presented in [46, 47]. The experiments were performed with AFM. Drops of water were deposited on three different substrates of hydrophilic mica, glass and hydrophobic highly ordered pyrolytic graphite

(HOPG). The study showed that for HOPG the oscillatory force due to confinement is less explicit in comparison with mica and glass.

1.3 Properties of confined fluids

A liquid confined in a narrow gap departs by distinctive features from bulk liquid. The confinement of a liquid to few molecular layers can strongly modify the dynamical properties of the liquid, such as the shear viscosity, the diffusion of its constituents. It also affects many other macroscopic properties of the liquid, from capillary condensation to melting/freezing phase transitions. For example, in [27, 48], the liquid was placed between two parallel solid substrates and then sheared (it needs less force to shear the liquid film than to squeeze it out). From such measurements the analysis of the effective viscosity of a variety of non-polar liquids of various sizes, shapes and flexibilities has been performed. It was shown that the effective viscosity of confined liquid is larger than in the bulk and grows with a decrease of the thickness and the relaxation is much slower than in bulk, $>10^8$ times slower than in the bulk.

In [49] by squeezing OMCTS to 6 molecular layers the effect of liquid-to-solid transition under confinement was discovered. The liquid film compression from 7 to 6 molecular layers all at once rendered the film solid enough to resist the lateral shearing motion. The ability of thin liquid films to sustain shear stress pointed out the authors to the fact that the liquid underwent liquid-to-solid transition, because a liquid by definition cannot sustain such a stress. This is a fundamental signature of a solid state.

Investigations of water by use of the AFM technique in [17] showed that the stiffness of water oscillates upon confinement with a period corresponding to the molecular spacing of water layers and becomes higher when the liquid film thickness decreases. Under some experimental conditions, a damping reduction was observed while the stiffness was increasing. This observation means that when the liquid is ordered, the liquid has a strong elastic response but a weak dissipative response. In this regime the liquid behaves solid-like.

Experimental measurements of diffusivity, and thermal expansion coefficient of water and aqueous solutions confined in small pores were interpreted by molecular dynamics simulations (MD) [51]. It was demonstrated that the diffusivity of the liquid confined in 5 nm pores measured using pulsed field gradient NMR analysis is reduced by about a factor of 5 compared to bulk liquid. MD simulations show that the mobility is reduced by about an order of magnitude within 6 Å of the surface, but when averaged

over the 3 nm gap, the diffusivity is only about 30% lower than the bulk value. This shows that the reduction in measured diffusivity is not simply a consequence of the low mobility near the pore wall, but results primarily from the tortuosity of the pores. MD simulations also show that the layer of water within 6 Å of the pore wall has a high thermal expansion coefficient [51]. Using a simple volume average to take into account the influence of that layer, one can semiquantitatively account for the high values of thermal expansion observed in confined water and solutions.

Computational simulations and theoretical investigations have shed much light on the molecular details underlying both structural and dynamic behaviors in highly confined regime [52–56]. For example, in [28] by using conventional Metropolis Monte Carlo simulations they calculated the local, wave-number-dependent (k), high-frequency elastic properties of a Lennard-Jones fluid confined between two walls. Firstly, the bulk liquid was simulated, then the confined liquid in order to compare the results. It was found that local elastic properties correlate with the inhomogeneous fluid density and the strength of the wall-liquid interaction. Thus, position-dependent elastic constants were calculated whose values decay to their corresponding bulk values as one probes regions far from the walls.

Computer simulations are very useful in the interpretation of experimental results measured by different techniques. Still, information on confined liquid properties remains incomplete. This is connected to the fact that the investigations of confined liquids properties are more troublesome, involving and requiring strenuous effort, difficult and tiring. Still it maintains a great interest to this phenomenon. Once the research panel will manage to gather more data, the huge possibility in the development of future applications in biology and medicine, such as the design of intelligent artificial implants, and nanotechnology (micro-electronic, micro-mechanical devices) will be opened.

One of the liquid studied during this work is a liquid crystal (LC), that is why in the following section, various aspects will be considered to spell out the increasing interest to LC. The additional information on LC can be found in Appendix A.

1.4 Investigation of liquid crystal confinement

Despite a large variety of liquids, in latter years, the researchers over the world have become engaged in answering the question - what happens in confined configuration with LC, particularly interesting, both from practical and fundamental reasons, how their properties are changing under confinement? Liquid crystals are very in-

triguing both for fundamental research and for applications, because although they combine the properties of a solid and of an isotropic liquid, they exhibit very specific electrooptical phenomena, which have no corresponding analogues in solids or in isotropic liquids [57, 58]. The occurrence of translational symmetry and orientational order has been extensively studied in confined geometry.

The first investigations of confined LC dates back to the early 1990s when the interest in the macroscopic properties of bulk LC was still in its inception [59]. From those years a lot of work have been done to give some answers [60–66]. Confined LC samples are systems in which the confining boundaries strongly influence both the static and the dynamic properties of the liquid crystal. Depending on the type and the shape of the surface, the order in a liquid crystal can be either enhanced or reduced, liquid crystal molecules can be in average oriented in one direction or otherwise manipulated. Confinement geometries usually include thin planar slabs (two solid flat surfaces), cylindrical pores, liquid crystalline droplets or random structures in porous glasses and silica aerogels [67]. Here the discussion is mainly about LC between two flat plates, the simplest one but not least useful. Such studies on nematic LCs are important both from fundamental and technological point of view. For example, nematic liquid crystals are sandwiched between two parallel glass plates for display (LCD) applications. Relaxation dynamics in systems where the LC is confined only in one direction, has been extensively studied both theoretically and experimentally [67–69]. This has mostly been used to study interactions of LC with boundaries and aligning layers. And it was demonstrated that dynamic light scattering experiments on planar thin samples can be used to determine the anchoring coefficients of a liquid crystal on a given substrate. Therefore the measurement of their relaxation rates by dynamic light scattering can be used to obtain the information on the interaction of LC with confining surfaces. In [65] LC structures confined in different geometries exhibit changes in their exceptional physical properties such as a shift of the phase transition temperature, formation of pseudo-layer structures and an increase of the viscosity as evidenced by the various analytical techniques. Confinement shifts the chemical potential for the nematic-isotropic transition in a quantity $\delta\mu$ with respect to the bulk value [66].

The investigations [70–74] have laid the groundwork for understanding the structure and dynamics for sheared 8 CB (the LC we have been working on) under confinement. Using a high-resolution x-ray scattering spectrometer they have studied the microscopic structure of the nematic and Sm A phases in 4-cyano-4'-octylbiphenyl (8 CB) under non-equilibrium steady-state shear flow conditions. It was shown that

the flow-induced fluctuation forces on the nematic director lead to a rich sequence of regimes where the orientational phase space traversed by director $\vec{n}$ evolves as the N - SmA transition approaches [70]. With X-Ray SFA they demonstrated that the LC can take one of three possible orientations [72]. In one, $\vec{n}$ aligns with the direction of the shear flow, in two others it is perpendicular.

This suggests that the confinement alters the properties and the behavior of confined crystals which for instance should be investigated thoroughly and substantially.

1.4.1 Brief overview of state of the art

Regardless the increasing interest to interfacial and confined liquids at nanoscale, there is no full understanding of fundamental physics. Despite of a sufficient number of experimental tools and techniques, a complete picture of the physical properties and dynamic response of these nanoscale quasi-periodic structures (nanostructures) present near liquid/solid interfaces has never been resolved till now. Fig. 1.3 presents a set of non-destructive techniques that reveal information about crystal structure, the size distribution profile of small particles/molecules, chemical composition. These technique are appropriate for investigation of molecular ordering as well. However, all these techniques are limited in size of investigated particules/molecules and temporal resolution. The advantages of some of them for molecular ordering we consider below. The main extracted information from the techniques such as scanning probe microscopy [14], surface forces apparatus [22], diffraction techniques [42], nonlinear optical spectroscopy [9, 75], and infrared and THz spectroscopy [76], limited to their quasi-static properties or dynamics of liquids under inhomogeneous confinement, concerns the fact that the interfacial liquids are less mobile and usually highly structured. Nonetheless, molecular-level picture of the intermolecular forces in the hydration structure is still lacking. In the following, some more detailed information will be given to present and describe the methods that are already used for the diagnostics of liquid structuring near solid/liquid interfaces.

Surface forces apparatus (SFA) and atomic force microscopy (AFM) are well-established approaches to measure distances, normal or friction forces between interacting surfaces across the liquid media [9, 17]. These techniques have contributed the most in the development of modern surface science. These approaches are based on measuring the interaction force between two surfaces (or between a surface and an AFM tip) as a function of distance, with a high precision distance control. In case of SFA experiment, the fluid is placed between two surfaces, both flat-curved and

curved-curved configurations are possible. Quasi-static elastic and inelastic properties of liquids near the interfaces may be measured and one can obtain the information of electrostatic forces, Van der Waals forces, and also solvation (hydration) forces as a function of the thickness of confined liquids. In case of AFM, the liquid is compressed between the solid substrate and spherical AFM tip which induces the residual inhomogeneous stresses in the liquid. Since both methods use curved surfaces or tips to confine the liquid molecules at the nanometer scale, these invasive methods were relevant only for the study of inhomogeneously confined liquids.

An other technique widely used for the investigation of interfacial liquids is sum-frequency vibrational spectroscopy (SFVS) [77]. It is a nonlinear laser spectroscopy method that is applied to deduce the composition, orientation distribution, and some structural information of molecules at gas-solid, gas-liquid and liquid-solid interfaces. The application of this method for the investigation of interfacial liquids is possible due to specially designed laser wavelengths that make the energy of output SFVS photons close to the vibration energy of the intramolecular vibrations. In this way, this noninvasive tool provides information about intramolecular vibrations. However, this

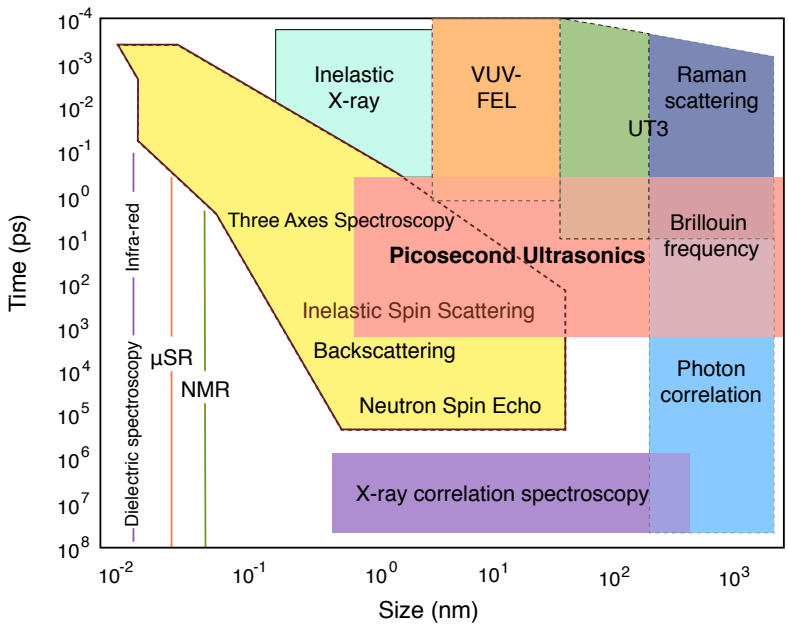

Figure 1.3. Graphical representation of the experimental techniques used for investigation of atomic, molecular, crystalline structure of materials. (VUV-FEL - Vacuum UltraViolet Free Electron Laser; UT3 - Ultrasonic Testing Tandem Technique; NMR - Nuclear Magnetic Resonance; μSR - Muon Spin Rotation).

technique cannot be adopted for the substrates with second-order optical nonlinearity, such as metals, and many semiconductors, and it also lacks the information on the interactions between the layers of the interfacial or nanoconfined liquids.

Inelastic neutron scattering [32], nuclear magnetic resonance, and THz spectroscopy [76] are used to explore high-frequency dynamics of liquid molecules. However, those techniques are insensitive to the local features of interfacial liquids in the sense that they are not sensitive enough to reveal the liquid properties from interfacial to bulk in case of a microscopic liquid solid boundary. They can be utilized to study structured liquids only when all liquid molecules are confined between solid surfaces, such as adsorbed water in nanoporous media. These nanoconfined water is known to exhibit low diffusivity and mobility, and the collective dynamics of hydrogen-bond networks is strongly affected by the shape and composition of the surrounding materials.

Methods such as ultrafast electron crystallography [78], x-ray diffraction [13], and low energy electron diffraction (LEED) [79] provide transient and static information on the structure of the ordered materials. However these methods do not give the information on intermolecular interaction forces of liquid and the dynamics of intermolecular motion in the GHz frequency band. And as a disadvantage, they should be operated under vacuum condition, and at cryogenic temperatures for the study of interfacial liquids, except for x-ray diffraction.

Scanning tunneling microscopy (STM) has the capability to visualise the hopping of liquid molecules between the sites of the substrate atoms and also the aggregation of liquid clusters on solid surfaces. However, it can be used only for sub-monolayer water under vacuum conditions [80].

Of course molecular dynamic simulations is a robust and useful technique in this research area. The simulations may predict the liquid density layering due to nanoconfinement, but only between plane surfaces. There is much less information on the theoretically predicted forces in nanoconfined liquids [20, 30, 53, 81–83]. The theoretical predictions of the dynamic response of nanoconfined liquids under periodic loading and energy dissipation in nanoconfined liquids are absent. At this moment, quantitative first principles predictions of liquid ordering on the surfaces of solids are still beyond scrutiny.

There are many different techniques used for the study of the interfacial liquids and liquid confinement. Unfortunately, all of the above mentioned techniques are too invasive for confined liquids and they cannot provide a spatial resolution in the nanometer range or below, well suited for probing spatial inhomogeneities of structured

liquids near interfaces. In fact, X-ray or Neutron scattering cannot go below the THz frequency range that corresponds to wavelengths in the dispersion curve that would match the collective motion of interfacial liquids. Therefore the GHz-THz frequency bandwidth, which lies in between the highest frequencies that can be accessed in bulk liquids through UV Brillouin spectroscopy and the lowest frequencies that can be accessed in bulk liquids by X-ray or neutron scattering, is extremely valuable for the investigation of interfacial liquids. Unfortunately, this is beyond the capabilities of these scattering techniques.

The non-invasive contactless laser ultrasonic technique which employes ultrafast lasers for the excitation and detection of ultrasound in the GHz-THz frequency range could bridge the frequency gap between UV Brillouin scattering and X-ray or neutron scattering and could shed light on the problem of interfacial liquids. The present work is dedicated to the application of the picosecond laser ultrasonics technique for the investigation of ultrathin liquids. To our knowledge, there is only one single reference in the literature where researchers have employed the picosecond laser ultrasonic technique for the investigation of thin liquid layers [84] and a few references of our own in case of bulk liquids [85, 86]. The work that has been achieved during this PhD is devoted to the implementation of the picosecond laser ultrasonic technique employed in [87] for the study of the GHz ultrasonic transmission through ultrathin liquids. The principle of the method is described in Chapter 2.

1.4.2 Conclusion

Confined liquids are neither like bulk liquids nor like bulk crystalline solids. They appear to be an intermediate kind of matter whose finite size and surface-fluid interactions impart unique structural, thermodynamic, and dynamic properties which are different from bulk. Their inherently heterogeneous character and sluggish relaxation times are reminiscent of super-cooled liquids. The microfluidic and nanofluidic systems are very important from technological points of view. Understanding characteristics such as confinement induced layering (solidification), phase transition and lubrication is of primary importance to many applications of liquids, from energy devices to nanoparticle dispersion.

Chapter 2

Experimental and instrumental developments

As pointed out in the previous chapter, there exist a large number of techniques that can be applied to study the structure and mechanical properties of liquids at interfaces with solids, including scanning probe microscopy, surface force apparatus, diffraction techniques, nonlinear optical spectroscopy, infrared and THz spectroscopy, sum-frequency vibrational spectroscopy, scanning tunneling microscopy, atomic-force microscopy, neutron-scattering and X-ray diffraction. All these methods play significant roles in the development of modern science but they are limited in different ways for the study of structured liquids near interfaces with solids. Picosecond laser ultrasonics [88–90] could be an alternative experimental method providing new information on the liquid structuring at the nanoscale. Ultrafast lasers have been used for the excitation and detection of acoustic waves since the early sixties [91]. It was only in the 80th, after the advent of Titane:Sapphire lasers, that the interest of using subpicosecond laser pulses to excite picosecond acoustic waves (and the picosecond laser ultrasounics, also known as pump-probe technique) has quickly emerged.

This chapter is devoted to introduce the experimental technique that has been used for the investigation of ultrathin liquids. We focus on the description of the generation and detection processes of longitudinal acoustic waves. Herein will be described the developed experimental setup dedicated to the study of liquids, with a close view on the main experimental elements. Particular attention will be paid to the sample cell design and assembling. Some trial alternative setups, which have been used during this work, are presented in the Appendix B.

2.1 Picosecond laser ultrasonics

Picosecond laser ultrasonics refers to the study of materials using high frequency acoustic pulses generated and detected by ultrashort optical pulses. The generation process is schematically shown in Fig. 2.1 [88]. When an ultrashort optical pulse, known as a pump pulse, is focused on a free solid surface, part of the optical energy is absorbed and converted into heat. This heat results in a lattice temperature rise that leads to a thermal stress. The exact depth for the stress generation depends on the material involved and the optical pump wavelength. In metals and semiconductors, for example, ultrashort-timescale thermal and carrier diffusion tends to increase the depth that is initially heated within the first 1 ps. The thermal stress launches an elastic strain pulse propagating in three dimensions. In this work, we will consider only the acoustic propagation normal to the surface (plane longitudinal acoustic waves) because in this direction in an isotropic solid the frequency of such acoustic pulses is the highest and the wavelength smallest. The use of both shear and longitudinal pulses would be advantageous for measuring elastic constants or sound velocities. However, since shear waves excitation requires complex samples such as elastically anisotropic solids cut at oblique angles to the crystal axes [92–94], we will only consider longitudinal acoustic phonons in the following. Right after laser excitation within the optical penetration depth of the thin film, for instance a metallic film, the strain pulse propagates towards the interface between the metal film and the substrate. Then it is partially reflected back to the metallic transducer film and partially transmitted into the substrate. Strain pulses returning to the free surface from the buried interface are detected as a series of echoes (Fig. 2.1(a)) by the second delayed optical pulse, known as the probe pulse. For example, strain pulses propagating back and forth through a thin film produce a decaying series of echoes, from which one may derive, in particular, the film thickness, the ultrasonic speed, attenuation or dispersion [95, 96]. Assuming that the substrate is optically transparent, the transmitted strain into the substrate can be detected by the delayed probe pulse through time-domain Brillouin scattering [97, 98] (detailed hereinafter) from the substrate side (Fig. 2.1(b)). Such detection can give information about the ultrasonic attenuation and speed of sound of the substrate material [99–101].

2.1.1 Thermo-elastic generation of strain and stress

Ultrasound generation by laser-matter interaction depends on several physical parameters linked to the optically excited medium. A pump pulse, focused on the

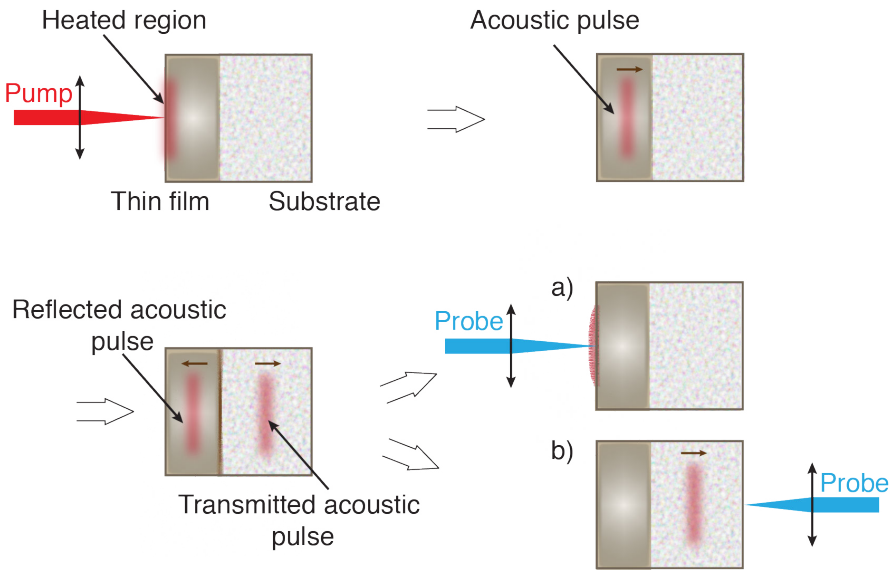

Figure 2.1. Schematic representation of the picosecond laser ultrasonics technique. When a pump pulse is incident on a metal surface, part of the optical energy is absorbed and converted into the heat which results in a lattice temperature rise leading to a thermal stress that launches a strain pulse. The strain pulse arriving at the interface between the thin metal film and the substrate is partially reflected back to the transducer film and partially transmitted into the substrate. The strain pulses returning to the surface from the interface are detected as a series of echoes by the delayed probe pulse(a). The strain pulses propagating through the optically transparent substrate can be detected via time-domain Brillouin scattering by the delayed probe pulse(b).

free solid surface, deposits energy on the optical penetration depth. The electronic kinetic energy of the solid system is increased by photon absorption, which affects the phonon bath. The excess energy causes an increase in amplitude of the vibration of the molecules or atoms, which leads to a shift from the equilibrium position. Collective displacement of excited molecules or atoms lead to changes of the volume of the solid. The propagation component of such collective displacement is an acoustic pulse and the driving mechanism of such generation is called thermal expansion. In the following we describe the theory for the strain generation process. For simplicity we assume a problem in which no acoustic diffraction effects occur, and we neglect the effect of electron or thermal diffusion processes [102–104].

The thermal expansion tensor α_{ij} of a solid is given by [105]

$$\eta_{ij} = \alpha_{ij}\Delta T \tag{2.1}$$

where η_{ij} is the strain tensor, ΔT is a change in temperature compared to the temperature before laser irradiation, $\Delta T = 0$ for $t < 0$ and $\Delta T = \Delta T(ij)$ is independent of time for $t > 0$ (in absence of thermal diffusion). The relation between the stress tensor σ_{ij} and the strain η_{ij} in the presence of a thermal stress σ'_{ij} is defined by [106]

$$\sigma_{ij} = C_{ijkl}\eta_{kl} + \sigma'_{ij} \tag{2.2}$$

where C_{ijkl} is the elastic constant tensor. For isotropic solids, $C_{ijkl}\eta_{kl} = 2\mu\eta_{ij} + \lambda\eta_{kk}\delta_{ij}$ ($\delta_{ij} = 1$ when $i = j$ and $\delta_{ij} = 0$ contrarily), where μ and λ are elastic constants (Lamé constants), and $\alpha_{ij} = \alpha\delta ij$, where α is the coefficient of linear thermal expansion. Therefore,

$$\sigma'_{ij} = -(2\mu + 3\lambda)\alpha\delta_{ij}\Delta T \tag{2.3}$$

otherwise,

$$\sigma'_{ij} = -3B\alpha\delta_{ij}\Delta T \tag{2.4}$$

with $(2\mu + 3\lambda) = B$, B being the bulk modulus. The generated thermal stress is hydrostatic and negative for positive α and ΔT.

A. Strain propagation in single layer structure

Let us consider the experimental situation shown in Fig. 2.2(a) of a thin film of thickness d deposited on a semi-infinite substrate. We assume that the area heated by the laser pulse is very large relatively to the film thickness, so that ΔT, σ and η only depend on the distance from the surface. In such case of one-dimensional problem, $\Delta T = \Delta T(z, t)$ is a function of depth z and time only, where $z = 0$ corresponds to the sample surface and $+z$ is directed into the material. The non-zero tensor component is only η_{zz}. Hence,

$$\sigma_{zz} = (2\mu + \lambda)\eta_{zz} - 3B\alpha\Delta T(z) = \rho_0 c_l^2 \eta_{zz} - 3B\alpha\Delta T(z) \tag{2.5}$$

with c_l the longitudinal sound velocity and ρ_0 the material density. The dynamic process of longitudinal strain propagation in a laser-excited metallic film can be examined

by solving the equation of elasticity

$$\rho_0 \frac{\partial^2 u_z}{\partial t^2} = \frac{\partial \sigma_{zz}}{\partial z}. \tag{2.6}$$

For an ultrashort optical pulse, the laser absorption at the surface of a homogeneous isotropic solid decays exponentially following the profile of laser intensity in skin layer, as for the temperature spatial profile $\Delta T(z)$ since we neglect thermal diffusion which happens at longer timescales. The amplitude can be expressed for two cases, $t < 0$, $\Delta T(z,t) = 0$ and for $t > 0$,

$$\Delta T(z,t) = \frac{(1-R)Q}{AC\zeta_0} e^{-\frac{z}{\zeta_0}} \equiv T_0 e^{-\frac{z}{\zeta_0}} \tag{2.7}$$

where R is the optical reflectivity of the film, Q is the deposited energy by the optical pulse, A is the area over which the energy Q is distributed, C is the specific heat capacity, ζ_0 is the optical absorption depth of the laser pulse light and T_0 denotes the temperature rise at the free surface. Since a restoring force cannot exist at the free surface, the boundary condition restricts any stress perpendicular to the surface at the surface itself. Thus, $\sigma_{zz} = 0$ at $z = 0$, which means from (2.5) and (2.7) that the strain at the free surface and at $t > 0$ follows,

$$\eta_0 = \frac{3B\alpha}{\rho_0 c_l^2} T_0. \tag{2.8}$$

Taking into account the following relationship [88],

$$3B = \rho_0 c_l^2 \frac{1+\nu}{1-\nu}, \tag{2.9}$$

where ν is the Poisson's ratio, the strain at the free surface in Eq. (2.8) can be expressed in the form,

$$\eta_0 = \frac{1+\nu}{1-\nu} \alpha T_0. \tag{2.10}$$

From Eq. (2.5) and (2.6), we can obtain

$$\frac{\partial^2 u_z}{\partial t^2} = c_l^2 \frac{\partial^2 u_z}{\partial z^2} + \frac{c_l^2 \eta_0}{\zeta_0} e^{-\frac{z}{\zeta_0}}. \tag{2.11}$$

The solution of Eq. (2.11) for $z > 0$, which is not straightforward [88], is given by

$$\eta_{zz} = \eta_0 e^{-\frac{z}{\zeta_0}} - \frac{\eta_0}{2} \left((e^{-\frac{-z+c_l t}{\zeta_0}} + e^{-\frac{|z-c_l t|}{\zeta_0}} sgn(z - c_l t) \right). \tag{2.12}$$

The simulation of the strain propagation following Eq. (2.12) is shown in Fig. 2.2 (b). The strain consists of a constant first term and the propagating second term. The propagating component is bipolar because the reflection coefficient for the strain at the surface is - 1. The region near $z = 0$ has a time-independent strain due to thermal expansion. The second part of the strain is a pulse which propagates away from the free surface at the speed of longitudinal sound c_l. It consists of two decaying exponentials stitched together with opposite signs. The time it takes for the strain to reach a significant strength is $\sim \zeta_0/c_l$, the sound propagation time across ζ_0. The inverse of this time is related to the frequency bandwidth of the excited ultrasonic pulse. After propagation across the thin metal film the strain will be reflected at the interface with the substrate (not included).

In case of a thin metal film, the launched strain pulses propagate back and forth through the transducer film of thickness d, make several round trips, and are partially transmitted into the substrate each time they arrive at the interface. The amplitude of the multiple reflected and transmitted waves incident normally at the interface between the transducer film and the substrate can be calculated from the coefficients of acoustic reflection and transmission at the interfaces. These coefficients are obtained by assuming that the displacements and the stresses must be equal at the interfaces. Thus, for $z = d$, it is required that

$$u_i + u_r = u_t \qquad and \qquad \sigma_i + \sigma_r = \sigma_t \tag{2.13}$$

where i, r and t correspond to incident, reflected and transmitted waves. After some calculation, the reflection R_σ and transmission T_σ coefficients of the stress (pressure) can be expressed and take the well known form,

$$R_\sigma = \frac{\sigma_r}{\sigma_i} = \frac{Z_2 - Z_1}{Z_1 + Z_2} \tag{2.14}$$

and

$$T_\sigma = \frac{\sigma_t}{\sigma_i} = \frac{2Z_2}{Z_1 + Z_2}, \tag{2.15}$$

where Z_1 and Z_2 correspond to the acoustic impedances, that are linked to the density and speed of sound of the materials through $Z_{1,2} = \rho_{1,2}c_{1,2}$. We recall that (1) denotes the thin transducer film and (2) the semi-infinite substrate. In general, since the detection process involves the acoustic strains rather than the acoustic stresses, it is preferred to express the reflection R_η and transmission T_η coefficients of the strains

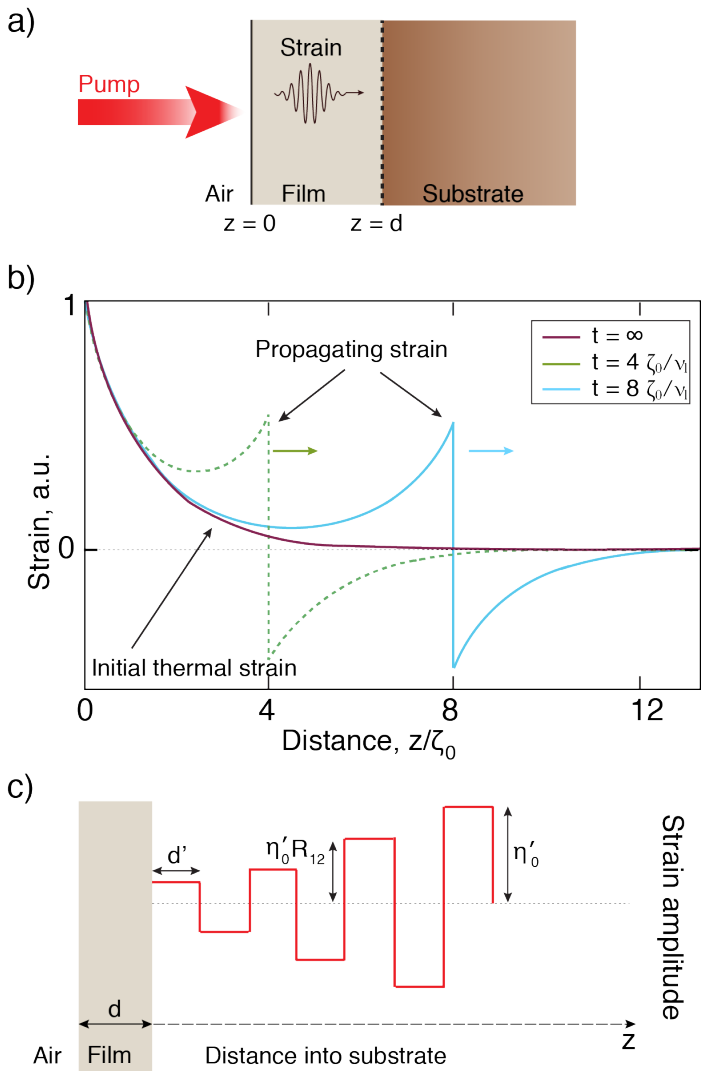

Figure 2.2. (a) Sketch of the experiment. (b) Calculated longitudinal strain distribution η_{zz} at different times after excitation at $t = 0$ of a metal film free surface from an ultrashort pump pulse (with ζ_0 being the optical absorption length and c_l the longitudinal speed of sound). Acoustic diffraction and any electron and thermal diffusion processes are neglected. (c) Schematic shape of the acoustic strain pulse after being transmitted from a thin transducer film of thickness d into a substrate. R_{12} corresponds to the acoustic reflection coefficient of the transducer-substrate interface, d' is the characteristic spatial extension of the strain modulation in the substrate, η'_0 is the amplitude of the firstly transmitted strain front.

which can be deduced from Eq. (2.14) and Eq. (2.15) as following,

$$R_\eta = \frac{\eta_r}{\eta_i} = \frac{\sigma_r}{\sigma_i} = \frac{Z_2 - Z_1}{Z_1 + Z_2} = R_\sigma \tag{2.16}$$

and

$$T_\eta = \frac{\eta_t}{\eta_i} = \frac{\sigma_t/C_t}{\sigma_i/C_i} = T_\sigma \frac{C_i}{C_t} = \frac{2Z_2}{Z_1+Z_2}\frac{Z_1c_1}{Z_2c_2} = \frac{2Z_1}{Z_1+Z_2}(\frac{c_1}{c_2}), \tag{2.17}$$

where C_i and C_t are the longitudinal elastic coefficients of the transducer film (1) and of the substrate (2), respectively. These coefficients follow the relationship $C_{i,t} = \rho_{1,2}c_{1,2}^2$. While the reflection coefficients R_σ and R_η of the acoustic strain or acoustic stress are strictly identical, it is not the case for the transmission coefficients T_σ and T_η that are not equal at all. In fact following Eq. (2.17), in case of the transmission from a solid to a soft medium such as a liquid medium, the transmission coefficient T_η can even be greater than 1.

The schematic shape of the transmitted acoustic pulse into a substrate is presented in Fig. 2.2(c). It corresponds to an hypothetic situation where the whole film of thickness d would be homogeneously laser excited in depth. Successive strain pulses are transmitted into the substrate with different amplitudes determined by the transmission and reflection coefficients of the strain expressed in Eq. (2.17). At the free surface (the interface transducer film/ air), the acoustic pulse is completely reflected with a sign change which transforms the incoming compressive strain into a tensile strain. The amplitude η_0 of the strain front transmitted into the substrate is

$$\eta_0' = \frac{1+\nu}{1-\nu}\alpha T_0 \frac{2Z_1}{Z_1+Z_2}\frac{c_1}{c_2} = \eta_0 \frac{2Z_1}{Z_1+Z_2}\frac{c_1}{c_2}. \tag{2.18}$$

The time duration of the acoustic waves being an invariant in the propagation, the characteristic spatial extension of the strain modulation $d' = d(c_2/c_1)$ is different from that in the transducer of thickness d because of the change in speed of sound during the transmission from the transducer to the substrate. Therefore, when the strain is transmitted from one to another medium with different acoustic speeds, it experiences a change in its spatial distribution to keep its temporal duration. For instance, the transmission from a solid to a soft material for which $c_1 > c_2$ impedes an increase in the spatial extension of the acoustic strain. Additionally, in order to comply with the acoustic conservation law of the "surface", when the spatial distribution of the strain broadens, then the strain amplitude tends to decrease. *Vice versa*, when the strain spatial distribution becomes narrower, it is followed by a decrease in the strain amplitude.

B. Strain propagation in a multilayer system

The strain propagation in case of single layer structure is a quite simple process. In case of a multilayer system with several interfaces, the analytical strain propagation

expression is more complicated. In this case, the multiple reflections and transmissions have to be taken into account. Let us consider the multilayer system depicted in Fig. 2.3(a). At zero time delay ($t = 0$) between the pump and probe pulses, the stress is laser generated by the pump pulse in medium 1 (this region is indicated in red). Subsequently, this strain is divided into two parts. At later time instants $t_1 \neq 0$, half of it propagates in the $+z$ direction and gets partially transmitted in medium 2 and partially reflected back to medium 1, the second half remains in medium 1 and propagates in the opposite direction (along $-z$ direction), see Fig. 2.3 (b). The strain which is transmitted into medium 2 propagates at later times $t_2 > t_1$ across medium 2 and further transmitted in medium 3 in a time t_3 that corresponds to the acoustic time of flight through medium 2. Technically, in the experimental situation that we have investigated further that will be described in the next chapters, the probe light detects the acoustic strain once it gets transmitted into medium 3. Therefore we are mainly concerned about the strain transmission from medium 1 to medium 3 and the good acoustic matching of the overall acoustic transmission of the strain through the three medium. Hence, the total strain transmission may be obtained from (2.17) and extended as

$$T_{\eta,total} = \frac{4Z_1Z_2}{(Z_1+Z_2)(Z_2+Z_3)}\frac{c_1}{c_3} \tag{2.19}$$

In order to quantify the strain propagation and transmission though a practical sample structure, let us take a multilayer structure analogous to the multilayer structure used in our experiments and presented in Fig. 2.3 (a). The structure is composed of Silicon as medium 0, Chromium as an optical transducer medium 1, glycerol as a liquid medium 2 and SiO_2 as a detection substrate medium 3 (the parameters of each medium are detailed in annexe). At first (at initial time $t = 0$), the strain of arbitrary amplitude of unity and arbitrary duration of 10 ps is laser generated in the Cr film. From the speed of sound in chromium of 5940 m/s, the spatial distribution and modulation of such arbitrary strain is 59.4 nm, as depicted in Fig. 2.3 (c). Half of this strain is directly transmitted into the adjacent glycerol film ($t \neq 0$) and shrinks to 28 nm because of the twofold decrease in the speed of sound, then it gets transmitted into the SiO_2 detection substrate and comes back to approximately its initial spatial distribution 59.4 nm. Note that the fact that the spatial distribution shrinks in the liquid means that the acoustic wavelength decreases in the liquid, which means that the ultrasounds get higher spatial sensitivity inside the liquid itself than inside the surrounding solid materials. According to Eq. (2.19) the transmitted strain front undergoes small losses during the transmission from the Chromium film up to the SiO_2 substrate through the liquid film. We calculate $T_{\eta,total} = 0.79$, that means

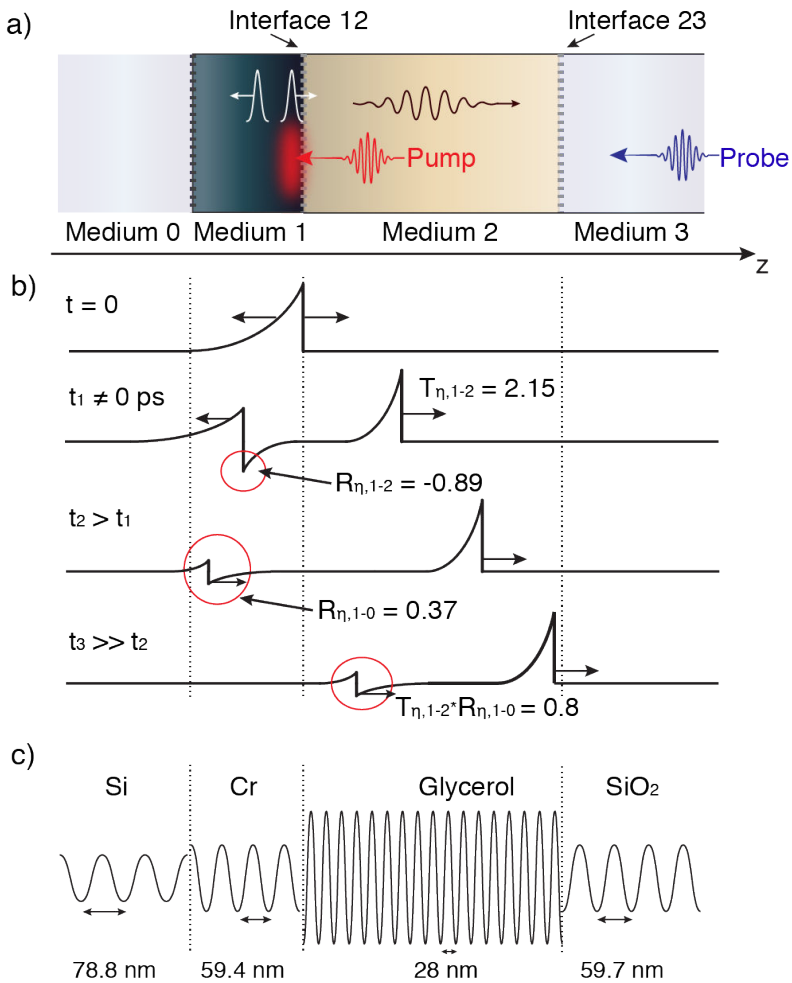

Figure 2.3. (a) Schematic representation of a multilayer system and (b) graphical description of the strain propagation through the multilayer system at different times. Initially the optical pump pulse is absorbed in the metallic film, launching a stress that is split into two parts, one part η_+ propagates in the $+z$ direction, the other one η_- in the $-z$ direction. At some time ($t > 0$ ps), η_+ is transmitted directly into medium 2 with small losses at interface 1-2 because of the acoustic reflection. The overall strain detected in medium 3 (at time moment $t > t_3$) is the superposition of the fastest strain front of maximum amplitude followed by a small part of the strain that was reflected at the interface 1-0 and transmitted to medium 2 and medium 3. (c) Schematic view of the spatial acoustic strain profile in the different media Si, Cr, Glycerol and SiO_2 analogous to the multilayer structure used in our experiments described in the next chapters. By passing from one medium to another with different speeds of sound and acoustic impedances, the strain undergoes spatial modifications of its shape in order to maintain its temporal duration.

that 79 % of the generated strain in Cr gets transmitted through the two interfaces between these materials. In fact, the final total strain propagating in the SiO_2 substrate is composed of the strain directly transmitted from Cr to glycerol and SiO_2, and a small part of the strain initially propagating in the $-z$ direction and reflected at the interface between Silicon and Chromium and then transmitted to glycerol and SiO_2. The contribution of such reflected strain on the final total strain propagating in the SiO_2 substrate can play an important role in case of acoustic impedances mismatch between the Cr transducer film and the Si substrate and should perhaps be taken into account as well. The amplitude of this reflected strain in case of our selection of materials is only $\sim$ 35% (we calculate $R_{\eta,1-0} = 0.35$) of the main strain that should not alter the overall strain detection by the probe pulse in the SiO_2 substrate. No acoustic attenuation effect was taken into account in our simple modeling, which means that the true reflected strain contribution is smaller in reality. Note that, as expected, the shrinking of the spatial distribution in glycerol induces an increase of the acoustic strain amplitude in glycerol, as depicted in Fig. 2.3 (b) and (c).

The influence of the transducer film thickness and in particular the influence of the above mentioned reflected strain for our optical measurements can be seen in Fig. 2.4. Thin films of Cr of different thicknesses ranging from 30 to 100 nm

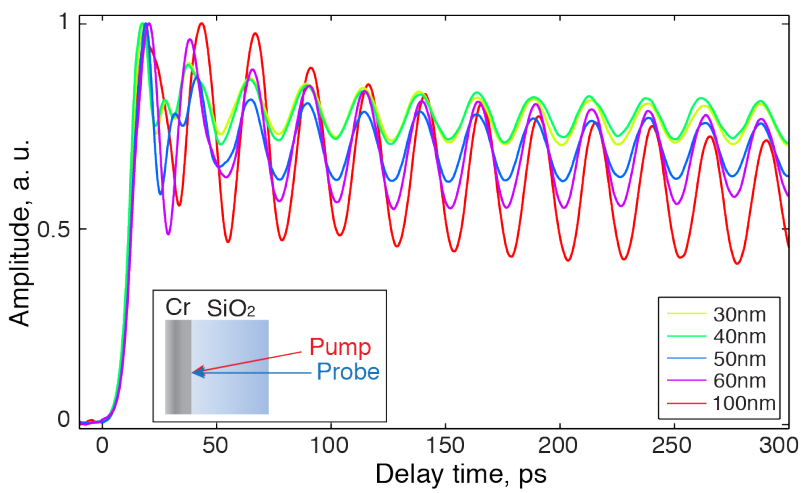

Figure 2.4. Transient reflectivity change of several Cr/SiO_2 samples of different Cr thicknesses. The inset shows the experimental single layer system. Upon laser generation in the Cr film, the acoustic strain is transmitted into the adjacent SiO_2 substrate where it is detected by delayed light probe pulses through Brillouin light scattering. The time oscillations at the frequency $f = 41$ GHz correspond to the Brillouin frequency in SiO_2.

were deposited on SiO_2 substrates by the evaporation method. At $t = 0$ ps the optical pump pulse gets partially absorbed by the Cr film, producing the strain. The strain pulse is then partially transmitted into the SiO_2 layer where it is detected by a delayed optical probe pulse by time-domain Brillouin light scattering (described in the following section 2.1.2). The sharp peak near $t = 0$ ps in Fig. 2.4 is caused by the initial excitation of the electronic system by pump pulse. The outward propagation of the strain pulse through the transparent SiO_2 substrate produces Brillouin oscillations arising from the interference between the light probe pulse reflected at the surface and the probe scattered by the propagating strain pulse. The frequency f of these Brillouin oscillations is given by $f = 2nc/\lambda =$ 41 GHz, where λ is the probe wavelength, n is the refractive index and c is the speed of sound in SiO_2. As we can notice in Fig. 2.4, the amplitude of the Brillouin oscillations increases with an increasing of the Cr film thickness. In fact this effect, linked to the Cr film thickness, can be simply explained by the contribution of the reflected strain η_- at the Cr/Si interface. As mentioned above, about $\sim$ 35 % of the strain propagating in SiO_2 comes from the reflection at the Cr/Si interface. Depending on the metal film thickness, the reflected strain is time delayed since it takes different times to make a round trip in the Cr film of thickness d and to cross the Cr/glycerol interface. This time should be as much as possible similar to the period of Brillouin oscillations so that the weak reflected strain would interfere constructively with the monochromatic Brillouin oscillation. In other words, to achieve the maximum detection efficiency, η_+ and η_- should be in phase. Accordingly, by knowing the Brillouin period of the detected acoustic waves, we can beforehand optimize the experimental multilayer system to achieve maximum detected Brillouin amplitude. From our calculations, we get $1/f = 24$ ps and $\tau_{100\ nm} = 33$ ps, $\tau_{60\ nm} = 20$ ps, $\tau_{50\ nm} = 16.5$ ps, $\tau_{40\ nm} = 13.5$ ps, $\tau_{30\ nm} = 10$ ps. We can conclude that among the presented thicknesses, the 60 mn and the 100 nm Cr films are the most efficient. At the same time, we are concerned not only about the strain generation efficiency but also about the surface quality that deteriorates with film thickness growth.

2.1.2 Detection of acoustic waves after propagation through a liquid film

In the following we will investigate meticulously the Brillouin scattering detection of strain pulses in the situation of a multilayer system such as the one presented in Fig. 2.3. This multilayer structure is relevant to our experimental scheme where a thin liquid film of interest is confined between two solid boundaries. This system

forms an optical and an acoustical cavity at the same time. The laser irradiation by the pump pulse of the transducer film launches an acoustic wavepacket δ_{ac} in the $+z$-direction. This acoustic wavepacket propagates through the liquid film of thickness d and then gets transmitted into the transparent substrate. We will focus on the analysis of the Brillouin scattering detection of the acoustic wavepacket after traversal of the liquid film and once it gets transmitted and propagates in the transparent detection substrate.

A. Time-domain Brillouin scattering

This section is an introduction of the basic principles of time-domain Brillouin light scattering (TDBS). The main principle of TDBS is the scattering of photons from sound waves and the interference of the multiply reflected light beam, as sketched in Fig. 2.1.2 (a). A pump laser beam generates an acoustic wavepacket at the transducer film that propagates deep into the substrate at the speed of sound c. A time delayed probe beam gets reflected at the transducer film and scattered by the propagating acoustic wavepacket. Depending on the distance from the transducer - wavepacket, the reflected probe beams may either interfere constructively or destructively with each other. This effect manifests itself in the time domain as an oscillatory interferometric modulation of the total reflected intensity as a fonction of time, see Fig. 2.1.2 (b). The analysis of the Brillouin signal can give information on the speed of sound and on the attenuation of the acoustic waves in the substrate.

The Brillouin scattering oscillations can be described by the functional form

$$\triangle R = A_0 \exp(-\Gamma t) \cos(2\pi f t + \phi) \tag{2.20}$$

where A_0 is the amplitude at zero time delay between pump and probe pulses, Γ is the attenuation rate and ϕ is an arbitrary phase.

The phonon frequency

$$f_{BS} = \frac{2n(\lambda)c_l}{\lambda} \cos\theta \tag{2.21}$$

is usually named the Brillouin frequency. Where θ is the back-scattering angle. A measurement of this frequency can give the sound velocity when the refractive index $n(\lambda)$ at the probe wavelength of the material is known. This type of measurements in an optically transparent medium is sensitive to the acoustic attenuation $\Gamma(f)$, that is related to the full width at half maximum (FWHM) $\triangle f/2$ of the Brillouin peak in a

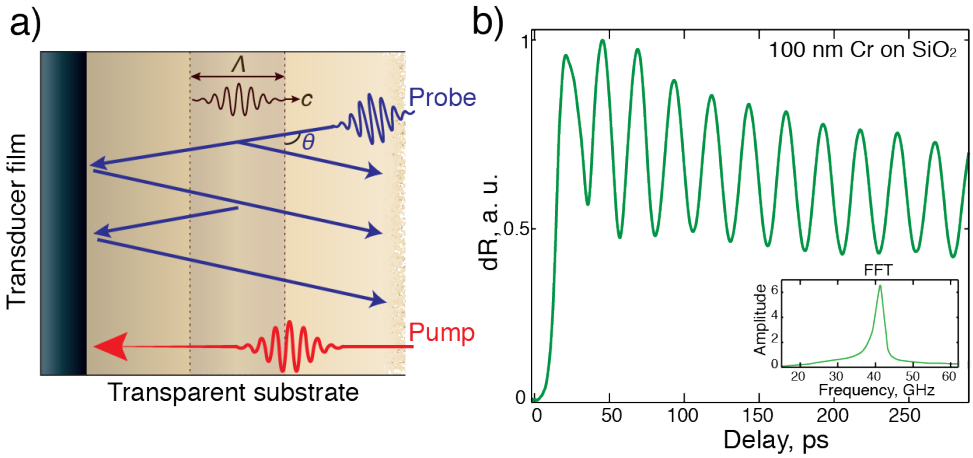

Figure 2.5. (a) Principle of time-domain Brillouin light scattering process. The acoustic wavepacket generated at the transducer film by the pump pulse propagates through the substrate at the speed of sound c. The probe light beam obliquely incident at some angle θ to the surface gets scattered several times by the acoustic wave due to acoustically induced changes in the refractive index. The reflected and scattered probe beams interfere constructively or destructively. (b) Brillouin signal obtained from a 100 nm Chromium film on a SiO_2 substrate. The inset presents the fast Fourier transform (FFT) of the signal showing a peak centered at 41 GHz, that corresponds to the Brillouin scattering frequency in SiO_2.

frequency-domain Brillouin scattering measurements by

$$\Gamma = 2\pi \frac{\triangle f}{2} \tag{2.22}$$

In real experimental conditions, the functional form of Eq. (2.20) does not allow the correct extraction of the acoustic parameters. The fitting of the raw data is no longer precise because of a smooth varying background (i.e. thermal background). This varying background is due to the change in reflectivity of the transducer film because of the temperature change caused by the pump pulse. So for proper fitting procedure, it is either required to perform the numerical time derivative of the recorded signals in order to filter the slow varying thermal component or, more appropriately, to include a term corresponding to the thermal background in the functional form of the reflectivity change of Eq. (2.20). As it was shown in [101], a single exponential

decay is usually sufficient, and Eq. (2.20) transforms into

$$\triangle R = A_0 \exp(-\Gamma t) \cos(2\pi f t + \phi) + B_0 \exp\left(-\frac{t}{\mu}\right) + \delta \tag{2.23}$$

B_0 being the initial amplitude of the temperature induced reflectivity change at the transducer film that cools within a characteristic time constant μ, δ is an artificial offset due to lock-in detection. For simplicity, we often perform the time derivative of the recorded signals in order to filter out the thermal background. It does not require any fitting model but it has the disadvantage to enhance the signal to noise on the time derivative Brillouin signal.

B. Theory for the optical detection of acoustic waves conforming our experimental scheme

Let us consider the multilayer system presented in Fig. 2.6 to analytically describe the optical detection of acoustic waves for the sample configuration used in our experiments. We recall that the acoustic waves are experimentally detected in the detection substrate after propagation through the liquid of thickness d. We will demonstrate that, even if the Brillouin scattering detection process takes place in the detection substrate, the optical time-domain Brillouin scattering signal gather crucial information on the acoustic properties of the liquid layer.

The electric field of an incoming optical pulse E_{in} at some position z at time t, can be written, assuming the probe pulse is at normal incidence to the plane of the acoustic waves, as

$$E_{in} = E_0(z,t) \exp(i[\omega t + k_2 z + (k_1 - k_2)d]) \qquad z \geq d \tag{2.24}$$

where $E_0(z,t)$ is the electric field envelope function, k_1 and k_2 are the wave vectors in the liquid and in the detection substrate, respectively, and ω is the angular frequency. We will further consider E_0 as a constant and the phase of the electric field is arbitrarily chosen so that the electric field of femtosecond optical probe arrives at the metal surface at $t = 0$. The complete electric field of the outgoing probe pulse E_{out} is the superposition of all electric fields reflected at the transducer-liquid and liquid-substrate interfaces ($E_{out,i}$ at the sketch), it follows [86]:

$$E_{out} = rE_0 \exp(i[\omega t - k_2 z + (k_1 + k_2)d]) \qquad z \geq d \tag{2.25}$$

with

$$r = r_{21} + \frac{r_{10}t_{21}t_{12}exp(-2ik_1d)}{1 - r_{10}r_{12}exp(-2ik_1d)} = |r|\, e^{i\phi} \tag{2.26}$$

Here r is the overall reflection coefficient whose expression is similar to the Fabry-Perot cavity, with r_{21}, r_{12}, r_{10} the Fresnel reflection coefficients from the substrate-liquid, liquid-substrate and liquid-transducer interfaces, t_{21}, t_{12} are the Fresnel transmission coefficients through the substrate-liquid and liquid-substrate interfaces, correspondingly, and ϕ the optical phase shift.

The general electromagnetic wave equation for the electric field can be written in the form,

$$\Delta\overrightarrow{E} - \overrightarrow{\nabla}(\overrightarrow{\nabla}\overrightarrow{E}) + \frac{\omega}{c^2}(\epsilon + \Delta\epsilon(z,t))\overrightarrow{E} = \overrightarrow{0}, \tag{2.27}$$

with ϵ being the dielectric constant and $\Delta\epsilon(z,t)$ the acoustic strain-induced change in the dielectric function. Based on the fact that light travels much faster than sound

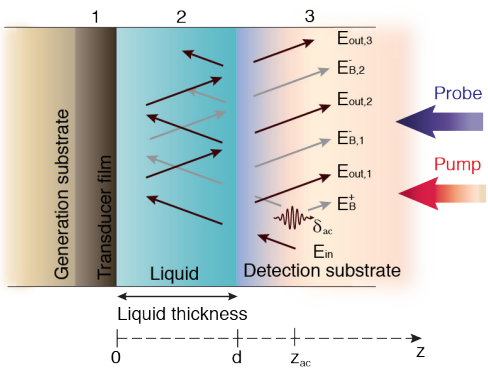

Figure 2.6. Schematic representation of our experimental multilayer liquid system. The liquid is confined between two solid media, the transducer film coated on the substrate on one side and the transparent detection substrate on the other side. The probe pulse is considered being at normal incidence to the sample surface or the plane of the acoustic waves. The acoustic wavepacket is generated by a pump pulse at the transducer film, then propagates in the $+z$ direction across the liquid film and after transmission to the detection substrate, it is detected by time-domain Brillouin scattering. δ_{ac} denotes the acoustic wave that propagates away from the transducer - liquid interface. E_{in} is the incoming electric field of the probe pulse and E_B^+ is a small portion of the backscattered E_{in}. $E_{B,1}, E_{B,2}$ represent backscattered portions of the electric field reflected by the transducer film $E_{out,1}$. Some portion of the reflected electric field $E_{out,1}$ makes few round-trips in the liquid film before being transmitted to the detection substrate. All these electric fields superimpose and interfere with each other and produce a Brillouin scattering interferometric signal.

and therefore the photoelastic interaction can be considered as quasistatic, we have taken the hypothesis that the time derivative of the photoelastic interaction can be neglected. Because of the weak nature of the photoelastic interaction, it is sufficient to only include first-order terms in the solution of Eq. (2.27) since higher orders corresponding to light scattered multiple times by the acoustic wave can be neglected. Under these assumptions, the first-order solution for the backscattered probe light from the photoelastic interaction can be written in the form [86],

$$E_B^+ = E_0 \exp(i[\omega t - k_2 z + (k_1 + k_2)d]) \int_d^z -i \frac{k_2 \Delta\epsilon(z', t)}{2n^2} e^{i2k_2(z'-d)} dz'. \tag{2.28}$$

A good approximation based on the fact that the acoustic wavepacket extension is small compared to the probe optical wavelength is that the acoustic wave is a delta function in space, localized at the coordinate $z = z_{ac}$ at time t. The solution for a longitudinal acoustic wave is

$$E_B^+ = r_B E_0 \exp(i[\omega t - k_2 z + (k_1 + k_2)d + 2k_2(z_{ac} - d)]) \qquad z \geq z_{ac} \tag{2.29}$$

with

$$r_B = \frac{1}{2} i n^2 k_2 p_{12} \eta_{33}^0 = |r_B| \, e^{i\psi} \tag{2.30}$$

where $r_B E_0$ is the amplitude of scattered electric field, n is the index of refraction, p_{12} is the photoelastic coefficient of the substrate linked to the longitudinal strain $\eta_{33}^0(z,t)$ and ψ is the phase of the complex number r_B. A more general solution would require to integrate over the spatial coordinate z, however, the simplified solution (2.28) is accurate and relevant. Similarly, the scattered electric field E_B^- coming up from the scattering of the probe light reflected by the cavity E_{out} is given by,

$$E_B^- = r^2 r_B E_0 \exp(i[\omega t - k_2 z + (k_1 + k_2)d - 2k_2(z_{ac} - d)]) \qquad z \geq z_{ac} \tag{2.31}$$

The overall intensity measured by the photodiode involves the scattered electric fields E_B^+, E_B^- and the outgoing electric field of the reflected unscattered probe light E_{out},

$$\begin{aligned} I = \left| E_B^- + E_B^- + E_{out} \right|^2 = I_0 (|r|^2 \, 2 \, |r| \, (1 + |r|^2) \, |r_B| \cos(2k_2(z_{ac} - d) - \phi) \cos\psi \\ + 2 \, |r| \, (1 - |r|^2) \, |r_B| \sin(2k_2(z_{ac} - d) - \phi) \sin\psi)) \end{aligned} \tag{2.32}$$

In case of a transparent medium, n and p_{12} are real numbers that means that r_B is

purely imaginary with $\psi = \pm\pi/2$ in Eq. (2.30)). Finally, the intensity change follows,

$$\Delta I = \pm 2I_0\sqrt{R}(1-R)\,|r_B|\sin\left(2k_2(z_{ac}-d)-\phi\right) \tag{2.33}$$

Taking into account that the acoustic wave propagates at the speed of sound $c_{l,i}$ (i=1 or 2 corresponds to the liquid or the substrate), the position z_{ac} changes depending on the pump - probe delay time t, the position of the acoustic wave will change as $d + c_2(t - d/c_1)$ and Eq. (2.33) becomes

$$\begin{aligned}\Delta I(t) &= \pm 2I_0\sqrt{R}(1-R)\,|r_B|\sin\left(2\pi\nu_{2,B}t-\phi_B\right) \\ &= I_{ac}(\nu_{2,B})\sin\left(2\pi\nu_{2,B}t-\phi_B\right)\end{aligned} \tag{2.34}$$

where $\nu_{2,B}$ determines the Brillouin modulation frequency, $\phi_B = \phi_1 + \phi$ determines the Brillouin phase shift of the signal at $\nu_{2,B}$, ϕ_1 is the acoustic phase shift and ϕ is the optical phase shift and $I_{ac}(\nu_{2,B})$ is the Brillouin scattering amplitude.

The optical phase shift can be determined as

$$\phi \sim -2k_1 d \tag{2.35}$$

which implies the optical phase shift is primarily due to the travel time of the optical probe with wave vector k_1 through the liquid of thickness d. Since the Brillouin frequency in the liquid follows $2\pi\nu_{1,B} = 2k_1c_1$, the optical phase shift can be written as

$$\phi \sim -2k_1 d = -2\pi\nu_{1,B}d/c_1. \tag{2.36}$$

Finally, the overall phase shift of the signal at the frequency $\nu_{2,B}$ measured by the photodiode is given by

$$\phi_B = \phi_1 + \phi = 2\pi(\nu_{2,B} - \nu_{1,B})d/c_1 \tag{2.37}$$

Thus, the measurements of the phase shift ϕ_B is connected to the speed of sound c_1 of the liquid and the liquid thickness d.

The signal level $I_{ac}(\nu_{2,B})$ is proportional to the amplitude of the acoustic wave which decreases exponentially with the liquid thickness. Therefore, the Fourier amplitude of the measured signal from the detection substrate at the frequency $\nu_{2,B}$,

$$\begin{aligned}I_{ac}(\nu_{2,B}) &= 2I_0\sqrt{R}(1-R)\,|r_B| \\ &\propto 2I_0\sqrt{R}(1-R)e^{-\alpha_1 d}\end{aligned} \tag{2.38}$$

is linked to α_1 which is the attenuation coefficient in the liquid film of the acoustic waves. Thus, the Fourier amplitude $I_{ac}(\nu_{2,B})$ of the measured Brillouin signal in the detection substrate enables the measurement of the acoustic attenuation in the liquid film at the Brillouin frequency, even thought the detection occurs in the detection substrate. The intensity of the reflected probe light from the Fabry-Perot cavity also depends on the liquid thickness in Eq. (2.26) since R depends on the cavity thickness d. It is responsible for the heterodyning at the Brillouin frequency $\nu_{2,B}$ and the optical cavity effect has an influence on the amplitude of the measured signal. Thus, the Fourier amplitude of the Fourier transformed measured signal in the detection substrate, I_{ac}, at the Brillouin frequency $\nu_{2,B}$, involves both contributions:

$$I_{ac}(\nu_{2,B}) \propto 2I_0\sqrt{R}(1-R)e^{-\alpha_1 d}. \tag{2.39}$$

However, the impact of the optical cavity effect can be reduced by decreasing the quality factor of the Fabry-Perot cavity, if possible, or by normalizing all recorded signals at different liquid thicknesses by the electronic signal component that appears only at $t = 0$ due to optically excited hot electrons in the transducer film. The amplitude of this electronic component, given by $\delta_e(t) \times E_0(\delta_e(t) \ll 1$, is also heterodyned with the field reflected from the transducer film in the absence of photoexcitation, giving a signal intensity

$$I_e(t) = 2I_0\sqrt{R}\delta_e(t). \tag{2.40}$$

This signal, which has vanished before the acoustic signal arrives, provides a normalization standard for the amplitude of the acoustic signal recorded at each liquid layer thickness and can be used to decrease the influence of the optical cavity effect in the measured Brillouin intensity.

2.2 Details of the experimental pump-probe set-up

This chapter introduces the details of the experimental setup used in this work. As it was mentioned already, picosecond laser ultrasonics technique uses an ultrashort laser system that allows the study of ultrafast processes in materials. The experimental system should perform three main functions: the laser generation of acoustic waves, the efficient laser detection of the reflected light from the acoustic waves and the data acquisition of the optical signals. During my doctoral work, I built a system that permits the successful implementation of all these tasks. A schematic containing the essential features of our pump-probe system is shown in Fig. 2.7. This system was

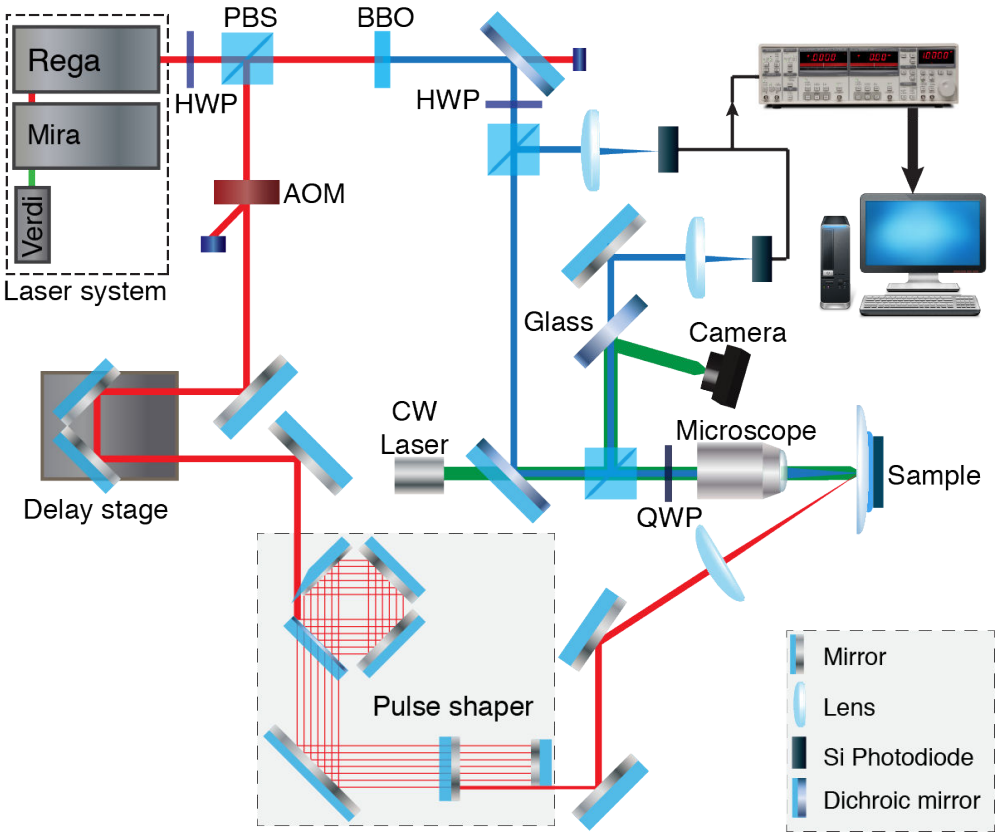

Figure 2.7. Time resolved pump-probe experimental setup. The output of the femtosecond laser system is split into two parts, a pump beam (790 nm) which is used for the generation of acoustic waves and a probe beam (395 nm) that is used for the detection of the acoustic waves propagating in the material. The propagation can be monitored at different time delays by a computer-controlled delay line which enables to delay the pump pulse from the probe pulse with a maximum delay of 2 ns. All the crucial elements of the setup are described in text.

constructed for single side pump - probe measurements, but it is easily changeable for two sides experiments. In the following sections all the experimental issues connected to the generation and detection of picosecond acoustics in ultrathin liquids through the measurement of the optical reflectivity changes will be discussed. Additionally, an overview of the equipments and their crucial role in the setup will be provided.

2.2.1 Femtosecond laser system

The Coherent system consists of:

- Verdi G5 (5 W, 532 nm, CW) used as pump laser for Mira - 900,
- Verdi G12 (12 W, 532 nm, CW) used as pump laser for Rega - 9000,
- Mira - 900 modelocked Ti:Sapphire laser (0.65 W, 700 to 980 nm, 76 MHz nominal),
- Rega - 9000 femtosecond Ti:Sapphire amplifier (1 W, 200 fs, 260 kHz).

This laser system emits a train of pulses with a Gaussian temporal profile with a FWHM of about 260 fs at repetition rate of 260 kHz tuned to a central wavelength of $\sim$ 790 nm. The average output power is about 1 W and the energy per pulse is about 4 μJ. The laser output is used for two experiments at the same time, that means that the main beam is split into two parts of approximately 500 mW power each. The main beam is then divided into two pump and probe beams with a polarizing beam splitter. The pump, the more intense beam, is synchronously modulated at some subharmonic frequency of the laser repetition rate by an acousto-optic modulator (AOM). After the AOM, the pump beam passes through the delay stage which allows a continuous modification of the time difference between the pump and probe pulses of different optical paths. Onwards, the pump beam goes through a pulse shaper called "Death Star" (see details below), and afterwards it is focused on the sample where it is used to generate acoustic waves at a metal transducer film. The probe beam, with significantly weaker intensity, is frequency doubled to 395 nm through second harmonic generation in a nonlinear birefringent crystal of BBO (β - BaB_2O_4). Further, it is separated into two parts. One part goes directly to a reference photodiode, the second part is focused with a 10$\times$ microscope objective at the sample surface to monitor the acoustic waves propagation in the liquid sample. In fact, the probe is split into two beams (so-called reference and probe) to decrease the noise level of the signal, that definitely improves the data acquisition quality. Next we will consider the key elements and their role in the experiment.

Half Waveplate and Polarizing Beam Splitter

To be able to control the beams intensities, the combination of a half waveplate (HWP) and a polarizing beam splitter (PBS) is used several times on the experimental setup. The half waveplate is used to change the direction of the linear polarization that entails a modification of the transmitted and reflected beams intensities through the PBS. This simple method enables balancing accurately the light intensity of both reference and probe beams on the dual detectors, to properly select the pump and probe laser powers on the sample.

Acousto-Optic Modulator

Acousto-optic modulators are used to vary, control or modulate the laser pump beam intensity. In our pump-probe setup the pump beam is modulated in intensity at a given frequency in order to perform lock-in detection that increases the signal-to-noise ratio and enables the detection of very small signals $\sim 10^{-3} - 10^{-6}$. The AOM is supplied by AA Opto - Electronic (AA.MT.110/B40/A1.5 - IR/(Z20)). The sketch of the main principle of the AOM is presented in Fig. 2.8. AOM uses the acousto-optic effect to diffract and shift the frequency of the light using sound waves. Note that the primarily use of the AOM in our setup is to diffract the light, the frequency shift is not relevant. A radio frequency (RF) signal applied to a piezo-electric transducer, bonded to a TeO_2 crystal, generates an acoustic wave. This acts like a "phase grating", traveling through the crystal at the acoustic velocity of the material and with an acoustic wavelength dependent on the frequency of the RF signal. Any incident laser beam will be diffracted by this grating, generally giving a number of diffracted beams. A parameter Q called the "quality factor", determines the interaction regime. In the Bragg regime $Q = 2\pi\lambda L/n\Lambda^2$ »1(λ is the wavelength of the laser beam, n is the refractive index of the crystal, L is the distance the laser beam travels through the acoustic wave and Λ is the acoustic wavelength) and at a single particular incidence angle θ_B, only one diffraction order is produced - the others are annihilated by destructive interferences. The diffraction condition is given by

$$\theta_B = \frac{f\lambda}{2nc_{AOM}} \tag{2.41}$$

where f is the acoustic carrier frequency ($\sim$ 110 MHz), n and c_{AOM} are the refractive index and the sound speed of the AOM crystal, respectively (for TeO_2, n = 2.2 (λ = 790 nm), $c_{AOM} = 4200$ m·s^{-1}. The angle of deviation $2\theta_B$ for TeO_2 cell is equal to 5° and the Bragg diffraction efficiency reaches about 95%. The conditions for maximum Bragg diffraction efficiency is drastic and highly sensitive on the beam size and beam divergence inside the TeO_2 crystal, that have been carefully optimized in our setup with a proper design of a telescope in front of the AOM (not shown in Fig. 2.7). The zero order beam is then forwarded to the delay stage while the first order diffracted beam is dumped. The advantage of using the "0" order beam rather than the "1" order beam, is based on the fact that, first, the zero order beam shape is not altered by the acoustic diffraction, since it is not diffracted, second, the beam is less sensitive to the day-to-day laser beam pointing fluctuation, that facilitates the daily operation of the experiment. The reference frequency of the pump modulation is synchronized with

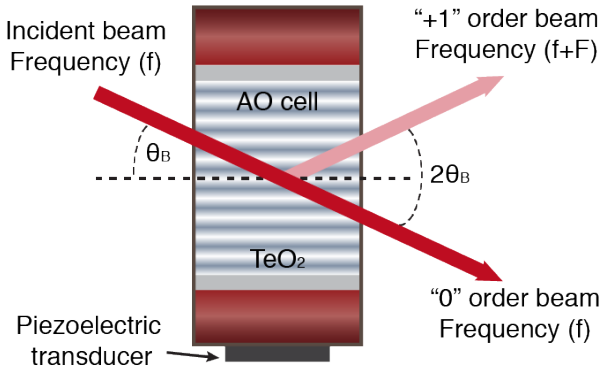

Figure 2.8. Sketch of operation principle of the AOM. The AOM is based on the interaction of sound (RF) and light in a crystalline material (TeO_2). An acoustic wave is generated in the crystal by applying a RF drive signal to a piezo-electric transducer. A modulated acoustic wave propagates in the AO cell and creates areas of compression and rarefraction, causing a refractive index perturbation i.e. an acoustic grating. "0" and "1" orders are respectively the direct beam through the cell and the beam diffracted by the acoustic diffraction grating.

the laser repetition rate in order to select a well define number of pump pulses. This frequency is set to 41 kHz, that corresponds to approximately to a time interval of 3 pump pulses. The reference frequency from the AOM is sent to the lockin amplifier for synchronization.

Delay Stage

The delay stage is a motorized linear translational stage (M - IMS 600PP) purchased at Newport® and computer controlled by a XPS - Q8 Controller. A retroreflector is mounted on this stage that enables to optically delay the pump pulse with respect to probe pulse. The travel range of such stage is 300 mm that corresponds to 2 ns single path delay. The motion speed of the stage is also controlled by the computer through the Labview acquisition program. After the delay line, the pump pulse passes through the pulse shaper often known under the fancy name "Death Star" [101].

DeathStar Pulse Shaper [107]

To enhance the frequency brightness of the Brillouin signal, a pulse shaper is placed on the beam path of the pump to allow the generation of narrowband acoustic waves. The incoming beam is introduced in the system and makes seven round trips inside the heart of the pulse shaper, i.e. the retroreflectors in Fig. 2.9, each time

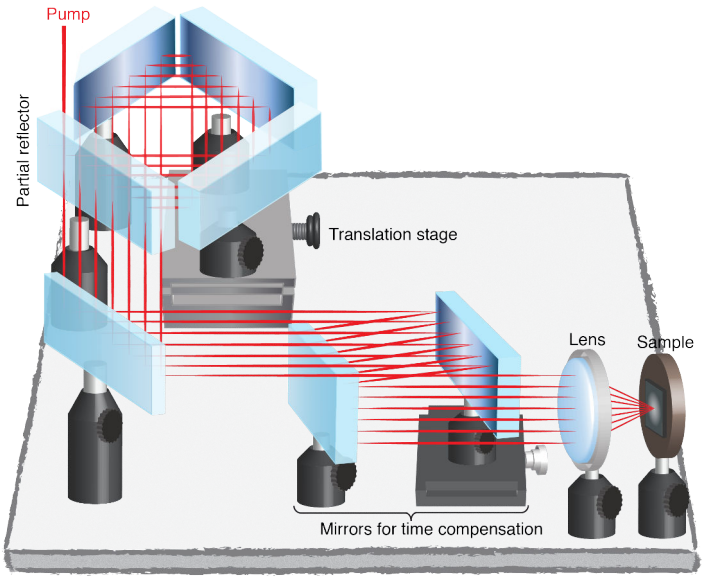

Figure 2.9. Sketch of the compact Death Star pulse shaper. The pump beam is introduced in the system of three mirrors (two of them are mounted on a translation stage) and a partial reflector and makes several round trips in this system, each time slightly displaced relatively to the previous pulse. The partial reflector has seven optical windows with different partial reflectivities, whereby we get seven pump pulses at the output. To compensate the time delay between each of the seven pulses traveling with different distances in the system, two parallel mirrors are set to compensate the round trip length in the circulating system. The seven pump pulses are then focused with a lens on the sample surface.

slightly displaced, so that seven evenly spaced pulses emerge from the partial reflector. The pulse intensities are determined by the partial reflector that has different partial reflectivities in the seven different optical windows. The difference in travel time of each individual pulse is compensated by a pair of parallel mirrors placed after the dual retroreflectors whose distance exactly matches the round trip length in the dual retroreflectors when the translation stage is set at its minimum delay. The pulse shaper allows the generation of an optical pulse sequence of seven pulses with variable repetition rates as low as 1 GHz and as high as 1 THz, selected by moving a single manual translation stage, see Fig. 2.9. The pulse shaper output is then focused onto the sample. The pump beam diameter on the sample surface was typically about 100 μm.

An example of transient reflectivity signal measured with the Death Star pulse shaper is presented in Fig. 2.10. A Niobium thin film was used as a sample. The seven

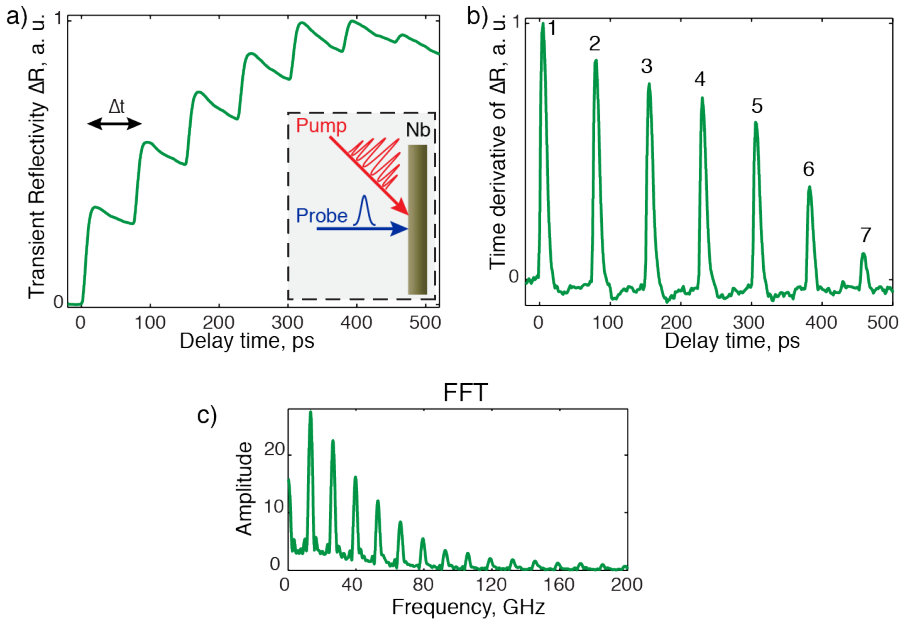

Figure 2.10. (a)Example of a normalized time domain reflectivity signal obtained with the pulse shaper. The optical pulse sequence was focused on Niobium thin film. The time difference between the individual pulses was arbitrarily adjusted to $\Delta t \sim 75$ ps. (b) Time derivative of the measured signal. (c) Frequency spectrum of the reflectivity signal.

peaks in Fig. 2.10 (a) and (b) highlight the arrival time of the seven pump pulses laser exciting the Niobium film. The time difference $\Delta t \sim 75$ ps was arbitrarily chosen to illustrate the capabilities of the pulse shaper in operation. In fact, the time difference is adjustable and can be selected to enhance the detection of a particular single frequency that we want to detect. In this case the time difference Δt of the excited narrowband acoustic wavepacket is set such that the detected frequency equals $f = 1/\Delta t$.

Second harmonic generation in a BBO crystal

As it was mentioned previously, the probe pulse is frequency doubled in a birefringent β - BaB_2O_4 (BBO) nonlinear crystal. BBO crystals are widely used for second harmonic generation (SHG). A scheme of the SHG process is presented in Fig. 2.11. SHG is a nonlinear optical process whereby the incident photons with the same frequency interacting with a nonlinear material are effectively "combined" to generate new photons with twice the energy, and therefore twice the frequency and half the wavelength of the initial photons. When using a wavelength of 790 nm, the SHG

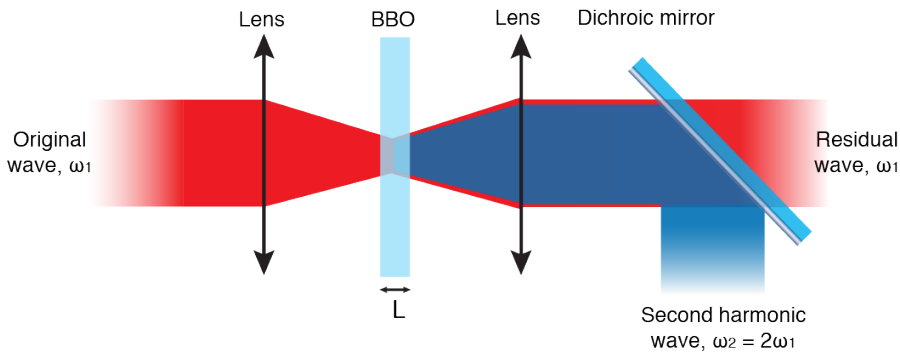

Figure 2.11. Illustration of the optical second harmonic generation process. An incident beam at a wavelength of 790 nm is focused into a BBO crystal. A fraction of the incident light is converted into light at the double frequency, leading to a blue beam at a wavelength of 395 nm. The 395 nm light is then filtered out.

converts the wavelength into 395 nm which lies within the blue light spectrum. The intensity of the second harmonic light scales quadratically with the input intensity. If the phase matching of both 790 nm and 395 nm beams is satisfied ($\Delta k = 0$), the efficiency of the second-harmonic conversion is optimum and the intensity of the second harmonic $I_{2\omega_1}$ can be expressed in the simple form

$$I_{2\omega_1} = \frac{C^2 I_{\omega_1}^2 L^2}{\pi \omega_1^2}. \tag{2.42}$$

The field-gain coefficient C introduced here contains all material properties. The crystal thickness L plays an important role, the thicker crystal is, the more intense the second harmonic will be. In our setup we have used a BBO of 0.5 mm thickness. As for the phase matching conditions, the focusing conditions of the incoming laser light inside the BBO has to be optimized. Experimentally, the SHG efficiency is in the range of 10%.

Probe detection at normal incidence

In order to minimize the probe spot size on the liquid sample, such that the probed region of the liquid can be assumed to be of homogeneous thickness, or at least that the variations of the liquid topography in the probed region can be neglected, we have designed the experiment at normal incidence of the probe light. The advantage of normal incidence detection being that optical aberrations are minimized and, with the use of high quality microscope objectives, the probe spot size on the sample can reach the diffraction limit.

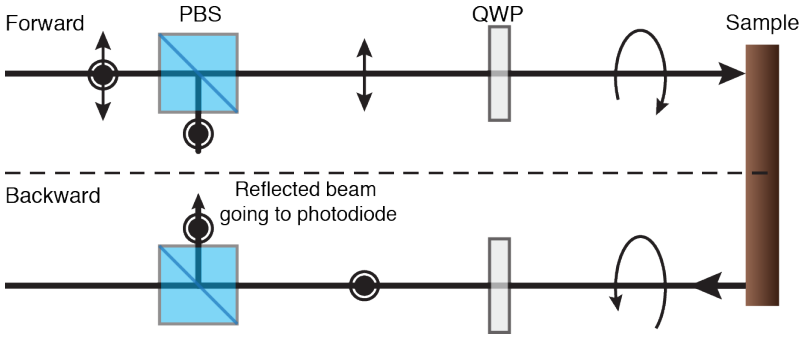

Figure 2.12. Brief illustration of the polarisation change occurring with the combination of a PBS and a quarter waveplate. The transmitted light from the PBS passes through the quarter waveplate, changing its polarization from linear to circular and reflects from the sample. After passing twice through the quarter waveplate, the probe polarization direction becomes vertical and the probe is reflected by the PBS.

In order to comply with this technical constraint, we have used the combination of a polarizing beam splitter (PBS) and quarter wave plate (QWP). The schematic of this setup is shown in Fig. 2.12. The incoming incident probe light passes through the PBS that allows to control the intensities of the reflected and transmitted beams. The horizontally polarized transmitted beam goes through the quarter waveplate that changes the polarization from linear into circular. The probe of circular polarization is then focused by a microscope objective (not shown) on the sample. The sample surface can be modeled as a mirror from which the probe beam is reflected backward along the same path. Since the circular polarization does not change its rotational direction at the reflection of the mirror, a 180 degrees retardation of the circularly polarized light occurs (left circularly polarized light becomes right circularly polarized and viceversa). This entails that after the second pass through the quarter waveplate, the linear polarization is rotated by 90 degrees with respect to the incident probe polarization direction. Therefore, the reflected probe light becomes vertically polarized right before passing a second time through the PBS where it will get reflected and directed to the photodiode.

The microscope objective that we used is a 10× long working distance Mitutoyo objective (M Plan Apo 10x). This objective has an advantage in comparison with traditional convex lenses, such as correction of chromatic and spherical aberrations. It ensures the possibility to get smaller spot diameters on the sample surface. The FWHM spot diameter of the probe laser beam focused at the sample surface that we have measured, using the knife edge technique or the imaging technique, is of $\sim 8\mu\text{m} \pm 1\mu\text{m}$.

2D imaging of the sample surface

In order to facilitate the day-to-day operation of the experiment, we have designed a simple 2D imaging setup of the sample surface. It allows the accurate alignment of the pump and probe beams, overlap and focusing on the sample surface, as well as, when possible, the convenient visualisation of the Newton's rings on the liquid sample cell or the inspection of the sample surface quality. A diverging lens, not shown in Fig. 2.13, is attached in front of a CW collimated laser module (Thorlabs, $\lambda = 532$ nm) in order to illuminate sufficiently wide sample area ($d_{probe} << D_{CW}$). The diverging CW laser beam passes through a dichroic mirror and overlaps with the probe beam path see Fig 2.13. A thick piece of wedge glass window is put right after the PBS in order to sample a weak part of the reflected beams that are sent to the CMOS camera. The main part of the transmitted beams through the wedge glass are focused on the photodiode. To capture the sample image, a CMOS camera is placed after the beams separation at the glass, at the focus of a 15 cm aspheric and achromatic lens, providing an optical magnification of the sample surface of about 10-15. The CMOS camera (Thorlabs DCC1645C, 5.2 μm pixel size, 1280×1024 pixels, color) is powered via a USB 2.0 cable and controlled by a special software supplied by Thorlabs and installed on the computer. The 2D imaging setup has been optimized to adjust the probe spot position on the sample with excellent accuracy. The laser module is switched on only prior to the measurements to fine tune the probe beam focusing and switched off to decrease undesirable noise in signal during the experiment. In order to avoid multiple interferences on the sample images caused by the long coherence length

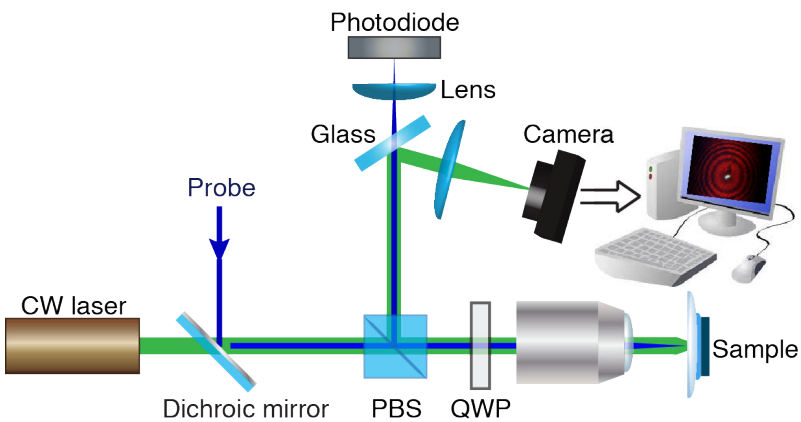

Figure 2.13. Simplified scheme of the simple 2D imaging setup. The collimated laser module illuminates the sample surface which is imaged in the CMOS camera.

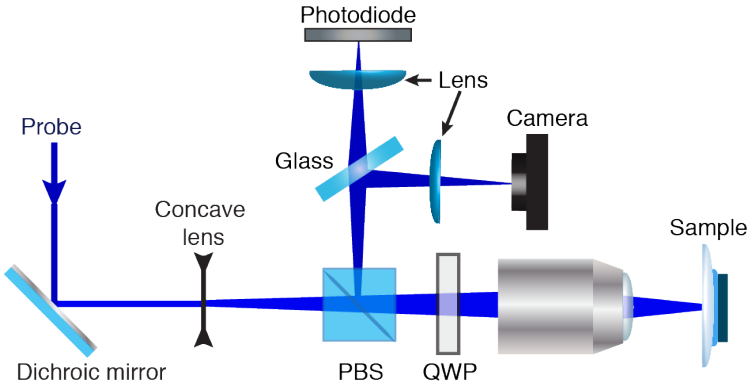

Figure 2.14. Scheme of the 2D imaging setup for illumination the sample surface by the femtosecond probe beam.

of the laser module, we sometimes used the femtosecond probe to get good quality images. For that a concave lens is mounted on movable mount before the microscope objective in order to broaden the beam illumination on the sample surface. In this case the inspection about surface quality, about damages on the sample are more reliable.

2.2.2 Data acquisition

In all experiments we used two balanced current photodiodes to improve the signal to noise quality of the acquired data. These balanced current photodiodes were used to remove laser fluctuations. The reference photodiode contains only noise produced by the laser because the reference beam is reflected from a PBS right after the SHG telescope and is not related to the sample. Its intensity is tuned by a half waveplate situated before the PBS, see Fig. 2.7. A second photodiode is used to collect the light from the probe pulse reflected from the sample surface. The photodiodes that were at our disposal generate currents of different signs, such that in parallel we obtain the subtraction from both photodiodes, and the subtraction of a large amount of the laser noise, as an input for the lock-in for synchronous detection. The subtraction of the photodiodes is adjusted, as much as possible close to zero, on the reference photodiode arm by the half waveplate to minimise the laser noise or other type of noise identical on both photodiodes. Since only the second photodiode contains the signal, it does not get filtered out from this procedure that can increase the signal-to-noise by several orders of magnitude. Synchronous detection is indispensable for such type of sensitive measurements because the detected signal are extremely weak and are disturbed by external factors such as vibrations, airflow, electronic fluctuations, laser

fluctuations as well as temperature change that can decrease the signal-to-noise ratio. Knowing that the signal level is very low (in the range 10^{-4} - 10^{-7}) and can strongly vary, the lock-in detection is imperative. To complete this task, a Stanford Research SR844 lock-in amplifier was used. The lock-in takes the input signal from the balanced photodiodes along with all the noise ($V_s(t) = R\cos 2\pi f_s t + \theta_s$) as well as the reference signal of the pump modulation ($V_r(t) = \cos 2\pi f_r t$) and couples both of them through a frequency mixer. The signal mixing is equivalent to multiplication of the two inputs ($V_s \cdot V_r$). When the signal and the reference are sin waves at frequencies f_s and f_r, this operation results simply into two components $f_s - f_r$ and $f_s + f_r$. In our case the signal and the reference frequencies are identical and equal to f ($f_s = f_r = f$) which is the modulation frequency of the pump light by the AOM. Thus the mixer output a DC component and another component at $2f$ frequency which is filtered by means of an adjustable low pass filter. In addition the lock-in integrates the mixer output to remove all remaining frequency components and to retrieve the DC component which is the true signal linked to the measurement. The entire principle of mixing and low pass filtering is called the phase sensitive detection or demodulation. The time constant of the time integration of the lock-in is an important parameter that has to be set accordingly to the motion of the delay line in order to obtain a reasonable acquisition time of the full scan and a reliable signal-to-noise.

The output signal of the lock-in amplifier is sent via GPIB from a National Instruments^{TM} GPIB-USB card on common Windows-PC. A homemade data acquisition program in LabView (or earlier in Agilent) controls the motion of the delay stage with an ethernet port and records the measured signal sent on the GPIB-USB card which are shown on the display of the monitor. The sophisticated LabView program controls several motor stages and the piezocontroler as well, see in 3.3, which enables lateral scanning and rastening of the sample surface, and extremely precise modification of the liquid thickness from the piezocontroler.

In the next chapter, we will describe in detail the different types of liquids investigated in this thesis and we will give a close view on the liquid sample cell which has been designed for the measurement of ultra thin liquid layers.

Chapter 3

Liquid cell

In our experiments, we need a special sample design that enables to maintain the liquid thickness stable and unperturbed during all measurements. The extraction of the information on the liquid mechanical properties (acoustic speed, attenuation coefficient etc.) relies on the comparison of the acoustic transmission through different liquid thicknesses. Therefore, it is indispensable to have an experimental access to a wide range of liquid thicknesses, ranging from several to hundreds of nanometers or even microns. In order to achieve this, a peculiar homemade liquid cell has been designed and built. This chapter/section is dedicated to the liquid cell description and characterization.

3.1 Sample cell configuration

As mentioned above, in our research, it is required to maintain the thickness of the liquid sample stable and unperturbed by outer factors such as temperature variation, humidity change etc. Also by virtue of the fact that all measurements have been performed in vertical position, this task was more complicated. Several sample configurations were developed and tested, see Annex, all based on the schematic sample structure shown in Figure 3.1. Samples were prepared by squeezing the liquid under study between two substrates. One of them, the generation side substrate, is coated with a thin metal film, that acts as a generation transducer film. The second, the detection side substrate, an optically transparent substrate, serves for the detection of the acoustic waves through Brillouin scattering after transmission across the liquid. Different types of measurements have been performed with liquids of different thicknesses, including thick liquid films of several microns and thin liquid

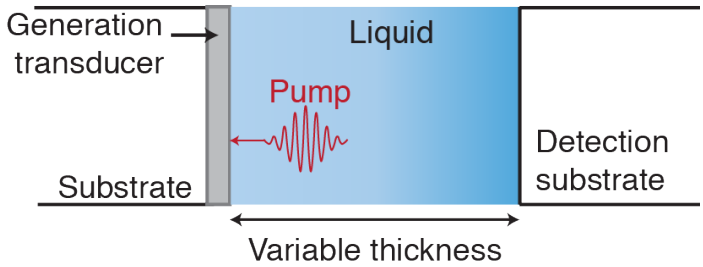

Figure 3.1. A liquid sample is sandwiched between two substrates that hold the liquid layer. Depending on the liquid thickness, the acoustic wavepacket generated in the metal transducer thin film may be detected either in the liquid or in the detection substrate by time-domain Brillouin scattering.

layers of few nanometers thickness.

In case of sufficiently thick liquid layers of about several microns, the acoustic wavepacket is generated in the transducer film by the pump pulse, propagates through the liquid film, and it gets detected by the time-delayed probe pulse from time-domain Brillouin scattering directly in the liquid itself. The liquid thickness being so large, the acoustic wave packet is damped before reaching the detection substrate and the detection process occurs directly in the liquid layer. In case of a thin liquid layer, after being generated in the transducer metal film, the acoustic wavepacket traverses the liquid layer and, after propagation through, gets partially transmitted to the transparent detection substrate, where it is detected by the probe pulse by time-domain Brillouin scattering (see Section 2.1.2). The liquid thickness being much less than the optical wavelength in the liquid, there is no detection directly in the liquid, only in the detection substrate. For intermediate liquid thicknesses, Brillouin scattering detection can occur in both media, in the liquid and in the detection substrate, at distinct Brillouin frequencies.

3.2 Choice of materials

The choice of the materials composing the liquid cell structure plays a crucial role. Different substrates configurations lead to differences in generation efficiency and acoustic transmission, and can result in significant unwanted sample heat. The influence of different sample configurations on the cumulative sample heating is described in the following Chapter 4. Our material choice has been motivated by the optimization of the generation efficiency, acoustic transmission across the liquid and minimization of cumulative heat effect.

3.2.1 Generation side substrate: Substrate and transducer film combination

The combination of a metal transducer film and the substrate is of key importance for the acoustic generation, heat diffusion processes as well as for the transmission of the generated acoustic wavepackets into the adjacent liquid film. After some investigations, estimates from the literature of the different material properties and trials, we have fixed our choice on Silicon as the generation substrate and Chromium as transducer film. Chromium films were grown on flat Silicon substrates under ultra-high vacuum ($\sim 10^{-6}$ - 10^{-7} Pa) by method of evaporation at the rate $\sim$0.1 nm·sec^{-1}. The Si substrates were cut from wafers (mainly, n - doped <100> wafers of 300 μm thickness) that before use are stored under the fume hood. A wide range of Chromium thicknesses (from 10 to 100 nm) were used during my PhD work.

Chromium is widely used as high frequency opto-acoustic transducer for the laser excitation of ultrashort acoustic pulses [108]. Its relatively short optical penetration depth (in the range of 15 nm at 800 nm and 9 nm at 395 nm), short diffusion depth ($\sim$10 - 20 nm), allows the excitation of high frequency acoustic pulses. Nonetheless, from the strain transmission point of view, it is not the most suitable transducer. The acoustic impedance of Chromium is relatively high ($z_{ac} = 43$ MRayls [3]), twice bigger than Silicon and impact the transmission of the strain into the liquid film ($T_{\eta,12} = 5.9$ in case of glycerol). Still, Chromium has a great advantage compared to other metals, by virtue of its easy deposition rendering a perfectly smooth surface, with a roughness below 1 nm. In addition, its thermal deposition is fully mastered and available at convenience in our laboratory. For these technical reasons, Chromium remains the most appropriate transducer film linked to our measurements of ultrathin liquids that requires ultra-smooth surfaces.

3.2.2 The choice of the liquid

The experiments performed in this work were made by using three categories of liquids - glycerol ($C_3H_8O_3$), octamethylcyclotetrasiloxane (OMCTS, $C_8H_{24}O_4Si_4$) and liquid crystal 4 - N - octyl - CyanoBiphenyl (8CB, $C_{21}H_{26}N$). Each of these liquids present an interest either for fundamental research or for applications. A short description of these liquids is presented in the following.

[3]The important parameters and physical properties of Cr and Si are presented in Appendix C.

A. Glycerol

The chemical structure of glycerol is depicted in Fig. 3.2. Each molecule contains 14 atoms and its size is equal to 4.3 Å. Physically, glycerol is a water-soluble, clear, almost colorless, odorless, viscous, hygroscopic liquid with a high boiling point. Chemically, glycerol is a trihydric alcohol, capable of being reacted as an alcoholyet stable under most conditions. With such an uncommon blend of properties, glycerol finds application among a broad diversity of end uses. Glycerol is well-known for its ability to supercool and to vitrify at low temperatures into a rigid glass. These features gave rise to a wide range of experiments on this substance's physical properties in the glass forming community [109–112] where glycerol is a well know intermediate glass forming liquid prototype. Despite plenty of analyses available presently, the accurate understanding of the structure at the molecular level is not completed yet. This knowledge would help to explain the behavior of a broad family of other glass formers.

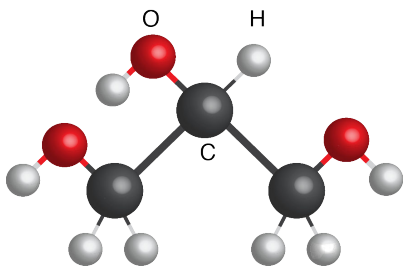

Figure 3.2. The molecule of Glycerol.

The essential temperature parameters are listed in table 3.1 and the crucial physical parameters are indicated in Appendix. Glycerol has a quite high boiling temperature about 563 K. It supercools below its melting point (T_m = 290.8 K) and forms an intermediate glass with a characteristic glass forming temperature of $\sim$ 186 K.

T_b, K	T_m, K	T_g, K
563	290.8	186

Table 3.1. The temperature parameters of glycerol, boiling point T_b, melting point T_m, and glass transition temperature T_g.

Glycerol exists as a liquid, supercooled, or glassy state. Under normal conditions glycerol does not undergo crystallization but it rather becomes a supercooled liquid during cooling, which can be vitrified at $T_g \sim 186$ K [113]. However, after special treatment, pure dehydrated glycerol can be crystallized [114] (cooled down below

the glass-transition point T_g and then slowly heated up). Glycerol crystallizes into an orthorhombic structure, with four symmetry-equivalent molecules per unit cell. Glycerol was the most frequent liquid involved in our research because of the wide information available on glycerol in the literature. Glycerol has been extensively used as a model system in many studies related to supercooled liquids and glass-forming dynamics [109–112]. We used it as the reference liquid on which we made not only the measurements but also the calibrations or adjustments of our experiments.

B. OMCTS

Octamethylcyclotetrasiloxane, also known as D4, is a low weight cyclic siloxane which molecule is presented in Fig. 3.3. lt is a colorless viscous liquid that belongs to the category of glass-forming liquids. OMCTS is prevalent for liquid structuration and confinement investigations because of its relatively big molecule size ($\sim$ 8.5 Å) and because it can be modeled as a sphere of the same diameter. Previously and nowadays, the confinement effect of OMCTS is explored by Surface Force Apparatus and Atomic Force Microscopy. OMCTS is in fact a prototype liquid for confinement investigations, and for this reason, we have performed some experiments with this specific liquid. The main disadvantage of OMCTS for our experiments is its volatility. OMCTS is volatile at normal ambient conditions and many times it was not possible to complete our measurements before full evaporation of the liquid sample.

T_b, K	T_m, K	T_g, K
449	290	260

Table 3.2. The temperature parameters of OMCTS.

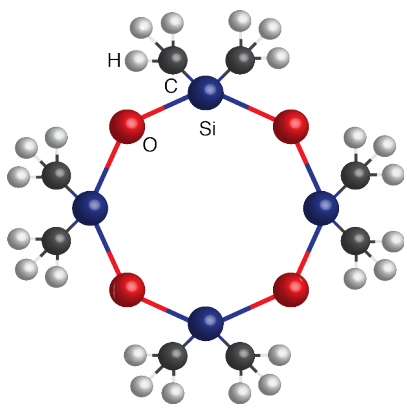

Figure 3.3. 2D representation of the OMCTS molecule.

C. 8 CB

Liquid crystal 4 - N - octyl - CyanoBiphenyl is a low molar mass liquid crystal, known under the name 8 CB, which shows different liquid crystalline phases depending on temperature conditions. Under normal temperature conditions 8 CB exists only as a bulk smectic-A phase. It has a white color and "butter" consistency. 8 CB belongs to cyanobyphenil class that was synthesized in 1973 by Gray. The molecule of 8 CB shown in Fig. 5.5, consists in a CN group, two aromatic cycles and aliphatic chain of 8 carbons. The length of such molecule is about 20 Å, with $\sim$ 10.3 Å length of the carbon chain and $\sim$ 9.7 Å length of the two aromatic cycles. In general, only liquid crystals of nCB groups that consist of at least 5 carbon atoms in the aliphatic chain are capable of forming the mesomorphic phases. This liquid crystal is one of the three of nCB groupe (8CB, 9 CB and 11 CB) that forms both mesophases: nematic and smectic phases. Others form only one, either nematic (n = 5,6,7) or smectic A (n = 10, 12). The temperature phase transitions of 8CB are listed in table Tab. 3.3. The crystalline to smectic A transition occurs at 294 K, the smectic A to nematic transition at 306.7 K and at 313 K the 8 CB is in the isotropic phase. There is a rising amount of work involving different experimental techniques on liquid crystals phase transitions, structuring near solid-liquid interfaces, and in particular concerning this liquid crystal. The experiments that we have performed with 8 CB are presented in the following chapter.

Name of phase transition	Crystalline - SmecticA	Smectic A - Nematic	Nematic - Isotropic
Temperature, K	294	306.7	313

Table 3.3. The phase transition temperature of 8 CB.

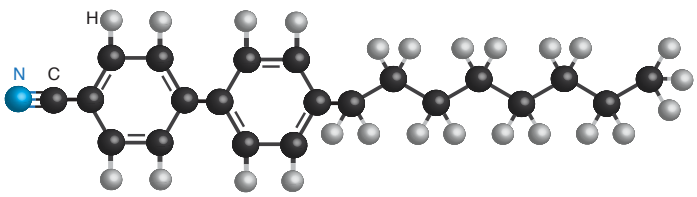

Figure 3.4. 8 CB molecule. This molecule consists of CN groups, two aromatic cycles and aliphatic chain of 8 carbons.

3.2.3 Detection substrate

As a detection substrate, we used plano - convex lenses with different focal distances, ranging from 300 mm up to 2500 mm, purchased either at Thorlabs or CVI. The lenses are made from borosilicate crown glass (N - BK7) with n = 1.516 at a wavelength $\lambda = 587$ nm.

Bringing in contact the flat generation substrate and the spherical detection substrate leads to phenomena known as Newton's rings. Newton's rings appear as a series of concentric rings, alternating bright and dark rings centered at the point of the contact between the two surfaces. The radius of the Newton's rings in our case can be measured considering the scale of the images taken by the CMOS camera from the 2D imaging setup. Thus, the liquid thickness can be calibrated and fitted from the Newton's rings interferometric effect, with a precision in the range of ten's of nanometers. Using the notation of Fig. 3.5, the thickness e of the liquid film at a given Newton's ring distance r of the contact, can be calculated as follows [115],

$$e = \frac{r^2}{2R} \tag{3.1}$$

where R is the lens radius of curvature, and r is the radius of Newton's ring.

Lenses of two classes were used in our experiments: uncoated or with antireflection AR coating (650 - 1050 nm). The lenses with AR coating are convenient for the imaging of the Newton's rings because of a better contrast between bright and dark rings. In fact the lens AR coating is optimized at the factory for minimum optical reflection at the AR-air interface, however, in case of a liquid, the AR coating has an opposite effect, it increases the optical reflection at the AR-liquid interface and enhances the Newton's rings interferences. The disadvantage of the AR coating is that it adds some interferometric artifacts on the signal for measurements at different liquid

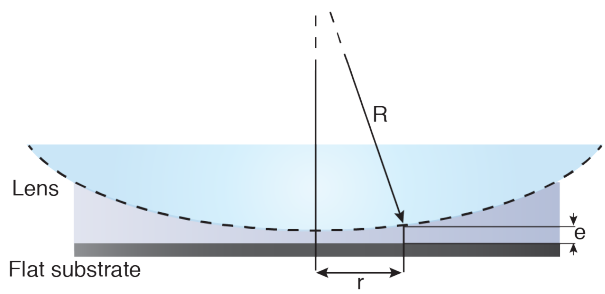

Figure 3.5. The curved-flat experimental setup of the Newton's rings. The liquid is squeezed in between the curved surface and the flat surface.

thicknesses. The variation of the liquid thickness modifies the optical interferences from constructive to destructive and entails a substantial change of the transient optical reflectivity. This interferometric artifact impacts the data acquisition since it is not possible to balance properly the dual photodiodes. For this reason, our experiments were performed lately with uncoated lenses only, with the disadvantage of the disappearance of the Newton's rings (the weak optical contrast between the liquid and the uncoated lens cancels the interferometric effect) and adds more technical complexity for the precise localization of the contact.

3.2.4 Impact of the surface roughness on the measurements

Since all measurements have been performed for ultrathin liquids, the surface quality is very critical. Especially, if the roughness is bigger than the molecule size, it may add a substantial thickness uncertainty and alter the liquid structuration near the solid-liquid interface. Fig. 3.6 provides a schematic view of the influence of the surface roughness on the liquid topography and structuration. If the roughness of one of the solid surfaces is bigger than the molecule size, the number of liquid layers at different positions is different. Similarly, if some dust particles or impurities are present on the surfaces or in the liquid, this will modify the number of molecule layers perpendicular to the surfaces and in turns, the thickness will be undetermined in this area. In view of the probe beam size of about 8 μm, the probed area covers a significant number of molecules along the surface ($\sim$4000$\times$4000 molecules of 8CB, $\sim$8000$\times$8000 molecules of OMCTS and $\sim$16000$\times$16000 molecules of glycerol), which means that the measured signal averages a huge number of molecules and gives an averaged signal over the whole probed area. Therefore, the surface roughness or the presence of impurities might not be as critical as in an AFM measurement, for example, where only few molecules are probed along the surface. Our laser ultrasonics measurements lead to an effective liquid thickness and an effective liquid medium. Of course the mechanical properties of the effective liquid medium depend on the local liquid topography which is influenced by the surface roughness and the impurities, but even in an non ideal situation, the effective liquid properties should differ from bulk to confined. For sure the measurements of the bulk and the confined liquids are influenced by surface roughness and the impurities, but there is no reason why experimentally the laser ultrasonics technique would not be able to indicate a difference between an effective bulk liquid and an effective confined liquid. The question is how much mechanical contrast can we expect in the laser ultrasonic measurement, and how much the surface roughness and the impurities can influence this mechanical contrast?

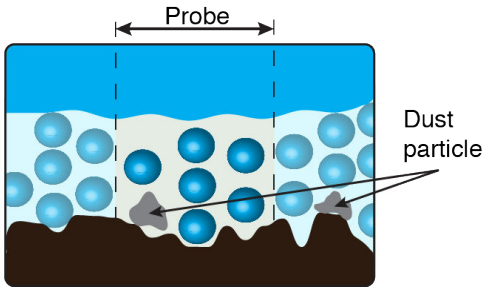

Figure 3.6. Simplified visual presentation of the impact of the surface roughness and of the presence of impurities on the molecules distribution.

Obviously, surface roughness plays a significant role in the cancellation of the confinement effect and needs to be minimized as much as possible. All the surfaces composing our samples were analyzed by AFM in tapping mode in order to choose the substrates with the best surface quality. AFM topographic images of the Silicon surface enabled the measurement of the RMS roughness in a 10 μm $\times$10 μm square of 0.22 nm RMS. Similarly, we have measured a RMS roughness of the Chromium film of 0.27 nm RMS and of the lens of 2.5 nm RMS. The roughness of the lens is high compared to the other surfaces, the reason being the fact that the polishing of a curved surface is not as good as for a flat surface. We have been exploring lately the possibility to use lenses made of blown glass that gives a more reliable surface quality. However, manmade blown glass yields quite unknown lens radii that are not necessarily uniform. Concerning the impurities, the surfaces are cleaned with acetone and dried in a clean hood, and the liquid is passed through porous filters of 0.2 μm in diameter, prior to the measurements.

3.3 Sample cell design and assembly.

Another important and time consuming technical problem consisted in designing and machining a sample holder for the liquid cell structure that allows dynamic liquid thickness change, from several nanometers to several microns. To achieve this technical challenge, a sophisticated construction was fabricated to hold the two substrates in order to squeeze the liquid and to change the liquid film thickness with nanometric resolution. In the past, broadband picosecond ultrasonics has been applied to measure acoustic properties of bulk liquids squeezed in between two flat surfaces [116]. Since extremely large pressures are needed to squeeze the liquid film down to thicknesses thinner than 1 μm, only bulk liquids were studied. The difficulty increases due to the

difficulty for the liquid to quick flow outwards when two flat substrates are brought close together. More recently, one of the flat substates has been replaced with a plano-convex lens [87, 117]. In this case, two substrates can get in contact one with another from small external pressures (even with lenses with large curvatures). In order to probe different liquid thicknesses, researchers moved away from the contact region in order to access liquid layers of a few hundreds of nanometers. However, away from the center, the two solid surfaces are no longer parallel at this point and the liquid thickness varies significantly over the probe spot size diameter and, additionally, the acoustic reflections occur at the angles resulting in a tilted acoustic wave front. Still, measurements at several lateral (x) positions on the lens corresponding to different liquid layer thickness were performed to retrieve the mechanical properties of bulk liquids in the 100 nm thickness range. The "nonlinear" quadratic liquid film thickness variation is governed by the lens curvature and the lateral displacement step. An example of a flat-curved liquid sample cell is shown in Fig. 3.7(a). The lower left hand image of Fig. 3.7(b) shows the Newton's rings recorded on the 2D imaging setup. The lower right hand image of Fig. 3.7(c) shows the variation of the liquid thickness across the lens.

In [87], researchers used a flat substrate and polished three regions of one face

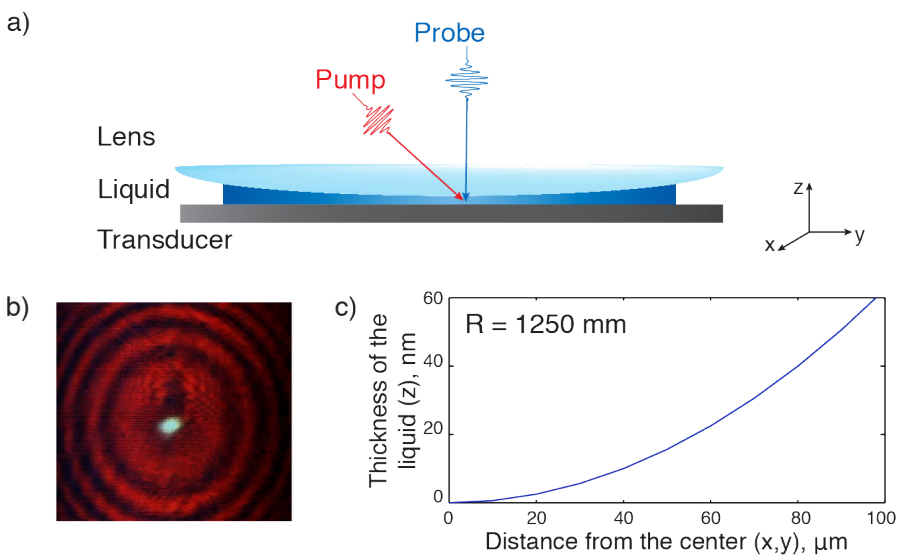

Figure 3.7. (a) Sketch of the flat-curved sample cell configuration. (b) Recorded image showing the Newton's interference rings. (c) Variation of the liquid film thickness at different lateral positions. The thickness variation is very small close to the center and rapidly increases away from the contact zone.

(to the top, bottom and to the right in order to leave a rectangular untreated area) at an angle of a couple of degrees. It is possible but challenging to having a liquid thickness increase of just a couple of tens of nanometers per millimeter. Moreover, the substrate surface has to be high quality after polishing.

Both flat-curved or flat-wedge configurations allowed to perform measurements at several lateral positions, which correspond to different liquid layer thicknesses from very thin liquid layer up to several microns. Since the flat-curved configuration is much easier to build and the liquid film thickness variation over the lens central zone is small, we have chosen to implement the flat-curved model, with similarities with the SFA technique that routinely measures liquids squeezed in between flat-curved or curved-curved surfaces.

Fig. 3.8 represents the schematic drawing of the optimum sample system. The lens is screwed with an aluminum ring to a monolithic aluminum holder attached to a 3D multi-axis positioning stage (Part C), rigidly, and remains motionless when the generation side holder approaches. The generation substrate with a thin transducer film coating is glued with epoxy on the aluminum barrel that can slide back and forth inside a square aluminum block. Sliding the barrel gives the possibility to set the generation substrate in a rough position relatively to the detection substrate lens. After being installed properly, the aluminum barrel is tightly screwed in order to ensure immobility during the measurements. Any slight motions of the lens holder or the generation substrate holder relative to each other would lead to undesirable liquid thickness variations that would perturb the results, especially with confined liquids. Therefore, the sample construction is a careful procedure which has been optimized on the mechanical point of view.

The block holding the generation substrate is then fixed on a piezostage (Piezoconcept, HS-1.10). The piezostage is a compact nanopositioner with 1-axis positioning (z-axis in Fig. 3.8) with 10 μm range of motion. This piezostage is fasten on a motorized linear stage (Newport®). This motorized stage is used to bring closer the generation side mount to the detection side mount within a 0.1 μm resolution. The whole generation assembly is then mounted on the same multi-axis positioning stage in order to modify the spot position along the x-, y- sample surface. The liquid is injected between the two substrates with a long needle and the generation side substrate is approached to the detection side substrate in order to squeeze the liquid and to obtain a thickness in the nanometer range, tunable and controllable with the piezostage.

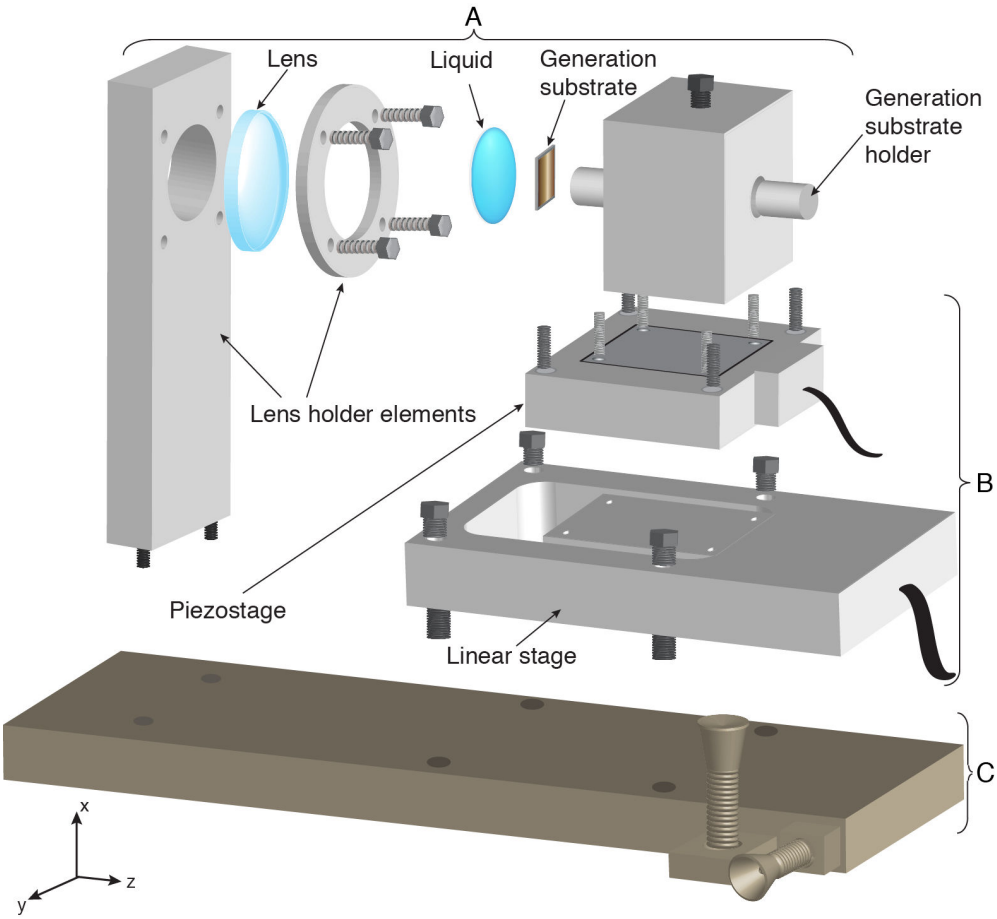

Figure 3.8. Schematic representation of the experimental sample cell. Part A: A liquid is sandwiched between a flat generation substrate holding a transducer and a plano-convex lens. Part B permits z-axis rough and ultra-precise displacements to control the liquid thickness variation. It consists of a motorized linear stage that changes the distance between the two holders of Part A with a 0.1 μm accuracy and a piezostage which vary the liquid film thickness with a nanometric resolution. Part C is a 3D stage that serves for lateral measurements along x-axis or y-axis.

Chapter 4

Heating effects

In this chapter, we describe several processes related to the laser mediated heating of the materials composing the liquid sample cell. We describe experiments where the influence of the laser pump pulse on the thermal relaxation or transport in the metallic transducer film and in the thin liquid film are investigated step by step. The purpose of the experiments described in the following have been to get insight and to quantify the influence of the laser mediated temperature rise in the perturbed sample structure, for the proper design of experiments on ultra thin liquids that will be described in the next chapter.

4.1 Nonequilibrium heating of Chromium films by ultrashort laser pulses

Nonequilibrium dynamics of the electron gas in metals illuminated by ultrashort laser pulses has been an area of intense research during the last couple of decades [118–123]. With the advent of femtosecond laser pulses, direct experimental studies of fundamental processes such as electron-electron scattering and electron-phonon interaction in metals have become possible [124–129]. Commonly known, laser illumination of thin metal films leads to local heating of the film, which in turns leads to the excitation of acoustic waves through a transient thermoelastic process. Laser heating of metals involves three general steps, as sketched in Fig. 4.1: the supply of laser energy to electrons (the free electrons absorb energy from the laser light); the reaching of thermal equilibrium by electrons and the density of states is now represented by the Fermi distribution (but the electrons and the lattice are still at two different temperatures, and heat transfer is mainly due to diffusion of the hot elec-

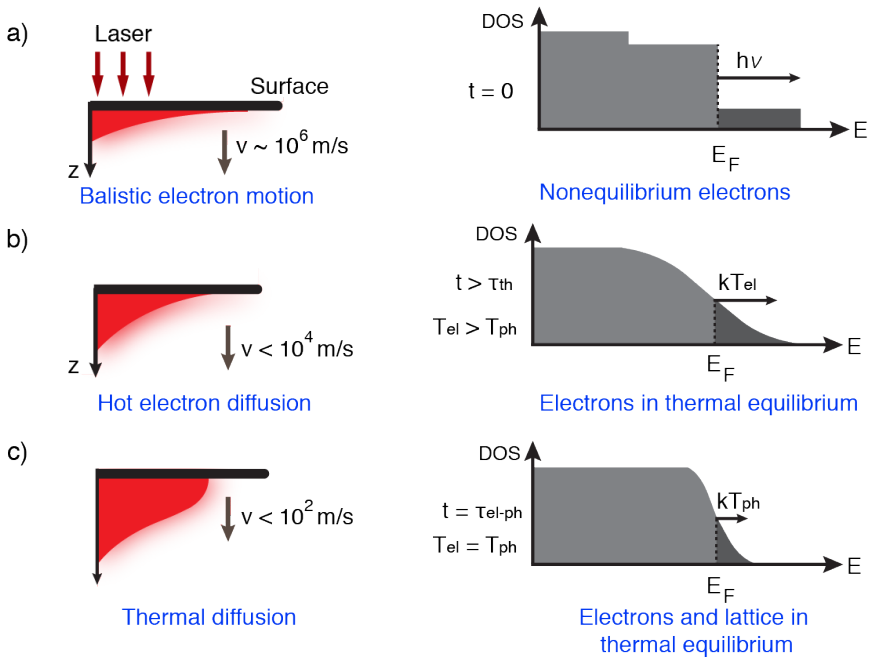

Figure 4.1. Three steps of optically excited electrons in metals. (a) Absorption of the energy deposited by laser illumination within the optical penetration depth generates at t = 0 s nonequilibrium electrons which move with ballistic velocities ($\sim 10^6$ m/s) deep into the sample. (b) Due to electron - electron collisions electrons equilibrates at t = τ_{th} forming a Fermi distribution with a well defined electron temperature T_{el}. Heat transfer starts due to diffusion of hot electrons. (c) At t = τ_{el-ph} the electrons come into equilibrium with the lattice via electron - phonon coupling. Then the energy propagates across the media through lattice thermal diffusion. Adapted from [127].

trons) and a last step of thermal equilibrium between electrons and lattice and the propagation of energy across media through heat diffusion. There exist two characteristic times for these processes: the thermalization time and the relaxation time. The thermalization time is the typical time for electrons and the lattice to reach thermal equilibrium. It represents the finite time needed to convert light energy into internal energy of the lattice. The relaxation time is the mean time for electrons to change their states [130].

4.1.1 Thermal relaxation between electrons and lattice

Absence of equilibrium between electrons and phonons is important already on a picosecond time scale. In a metal, first, free electrons absorb energy from the laser

while the lattice remains cold. On a femtosecond time scale the energy is distributed among the free electrons by electron-electron collisions leading to the thermalization of the electron gas. The energy exchange between electrons and the lattice is governed by electron-phonon collisions. Though the electron-phonon collision time may be as short as the electron-electron collision time, the energy transfer from the hot electrons to the lattice will last much longer than the thermalization of the electron gas due to the large mass difference of electrons and phonons, typically a few tens of picoseconds [121]. This process is described by the classical two-temperature model (TTM).

TTM had been firstly proposed in 1957 [131] and validated by many experiments [124, 125, 132]. It is a model for quantitative predictions of highly non-equilibrium changes and describes the temperature evolution of the electrons and phonons systems in metals after absorption of an optical femtosecond laser pulse. The time evolution of the electron temperature T_{el} and lattice temperature T_{ph} may be modeled by a set of coupled nonlinear differential equations:

$$C_{el}\frac{\partial T_{el}}{\partial t} = \frac{\partial}{\partial z}(K\frac{\partial T_{el}}{\partial t}) - g(T_{el} - T_{ph}) + S(z,t) \tag{4.1}$$

$$C_{ph}\frac{\partial T_{ph}}{\partial t} = g(T_{el} - T_{ph}) \tag{4.2}$$

where C_{el} and C_{ph} are the heat capacities of the electrons and of the lattice, g is the electron-phonon interaction coefficient and $K(T_{el})$ denotes the temperature dependent electronic thermal conductivity. The electronic heat capacity follows $C_{el} = \gamma T_{el}$, where γ is the electron specific heat. The first equation describes the electronic heat dissipation from the laser heat source of spatio-temporal profile $S(z,t)$, the heat diffusion among the electrons, and the heat transfer to the lattice. The heat source $S(z,t)$ can be written as,

$$S(z,t) = \frac{I(t)}{\lambda} exp^{-z/\xi} \tag{4.3}$$

where ξ is the optical penetration depth, $I(z,t)$ is the laser source intensity. The second equation stands for the lattice. Electron-electron collisions quickly result in thermalized hot electrons described by the Fermi - Dirac distribution. The hot electron gas dissipates the energy through the electron-phonon coupling term g and the heat conduction into the bulk. The phonon temperature is linearly coupled to the electron temperature through the electron-phonon coupling coefficient g.

Nonequilibrium electron heating may be observed experimentally through ultrafast transient reflectivity measurements performed with an optical pump-probe scheme. In the following we will consider electron and lattice dynamics following

ultrafast optical excitation of Chromium films.

4.1.2 Transient reflectivity of laser excited Chromium films

Transient reflectivity measurements were performed at room temperature using the optical setup described in the previous chapters and with a sample structure depicted in Fig. 4.2. The Chromium film of 40 nm thickness was deposited on n - doped Silicon substrate by thermal evaporation. We recall that the laser excitation and detection wavelengths are 790 nm and 395 nm, respectively. Optical pump pulses of 200 fs duration (full width at half maximum (FWHM)) were focused onto a 100 μm spot on the sample surface. The experiments were performed at a laser repetition rate of 260 kHz. The pump beam was modulated at 41 kHz and its fluence was varied between 0.5 and 8.5 mJ·cm^{-2} while the probe beam fluence was fixed at 0.15 mJ·cm^{-2}. Transient reflectivity measurements performed as a function of pump-probe time delay are shown in Fig. 4.3 (a). The time resolved response of the sample reflectivity change consists of two components. We observe a fast rise at time zero, followed by a slow decay that lasts over several hundreds of picoseconds. In all cases, the initial abrupt reflectivity change is attributed to the excitation and subsequent thermalization and cooling of metal free electrons (since the specific heat capacity of the electrons is low, the electronic temperature increases rapidly in a very short period of time): following laser excitation the initially excited non-thermal electrons thermalize through electron-electron and electron-phonon interactions. The reflectivity signals decay as thermal

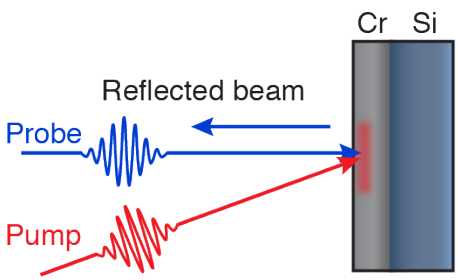

Figure 4.2. Sketch of the sample structure. A thin Chromium layer is deposited on a Silicon substrate. Optical pump pulses excite the Chromium film and create nonequilibrium electrons that transfer their energy with the lattice accordingly to the TTM model. The thermalization of the electrons and the lattice is probed optically by a delayed probe pulse that measures the transient optical reflectivity of the Chromium layer.

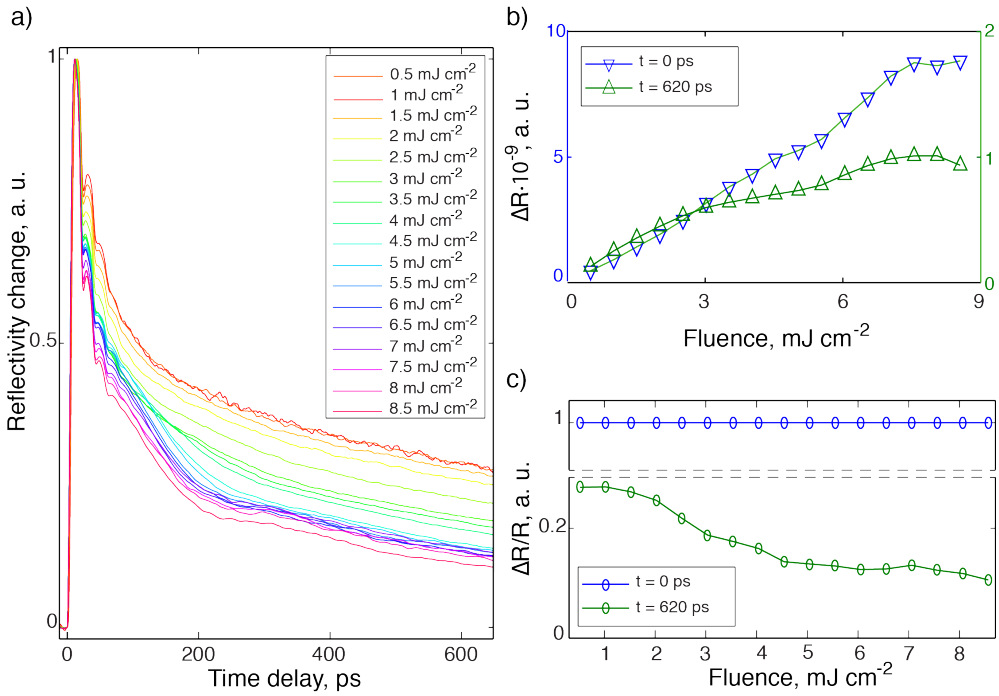

Figure 4.3. (a) Normalized transient reflectivity signals obtained in the configuration depicted in Fig. 4.2 at different pump fluences. The shape of the signals varies depending on the pump fluence due to the nonlinear laser excitation and thermalization process. Fluence dependence of the raw (a) or normalized (b) transient reflectivity signals at 0 ps and 620 ps.

and non-thermal electrons transfer their excess energy to the lattice through electron-phonon interactions, diffusion, and ballistic transfer. In Fig. 4.3 (a) we can observe that the electronic decay on the first tens of picoseconds is faster at higher fluences. The quicker electronic decay at higher fluences could be attributed to the momentum relaxation and thermalization among excited electrons, which takes shorter time at higher fluences because of stronger electron-electron scattering with increasing carrier density. The slow electronic decay could be associated with the electron-phonon coupling. The modification of the shape of the normalized transient reflectivity data shown in Fig. 4.3 (a) at different pump fluences evidences nonlinear laser excitation and thermalization processes of different amplitudes and timescales that evolves with the pump fluence through a complex non-linear relationship.

The peak amplitude of the raw (non normalized) transient reflectivity data at t = 0 ps for different pump fluences are plotted in Fig. 4.3 (b) (blue triangles). The peak amplitude of ΔR at t = 0 ps in Fig. 4.3 (b) varies from 0.46 mJ·cm^{-2} to

8.8 mJ·cm^{-2} with an increase of the pump fluence. It increases linearly with pump fluence until about 7.5 mJ·cm^{-2}, after which the increase probably saturates at fluences above 8.5 mJ·cm^{-2} which is the maximum pump fluence of our setup. High pump fluences results in greater electron temperatures and a corresponding increase in the electronic specific heat, implying longer thermal-relaxation times. Furthermore, at high temperatures the change in electronic occupancy begins to saturate and produces a transient-reflectivity relaxation time which is longer than the electron-cooling time [125]. The green triangles in Fig. 4.3 (b) show the pump fluence dependence of the amplitude of the longtime component, arbitrarily chosen at 620 ps, of the raw transient reflectivity data. This component increases monotonically with an increase of the pump fluence. The longtime component of the reflectivity signal results from residual lattice heating which cools in several hundreds of picoseconds from thermal heat diffusion. Fig. 4.3 (c) displays the amplitude of the normalized transient reflectivity data of Fig. 4.3 (a) at t = 0 ps and t = 620 ps. The peak amplitude of $\Delta R/R$ at t = 0 ps is constant due to normalization. The longtime component of the normalized reflectivity signal decreases monotonically with an increase of the fluence and saturates at high fluence as well. We can notice in the graphs of Fig. 4.3 (b) and (c) the coexistence of two regimes, a linear regime until about 3 mJ·cm^{-2} where the data scale linearly with pump fluence and a significant nonlinear regime for fluences above this threshold.

4.1.3 Conclusion

The time-resolved characterization of a thin chromium layer used in the liquid experiments as a transducer thin film, has evidenced several features of the transient relaxation response of the material under laser excitation. We have observed nonlinear laser excitation and thermalization processes of the electrons and of the lattice.

This experimental investigation of the chromium transducer film has highlighted a linear and a nonlinear regime of the behavior of the transient reflectivity signal. This quantitative estimate of a fluence threshold above which the sample response behaves non linearly gives a hint on the experimental conditions for a proper laser excitation of the chromium transducer film.

In the next section, we will investigate the concrete situation of a metallic transducer that launches an acoustic wave in contact to a surrounding liquid. We will demonstrate the usefulness of Brillouin scattering measurements to determine the local temperature distribution profile in liquid samples.

4.2 Cumulative laser heating in liquids

Thermal transport has been investigated in a variety of materials in the framework of ultrafast science, ranging from metals through the investigation of electron-phonon coupling, semi-conductors, insulators, gases, liquids and at solid-liquid-gas interfaces. Such investigations are often based on a femtosecond pump-probe technique in which the change in reflectivity of the sample following the partial absorption of a femtosecond laser pulse is monitored by a time delayed probe which is optically sensitive to the transient change in sample temperature. Recorded waveforms are then analyzed and compared to models to retrieve the thermal characteristics of the sample, such as thermal conduction, diffusivity or even Kapitza interfacial thermal resistance [134–138]. Similarly, time resolved photoacoustics implies ultrafast lasers to optically excite and detect ultrasound in a variety of materials. In this situation, well suited for the investigation of mechanical properties of ultrathin solid or liquid samples, the occurrence of time-domain Brillouin scattering (TDBS) phenomena in transparent materials has been used to investigate viscoelastic properties of matter at ultrasound GHz to THz frequencies [99]. Recently, several examples have shown that TDBS is sensitive to diverse phenomena, including spatial mechanical, optical or acousto-optical inhomogeneities [139–145], non-linear acoustic waves or weak shock waves [85, 146], and even GHz transverse acoustic phonons in viscoelastic liquids [86, 94, 147, 148].

In this section, elaborated from a paper from our group published recently [149], since temperature influences viscoelasticity, we demonstrate through TDBS measurements the intricate coupling of longitudinal acoustic phonons to thermal properties of the investigated liquids. We describe a tabletop pump-probe method which enables the measurement through TDBS of the absolute laser-induced temperature gradient in liquids in contact to an optical transducer. In the following, we will illustrate the performance of TDBS as a specific contactless local viscoelastic and temperature sensor in case of glycerol, which is a well known and well characterized prototypical glass forming liquid. Similar results were obtained for octamethylcyclotetrasiloxane (OMCTS), chosen as a confined liquid prototype, with the interest for future experiments related to molecular confinement in ultrathin liquid layers where the understanding of thermal effects remains elusive.

4.2.1 Temperature dependent measurements for glycerol and OMCTS. Temperature calibration

Since a temperature change influences both the speed of sound and the index of refraction, Brillouin frequency is temperature dependent [87]. The effect of sample heating from the laser itself, used for the Brillouin measurement, may give erroneous estimates in the determination of the mechanical parameters such as speed of sound and attenuation of the acoustic waves in the liquids of interest. For a better understanding of the behavior of a liquid under cumulative laser heating and in order to retrieve accurate results concerning the viscoelastic properties of liquids measured through TDBS, we have performed different sets of measurements to calibrate the laser induced temperature modification in different liquids and sample configurations. This section is aimed to determine the key parameters linked to the laser-induced cumulative effect in bulk liquids that could be extrapolated in our further experiments on ultra thin liquids. The temperature calibration measurement takes advantage of the fact that the Brillouin frequency can be used as a sensitive probe to determine the absolute temperature in the experimentally investigated local region of a liquid.

The optical experiment is based on the TDBS technique, suitable for the inves-

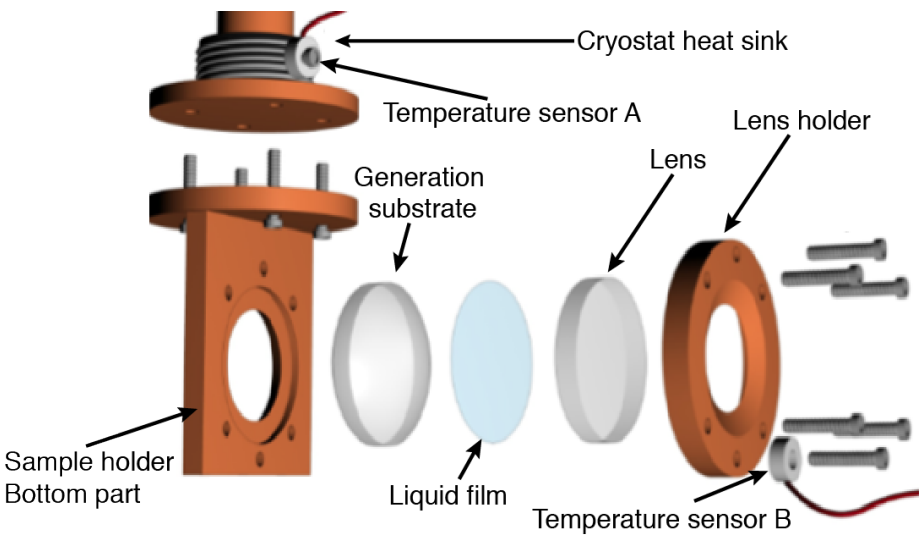

Figure 4.4. Sketch of the sample holder designed for use in a cryostat chamber. The liquid is squeezed between two substrates - flat generation substrate and the lens which are placed in a copper holder. The whole construction is attached to a heat sink of a cryostat. Two temperature sensors are placed to control the temperature of the cryostat chamber (sensor A) and of the sample (sensor B). Reprint from [87].

tigation of the frequency and temperature dependences of ultrafast acoustic dynamics in liquids at GHz frequencies [86,94,101,147,148,150]. Measurements were made using an ultrafast optical pump-probe experimental setup as illustrated in Fig. 2.7.

The sample configuration used in these experiments is depicted in Fig. 3.1. The liquid under study was squeezed between a flat n-doped Silicon substrate, that holds a 40 nm Chromium film, deposited by thermal evaporation technique, and a plano-convex lens with antireflection coating (supplied by Thorlabs). The thickness was well over 10 microns. The studied liquids were glycerol (Acros Organics®, 99+% purity) and OMCTS (Fluka®, 99+% purity), forced through several linked 0.2 μm teflon millipore filters to remove dust particles for the injection of the liquid into the sample holder cell, see Fig. 4.4. The liquid sample cell was then transferred to a cryostat and the sample chamber was immediately evacuated, because both liquids are extremely hydroscopic and can absorb up to 10 % of water. At each temperature, the sample was given sufficient time to equilibrate before data acquisition. A Peltier temperature sensor was attached on the sample holder mount, about 1 to 2 cm away from the experimental volume. All measurements shown below were obtained at sufficiently low pump fluence, since the laser pump itself can lead to the Brillouin frequency shift due to temperature rise.

OMCTS

As the physical properties of the investigated liquids depend on the water content, all measurements in the cryostat chamber were made under vacuum to avoid condensation and the liquid hydratation. Since OMCTS is rather volatile, it was challenging to perform experiments with this liquid under these conditions. In fact, OMCTS was immediately evaporating right upon starting the vacuum pumping of the chamber. The way to bypass this problem was to properly seal the liquid from the cryostat chamber. We have tested different possibilities and the best strategy so far consist in using silicone seal around the copper sample jig. Silicon grease and paraffin films were tested too, but they are less appropriate and efficient.

The measurements for OMCTS were obtained for a temperature range from 295 K to 230 K. The temperature influences the Brillouin frequency and the attenuation rate of the acoustic waves as shown in Fig. 4.5 (a). As can be seen in Fig. 4.5 (b), OMCTS exhibits an abrupt Brillouin frequency variation at the vicinity of 260 K, which can be assigned to a sharp crystalline to liquid phase transition [151–153].

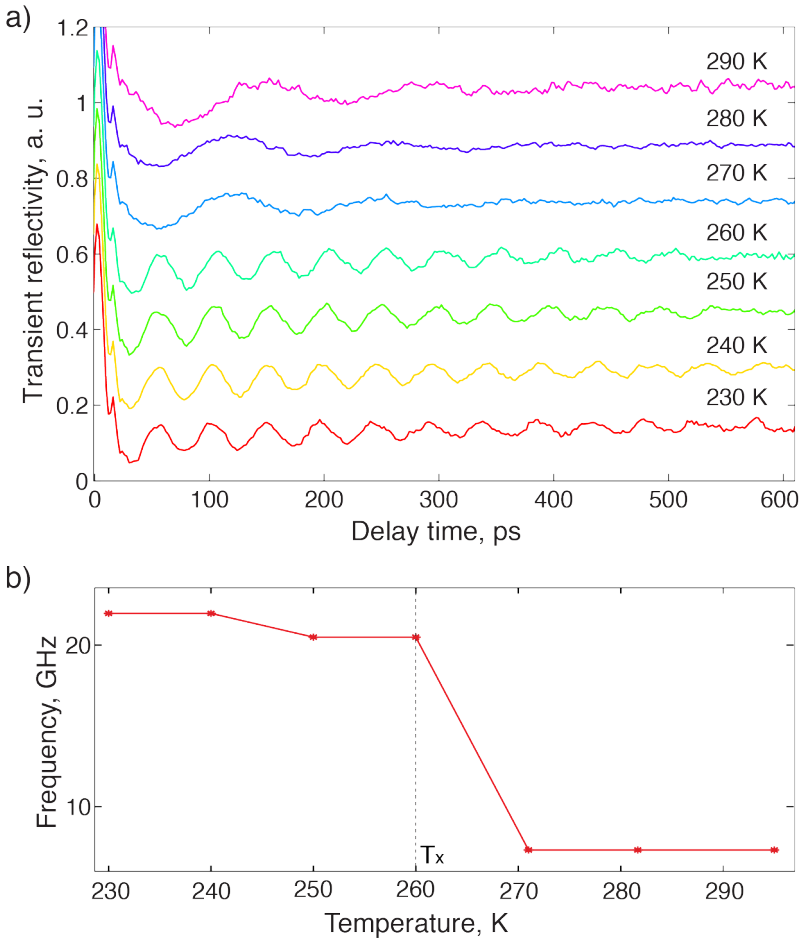

Figure 4.5. (a) Time derivative of recorded transient reflectivity signals obtained with OMCTS at different temperatures and at a given pump fluence 0.75 mJ.cm^{-2}. The time derivative was taken for better display. (b) Temperature dependent Brillouin frequency. T $_x$ indicates the liquid to crystalline phase transition temperature.

Glycerol

Glycerol, which is an intermediate fragile glass former with a glass transition temperature around $T_g = 186$ K, was chosen because it is a well characterized material with readily available temperature dependent speed of sound data in the literature from other techniques. Selected data at several different temperatures are shown in Fig. 4.6 (a). It illustrates clearly that the strong acoustic attenuation caused by temperature increase. The derivative is only taken for easy display. Fig. 4.6 (b) shows the temperature dependence of the Brillouin scattering frequency ν_B extracted from

our experiments and from [148, 154]. The Brillouin frequency variation is way more gradual than for OMCTS (see Fig. 4.5 (b)). For this technical reason, for simplicity, we have performed a meticulous temperature calibration for glycerol only. For each temperature measurement in glycerol such as the ones displayed in Fig. 4.6 (a), the Brillouin oscillations observed in the transient reflectivity signal were fitted following a sinusoidal damped function in the form

$$\Delta \mathrm{R}(t) \sim \sin(2\pi\nu t + \phi)\ \exp(-\Gamma t), \tag{4.4}$$

ϕ being a phase parameter, ν the frequency and Γ the attenuation rate of the Brillouin oscillations. As indicated in Fig.4.6 (b), the relevant Brillouin scattering frequency fit parameter ν changes significantly as a function of temperature. The experimental temperature calibration of the Brillouin frequency has been further fitted by a smooth polynomial function in order to extract an even more reliable temperature behavior of the Brillouin scattering frequency of glycerol under our experimental conditions at 395 nm probe wavelength and at normal incidence scattering angle. Since we did not have the possibility to record the Brillouin scattering frequency at higher temperatures than 320 K, we have used a calculated calibration curve from literature data obtained from Comez et al. [154] and Klieber et al. [148] as a reference function to link the Brillouin frequency to the absolute glycerol temperature. In [154], the temperature dependence of the speed of sound in glycerol was determined from conventional Brillouin measurements at a scattering wavevector q=0.036 nm^{-1}. This speed of sound is used to estimate in [148] the temperature dependence of the Brillouin scattering frequency of time-domain Brillouin scattering measurements at a wavevector q $\sim$ 0.048 nm^{-1}. Note that the twofold change in Brillouin frequency with temperature in Fig. 4.6 (b) is mainly due to the significant change in speed of sound over the examined temperature range (200 K - 400 K) [154], rather than the change of the index of refraction which varies only a few percent over the same temperature range [148].

We observe a slight Brillouin frequency shift of about 0.8 GHz in between our experimental data and the calculated calibration curve, which we attribute to a slight temperature shift caused by laser cumulative heating of the liquid, even at this relatively low pump fluence, or to a slight variation of the water content in the different glycerol samples. This discrepancy does not affect, in any way, the interpretation of the steady state cumulative thermal heating effects detailed in the following.

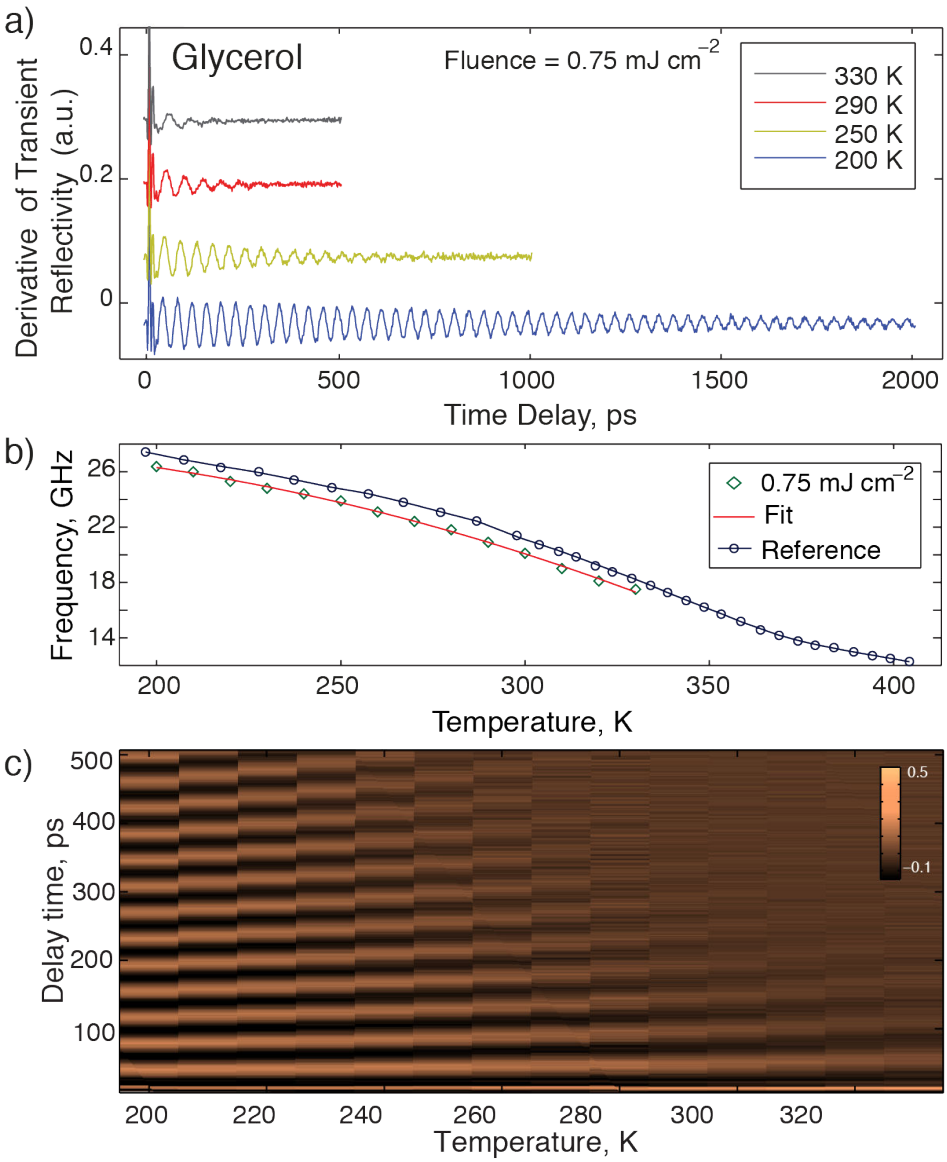

Figure 4.6. (a) Time derivative of recorded transient reflectivity signals obtained in glycerol at different temperatures and at a given pump fluence of 0.75 mJ·cm^{-2}. The pump power for each plot is sufficiently low to neglect the impact on Brillouin frequency. The time derivative was taken for better display. (b) Temperature dependent Brillouin frequency in glycerol, from our measurements, and calculated from Comez et al. [154] and Klieber et al. [148]. The temperature calibration curves displayed in (b) can be used to estimate the absolute liquid temperature from the measured Brillouin frequency. (c) Interpolated 2D plot of TDBS in glycerol at different temperatures.

4.2.2 Cumulative thermal heating

As in any optical pump-probe experiment, the laser pump pulse can cause permanent or irreversible sample modification. This effect can be experimentally observed once the recorded data become fluence dependent such as the excitation of shock waves at high laser fluences [85] which reveals the departure from the linear acoustic regime to the non-linear acoustic regime. It can be a consequence as well of a local temperature rise caused by cumulative heating of the sample from the multiple laser pump pulses which brings the sample into a steady state temperature regime correlated to the laser pump fluence [134–138]. Fig. 4.7 (a) and (b) displays recorded data obtained in OMCTS and glycerol at a temperature of 260 K and 230 K, respectively, as indicated by the Peltier temperature sensor, at different laser pump fluences. The sample

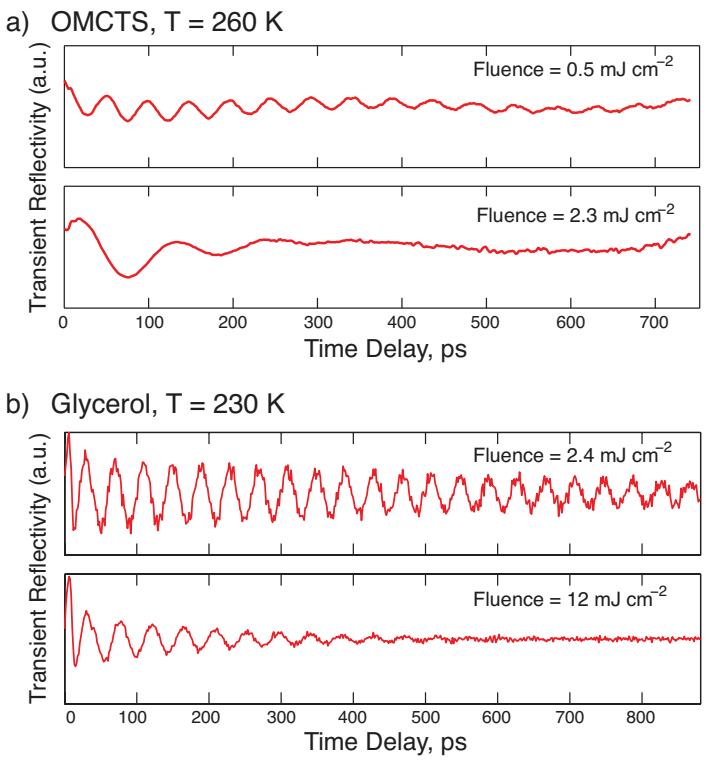

Figure 4.7. Recorded transient reflectivity data recorded for OMCTS (a) and glycerol (b) at several pump laser fluences - i.e cumulative thermal heating temperatures - and at different temperatures of the cryostat. The Brillouin scattering frequency drastically changes in case of OMCTS from a fivefold change in laser fluence, which indicates melting mediated by the laser thermal heating. In case of glycerol, the Brillouin frequency changes by over 10% for a fivefold increase in laser pump fluence.

structure consists of a silicon generation substrate coated with a 40 nm Chromium film or a glass generation substrate with 80 nm of Aluminum as a transducer film, in case of OMCTS and glycerol, correspondingly. As seen in Fig. 4.7 (a), a fivefold increase in the laser pump fluence induces a drastic change in the Brillouin oscillations frequency, from 20.5 GHz to 8.8 GHz, and in the attenuation rate. Since the general trend of any material is such that it is stiffer in the solid state than in the liquid state, we assume that the 20.5 GHz high frequency Brillouin scattering corresponds to the OMCTS crystalline phase and that the lower 8.8 GHz frequency corresponds to the liquid phase, see Fig. 4.5 (a). This is consistent with the observation that the cumulative heating of the multiple laser pump pulses could melt OMCTS from a fivefold increase in the laser pump fluence. In case of glycerol, the Brillouin frequency changes slightly from 25.1 GHz to 22.8 GHz, for a fivefold modification of the laser pump fluence. It indicates a monotonous temperature modification of glycerol, which remains in its supercooled liquid phase. The corresponding attenuation rate evolves with a modification of the laser fluence as well, however, its pertinence is out of scope of the manuscript, which focuses mainly on the analysis of the Brillouin frequency versus laser fluence or temperature.

It is important to keep in mind that for the appearance of shock waves as in [85], the Brillouin frequency tends to increase with an increase of the laser pump fluence, which is opposite to our current experimental observations. Therefore, we have neglected the effect of non-linear shock waves and solely assumed cumulative laser heating as the main mechanism responsible for the evolution of the Brillouin frequency in our present measurements. On the assumption that strong pump power influences the viscoelastic properties of liquids by inducing a local temperature increase, it is critical to find the most favorable conditions that can discard any impact due to laser heating on the experiments involving ultra thin liquids.

Different sample configurations at different laser pump fluences

Different configurations of generation side and transducer film can demonstrate different effects on the cumulative heating effect. These differences are important and influence the choice of sample structures for the experiments. Figure 4.8 shows the pump fluence dependence of the Brillouin scattering frequency for a variety of sample configurations at two different temperatures of the cryostat, 229 K and room temperature 295 K. Among the different sample configurations investigated, two samples have a 80 nm aluminum transducer film coated either on glass or sapphire substrates, two samples feature canted, molecular beam epitaxially (MBE) grown iron thin films, on either

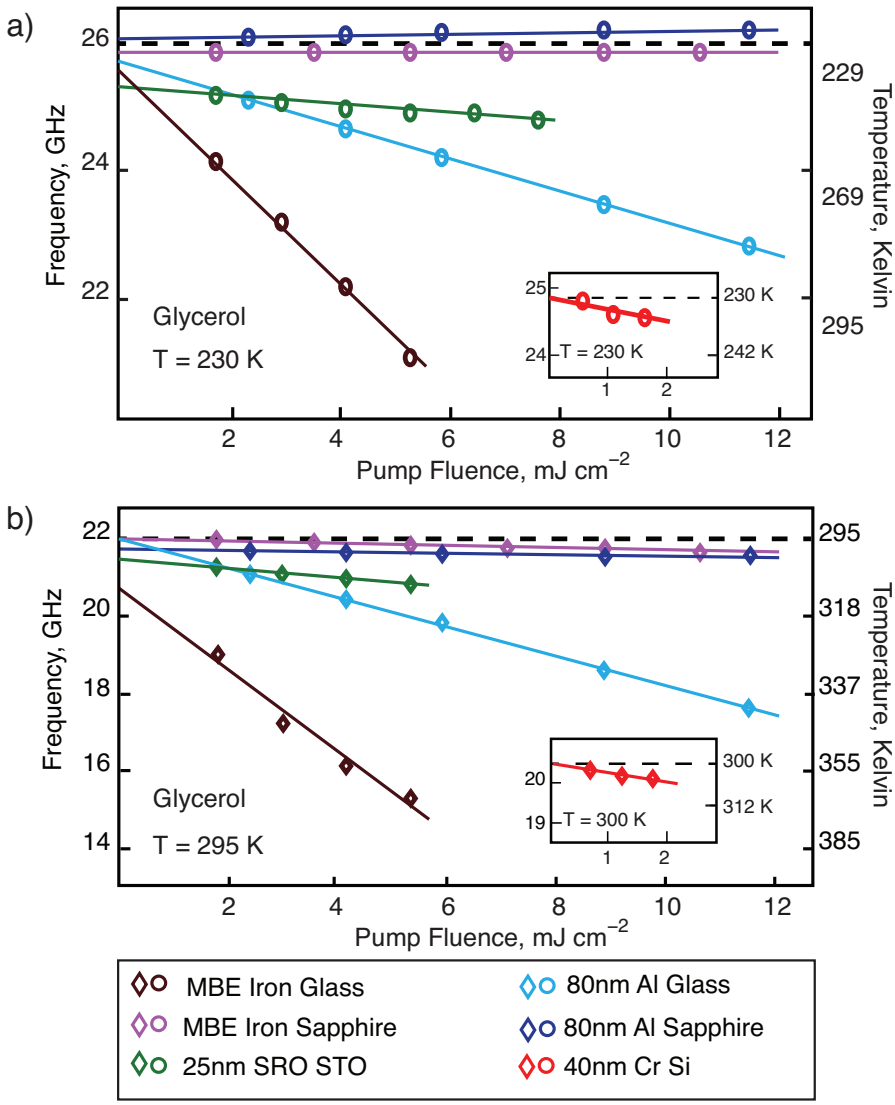

Figure 4.8. Brillouin scattering frequencies measured in glycerol at various laser fluences cause strongly different effects in cumulative sample heating for various sample structures. Different substrate materials holding different types of transducer films materials were studied. A transparent glass cover substrate and glycerol was used in all the sample configurations. Measurements on each sample assembly were made at two distinct temperatures of 229 K (a) and room temperature 295 K (b).The Brillouin scattering frequency were extracted from the recorded Brillouin scattering oscillations. The vertical temperature scales for both figures were deduced from the temperature calibration curve of Fig. 4.6 (b), as in [148]. Two inserts show measurements with Cr on glass configuration made at 230 K and 300 K. The temperature scales were deduced from our temperature calibration curve in Fig. 4.6 (b). Part of the data reprinted from [101].

glass or sapphire substrates, and a sample with a 25 nm strontium ruthanate ($SrRuO_3$, SRO) thin film on an off-axis cut strontium titanate ($SrTiO_3$, STO) substrate. MBE transducer films were used for shear wave generation as described in [86, 94, 147, 148]. The SRO sample was chosen because it attracted attention as a promising photoacoustic transducer material after a high laser-induced strain amplitude in a multilayer SRO structure was reported [155, 156]. In all configurations, the cover transparent substrate was glass and the liquid glycerol. The mean probe light intensity at each measurement was adjusted to account for differences in optical reflectivity among the different samples, such that the voltage on the detection photodiode was kept constant for all measurements. As shown in Fig. 4.8, the Brillouin scattering frequency and the liquid temperature rise, deduced from Fig. 4.6 (b), is strongly influenced by variation in pump fluence for a glass substrate, as opposed to the situation of sapphire or STO substrates. These discrepancies highlight the cumulative heating effect, which manifests differently depending on the sample structures. Strong cumulative heating was always observed with a glass substrate holding a metallic transducer film deposited on it. The fluence-temperature slope, deduced from Fig. 4.8, was substantial in this sample configuration, about ~ 40 K/10 mJ·cm^{-2} for glass-aluminum and over ~ 100 K/10 mJ·cm^{-2} for glass-iron. The ratio of about 1:3 reflects the difference in optical absorbance of aluminum and iron at 790 nm of 13% and 39% respectively. In strong contrast to this was the cumulative heating observed in two sample configurations which have a transducer film on sapphire substrates. In this case, the pump fluence dependent heating was determined to be only 3 to 5 K/10 mJ·cm^{-2}. The explanation of this large difference in cumulative heating lies in the difference in thermal conductivity, $\kappa_{\text{glass}} \approx 1.4$ W·m^{-1}·K^{-1} and $\kappa_{\text{sapphire}} \approx 45$ W·m^{-1}·K^{-1} for glass and sapphire. Therefore, the large difference is simply due to the thermal conductivity of glass that does not favor efficient thermal diffusion and dissipation, as compared to sapphire. Finally, $SrTiO_3$ is almost as good a thermal conductor as sapphire, $\kappa_{\text{STO}} \approx 20$ W·m^{-1}·K^{-1} when subjected to a heating of ~ 10 K/10 mJ·cm^{-2}. The only difference compared to the previous samples is the large offset at zero pump power which was likely caused by strong absorption of the 395 nm probe light which was at least twice as much for measurements on $SrTiO_3/SrRuO_3$ samples compared to the highly reflective metal films. Two inserts present the pump fluence dependence of the Brillouin scattering frequency in the configuration of a 40 nm Cr film on a n-doped Silicon substrate at two different temperatures, 230 K and 300 K. The cover transparent substrate was glass and the liquid glycerol. The fluence-temperature slope is less significant, about 30 K/10mJ·cm^{-2}, in the chromium - silicon configuration which is

not as good than in case of a sapphire transducer. Still, the laser induced temperature rise for the chromium - silicon configuration, which is the one adopted for technical reasons for the experiments on ultrathin liquids, induces a reasonable heating of about 3 K at the typical laser fluence of 1mJ·cm^{-2} used in our measurements.

These differences among the variety of generation side substrate configurations clearly demonstrate the influence in the choice of sample structures for experiments where the liquid sample has to be kept undisturbed in order to proceed to non-invasive pump-probe measurements. In order to avoid strong cumulative thermal effects, materials with good thermal conductivity are required.

Simulation of cumulative heating

In order to confirm our experimental observations, we have simulated the cumulative heating through modeling different sample structures and solving the time-independent heat equation in cylindrical geometry in COMSOL® Multiphysics. The sample structure used in all simulations includes a substrate holding a 50 nm iron transducer film, glycerol, and a transparent cover substrate. An absorption of 39% of a 100 mW laser beam with a Gaussian beam profile and a FWHM spot size of 100 microns, which corresponds to a pump laser fluence of 5.9 mJ·cm^{-2}, throughout the depth of the transducer film was used as the heat input to the model system. Since the simulations were steady state and did not include the impulsive nature of heat deposition, the temperature profile obtained from these time-independent heat equation simulations gives an upper bound for the actual cumulative temperature rise.

Results from simulating several different substrate combinations are depicted in Fig. 4.9 (a) and (b). Acoustic waves at our detection wave vector propagate very far into the liquid, at least 5 to 10 microns, at low temperatures. Accordingly, the liquid thickness of glycerol in our simulations has been arbitrary chosen to be of 10 microns. The glass transition temperature of glycerol, T_g = 186 K, was used as the initial temperature in all simulations. The top plot shows the 2D temperature distribution in a glass-glass configuration with a substantial temperature rise close to the transducer film of 84 K, the case with the highest temperature increase in our measurements. The corresponding temperature distribution within the probe spatial range, displayed in Fig. 4.9 (b), changes linearly by about 5 K/micron of propagation distance. In case of a sapphire-glass combination, see the bottom plot in Fig. 4.9 (a), our simulations confirm the fact that the temperature rise is more gentle, of about 15 K, in close agreement to our experimental observations. As opposed to a glass substrate, the linear temperature variation of a sapphire substrate is significantly reduced to 0.2 K/micron.

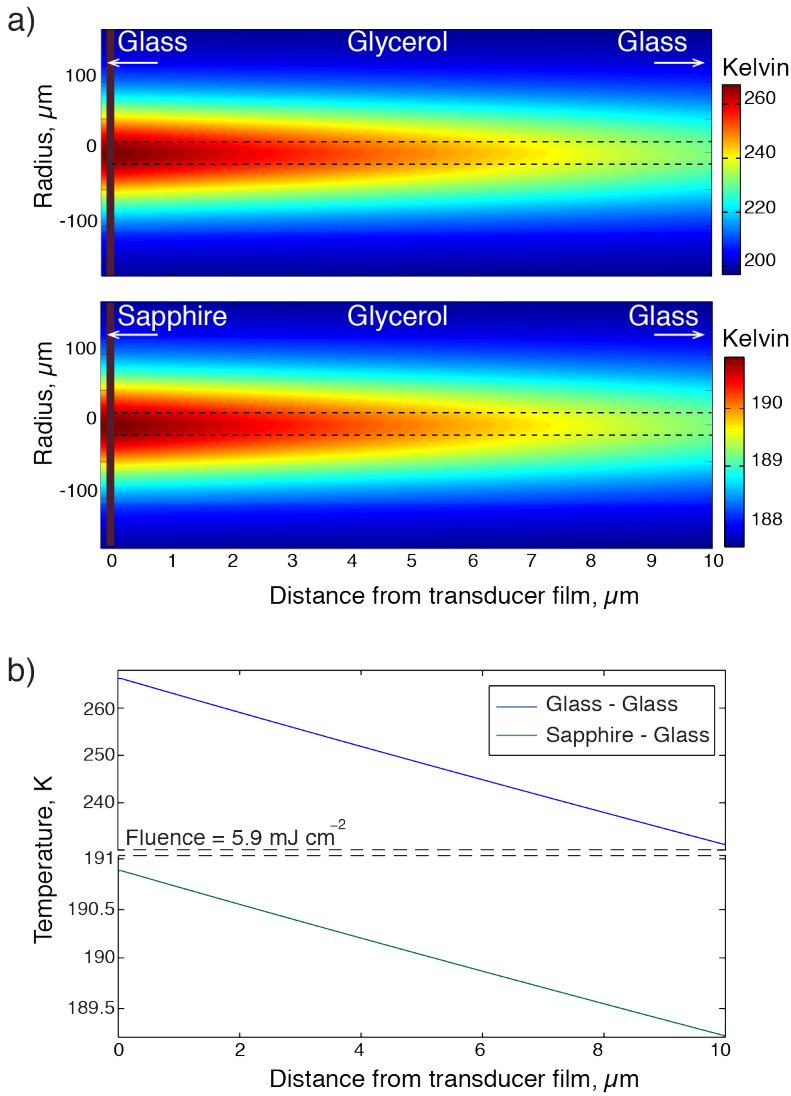

Figure 4.9. (a) 2D Results from simulations of cumulative heating in two different sample structures: a 50 nm iron transducer film, on either glass (Top) or sapphire (Bottom) substrate, which absorbs 39% of a laser pump pulse of 5.9 mJ.cm^{-2} fluence. The transparent cover substrate is glass. The resulting steady state heat distribution in a 10 microns glycerol film sandwiched between both substrates is calculated with the commercial software COMSOL® Multiphysics. The glass transition temperature of glycerol T_g = 186 K was chosen as the initial temperature in all the simulations. The dashed lines indicate the probe beam diameter. Data reprinted from [87]). (b) Extracted temperature distribution plot from the 2D simulations displayed in (a). Note the linear temperature distribution and the pronounced different temperature scale and gradient in each plot.

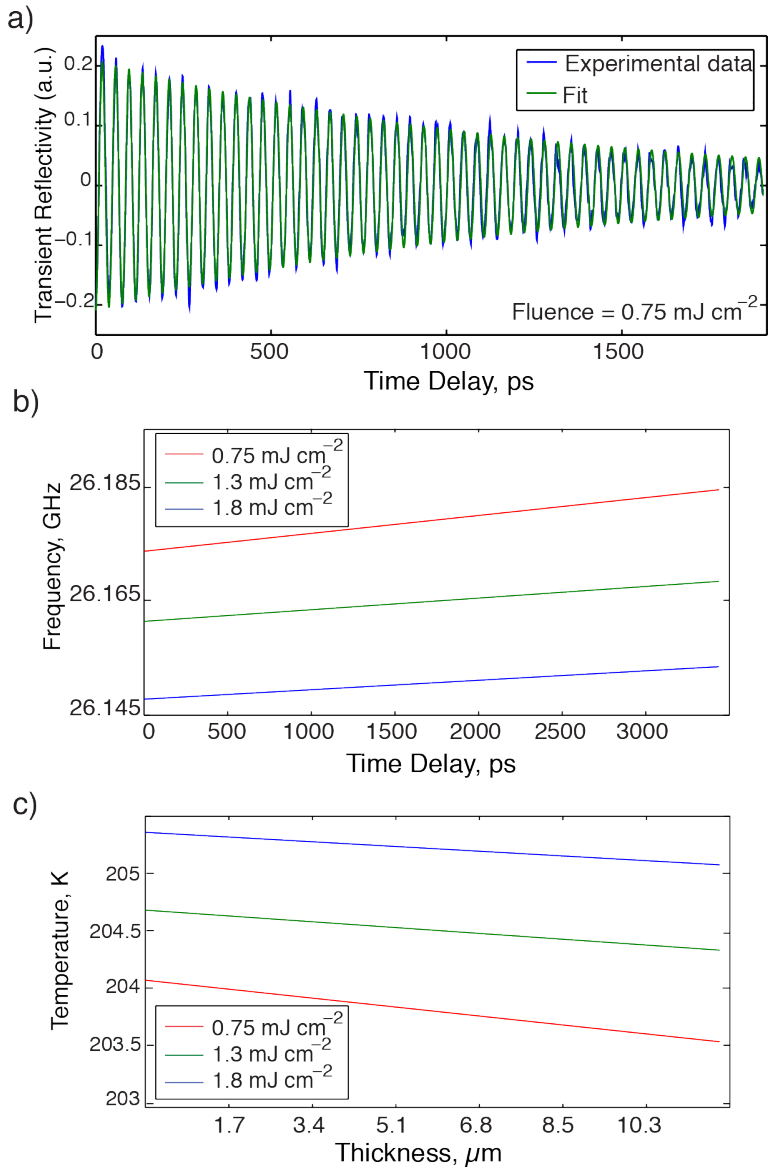

Figure 4.10. (a) Recorded transient reflectivity data for glycerol at 200 K for a laser fluence of 0.75 mJ·cm^{-2} and fit of the experimental data. (b) Time-resolved Brillouin frequency chirp fitted from our experimental results obtained from a 40 nm chromium transducer film deposited on a silicon substrate. The Brillouin frequency up-chirp matches the temperature distribution profile in glycerol at 200 K, for several laser fluences. (c) From the fitted Brillouin frequency in (b), we have obtained the temperature distribution through the liquid thickness, accordingly to the temperature calibration curve of Fig. 4.6 (b).

In order to experimentally reveal the in-depth temperature distribution in the liquid, we have examined further our TDBS data, searching for a frequency chirp in the measured Brillouin frequency. Accordingly to [85], we have modified the functional form given in Eq. (4.4) by allowing the Brillouin frequency to vary in time, during the propagation of the acoustic pulse throughout the temperature gradient in the liquid. The modified Brillouin frequency functional form is then expressed as

$$\Delta \mathrm{R}(t) \sim \sin(2\pi\nu(t)\, t + \phi)\, \exp(-\Gamma t) \tag{4.5}$$

where

$$\nu(t) = \nu_0 + C \cdot t \tag{4.6}$$

represents a linearly chirped frequency, ν_0 being the initial Brillouin frequency at time zero, i.e. close to the transducer film, and C being the linear chirp coefficient. Even though a linear chirp does not reflect the true change in frequency, which has to model the temperature dependence of the Brillouin frequency, it provides a more stable algorithm and can be considered sufficient for the present analysis with little temperature variations across the liquid thickness. Figure 4.10 (a) represents the recorded transient reflectivity data for glycerol at 200 K at 0.75 mJ·cm^{-2} and a fit of the experimental data. The extracted Brillouin frequency up-chirp from Eq. (4.5) for a 40 nm chromium transducer film on a silicon substrate at 200 K and at several different laser fluences are depicted in Fig. 4.10 (b) and (c). The results from the numerical fitting of our experimental data confirm that a temperature gradient is present in our liquid sample and that a good thermal conductor substrate such as silicon lead to weak cumulative laser heating effects, of only a couple of Kelvins. In addition, we notice that the Brillouin frequency decreases with an increase of pump fluence, which is in agreement with a stronger temperature rise at higher pump fluences.

Multilayer structure for enhanced thermal insulation

In order to further decrease the influence of cumulative laser heating effects, which could be detrimental in sensitive experiments such as in studies of confined liquids [37, 38, 157], more complex sample configurations could be explored. We have investigated a multilayer sample structure configuration where an additional thermal insulator layer is added as a thermal barrier between the hot metallic layer and the liquid, see Fig. 4.11. In this case, the sample has an additional silicon dioxide SiO_2 layer on top of the metallic film. First, a 40 nm chromium transducer film was deposited on a silicon substrate, and then a 19.7 nm SiO_2 layer was deposited on half of the metallic film for a straightforward comparison of the cumulative heating effect with or without silicon dioxide film. Measurements with this structure were made for a wide range of pump fluences for both sample configurations. Each recorded transient reflectivity data, see Fig. 4.12 (a) which corresponds to both situations, with or without SiO_2 buffer layer, was further processed in order to numerically extract the initial frequency ν_0 and the chirp coefficient C expressed in Eq. (4.6). The result of the fitting procedure for several different laser pump fluences is shown in Fig. 4.12 (b) and (c). We recall that the initial frequency ν_0 reveals the change in liquid temperature whereas the chirp coefficient C is related to the change in temperature distribution. Therefore, the frequency shift between both configurations, with or without SiO_2 layer, which appears in Fig. 4.12 (b) indicates the temperature rise in the liquid to be substantially minimized through the SiO_2 insulator layer. The temperature rise at the lowest fluence of 0.75 mJ·cm^{-2} is only of 1.5 K with the SiO_2 insulator layer whereas more than twice as much at 3.6 K without the insulator layer. The efficiency of the insulator

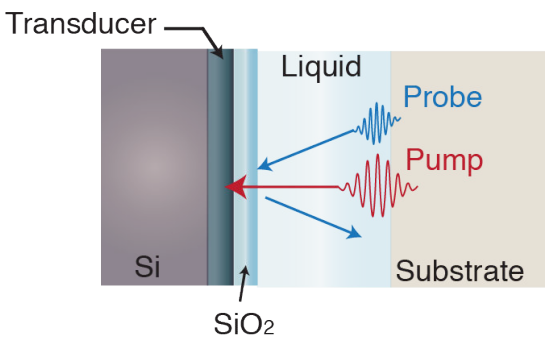

Figure 4.11. Schematic of the multilayer sample. A thin SiO_2 capping layer is introduced in order to thermally insulate the liquid from the laser heated Cr metallic transducer film. As before, a transparent glass cover substrate and glycerol was used in this specific sample configuration.

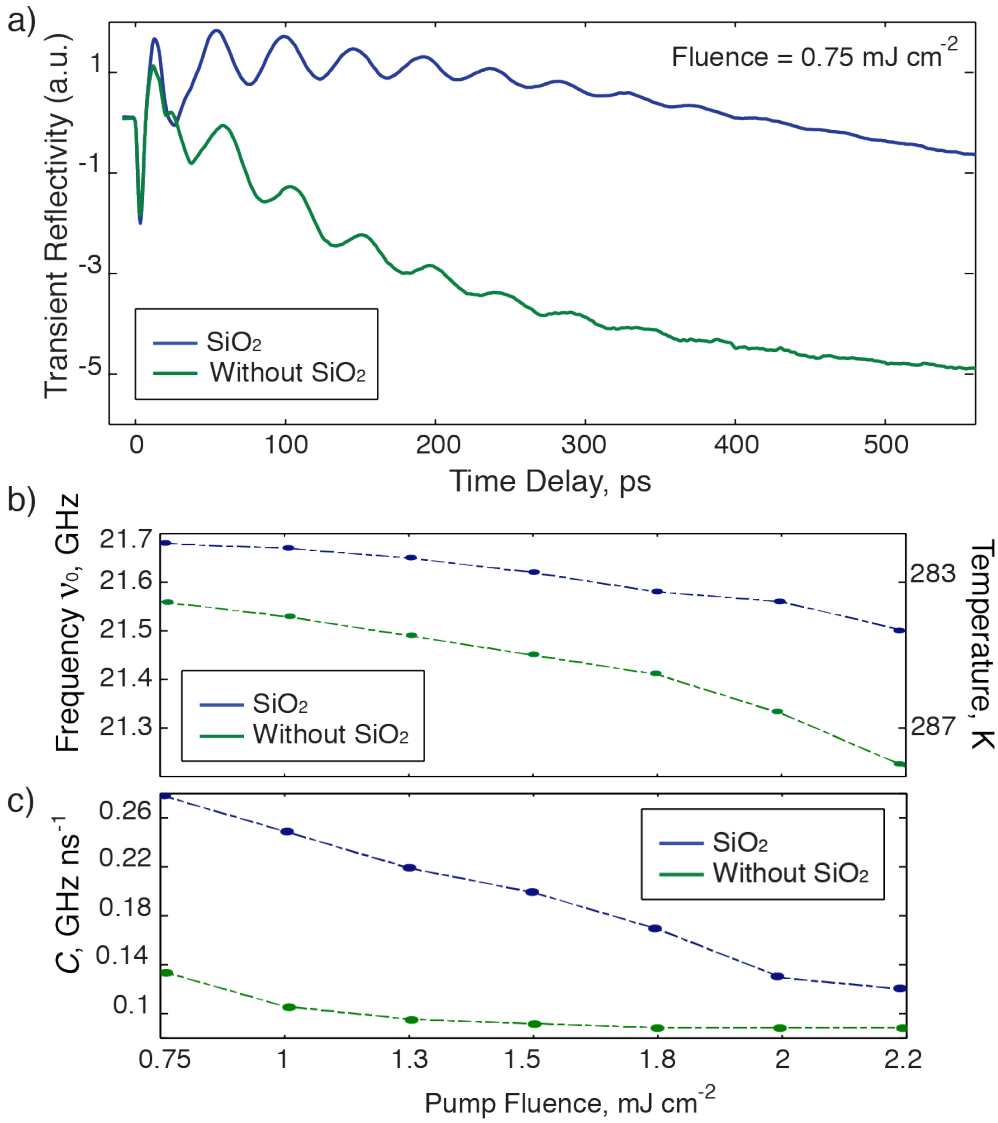

Figure 4.12. (a) Results of the transient reflectivity signals measured in glycerol for both configurations, at a temperature of 280 K, as indicated by the Peltier temperature sensor. Evolution of the Brillouin frequency chirp coefficients ν_0 (b) and C (c) defined in Eq. (4.6) at several laser pump fluences, extracted from the transient reflectivity signals obtained in both configurations, with or without thermal insulator SiO_2 layer. The vertical temperature scale in (b) was deduced from the temperature calibration curve of Fig. 4.6 (c). A noticeable discrepancy in (a) and (b) between both configurations reveals the benefit of the SiO_2 thermal insulator which prevents the liquid from cumulative laser heating.

layer is clear, even at the highest pump fluence where the temperature rise is kept as little as 4.5 K, as compared to an uncapped chromium layer with 8.6 K temperature rise. The obvious difference in the thermoreflectance background signals in Fig. 4.12(a) indicates that the transient temperature rise relaxes to thermal equilibrium quicker in case of an SiO_2 insulator layer, in agreement with our interpretation of the initial frequency chirp ν_0 evolution with pump fluence in Fig. 4.12 (b). Note that since the optical constants mismatch between glycerol and the SiO_2 insulator layer is negligible, we can rule out any optical artifact in our interpretation of the data displayed in Fig. 4.12 (b) and (c).

The interpretation of the frequency chirp coefficient discrepancy between both configurations is not as straightforward. In Fig. 4.12 (c) we notice the chirp coefficient C being higher for the SiO_2 insulator layer case, which means that the temperature gradient is more pronounced than without SiO_2 insulator layer. This behavior is inherent to the higher thermal effusivity ε of the SiO_2 insulator layer in comparison with glycerol. Since $\varepsilon_{SiO_2} = 1.7 \times 10^3$ J·K^{-1}·m^{-2}·s$^{-1/2}$ $> \varepsilon_{glycerol} = 0.9 \times 10^3$ J·K^{-1}·m^{-2}·s$^{-1/2}$, i.e. $\varepsilon_{SiO_2}/\varepsilon_{glycerol} \approx 2$, the SiO_2 layer increases the stationary heat flux from the optically heated chromium film into glycerol [158, 159] that leads to the rise of the temperature gradient in glycerol. Therefore, the temperature rise in glycerol is localized at close vicinity of the chromium film. At the contrary, since the temperature gradient is weaker without insulating layer, the temperature rise is much less localized and homogeneously distributed in depth of the liquid sample. In Fig. 4.12(c) we notice an up-chirp coefficient C decrease with an increase in pump fluence, which means that the temperature gradient weakens at higher fluence for both sample configurations. This may be due to reduced viscosity and/or increased flow of the liquid sample which would moderate the temperature gradient.

4.2.3 Conclusion

These experimental studies and simulations of different sample structures have shown the importance of the proper selection of sample substrates holding the metallic transducer films to avoid cumulative thermal heating effects. Such effects can be efficiently minimized by using a good thermally conducting substrate like sapphire or silicon. To further decrease the influence of cumulative thermal heating effects we have investigated a multilayer sample structure where a thermal insulating SiO_2 layer was added in order to shield the liquid from the laser heated metallic transducer film. We have experimentally demonstrated the benefit of this alternative sample structure which could be required in experimental situations where even slight temperature

changes have to be avoided.

The extrapolation of our results at the nanoscale gives insight on the thermal properties of ultrathin liquid films [37, 38, 157] and shed light on the understanding of nanoscale heat transport [137, 160, 161]. In particular, our quantitative results bring attention to the laser cumulative heating effect that should be accounted in the TDBS experiments performed on ultra thin liquids, described in the next chapter.

Chapter 5

Mechanical properties of ultra thin liquids at GHz frequencies. Results and discussions

In this chapter, we describe experiments on ultra thin liquids performed in the liquid cell specially designed for the TDBS measurements. We recall that the laser excitation takes place at the generation side substrate, composed of a thin Chromium film on a silicon substrate, and the detection of the acoustic waves is performed through TDBS either in the liquid in contact to the transducer, in case of micrometer thick liquid films, or in the detection substrate after traversal of the liquid film, in case of ultrathin liquids. In the following, we review and discuss experimental results that were obtained in different liquids, glycerol, OMCTS and 8 CB.

5.1 Data analysis

From the detection theory in an acoustic/optical cavity described in Chapter 2, in particular, from Eq. (2.34), we know that the detected probe light intensity I_{sig}, undergoes time-dependent modulation at the Brillouin frequency ν_{sub} of the substrate material,

$$I_{sig} = I_{ac} cos(2\pi\nu_{sub} + \delta\phi) \tag{5.1}$$

with

$$I_{ac} \propto \exp(-\alpha d), \tag{5.2}$$

$$\delta\phi = 2\pi(\nu_{sub} - \nu_{liq}) \cdot \frac{d}{c_l(\nu_{sub})}. \tag{5.3}$$

The Brillouin scattering amplitude I_{ac} is given by the sample thickness d and the attenuation coefficient α. The Brillouin phase shift $\delta\phi = \phi_{ac} - \phi_{opt}$ is determined by the time of flight of the acoustic waves through the liquid of thickness d at the acoustic speed c_l, and the Brillouin frequency ν_{liq} of the liquid. However, this expression is valid only if the speed of sound in liquid at ν_{sub} and ν_{liq} is identical, which is not appropriate for many liquids, where the speed of sound is dispersive. A more general formula deduced from Eq. (2.34), can be written in the form:

$$\delta\phi = 2\pi \cdot d(\frac{\nu_{sub}}{c_l(\nu_{sub})} - \frac{2n_{liq}}{\lambda}). \tag{5.4}$$

The only inconvenient in this formula is that the index of refraction $n_{liq}(\lambda)$ needs to be known in advance.

Accordingly, the analysis of the recorded data from different liquid thicknesses follows equations (5.2) and (5.4). A simple example of data analysis is presented in Fig. 5.1. Figure 5.1 (a) shows the time derivative of the measured reflectivity change for two distinct lateral positions X_1 and X_2 in a glycerol sample with a glass detection substrate. These positions correspond to two distinct liquid layer thicknesses $d_2 < d_1$. Data were normalized by the electronic peak intensities before the derivatives were taken. In the following time interval between $\sim$ 35 to 500 ps, oscillations due to longitudinal acoustic waves in the glass detection substrate and their Fourier amplitude and phase are shown in Fig. 5.1 (b) and Fig. 5.1 (c). From these data, we determine the longitudinal acoustic parameters of the liquid at the Brillouin longitudinal acoustic frequency of the detection substrate ν_{sub}. The ratio of the measured Fourier amplitudes, $A_1(\nu_{sub})$ and $A_2(\nu_{sub})$, allows to extract the acoustic attenuation for the liquid thickness difference $\Delta d = d_2 - d_1$ by

$$\alpha_s = \frac{1}{\Delta d} ln \frac{A_1(\nu_{sub})}{A_2(\nu_{sub})} \tag{5.5}$$

and the speed of sound follows from the extracted phase difference $\delta\phi(\nu_{sub})$ by

$$c_l = \frac{\nu_{sub}}{\frac{\delta\phi}{2\pi\Delta d} + \frac{2n}{\lambda}} \tag{5.6}$$

where ν_{sub} and ν_{liq} are the Brillouin frequencies of the liquid and of the substrate material, respectively. Of course, this procedure of extracting the speed of sound and

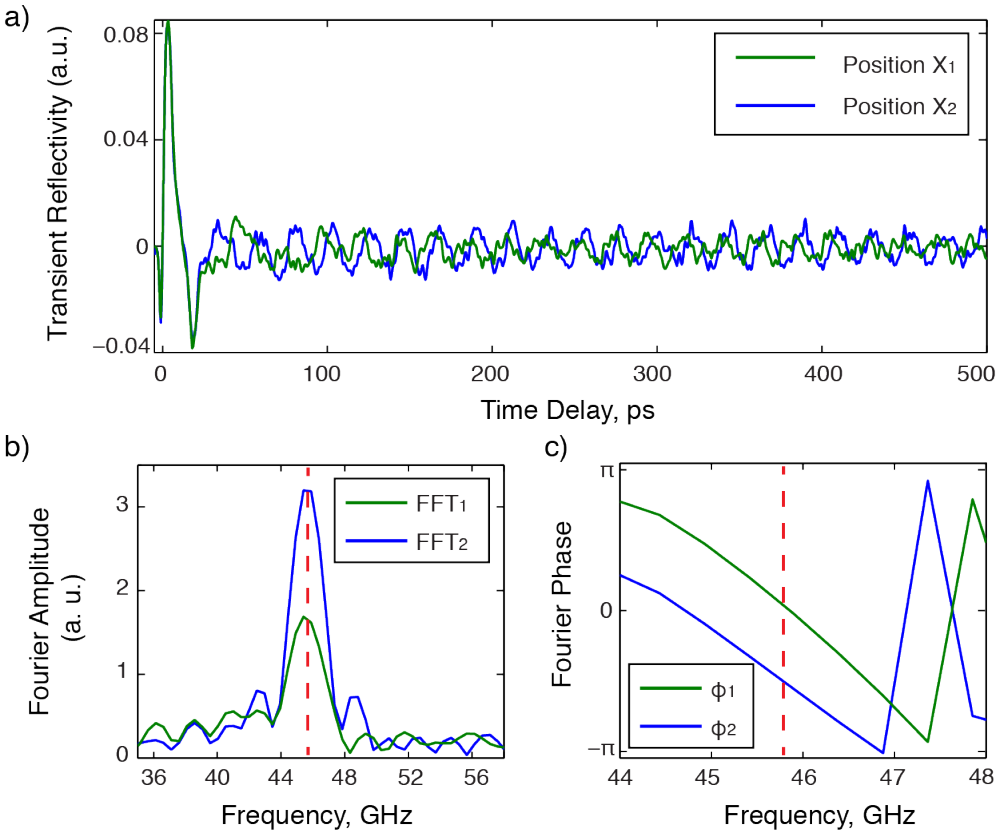

Figure 5.1. TDBS results from a sample configuration with a Chromium acoustic transducer on a silicon substrate, glycerol at room temperature, and a glass detection substrate. (a) Time derivative of the measured signal intensity for two distinct lateral positions X_1 and X_2 of the sample, corresponding to two distinct liquid layer thicknesses d and $d_2 < d_1$. The excitation pulse appears at t = 0 ps due to the electronic response induced in the Chromium film, which is detected by the probe light. This signal is followed by oscillations due to coherent longitudinal waves in the glass detection substrate. (b) Acoustic amplitude spectra of both acoustic signals, FFT_1 and FFT_2 and (c) the corresponding phases, ϕ_1 and ϕ_2. The phase and amplitude differences yield the acoustic speed and attenuation length, respectively, in the liquid at the specified Brillouin frequency. Note that only the phase in (c) at frequencies around the Brillouin peak in (b) at 45.5 GHz contains useful information.

the acoustic attenuation from the FFT spectrum is valid only if the liquid thickness difference is known precisely, otherwise, these quantities are coupled to the liquid thickness Δd and it is not possible to conclude. The determination of the liquid topography or the a priori known relationship of the liquid topography is crucial for the extraction of the relevant acoustic parameters of the liquid. In the following

sections, we will show how an entire set of FFT phase shifts and amplitudes resulting from various liquid thicknesses for different liquids can be used to determine the sound speed and the acoustic attenuation. This procedure provides a high level of precision for the values determined.

5.2 Adjustment of the initial liquid film thickness gap

For each sample assembly, the subtle starting point concerns the initial liquid thickness gap, set at the beginning of each run of measurements, that should be in a small range of liquid thicknesses, roughly well below one micrometer. This is delicate to achieve but crucial since the ultimate goal of these types of measurements is to measure many data over a short range of liquid thicknesses (in the micrometer range), with nanometer precision, and until the contact position. Therefore, all the measurements are performed from an initial liquid thickness gap that is decreased step by step until the contact position of the lens with the substrate, that ends the measurement run. If the initial liquid thickness is over 10 μm, the whole piezostage displacements will not be enough to bring into contact the lens and the flat generation substrate in order to confine the liquid until few molecular layers. So the highest difficulty of the measurement is to adjust the initial liquid thickness gap well below 10 μm and to align the pump-probe spots right at the tip of the lens at the liquid thickness gap, where the liquid thickness is the thinnest. Specifically, we use TDBS lateral measurements in the liquid themselves as a sophisticated tool for the determination of the liquid-lens interface position, with an accuracy in the range of 100 nm. If the liquid thickness gap is wide, the data analysis of the lateral measurements at the Brillouin frequency of the substrate, which contains all the relevant information on the acoustic properties of the liquid, is problematic, challenging and often impossible because of high attenuation of the acoustic waves propagating through thick liquids. In Fig. 5.2 (c) we can clearly distinguish on the TDBS lateral measurements the liquid/lens interface in case of a thick liquid gap at the tip of the lens, but the information on the acoustic waves transmitted from the liquid into the lens is undetectable. If the lens is in contact to the flat generation substrate, as for the TDBS lateral measurements displayed in Fig. 5.2 (a), it is also problematic, since we won't get any useful information on the acoustic wave propagation through the liquid of different thicknesses since there is no liquid in contact zone between the lens and the flat substrate. The only possible scenario for the proper measurement of the Brillouin scattering in the substrate is in the situation of a relatively thin liquid gap, of some hundreds of nanometers, as a

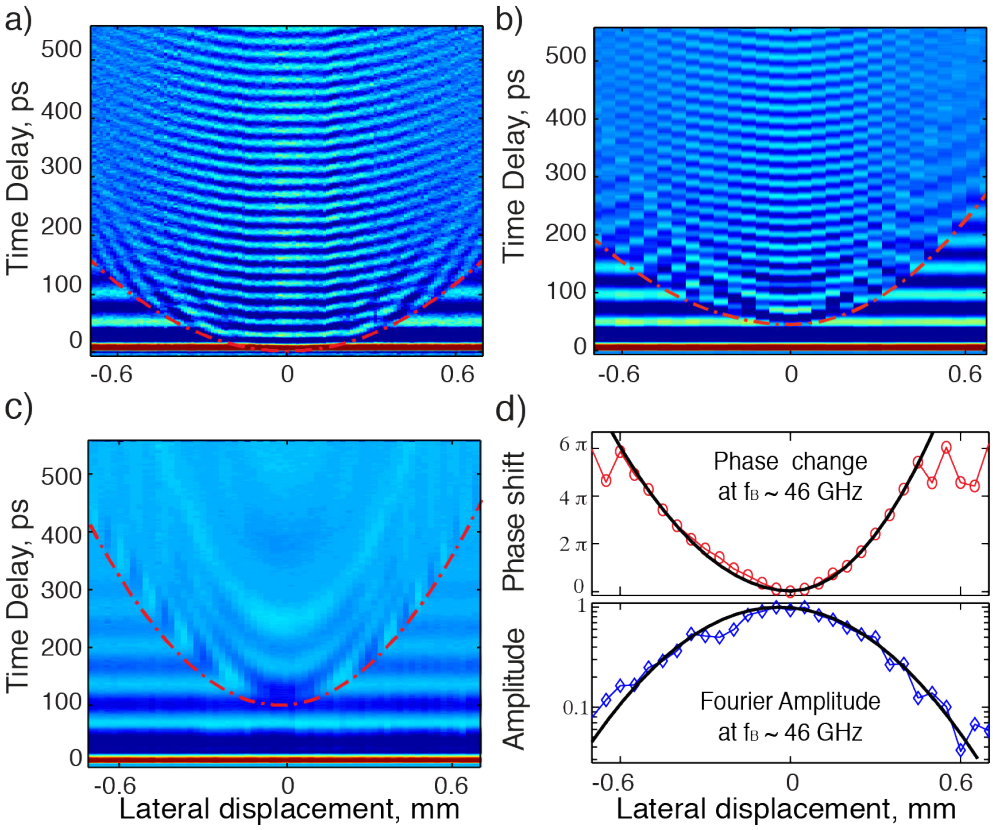

Figure 5.2. Adjustment of the liquid film thickness gap from lateral TDBS measurements. Interpolated 2D plots of several TDBS longitudinal data sets, recorded in glycerol at room temperature at different lateral positions. (a) The lens and the generation substrate are in contact. It is evidenced by flattened dark/bright fringes around the center of the horizontal axis. (b) The lens is separated from the generation substrate by a thickness gap in the range of two hundreds of nanometers of liquid. This is the perfect scenario as a starting liquid thickness gap for the piezo measurements. (c) The lens is separated by several hundreds of nanometers of liquid gap from the generation substrate. (d) Phase shifts and Fourier amplitudes of the 46 GHz Brillouin oscillations in the glass lens extracted from the Brillouin scattering data displayed in (b).

starting liquid thickness. This scenario is achieved with the help of lateral TDBS that is used to control and adjust the liquid thickness gap, until we obtain a lateral TDBS scan that resembles the lateral data displayed in Fig. 5.2 (b). As it was described in Chapter 3.3, the sample holder stands on a motorized linear stage that is used for the rough adjustment of the liquid thickness gap with about 0.1 μm resolution. The procedure is as follows: when all parts are assembled together and fixed, we

run lateral TDBS measurements to detect how far the lens is from the generation substrate as in Fig. 5.2 (c). In the situation of Fig. 5.2 (c), we roughly estimate the liquid thickness from the number of Brillouin scattering oscillations we detect at the tip of the lens, and we decrease the liquid thickness until we obtain a lateral TDBS such as in Fig. 5.2 (b). The situation displayed in Fig. 5.2 (b) is the perfect scenario to start the piezo measurements. The thickness is neither in excess nor in lack. By applying a voltage to the piezostage, it brings closer the lens to the generation substrate, thereby reducing the thickness of the liquid film, step by step. The situation that corresponds to the lateral measurements of Fig. 5.2 (a), are not appropriate with the piezostage, as the lens is already in contact with the generation substrate. So in this case, the linear stage is used to retrograde the lens in order to move away the lens from the generation substrate and add a few hundreds of nanometers of liquid, until we obtain a lateral scan as in Fig. 5.2 (b). After each step, we repeat the lateral measurements to be sure that the thickness of the liquid film is well adjusted. These operations may be repeated several times before the final measurements. Often all these adjustments take more time than the actual measurements of ultrathin liquids with the piezostage.

The measurements presented in Fig. 5.2 were recorded at room temperature in glycerol, squeezed in between a plano-convex lens (ROC = 386.3 mm) without AR coating and a flat n-dopped Silicon substrate holding a 40 nm Chromium transducer film. The raw data analysis of the phase shifts and of the amplitudes of the Brillouin frequency at 46 GHz of the TDBS lateral measurements allows to estimate the speed of sound and the attenuation coefficient in glycerol under these particular experimental conditions, as described in the next section.

The procedure for the adjustment of the liquid thickness gap between the lens and the detection substrate is indispensable prior to the measurements of ultra thin liquids performed with the piezostage. In addition, this routine lateral TDBS procedure, in conjunction to the piezostage, enables to cover a wide range of liquid thicknesses - from bulk to few molecular layers. Note that the lateral TDBS measurements can be used as an opto-acoustic sensor to detect and image the interface of transparent objects, that can't be detected optically.

5.3 Time domain Brillouin scattering study of glycerol

Despite not being the best option among all existing liquids for the investigation of confinement effects, because of quite small molecule size, glycerol has been chosen as a glass forming liquid prototype through the availability of information on both its mechanical and thermal properties. Glycerol was used as a well known material in order to set and improve the experimental and theoretical issues and to ascertain the accuracy of the measurements and calculations.

5.3.1 Lateral TDBS measurements on glycerol

Before proceeding to the measurements of changeable liquid thicknesses via the piezostage displacement, we have performed TDBS lateral measurements in order to measure the bulk mechanical properties of glycerol and validate the accuracy of the TDBS lateral method. The advantage of such measurements is the relative ease in calculating the liquid thickness from the lens radius of curvature in Eq. (3.1), which is always known, to access the speed of sound and acoustic attenuation from the Fourier analysis of the TDBS lateral measurements in the lens.

After sample assembly, the sample is placed on the motorized multiaxial stage and in general, unless of a lucky coincidence, the pump-probe overlap is far from the liquid thickness gap at the Newton's rings center. Therefore we run many lateral scans along the X (horizontal) and Y (vertical) directions to locate the liquid thickness gap (the tip of the lens) that can be later adjusted with the linear stage at the beginning of each run of measurements. All the parameters of the measurements are computer controlled from a Labview program. The user select the parameters of the measurements in the LabView program such as the scanning time window, the lateral displacement distance and step in X or Y direction, the velocity of the delay stage motion, the number of averages and so on. Thanks to this program, that fully automate the data acquisition, all the measurements were made continuously by itself in a non-stop mode, that allowed to capture a wide range of liquid thicknesses with equal step. When the full run of lateral measurements is recorded, the next step consists in the data analysis. Lateral TDBS data sets are presented in Fig. 5.3 (a). Data were recorded for a glycerol sample squeezed in between a plano-convex lens without coating of radius ROC = 206 mm and a flat silicon substrate holding a 40 nm thick Chromium film. The sample was held at room temperature of about 295 K. The pump power was set to 30 mW that corresponds to about 1.5 mJ·cm^{-2}, in order to prevent the cumulative

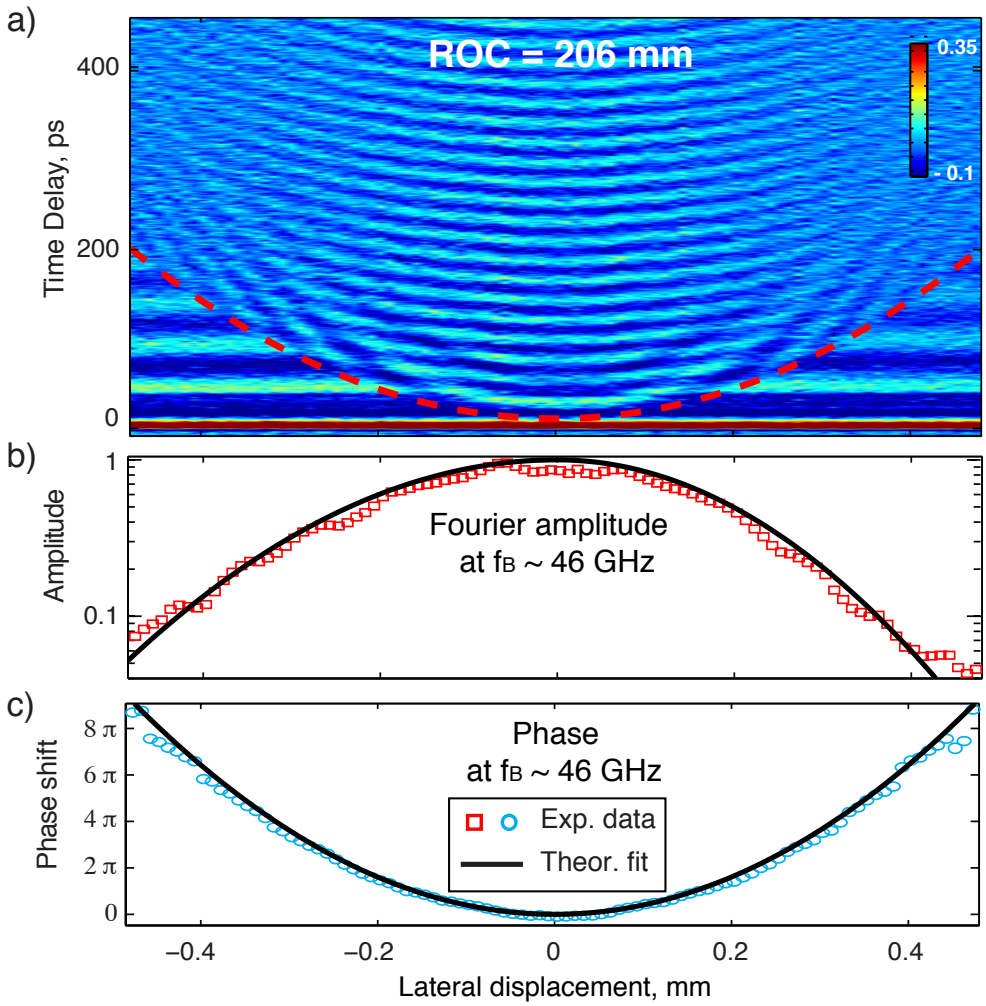

Figure 5.3. (a) Interpolated 2D plot of 111 longitudinal wave data sets, recorded in glycerol at room temperature, as a function of time delay at different lateral positions X. The central part illustrates the high-frequency signal oscillations at 46 GHz that corresponds to Brillouin scattering from longitudinal acoustic waves in the N-BK7 glass lens. Side regions correspond to low-frequency signal oscillations at $\sim$ 21 GHz due to Brillouin scattering from longitudinal acoustic waves in liquid glycerol. In the central zone, the signal oscillations detected in the lens begin promptly. Away from the center the signal oscillations due to acoustic wave propagation in the lens are more time delayed and phase shifted. (b) Normalized acoustic amplitude and (c) normalized phase shifts of the 46 GHz signal oscillations extracted from Brillouin scattering in the lens. The extracted amplitude and phase provide the information on the acoustic attenuation coefficient α and the sound velocity c_l in glycerol.

laser-induced heating of the liquid. The X step was set to 10 μm that is about the same size than the focused probe diameter of 8 μm. In Fig. 5.3 (a), an interpolated 2D plot of 111 longitudinal TDBS data sets as a function of delay time at different lateral positions X is presented. The central part illustrates the high-frequency signal oscillations at 46 GHz that corresponds to Brillouin scattering from longitudinal acoustic waves in the N-BK7 glass lens. While side regions correspond to low-frequency signal oscillations at $\sim$21 GHz due to Brillouin scattering from longitudinal acoustic waves in liquid glycerol. In the central zone, the generation and detection substrates are presumably close to contact, the liquid gap is below 100 nm. Signal oscillations detected in the lens begin promptly. Away from the center the signal oscillations due to acoustic wave propagation in the lens are more time delayed and phase shifted as it can be noticed in Fig. 5.3 (c). Starting from X $\approx$ 0.1 mm, the signal oscillations arises from the acoustic wave propagation first in the liquid and then from acoustic wave transmitted into the lens. We can even notice on the 2D image the reflection of the acoustic wave from the inclined lens surface, away from X $\approx$ 0.3 mm.

As described in Section 5.1, the FFT data analysis of the lateral TDBS measurements lead to the amplitude and phase evolution at different lateral positions of the Brillouin oscillations at 46 GHz, that lead to the acoustic attenuation coefficient α and the sound velocity c_l in glycerol. By fitting the computed curves of normalized Fourier amplitude and phase with Eq. (5.5) and Eq. (5.6) as a function of lateral position, that corresponds to different liquid thicknesses, the values for the acoustic attenuation coefficient and speed of sound in glycerol were derived. The obtained values are in full agreement with those that can be found in literature [148] at the same frequency, $\alpha = 5.1 \pm 0.9 \cdot 10^6$ m^{-1} and $c_l = 2900 \pm 60$ m/s.

The aforementioned experiments, that are in fact routinely used to adjust the liquid gap thickness prior to each run of experiments, were repeated many times, with different liquids and give an easy access to the values for α and c_l in bulk liquids. The results of such type of experiments performed for other liquids are discussed in Sections 5.4 and 5.5.

5.3.2 TDBS piezo measurements of ultrathin glycerol

The lateral TDBS measurements are the first step toward the measurements of ultrathin liquids that uses the piezostage in order to modify the liquid thickness gap with a nanometer resolution. As it was already mentioned, the liquid "stiffening" effect happens on ultra-small sizes comparable to the molecular dimensions, it is hard to observe and the lateral measurements are not appropriate since the liquid thickness

variation is too extreme upon a slight modification of the lateral position. The difference in liquid thickness Δe between two distinct lateral positions X_1 and X_2 in case of a lens with a radius of curvature ROC follows the Newton's ring relationship in the form,

$$\Delta e = \frac{(X_1 - X_2)^2}{2ROC}. \tag{5.7}$$

In general the ROC radius of curvature of the lens is in the range of 200 - 400 mm, to enable an easy liquid flow when the liquid gap thickness is modified by the piezostage. Under the experimental conditions described above, the thickness difference Δe between two nearest lateral positions at the tip of the lens separated by 10 μm, which is about the size of the probe spot, is in the range of 0.1 - 0.2 nm but it reaches 50 - 00 nm at a distance of 100 μm from the center. Therefore the measurements on ultrathin liquids are incompatible with lateral displacements that lead to disproportionate liquid gap thicknesses and should be performed at the tip of the lens where the thickness inhomogeneity from the curvature is well below the piezo stage resolution. The piezo stage accuracy or thickness resolution is limited by the piezo sensor resolution that lies within 1 - 2 nm. According to our experience, a reasonable thickness step should be set in the range of 5 nm in order to avoid uncertainties on the piezo stage position sensor. To reach a better resolution, it is required to perform several runs of measurements with slightly different and shifted thicknesses.

The principle of the sample assembly and procedure for the piezo measurements are described in Chapter 3.3. Initially, the liquid is thick enough and the thickness is not known exactly before the experiments. Once the initial liquid thickness gap at the tip of the lens is adjusted with the help of the lateral TDBS procedure, we launch the LabView acquisition program in automated mode to control the piezo stage. In this case, the lateral displacement step is disabled and the main parameters selected on the user interface are the piezo displacement step and the full range of displacements.

Fig. 5.4 demonstrates an example of TDBS measurements using the piezo stage. Glycerol was squeezed in a standard sample configuration consisting of a plano-convex lens (ROC = 386 mm) and a flat n-dopped Silicon substrate that holds a 40 nm Chromium film. The data were recorded at room temperature and the laser power was selected in order to avoid unwanted liquid heating. The piezostage step was set to 5 nm. Fig. 5.4 (a) shows a set of about 102 longitudinal TDBS data recorded in glycerol at different liquid thicknesses that correspond to relative different piezo displacements. Starting from an arbitrary negative values to 0 nm, we can observe high-frequency signal oscillations at ν_B = 46 GHz which correspond to Brillouin scattering from longitudinal acoustic waves in the glass lens.

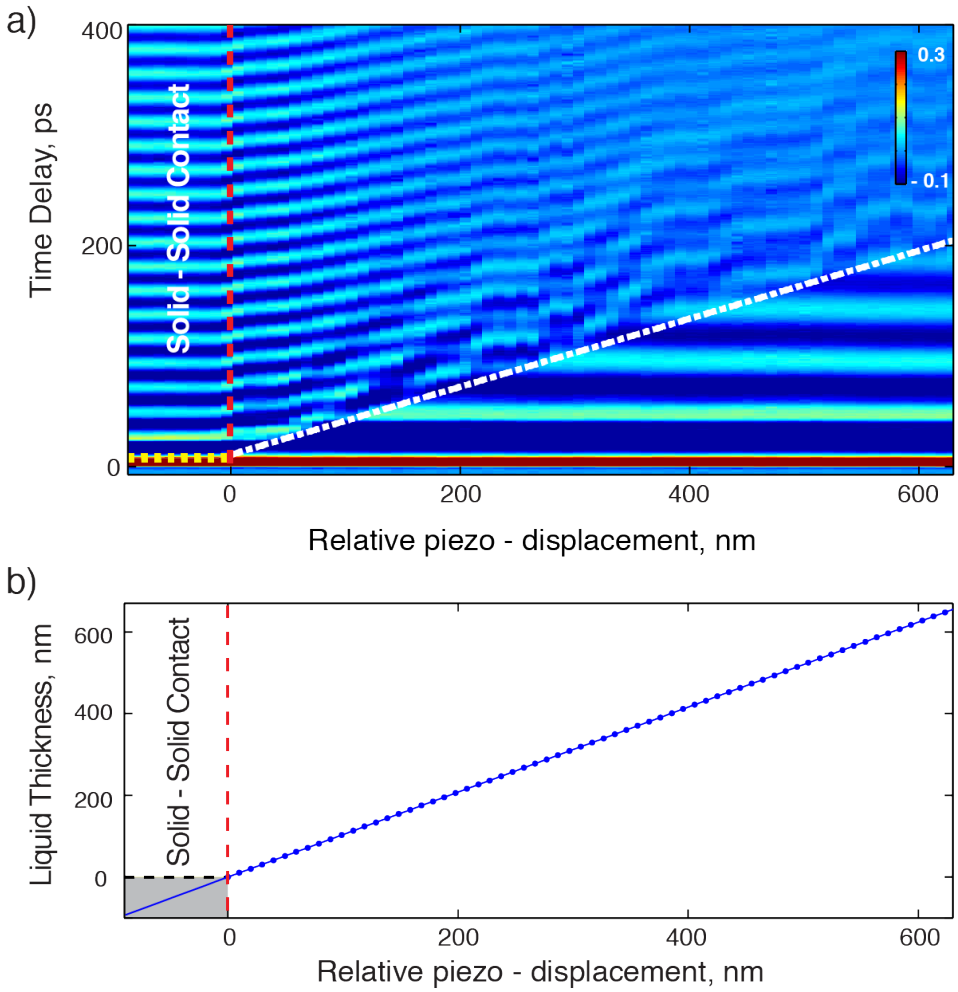

Figure 5.4. (a) Interpolated 2D plot of 102 TDBS longitudinal data sets, recorded in glycerol at room temperature, as a function of delay time and at different liquid thicknesses. The arbitrary negative values of piezo - displacement correspond to solid-solid contac. The high-frequency signal oscillations at $\nu_B = 46$ GHz correspond to Brillouin scattering from longitudinal acoustic waves in the lens. The region from 0 to 630 nm shows large oscillations of Brillouin scattering in glycerol at $\nu_B = 21$ GHz, until the acoustic waves reach the liquid/lens interface. Then the acoustic pulse gets partially transmitted into the glass lens, as evidenced by high-frequency signal oscillations. The whight dotted line highlights the liquid/lens interface. (b) The change in liquid thickness scales linearly with the tension applied to the piezostage and is identical to the relative piezo displacement. The lens/generation substrate contact is evidenced by gray rectangle.

This region correspond to the contact between the generation substrate and the detection lens substrate. From about 0 to 630 nm, the large oscillations of Brillouin scattering in glycerol at $\nu_B = 21$ GHz are visible as for the reflection of the acoustic wave at the liquid/lens interface. The acoustic pulse that gets partially transmitted into the glass lens after crossing the liquid of variable thickness is also evidenced by the high-frequency signal oscillations from 0 to 400 nm. Additionally, one observes weak oblique waves after reflection at the liquid/lens interface that correspond to the reflection of the acoustic waves from the interface and, most probably, to acoustic round trips in the liquid cavity. The white dotted line in the figure highlights the liquid/lens interface. Using the slope of this curve, the sound velocity of bulk glycerol may be calculated. The derived value of the sound velocity of bulk glycerol at ν_B ~21 GHz is $c_l = 2900 \pm 120$ m·s^{-1}, which agrees very well to that extracted from Eq. (2.21), $c_l = 2890 \pm 60$ m·s^{-1} and with the readily available data in the literature [87].

During data recording, the program stores the pump-probe data obtained from the lock-in amplifier as well as the tension applied to the piezo stage in order to control the true position of the step-by-step motion of the piezo stage. The information gathered on the tension is used afterwards to control the proper motion of the piezo stage and to confirm the correctness of the displacements. According to the tension applied to the piezostage, we can derive the liquid thickness change with nanometric resolution. The piezo displacement d varies linearly with the applied tension $d \approx 1.04$·U, where U is the applied tension, and as a result the liquid thickness decreases linearly with a 1:1 slope as a function of the piezo - displacement, as shown in Fig. 5.4 (b). Once we can notice on the piezo acquisition a flat region where the Brillouin scattering in the glass remains constant, as in Fig. 5.4 (a) in the negative region of piezo displacements, that corresponds to the region of solid-solid contact, we can calculate the absolute value of liquid thickness for any recorded data.

We have further analysed the TDBS oscillations recorded with the piezo stage by performing FFT, as previously, to retrieve the information on the Fourier amplitudes and phase shifts at different liquid thicknesses. The FFT data corresponding to the Brillouin frequency in the glass lens at $\nu_B = 46$ GHz are presented in Fig. 5.5. The examination of these parameters yielded accurate values for the speed of sound and the acoustic attenuation coefficient in bulk glycerol. The slope of the entire set of phase shifts resulting from various liquid thicknesses, as shown in Fig. 5.5 (a), was used to determine a single quantity, the speed of sound through Eq. (5.6). Similarly, the slope of the entire set of normalized Fourier amplitudes recorded at multiple liquid thicknesses as shown in Fig. 5.5 (b), was used to determine the attenuation coefficient

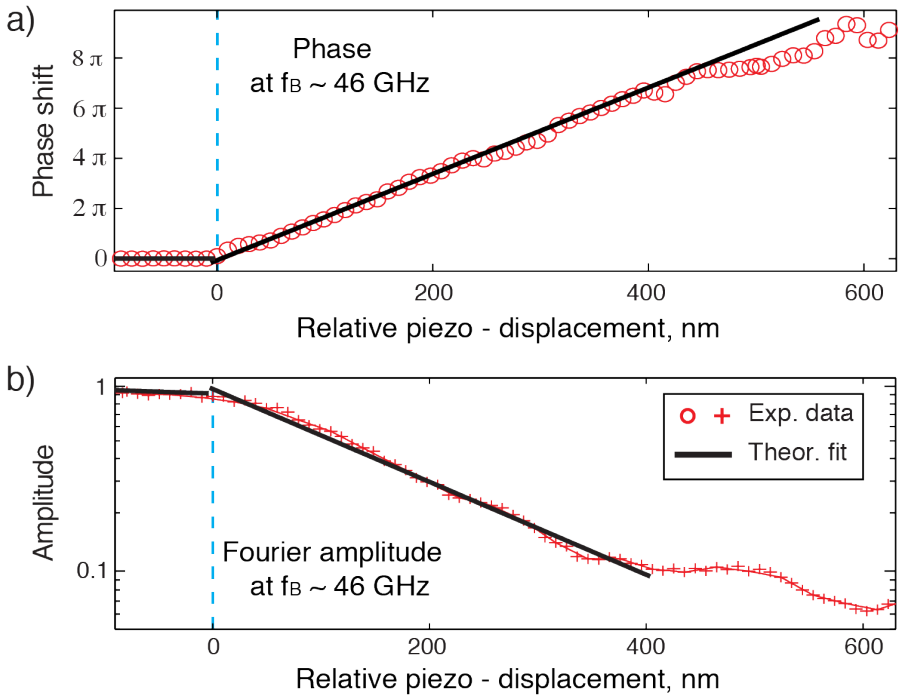

Figure 5.5. Fourier phase shift (a) and amplitude (b) of the 46 GHz Brillouin oscillations in glass, extracted from TDBS piezo measurements with Glycerol. The raw data are presented in Fig. 5.4.

α at the Brillouin frequency ν_B through Eq. (5.5). Measurements were repeated many times and gave consistent results. The values of the extracted acoustic parameters are $\alpha = 5.8{\cdot}10^6$ m^{-1} and $c_l = 2940$ m/s, that are consistent to our previous measurements. We can conclude that our TDBS experimental setup based on the piezostage, is reliable and accurate for the study of ultrathin liquids presented in this work.

5.4 Time domain Brillouin scattering study of OMCTS

From a general standpoint, OMCTS is more "adapted" for the investigation of confinement effects than glycerol. OMCTS has been extensively used as a model in SFA (Surface Force Apparatus) experiments [5,22,162], because the OMCTS molecule is relatively rigid and its dimensions are well characterized. The oblate spherical model of OMCTS has a major diameter of 1.0 nm to 1.1 nm and a minor diameter of 0.7 nm to 0.8 nm that is most often modeled as a spherical molecule. It is also widely used as a testing sample by other techniques, especially by AFM [163–165] for better understanding of liquid structuring. Great contributions have been made by computational modeling [166–168] that investigated confined OMCTS. Nonetheless, the information on mechanical and optical properties of this liquid, even in bulk, is very limited. As a result, the experimental information on the acoustical properties of confined OMCTS still remains missing.

5.4.1 Lateral TDBS measurements of OMCTS

The first intricacy that we have faced was the absence of available information on the speed of sound and acoustic attenuation of bulk liquid OMCTS at high frequencies, in the GHz frequency range. Therefore the prevailing task for us was to experimentally determine these quantities. As it was shown earlier, the lateral measurements and the piezo stage measurements are suitable to ascertain these parameters with high accuracy. Thus, firstly, we have performed the same TDBS lateral experiments as for glycerol in Section 5.3).

TDBS data sets for a sample that consisted of a n-dopped Silicon substrate holding a 40 nm of Chromium film, a thin liquid film of OMCTS and a plano-convex lens with antireflection coating (ROC = 386 mm), were recorded at room temperature for multiple lateral positions X, corresponding to different liquid thicknesses. Fig. 5.6 (a) shows the set of 141 TDBS longitudinal wave data recorded with the liquid OMCTS sample. These data were recorded with X steps of about 10 μm. The central part of Fig. 5.6 (a) indicated by a red stippled line corresponds to the high - frequency Brillouin oscillations at $\nu_{substrate} \approx 46$ GHz. This signal corresponds to Brillouin scattering from longitudinal acoustic waves in the N-BK7 glass lens. The low-frequency signal at $\nu_{liquid} \approx 8$ GHz on the left and right sides corresponds to Brillouin scattering from longitudinal acoustic waves in OMCTS.

As one might notice, the 2D image is not as clear as in case of glycerol. This

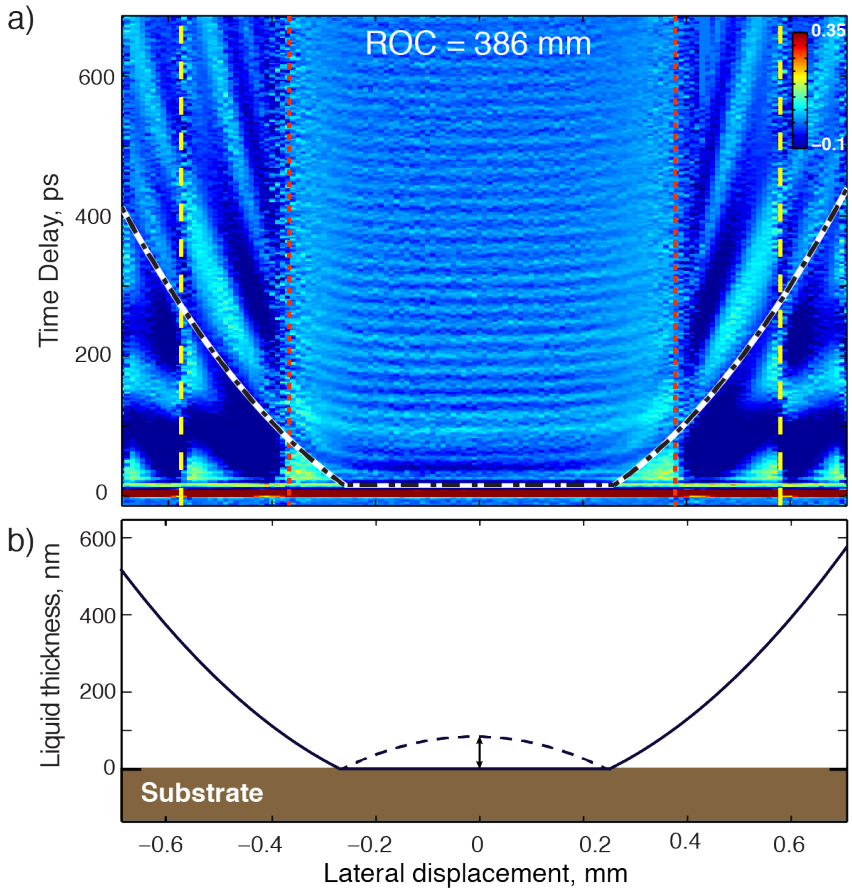

Figure 5.6. (a) Interpolated 2D plot of 141 longitudinal wave data sets, recorded in OMCTS at room temperature, as a function of delay time, at different lateral positions X. The central part illustrates the high-frequency signal oscillations at 46 GHz that correspond to Brillouin scattering from longitudinal acoustic waves in the N-BK7 glass lens. Side regions correspond to low-frequency signal oscillations at 8 GHz due to Brillouin scattering from longitudinal acoustic waves in liquid OMCTS. On the central zone, the two substrates are in direct contact. This is evidenced by the flattened dark/clear fringes in this zone and by the negligible phase change. Signal oscillations detected in the lens begin promptly. Away from the center, the signal oscillations due to acoustic wave propagation in the lens are more delayed and phase shifted, see Fig. 5.7. Starting from $X \approx 0.35$ mm, the signal oscillations arise from acoustic wave propagation in the liquid. The oblique waves on the 2D plot from 400 ps at $X = 0.65$ mm are consequently to the reflection of the acoustic wave from the inclined lens surface. (b) Liquid thickness topography extracted from the fit of the reflection of the acoustic wave at the liquid-lens interface, highlighted in (a) with black and white dashed lines.

is due to the fact that we used an AR lens instead of an uncoated lens for these measurements. As mentioned in Annex B, the contrast of clear and dark Newton's rings is much higher with the use of AR lenses, in comparison with the use of uncoated lenses. The visualization of the Newton's rings simplifies the process of finding and aligning the Newton's rings center with the pump-probe spots. Nevertheless, the TDBS amplitude depends on which interference fringes it was detected and in turn, the detected TDBS signal level vary from the optical point of view during lateral TDBS measurements. The TDBS acquisition at multiple lateral positions cannot be accomplished in an automatic manner. At each small lateral displacement, the balancing between the probe beam reflected from the sample and the reference beam should be manually improved to maintain a descent signal to noise ratio. To bypass this problem, we have tested an auto-balanced optical receiver (Nirvana from Newport), but it was not very satisfactory, the recorded signals were still more noisy and the problem was not completely solved. For this reason, we prefer to use uncoated lenses when mounting our liquid samples. The comparison of the sample surface imaging and automated TDBS lateral acquisitions for a sample composed of a lens with or without AR coating is presented in Annex B. The yellow dotted lines on both sides in Fig. 5.6 (a) indicate the position of the dark Newton's rings. The relevant information about the transmission and propagation of the acoustic waves in the glass lens at a distance of about 20 microns is completely lost due to these dark rings. Unfortunately, the signal recorded in these regions is at the noise level.

Fig. 5.6 (b) reveals the computed liquid thickness topography, deduced from the extraction of the liquid-lens interface tracked on Fig. 5.6 (a) and highlighted by dark and wight dashed line. The fit of the liquid-lens thickness variation along the displacement X is performed based on Eq. (3.1). Knowing the liquid thickness topography, we can estimate the sound velocity of liquid OMCTS at 8 GHz. The extracted sound velocity value is $\sim 1330 \pm 100$ m·s^{-1}. This value cannot be compared to any others because of lack of analogue measurements in the literature.

Additional acoustic informations can be derived from the data displayed in Fig. 5.6 (a), from the analysis of the Fourier amplitude and phase shift of the acoustic waves detected in the lens at 46 GHz. The Fourier analysis yield values for the speed of sound and acoustic attenuation in OMCTS at 46 GHz. Fig. 5.7 displays the analysis of the Fourier amplitude and of the phase change of the acoustic wave at $\nu_{substrate} \approx 46$ GHz. As it was already mentioned before, in the central zone, the lens is in direct contact to the flat generation substrate. The normalized amplitude and phase shift evidence the contact zone where the phase or the amplitude remain

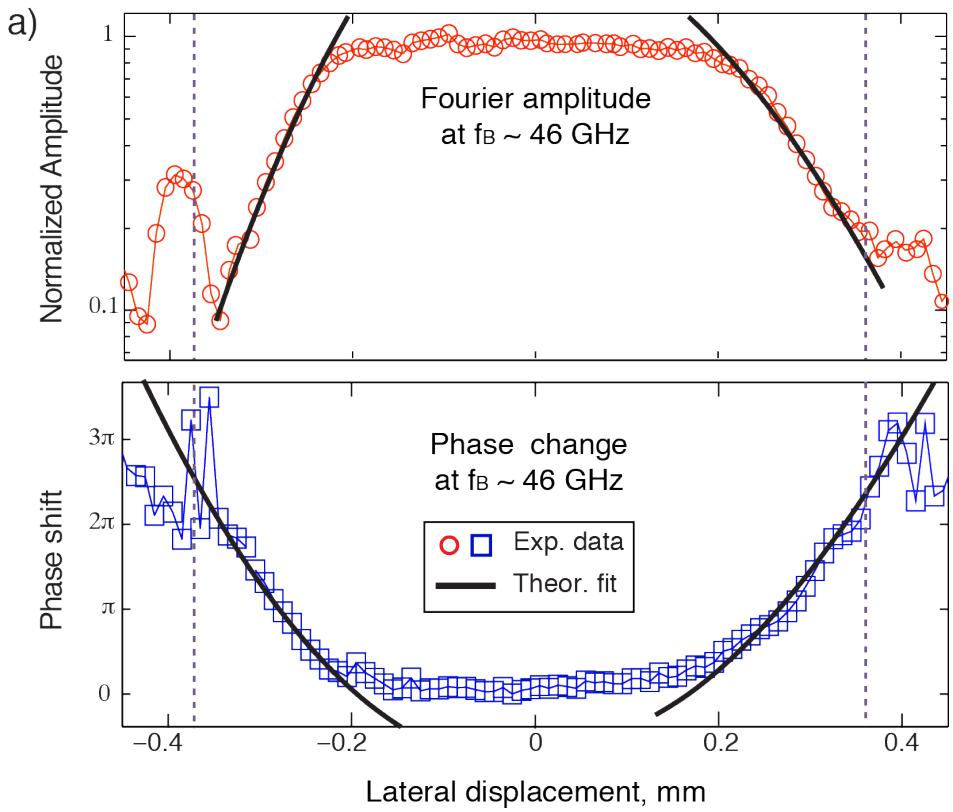

Figure 5.7. (a) Normalized acoustic amplitude and (b) phase shifts of the 46 GHz signal oscillations extracted from Brillouin scattering in the lens (see raw data in Fig. 5.6 (a)). The extracted amplitude and phase shift provide information on the acoustic attenuation coefficient α and the sound velocity c_l in OMCTS.

constant. Signal oscillations detected in the lens begin promptly in this contact zone. Away from the center ($X \approx 0.2$ mm), the transit time through the liquid layer of different thicknesses manifests as a phase shift and an amplitude decrease in the signal oscillations. With further displacements from the center, the signal oscillations due to acoustic wave propagation in the lens are more phase shifted. And starting from $X \approx 0.35$ mm, the low - frequency signal oscillations arising from the acoustic wave propagation in the liquid OMCTS becomes predominant, that is why the Fourier amplitude and phase shift at 46 GHz gets noisy.

Based on Eq. (5.5) and (5.6), the fit of the extracted Fourier amplitude and phase shifts of the 46 GHz Brillouin oscillations in the lens allowed us estimate the acoustic attenuation coefficient α and the sound velocity c_l in OMCTS at 46 GHz. The values that we have found are $\alpha = 21.5 \pm 1{\cdot}10^6$ m^{-1} and $c_l = 3100 \pm 120$ m·s^{-1}.

The extracted value for the speed of sound at 46 GHz is about twice higher than the value obtained at 8 GHz. An increase of the speed of sound at higher frequencies can be expected, since in general materials become stiffer at higher frequencies [101], but this jump in speed of sound is unexpected.

In the following, we will describe the measurements with the use of a piezostage, in order to measure by other means the speed of sound and acoustic attenuation for thiner liquid films.

5.4.2 TDBS piezo measurements of ultrathin OMCTS

As for glycerol, TDBS measurements of ultrathin OMCTS with the use of a piezostage have been performed. The sample was prepared by squeezing OMCTS between an uncoated lens (ROC = 386.3 mm) and a flat Silicon substrate covered by 40 nm of Chromium. The liquid thickness gap was adjusted to several hundreds of nanometers in order to perform the TDBS piezo measurements over a relevant range of liquid thicknesses and increase the accuracy of the calculations. The experiment has been performed at room temperature and at low laser power. The data are presented in Fig. 5.8 (a). The figure displays a set of 138 TDBS longitudinal data recorded with OMCTS as a function of delay time and relative piezo displacement (the origin of the displacement is arbitrary chosen as the starting point of the measurement). The step of the piezostage displacement was set to 10 nm in a piezo displacement range from 0 to 950 nm, and decreased to 5 nm in the piezo displacement range from 950 to 1550 nm that requires higher thickness resolution. The black curve in Fig. 5.8 (a) highlights the liquid/lens interface. The low-frequency signal oscillations at $\sim$ 8 GHz, in the displacement range from 0 to 950 nm, correspond to Brillouin scattering from longitudinal acoustic waves in OMCTS. Whereas, the high-frequency oscillations at $\sim$ 46 GHz, in the displacement range from 1200 to 1550 nm, correspond to Brillouin scattering from longitudinal acoustic waves in the lens. There is a wide region, from 1000 to 1200 nm, where there are no obvious oscillations on the signal and it is impossible to visualize any frequency in this region, possibly due to strong acoustic attenuation in OMCTS. The red dotted lines enclose this region in Fig. 5.8 (a).

From these measurements it is possible to double-check the previously found value of speed of sound at 8 GHz. First, since the Brillouin oscillations in the liquid OMCTS are well defined in Fig. 5.8 (a), at the contrary with Fig. 5.6 (a) where the Newton's rings hide the Brillouin oscillations in the liquid, we can use the low-frequency Brillouin oscillations from longitudinal acoustic waves in OMCTS to retrieve the acoustic velocity in the liquid. The Brillouin scattering oscillations were fitted by

the functional form of Eq. (2.20), which allows the extraction of a precise value for the Brillouin scattering frequency in bulk OMCTS, we obtain $\nu \approx 8.2$ GHz. Since we have measured the index of refraction of OMCTS at the probe wavelength from the interferometric detection of the Newton's rings in Annex B, we obtain $n = 1.37$, the straightforward calculation of the longitudinal sound velocity from Eq. (2.21) leads to the value of $c_l = 1185 \pm 100$ m·s^{-1}, which conforms our prior calculations. The uncertainty comes from the large width of the Brillouin frequency peak in OMCTS that is due to a strong acoustic damping.

We have further analyzed the Fourier amplitude and phase shifts in the glass lens in order to get the information about acoustic attenuation and speed of sound in OMCTS at 46 GHz, as shown in Fig. 5.8 (b) and Fig. 5.8 (b) and (c). In Fig. 5.8 (b) we can notice two different slopes of the phase shifts at 46 GHz. The region with a steeper slope, in the displacement range from 1000 to 1200 nm, corresponds to the zone with poorly defined frequency, therefore the extracted phase shifts do not provide a definite value of the speed of sound in OMCTS at 46 GHz. The phase slope of this small displacement region leads to a hypothetical speed of sound in the range of 4030 m·s^{-1}. The derived value of the speed of sound is excessively high. The incorrectness of the extracted value may be linked to technical problems of the piezostage displacement or to additional elements on the system influencing the TDBS phase (slight variation of the temperature of the sample holder, mechanical deformation of the holder...). Or it could be simply caused by impurities in the liquid. Unfortunately, this zone is the more interesting for us, a zone where we could observe molecular ordering.

We can observe as well in Fig. 5.8 (b) a region from ∼1200 to 1550 nm displacements with a slight gradual phase slope. In contrast to the case with glycerol as in Fig. 5.4, where the phase of the Brillouin oscillations detected in the lens stops varying from the moment when the lens and the generation substrate are in contact, in this case the phase keeps changing monotonically during the so-called contact zone. That means that the lens and the generation substrate are still not in direct contact and there remains some liquid molecules trapped in between. We assume that this zone may point out to a phenomenon known as jamming. When molecules or particles become locked in a nonequilibrium configuration, they are said to become jammed. The molecules can remain squeezed in between two surfaces, but be more compressed. The jamming state can be ordered as well as disordered. Jamming is ultimately a result of insufficient "excluded volume" available for molecules or particles to rearrange. This volume has to exceed that of "random loose packing" for the molecules to be able to adopt a new structure [9].

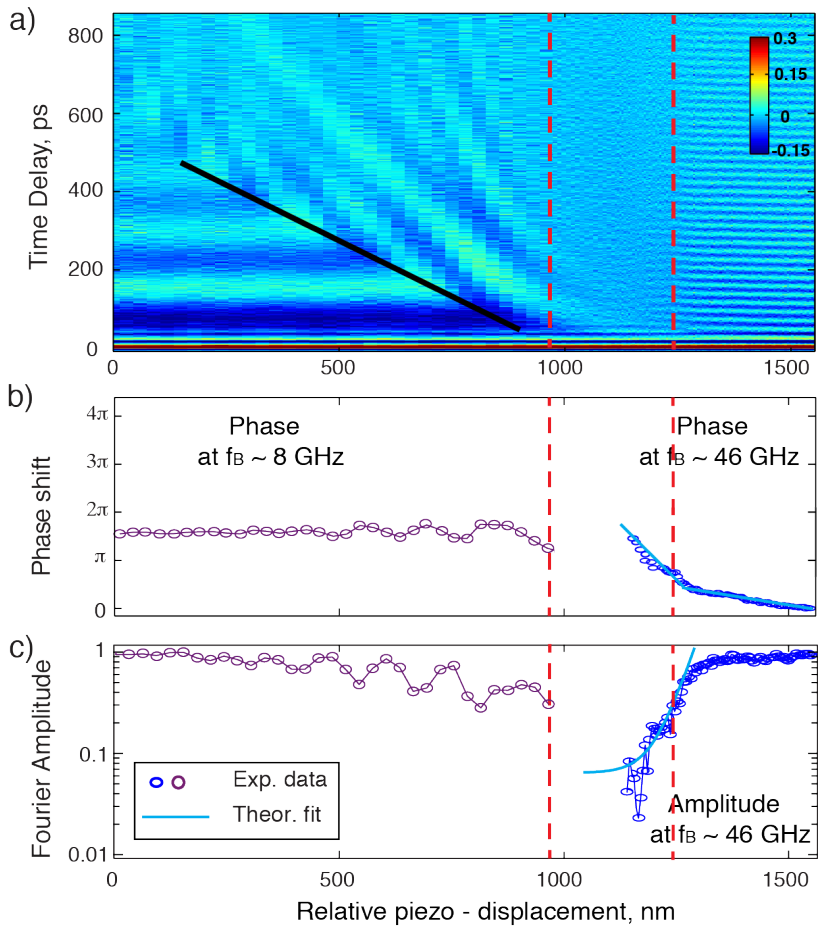

Figure 5.8. (a) Interpolated 2D plot of 138 TDBS longitudinal data sets, recorded in OMCTS at room temperature, as a function of delay time and at different piezo displacements. OMCTS is sandwiched between an uncoated lens of ROC = 386.3 mm and a flat Silicon substrate holding a 40 nm film of Chromium. The liquid thickness was varied by means of piezostage displacements. The data were recorded from thick to ultrathin liquids. The low-frequency signal oscillations at ~ 8 GHz, in the displacement range from 0 to 400 nm, corresponds to Brillouin scattering from longitudinal acoustic waves in OMCTS. The high-frequency oscillations at ~ 46 GHz, in the displacement range from 850 to 1550 nm, corresponds to Brillouin scattering from longitudinal acoustic waves in the lens. The red dotted lines enclose the region of poorly defined frequency. There are no significant oscillations on the raw signal, most probably due to strong acoustic attenuation in OMCTS. The black line shows the liquid/lens interface. (b) Phase shifts and (c) normalized Fourier amplitude of the 8 GHz and 46 GHz signal oscillations extracted from Brillouin scattering in bulk OMCTS and in the lens, correspondingly.

The analysis of the Fourier amplitudes in Fig. 5.8 (c) yields the acoustic attenuation in OMCTS at 46 GHz, in the displacement range from 1000 to 1200 nm, we obtain $\alpha = 13.5 \cdot 10^6$ m^{-1}, which is somehow plausible. The analysis and fitting of the Brillouin oscillations detected in liquid OMCTS at $\nu_B \approx 8$ GHz and shown in Fig. 5.8 (c), lead to $\alpha = 2.1 \cdot 10^6$ m^{-1} which is consistent with the rule that the acoustic attenuation decreases at lower frequencies. The weak amplitude modulation on the FFT amplitude in Fig. 5.8 (c) are caused by the reflection of the acoustic wave at the liquid/lens interface which perturbs the propagation of the 8 GHz longitudinal acoustic waves through the liquid film.

In spite of great suitability for confinement effect investigations, we have encountered several problems while using the OMCTS as a sample. In particular, we are dealing with the propagation of acoustic waves which are very attenuated in OMCTS in the GHz frequency range, that aggravate the experimental and analytical issues and makes even more challenging the pump-probe investigation of confinement effects in such prototype sample.

5.5 Time domain Brillouin scattering study of 8 CB liquid crystals

LC materials are well known from their unique phase transitions and thermal properties that make them useful for a number of potential applications. The liquid crystalline materials exhibit a rich variety of polymorphism. One can predict the order of stability of the different phases on a scale of increasing temperature simply by utilizing the fact that a rise in temperature leads to a progressive destruction of the molecular order. Thus, the less symmetric is the mesophase, the closer in temperature it lies to the crystalline phase [169]. This means that upon cooling the isotropic liquid, first the nematic, then the smectic phases and finally the solid/crystalline phases appear in a fixed sequence. One of the LCs, 8 CB (4-cyano 4-octylbiphenyl) with a molecular formula $C_{21}H_{25}N$, has drawn considerable attention in research regarding its prototypical thermotropic nature in phase transition studies. The shape of 8 CB molecule is rod - like with the length about 20 Å. The 8 CB in bulk shows two intermediate mesomorphic phases between the solid phase and the isotropic phase: the nematic and smectic phases. Pure 8 CB demonstrates isotropic to nematic phase transition at 313.7 K and a melting point at 294.5 K. On the other hand, the 8 CB presents a crystalline polymorphism, several phases can be obtained according to the particular heat treatment conditions. The transition between different phases corresponds to the breaking of some symmetry [170].

The properties of 8 CB in bulk or confined in a narrow gap have been widely studied through light scattering, X-ray, dielectric, and calorimetric spectroscopic analysis by various authors [171–175]. Nonetheless, there is barely any information about mechanical properties of this LC, in which we are interested (speed of sound and attenuation of the acoustic waves). Thus, our initial challenge was to investigate different phases of 8 CB with our experimental setup and to check whether it is doable to distinguish them from TDBS. As physically expected, the most common examples of phase transitions involve a transformation from an ordered (lower symmetry) phase to a relatively disordered (higher symmetry) phase (or vice versa) as the transition temperature is crossed, thus the propagation of the acoustic waves through “ordered” and “disordered” phases of 8 CB should differ (the speed of sound and the attenuation of acoustic waves should vary).

5.5.1 Investigation of 8 CB liquid crystals phase transitions

To achieve this point, we have performed temperature dependent measurements of 8 CB at several temperatures that correspond to each phase of 8 CB. The sample was placed in a temperature controlled stage Linkam (HFS600, Linkam Scientific Instr.) that allows to heat up the sample up to 600° C and cool down up to - 196° C. The Linkam stage is schematically presented in Fig. 5.9. In general this stage is used in horizontal position and we had to make some modifications on the Linkam stage to adapt our sample cell holder and to properly fix the generation substrate and the lens vertically. The generation substrate is placed on the silver heating element, which is located at the center of the Linkam chamber. Then a small amount of 8 CB is deposited on the generation substrate and covered by a plano-convex lens. On the sides we installed two quite strong permanent magnets that hold an arched piece of metal (called lens holder in Fig. 5.9) with a hole at the center, that covers the lens. Such

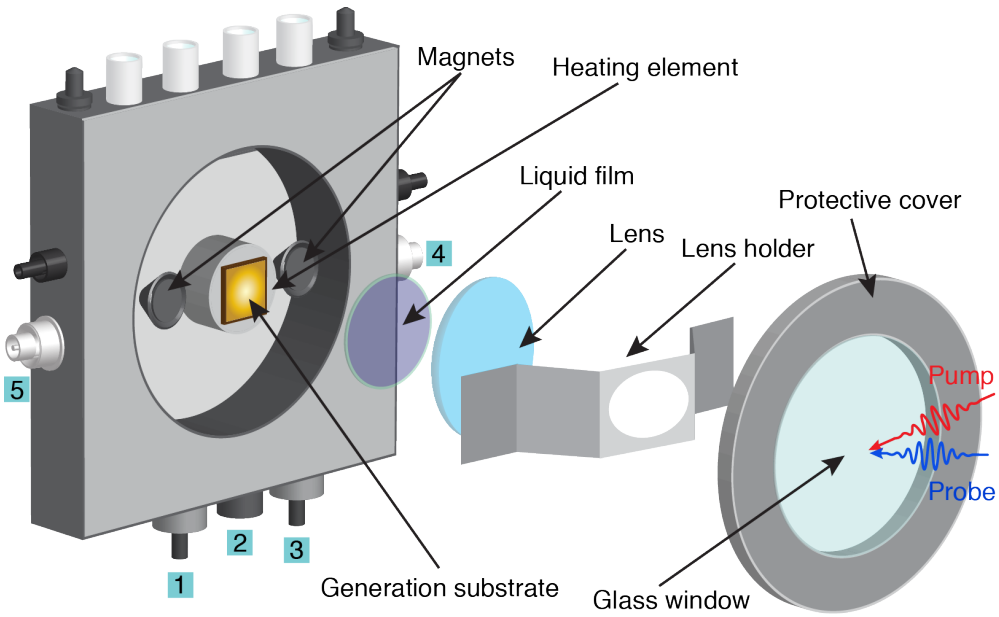

Figure 5.9. Schematic sketch of the temperature controlled stage Linkam. The generation substrate is placed on the silver heating element, which is located at the center of the Linkam chamber. Then a small amount of 8 CB is deposited on the generation substrate and covered by a plano-convex lens. An arched piece of metal with a hole at the center covers the lens in order to tightly fix the sample cell. Afterwards the Linkam chamber is enclosed with a protective cover with a large glass window. The Linkam stage is connected to the temperature controller via connector (2), the nitrogen cooling connections from valve (1) and the purging on valve (3, 4, 5).

system can be easily placed vertically and prevent any sample cell movements/liquid thickness changes/liquid outflow etc. As soon as the sample is ready for the TDBS measurements, the Linkam chamber is enclosed with protective cover with a large glass window, through which pump and probe pulses are transmitted. Next, the Linkam stage is fixed on the three-dimensional stage. After establishment of all connections (electronics, computer control, cooling, purging), the system should be purged. For that, we heat up the sample chamber to 40° C and hold the sample at this temperature during the purging process. This temperature controlled stage ensures the temperature stability less than 0.1° C. The purging method, that we have employed, uses recycled nitrogen gas produced by the cooling system. The nitrogen gas flowing through the sample chamber mixes with residual air inside the sample chamber, and the air inside is being diluted with nitrogen gas. After purging, all connectors are blocked to avoid the air contamination by ambient gases of the laboratory. Then the sample is ready for TDBS measurements.

Since we are obliged to heat up the sample chamber for stage purging, the measurements, presented below, were performed from the highest to the lowest temperatures. Brillouin scattering data were recorded at various temperatures from a bulk 8 CB sample squeezed in between a 40 nm Chromium transducer film on a flat Silicon substrate and a plano-convex lens with a large ROC = 2060 mm. The laser power was kept the lowest possible to avoid additional liquid overheating. Figure 5.10 shows the time-dependent reflectivity change at several temperatures (318 K, 306.5 K, 295.3 K, 288 K), that correspond to different phases of 8 CB. Even using low rate of temperature change ($\sim 1°$C/min), the sample was held at constant temperature for a long time for liquid homogenization and temperature stabilization. The fit parameter for different temperatures shows that the Brillouin scattering frequency ν_B changes as a function of temperature.

At T = 318 K both types of order (positional and orientational) disappear at the same time and the resulting phase of 8 CB is an isotropic liquid (as most thermotropic LCs that have an isotropic phase at high temperature). The heating eventually drives 8 CB into a conventional liquid phase characterized by random and isotropic molecular ordering (little to no long-range order), and fluid-like flow behavior. An isotropic liquid possesses full translational and orientational symmetry [169]. The Brillouin frequency of such phase of 8 CB is $\nu_B = 14.3 \pm 0.2$ GHz and the attenuation rate $\Gamma = 7.8$ ns^{-1}. Cooling the liquid down to T = 306.5 K leads to Isotropic-to-Nematic phase transition. The nematic phase is the simplest liquid crystal phase. In this phase the molecules maintain a preferred orientational direction as they diffuse throughout the sample. In

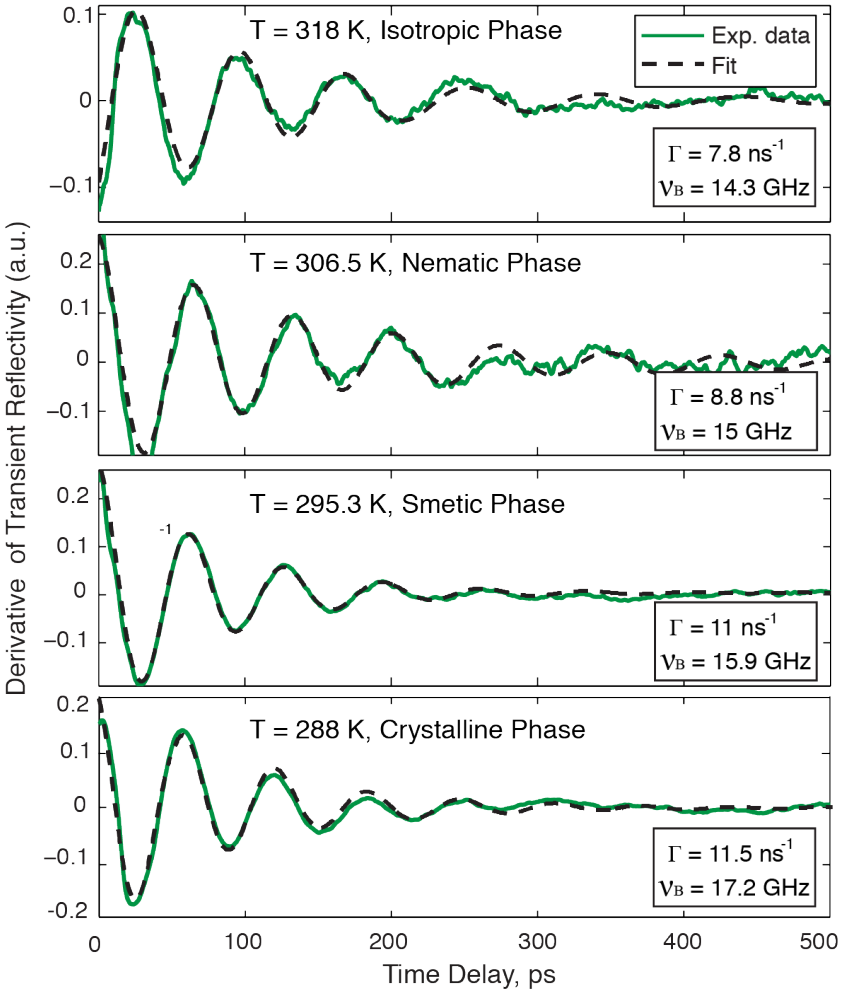

Figure 5.10. Representative TDBS longitudinal signals taken in 8 CB at different specified temperatures. While cooling down the LC from 318 K to 288 K, the liquid undergoes three phase transitions. The fit parameters for different temperatures show that the Brillouin scattering frequency ν_B and the damping rate Γ varies as a function of temperature. At T = 318 K the material is in an isotropic state where $\nu_B = 14.3$ GHz and $\Gamma = 7.8$ ns^{-1}. T = 306.5 K corresponds to the nematic phase of 8 CB with $\nu_B = 15$ GHz and $\Gamma = 8.8$ ns^{-1}. T = 295.3 K matches the temperature of the smectic phase transition with a corresponding frequency of 15.9 GHz and damping rate of 11 ns^{-1}. And at T = 288 K the LC is in the crystalline phase where $\nu_B = 17.2$ GHz and $\Gamma = 11.5$ ns^{-1}. Despite the fact that 8 CB exhibits high optical birefringence, we could only detect one Brillouin scattering frequency ν_B since the measurements were performed with circularly polarized light.

case of I-N transition the translational symmetry remains as in isotropic liquid, but the rotational symmetry is broken. The molecules tend to align along the director $\vec{n}$. The Brillouin frequency of the nematic phase of bulk 8 CB is $\nu_B = 15 \pm 0.2$ GHz and the corresponding attenuation rate $\Gamma = 8.8$ ns^{-1}.

With further temperature decrease at T = 295.3 K, the liquid undergoes Nematic-to-Smectic phase transition. The smectic state is more "solid-like" than the nematic. The smectic liquid crystals have layered structures, with a well-defined interlayer spacing which can be measured by X-ray difraction [176, 177]. The smectic molecules exhibit some correlations in their positions in addition to the orientational ordering. In most smectics the molecules are mobile in two directions and can rotate about one axis, with the restriction that the director remains perpendicular to the smectic layers. The interlayer attractions are weak compared to the lateral forces between the molecules, and the layers are able to slide over one another relatively easily. This gives rise to a liquid property of the system with higher viscosity than nematics. Consequently, the local density fluctuates at the N-SmA transition from homogeneous to periodic and the Brillouin scattering frequency increases to $\nu_B = 15.9 \pm 0.2$ GHz and the attenuation rate increases to $\Gamma = 11$ ns^{-1}. The acoustic waves propagate faster and but are more attenuated in the periodic somehow ordered phase compared to the disordered phase. In the smectic phase, 8 CB is uniaxial and strongly birefringent, the difference between the refractive indices for the ordinary, n_o, and extraordinary n_e, rays is about 0.18 (Δn $\sim$ 0.18). For example at 24°C, n_e is 1.691 and n_o is 1.513 indicating that this material is a positive uniaxial birefringent crystal.

At T = 288 K, the 8 CB is in the crystalline phase, $\nu_B = 17.2$ GHz and $\Gamma = 11.5$ ns^{-1}. Despite the fact that 8 CB exhibits high optical birefringence, we could detect only one Brillouin scattering frequency for smectic and crystalline phases, because the measurements were performed with circularly polarized light. The measurements with linearly polarized light at low temperature are presented in the following section.

Using the extracted Brillouin scattering frequency at T = 318 K, the speed of sound of bulk 8 CB at $\nu_B = 14.3$ GHz was calculated using Eq. (2.21). The refractive index was taken in the range $n = 1.56 \pm 0.02$ (isotropic phase). In the isotropic phase, n increases linearly for a decrease in temperature from 1.5599 at 333 K to 1.5649 at 312 K [178]. The obtained value of $c_l = 1830 \pm 90$ m·s^{-1} seems appropriate and of the same order of magnitude with the value extracted from classical Brillouin scattering measurements [178].

With the subsequent slow decrease in temperature, we observe the existence of

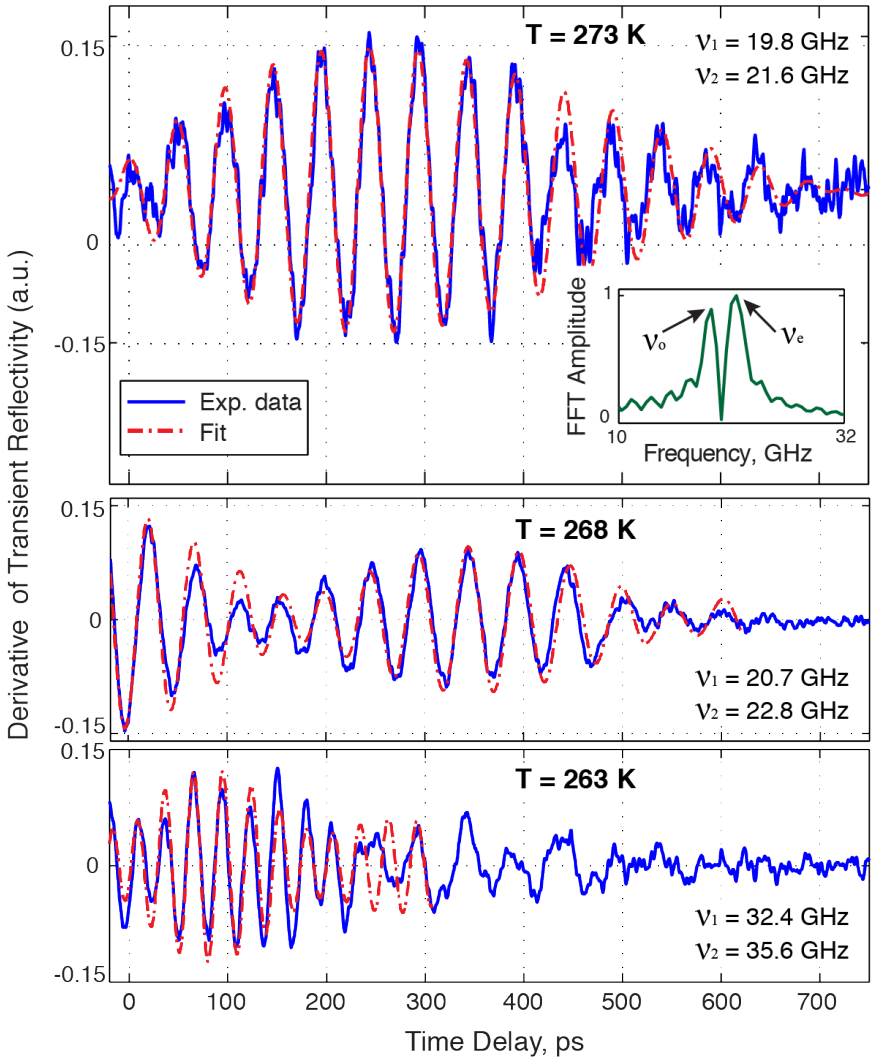

Figure 5.11. Recorded TDBS signals for a thick layer sample of 8 CB squeezed in between a 40 nm of Chromium film on a flat Silicon substrate and a plano-convex lens with a large ROC = 2060 mm, measured at low temperatures that correspond to the crystalline phase of this LC. Fit of the experimental data are shown in red. The pump power for each plot was the lowest possible to avoid additional liquid overheating (Fluence = 0.5 mJ·cm^{-2}). Since 8 CB is strongly birefringent in the crystalline phase, we observe the existence of two modes, as revealed by the FFT in inset of the top plot and it manifests as a frequency beating in the transient optical reflectivity. The fit parameter of interest, the Brillouin scattering oscillation frequency ν_B, shows that the frequency increases progressively with a decrease in temperature.

two modes, as revealed by the FFT in Fig. 5.11 (top) inset. When the probe polarization is circular, the transient optical reflectivity exhibits some beatings in the time domain that corresponds to the presence of two modes - ordinary and extraordinary - of slightly different frequencies. The frequency beating is clearly visible in each plot of Fig. 5.11, that show the experimental data and the theoretical fit of Brillouin scattering oscillations in bulk 8 CB at low temperature. The functional form used for the analysis of the Brillouin oscillations data is given by,

$$\Delta R = A_0\big(\exp(-\Gamma_o t)\cos(2\pi\nu_1 t + \phi) + \exp(-\Gamma_e t)\cos(2\pi\nu_2 t + \phi)\big) \tag{5.8}$$

where $\nu_1 = 2\mathrm{n}_o\ c_l/\lambda$ and $\nu_2 = 2\mathrm{n}_{eff}\ c_l/\lambda$ are the Brillouin frequencies corresponding to the longitudinal acoustic waves detected by the ordinary and extraordinary light pulses, respectively, and $n_{eff} = 1.69$ represents the effective refractive index. The Brillouin frequencies ratio $\nu_{B,e}/\nu_{B,o} \approx 1.09$ for all range of temperatures measured experimentally are close to the ratio of $n_{eff}/n_o = 1.1$ [179]. The fit parameter shows that the Brillouin scattering frequency increases progressively with a temperature decrease. We interpret the change in the detected Brillouin frequency at different temperatures in the crystalline phase as a signature of a modification of the sample texture of the micro-crystallites from a temperature modification. The fact that the Brillouin frequency increases while decreasing the temperature is consistent with the fact that the crystalline phase becomes stiffer when the texture resembles more and more to a well defined bulk crystal. These arguments will be further detailed in the following.

Additional measurements were carried out with linearly polarized light and the use of an half wave plate (HWP) to rotate the incoming polarization. The HWP angle θ refers to vertically polarized light when $\theta = 0°$ and to horizontally polarized light when $\theta = 90°$. In fact, we have replaced the QWP in Fig. 2.7 by a HWP and the sample was turned at about 45° relatively to the incident probe beam such that the TDBS occurs at oblique incidence of the probe light. The data were compared to the previously measured data recorded with circularly polarized probe light. Brillouin scattering raw data from 8 CB at a temperature of 278 K recorded with various polarizations of the oblique probe beam are presented in Fig. 5.12. The measurements at $\theta = 0°$ (middle plot) indicates that only the ordinary Brillouin mode is detected with $\nu_{B,o} = 17.9$ GHz. And the measurements at $\theta = 90°$ (bottom plot) indicates that only the extraordinary Brillouin mode is detected with $\nu_{B,e} = 19.1$ GHz. While with circularly polarized light we observe both modes. The ratio of these two Brillouin frequencies ($\nu_{B,o}/\nu_{B,e} = 1.07$) is in agreement with the ratio of the refractive indices.

Note that the beating Brillouin frequencies are slightly higher since in this case the detection was performed at normal incidence.

The extracted values of Brillouin scattering frequencies allowed to calculate the sound velocity of bulk 8 CB in the crystalline phase at T = 5° C using Eq. (2.21). The values derived from both QWP or HWP measurements are very close and the average is $c_l = 2660 \pm 60$ m·s^{-1}.

LCs are widely investigated from the point of view of texture. The term LC "texture" designates the image of a thin layer of LC. The features of the various textures observed are caused by the existence of different kinds of characteristic crystallites or defects. Often, these textures are distinctive and may be used to identify the LC type [180, 181]. Although there are many experimental techniques available to investigate the structure of LC phases, microscope observations using polarized light microscopy often give enough information to determine the structure [182, 183]. In thin liquid crystal sample cells placed between two crossed polarizers under an optical microscope, a variety of textures and birefringence colors can be observed [180]. These textures and colors provide a lot of information about the microscopic structure of the LC phases.

We used the 2D imaging microscope of our experimental setup to get the image of the LC structure under experimental conditions, without any modification of the TDBS data acquisition which can be performed in parallel. Figure 5.13 shows different textures of 8 CB at various temperatures. We see that the texture of 8 CB is changing depending on the temperature. The texture that 8 CB takes, depends on such parameters as local molecular director alignment, micro texture of the crystallites, surface anchoring, thermal and phase history of LC etc. The obvious variation of the LC crystal texture at different temperatures in the crystalline phase evidence a modification of the crystalline texture of the crystallites that is activated below the crystalline phase transition. These images confirm our TDBS experimental results and interpretations and confirm the sensitivity of TDBS on the micro-texture of LC samples.

5.6 Lateral TDBS measurements of 8 CB

Results from lateral measurements recorded for 8 CB at room temperature are presented in Fig. 5.14 (a). 8 CB was squeezed in the commonly used configuration that consists of an uncoated plano-convex lens (ROC = 386.3 mm) and a flat n-dopped Silicon substrate holding a 40 nm Chromium film. The lateral displacement step was

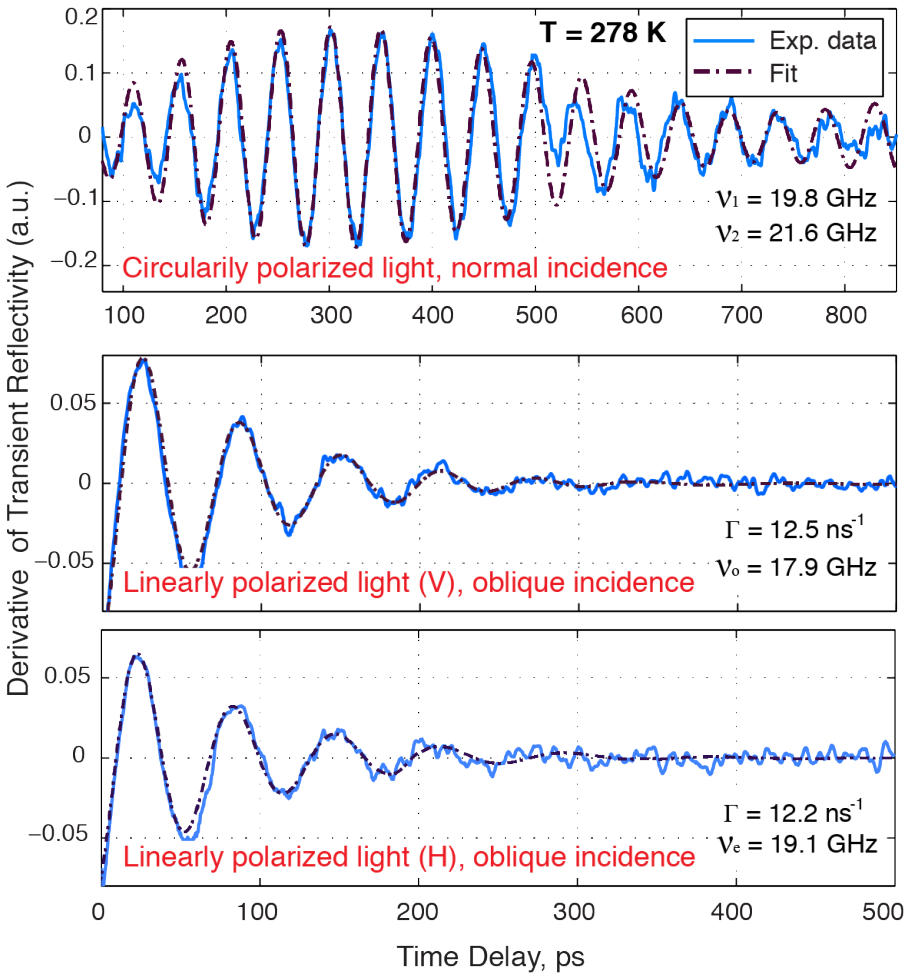

Figure 5.12. Recorded TDBS signals for a thick layer 8 CB sample squeezed in between a 40 nm Chromium film on a flat Silicon substrate and a plano-convex lens with a large ROC = 2060 mm, measured at T = 5 °C. Fit of the experimental data is shown in purple. The measurements at $\theta = 0°$ (middle plot) indicates that only ordinary Brillouin mode exists with $\nu_{B,o} = 17.9$ GHz. And the measurements at $\theta = 90°$ (bottom plot) indicates that only extraordinary Brillouin mode is detected with $\nu_{B,e} = 19.1$ GHz. While with circularly polarized light we observe a beating of both modes.

set to 25 μm. Even though the step is twice larger than the diameter of the focused probe beam, it is still consistently good to interpolate the signal between them. On the central zone we observe the high-frequency signal oscillations due to Brillouin scattering from longitudinal acoustic waves in the lens at $\nu_B \approx 46$ GHz. While away from the center, the low-frequency signal oscillations at $\nu_B \approx 19$ GHz correspond to

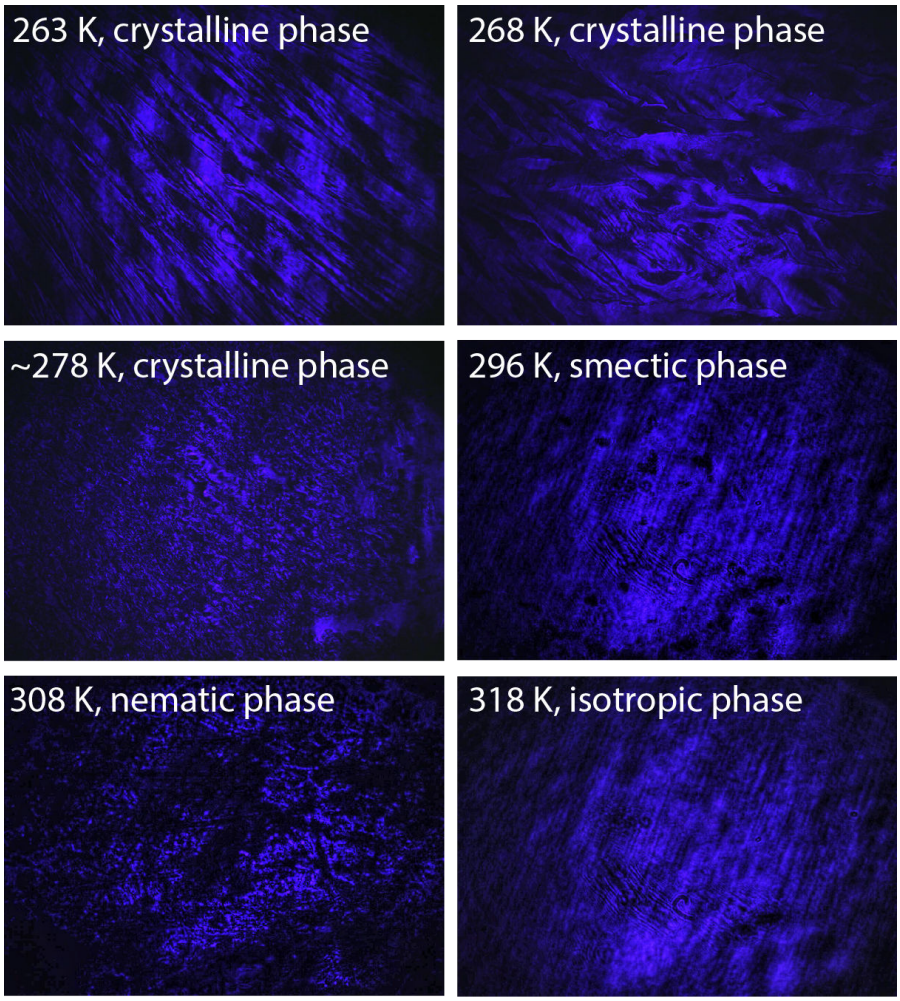

Figure 5.13. Example of images showing the 8 CB texture at various temperatures. The images were obtained using the 2D imaging technique.

Brillouin scattering from longitudinal acoustic waves in 8 CB. The Brillouin frequency of 8 CB is higher than previously found values for smectic and crystalline phases ($\nu_{B,Sm} \approx 15.9$ GHz and $\nu_{B,crystalline} \approx 17.2$ GHz). From our interpretation, it evidences the molecular ordering induced by liquid/surface interaction. Indeed, in the temperature measurements performed with 8 CB reported in the previous section, the liquid thicknesses investigated were well above 10 μm, whereas here the liquid thickness gap is well below 1 μm. Surface effect might lead to structuring of the 8 CB even at room temperature that corresponds to the smectic phase. Using the above described fitting procedure of the liquid/lens interface on the TDBS 2D image, we

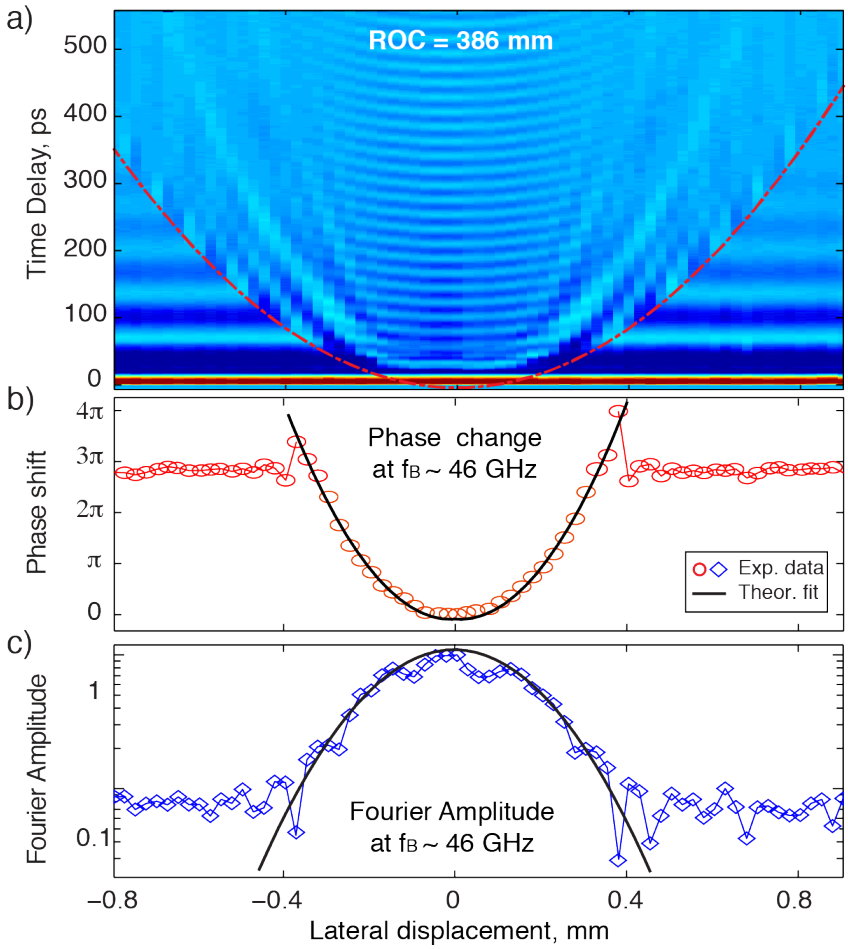

Figure 5.14. (a) Interpolated 2D plot of 70 TDBS longitudinal data sets, recorded in 8 CB at room temperature, as a function of time delay at different lateral positions X. The central part illustrates the high-frequency signal oscillations at 46 GHz that correspond to Brillouin scattering from longitudinal acoustic waves in the lens. While side regions correspond to low-frequency signal oscillations at ∼19 GHz are due to Brillouin scattering from longitudinal acoustic waves in 8 CB. (b) Phase shift and (c) normalized acoustic amplitude of the 46 GHz signal oscillations extracted from Brillouin scattering in the lens. The extracted amplitude and phase provide the information on acoustic attenuation coefficient α and the sound velocity c_l in 8 CB at 46 GHz. The extracted values of these parameters can be found in the text.

have calculated the sound velocity of 8 CB at $\nu_B \approx 19$ GHz. Using Eq. (3.1), we derive the liquid thickness along the whole range of lateral displacements and then, taking the sound velocity as an input parameter, we match the liquid/lens interface in Fig. 5.14 (a) from the simple equation $e = c_l/t$, where e is the liquid thickness calcu-

lated from the ROC. The derived value of sound velocity $c_l = 2420 \pm 50$ m·s^{-1} matches the value of sound velocity calculated with Eq. (2.21), that is $c_l = 2380 \pm 70$ m·s^{-1}, taking $n = 1.6$. The corresponding fitted attenuation rate of the Brillouin oscillations in 8 CB at 19 GHz is $\Gamma = 12.5$ ns^{-1}. Both, the frequency and the attenuation rate match the values obtained in the 8 CB crystalline phase and indicate molecular structuring of the smectic phase at room temperature.

Phase shifts and normalized Fourier amplitude analysis of the 46 GHz signal oscillations extracted from Brillouin scattering in the lens, as well as a fit of the data are presented in Fig. 5.14 (b) and (c). Using the above described fitting procedure based on Eq. (5.5) and Eq. (5.6), we retrieve the speed of sound and the acoustic attenuation coefficient of 8 CB at 46 GHz. The derived value of sound velocity is $c_l = 2600 \pm 50$ m·s^{-1} and for the acoustic attenuation coefficient is $\alpha = (11.5 \pm 0.5)\cdot 10^6$ m^{-1}. The values of these parameters seem pertinent to our particular experimental conditions and can not be compared with literature data because of the absence of similar measurements at such high frequency. The measured speed of sound at 46 GHz matches well the crystalline phase, indicating an interface structuring of 8 CB.

5.7 TDBS piezo measurements of ultrathin 8 CB liquid crystals

Fig. 5.15 shows an example of TDBS measurements performed for a 8 CB sample with the use of a piezostage. 8 CB was squeezed in the standard configuration consisting of a plano-convex lens (ROC = 206 mm) and a flat n-dopped Silicon substrate that holds a 40 nm Chromium film. The data were recorded at room temperature and the laser power was minimized in order to avoid liquid overheating. The piezo stage displacement step was changed during the full displacement range. In the displacement range 0 - 950 nm, the displacement step was set to 30 nm, from 950 to 1200 nm to 5 nm and from 1200 to 1650 nm to 2 nm. Fig. 5.4 (a) shows a data set of about 291 TDBS longitudinal wave data recorded in 8 CB for different piezo displacements. At the beginning of the piezo measurements, we observe approximately five oscillations of Brillouin scattering in 8 CB. These low-frequency oscillations at $\nu_B = 15.7 \pm 0.3$ GHz matches the Brillouin scattering in bulk 8 CB in the smectic phase. It is unexpected that the Brillouin frequency does not coincidence with the Brillouin frequency of 19 GHz extracted in the TDBS lateral measurements. It can't come from any experimental artifacts, the time delay is extremely reliable and so for the frequency. The only plausible explanation is that the piezo stage motion perturbs

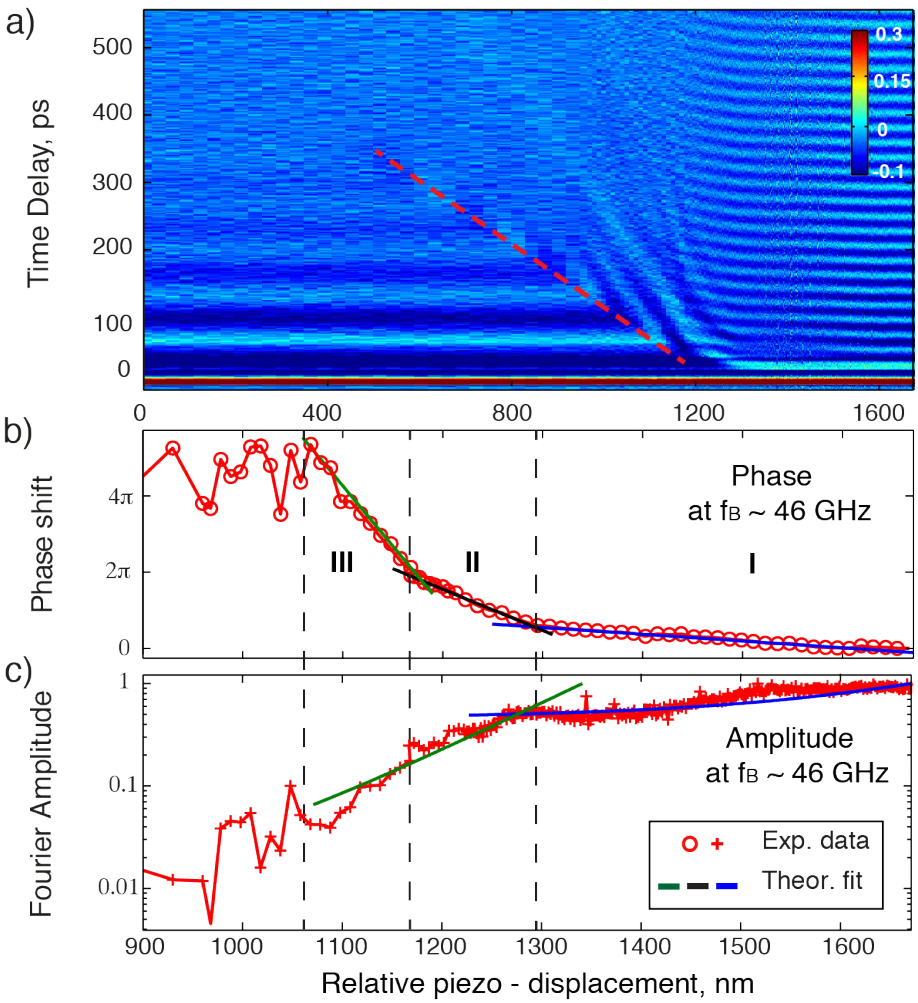

Figure 5.15. (a) Interpolated 2D plot of 291 longitudinal wave data sets, recorded in 8 CB at room temperature, as a function of time delay at different thicknesses. 8 CB is sandwiched between an uncoated lens with ROC = 200 mm and a flat Silicon substrate holding a 40 nm Chromium film. The liquid thickness was changed by means of piezostage displacements. The data were recorded from thick to ultrathin liquid. The low-frequency signal oscillations at $\sim$ 15.7 GHz correspond to Brillouin scattering from longitudinal acoustic waves in 8 CB. Whereas the high-frequency oscillations at $\sim$ 46 GHz, in the range from 1200 to 1650 nm correspond to Brillouin scattering from longitudinal acoustic waves in the lens. The red dotted lines shows the liquid/lens interface. (b) Phase shifts and (c) normalized Fourier amplitude of the 46 GHz signal oscillations extracted from Brillouin scattering in the lens.

the liquid structuring at each displacement step, which is not the case for the lateral TDBS measurements where the liquid sample remains unperturbed for hours. When

the distance between the lens and the generation substrate and correspondingly the liquid thickness decreases sufficiently, the acoustic wave reaches the liquid/lens interface where it gets partially transmitted into the lens. Due to strong acoustic attenuation, we can only notice on Fig. 5.15 (a) two Brillouin oscillations until the acoustic wave reaches the liquid/lens interface. The red dotted line on Fig. 5.15 (a) highlights the liquid/lens interface. Using the slope of this red dotted line, the sound velocity of bulk 8 CB in the smectic phase may be calculated. The derived value of the sound velocity of bulk 8 CB at $\nu_B \sim 15.7$ GHz is $c_l = 2100 \pm 160$ m·s^{-1} which matches with the value calculated with Eq. (2.21) $c_l = 1950 \pm 50$ m·s^{-1}.

Starting from 1100 nm of relative piezostage displacement, one observes high-frequency signal oscillations that correspond to Brillouin scattering from longitudinal acoustic waves transmitted into the glass lens at $\nu_B = 46$ GHz. The change in the phase and in the acoustic amplitudes of the 46 GHz Brillouin oscillations are presented in Fig. 5.15 (b) and (c). The phase shifts, that result from the different transit times of the acoustic wave through different liquid thicknesses, provide an information on the sound velocity of 8 CB at 46 GHz. In Fig. 5.15 (b), we can distinguish three zones. From our assumption, the first zone denoted (I), where the phase is barely changing, can be linked to the jamming effect as in case of OMCTS measurements. The second zone (II) is intriguing. The accurate examination of the phase shifts in this zone with Eq. (5.6) yielded the value for the speed of sound of $c_l = 3530 \pm 120$ m·s^{-1}. This value is of the same order of magnitude as for some solids. However, we do not exclude that this may be a sign of liquid structuring. In the third zone (III), the low-frequency and high-frequency acoustic waves are detected. This zone corresponds to bulk 8 CB in smectic phase. From the phase shift we extracted the value of speed of sound $c_l = 1970 \pm 60$ m·s^{-1} which matches the values extracted dirrectly from Brillouin oscillations and from the slope. So, we evidence three regions - bulk liquid, ordered liquid, and zone of trapped 8 CB molecules between two confining boundaries or probably jamming (with an increase in the surface roughness, the probability of jamming increases too).

The difference in the acoustic amplitudes is a result of the propagation through different liquid thicknesses. The set of normalized Fourier amplitudes recorded at multiple liquid thicknesses was used to determine the acoustic attenuation length α at the Brillouin frequency $\nu_B = 46$ GHz through Eq. (5.5). In Fig. 5.15 (c) we can roughly distinguish two zones with two different values of α. The extracted values are $\alpha = 4.3 \cdot 10^6 \mathrm{m}^{-1}$ for zones denoted (II), (III) and $\alpha = 2.3 \cdot 10^6$ m^{-1} for zone (I).

Comparison with lateral measurements First of all, we notice that the Brillouin frequency of bulk 8 CB and correspondingly the speed of sound are different in two types of measurements, $\nu_B = 19$ GHz for lateral and $\nu_B \sim 15.7$ GHz for piezo measurements. The discrepancy can be explained by the initial phase of 8 CB. In lateral measurements the liquid is tightly squeezed between the lens and the flat generation substrate from the start of measurements and remains unperturbed for hours. This confinement may lead to the ordering of LC molecules and the detected Brillouin frequency corresponds to crystalline, "ordered" phase of 8 CB. At the beggining of piezo measurements, the liquid is a few microns thick, in "bulk" state and the liquid is perturbed at each step motion of the piezostage. For this reason we believe that the detected Brillouin frequency corresponds to smectic phase for piezo measurements.

Secondly, the speed of sound and acoustic attenuation coefficients at 46 GHz frequency are different too between lateral and piezo TDBS measurements. From our interpretation, it is linked to the initial phase of the liquid and the position of liquid molecules with respect to the surfaces. Since the molecules of 8 CB are rod-like, they can be perpendicularly, parallel aligned or tilted to the surface.

5.8 Conclusion

In this chapter we have demonstrated the extensive measurements for liquids of large range of thickness, from few microns to few nanometers. The method is examined under two different modes: lateral measurements for the sample cell using the flat-curved geometry and direct liquid thickness change by means of a piezostage. Both give different resolution in liquid thickness change. Each modes have its own advantages and disadvantages. Nonetheless, two methods provide reliable quantitative values for frequency-dependent longitudinal sound velocity and acoustic attenuation coefficient at ten's of GHz acoustic frequencies. The extracted values are consistent with the values available in literature.

Finally, this pioneering method may be applied to extremely thin liquids, down to a couple of monolayers. At the moment, we can perform measurements with an accuracy of a couple of nanometers (2 - 5 nm), pretty soon we expect to reach 1 nm or below to finally reach the requirements for the proper investigation of liquids under nanoconfinement. The liquid under study showed different behavior in the ultrathin "regime". In the measurements for 8 CB liquid crystals and OMCTS, we have observed a surprising surface effect. When the lens is brought into contact to the generation substrate, the phase of the high frequency 46 GHz longitudinal Brillouin oscillations keeps changing gradually as shown in Fig. 5.16 in the thickness range from 200 - 600 nm. This slight phase change lasts for hundreds of nanometers. This effect is negligible in case of glycerol, is maximum for OMCTS with a slope of 1.5 rad / 100 nm and

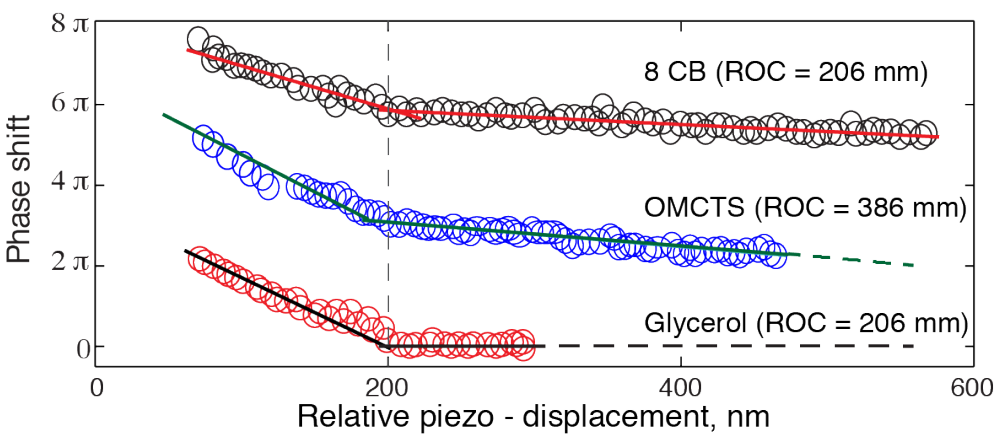

Figure 5.16. Phase shifts of the 46 GHz Brillouin oscillations in the glass lens at different piezostage displacements, extracted from Brillouin scattering data for three investigated liquids, glycerol, OMCTS and 8 CB.

about 0.9 rad / 100 nm in case of 8 CB. As soon as the lens touches the generation substrate, with further piezostage displacement, the lens squeeze the few molecules trapped between both surfaces. After the exclusion of the effects of liquid impurities, surface roughness, sample holder distortion/deformation, that should be present on the measurements for glycerol as well, we venture upon to make a hypothesis that such behavior may evidence the effect of jamming of liquid molecules.

Conclusions and outlook

In this work we used the picosecond laser ultrasonics technique to investigate thermal and mechanical properties of liquids at GHz frequencies, from bulk liquids to ultrathin liquids. The TDBS measurements of ultra thin liquids of different thicknesses were made in two different modes: direct liquid thickness change from a piezostage, or lateral measurements. Each lateral position corresponds to different liquid thickness, which has been achieved by using a flat-curved sample configuration.

We have investigated in Chapter 4 the intricate coupling of longitudinal acoustic phonons to thermal properties of the investigated liquids, by use of an optical technique based on picosecond laser ultrasonics to determine the local temperature distribution profile in liquid samples in contact with a laser heated optical transducer. This ultrafast pump-probe experiment uses time-domain Brillouin scattering (TDBS) to locally determine the light scattering frequency shift. As the temperature influences the Brillouin scattering frequency, the TDBS signal probes the local laser-induced temperature distribution in the liquid. We have demonstrated the relevance and the sensitivity of this technique for the measurement of the absolute laser-induced temperature gradient of a glass forming liquid prototype, glycerol, as well as for OMCTS, at different laser pump powers i.e. different steady state background temperatures.

The experimental studies and simulations of different sample structures presented in Chapter 4 have shown the importance of the proper selection of sample substrates holding the metallic transducer films to avoid cumulative thermal heating effects. Such effects can be minimized by using a good thermally conducting substrate like sapphire or silicon. To further decrease the influence of cumulative thermal heating effects, we have investigated a multilayer sample structure where a thermal insulating SiO_2 layer was added in order to shield the liquid from the laser heated metallic transducer film. We have experimentally demonstrated the benefit of this alternative sample structure which could be required in experimental situations where even slight temperature changes have to be avoided. Ultimately, our results could shed

light on the thermal properties of ultrathin confined liquid films. This is a fascinating experimental challenge for the understanding of nanoscale heat transport.

In Chapter 5.1, we have shown that picosecond laser ultrasonics can be applied not only for the measurements of longitudinal properties of bulk liquids but also of ultrathin liquids. We have demonstrated the capabilities of the measurements for liquids in a wide range of thicknesses, from few microns to few nanometers, performed either with TDBS lateral measurements or with a piezostage.

The developed TDBS technique was used to determine the high-frequency longitudinal properties of three different liquids, glycerol, OMCTS and 8 CB. Our experiments yield direct access to the longitudinal speed of sound and the acoustic attenuation coefficient of liquids at GHz frequencies. The longitudinal speed of sound was deduced from the phase shift extracted from TDBS measurements. And the attenuation of longitudinal acoustic waves was deduced from the measurements of the longitudinal Brillouin amplitude by averaging over all calculated values in a data set. The found values are consistent with the values available in literature in case of glycerol.

Three different liquids, glycerol, OMCTS and liquid crystal 8 CB were investigated with different sizes, shapes and nature of the molecules. These three liquids are dissimilar, thus they may behave differently in nanoconfinement. Some molecules can be attached stronger to the surface, some of them weaker. We observed various behaviours of liquids in ultrathin "regime". From our assumption, the measured difference can be explained by interaction of liquid molecules with confining solid boundaries. This effect is negligible in case of glycerol, and most prominent for OMCTS. We suppose that the molecules can be stuck between two confining surfaces. As soon as the lens touches the generation substrate, the few molecules could stay trapped between two solid boundaries and with further piezostage displacement, the lens squeeze them more and more. This might lead to the effect of molecules jamming. We are looking forward to more studies to explain this behaviour quantitatively.

Nonetheless, our technique of TDBS offers substantial advantages since the frequencies are much higher compared with frequencies available by other techniques used for the investigation of confined liquids and interfacial effects. This pioneering TDBS experimental scheme is a first step towards the investigation of confined liquids measured by GHz ultrasonic probing.

Appendix A

Liquid crystals

There are three main states of matter, as solid, liquid and gas. All this three states is characterized by different properties proper for each phase. The predominant distinction is made by the degree and type of ordering. For example, the solid state is highly ordered state, while the gas state doesn't have at all any ordering, and the liquid state is charecterized by a structure with a short-range ordering. In 1888, it was discovered another intermadiate state between solid and liquid, called mesophase [59]. This state exhibits a degree of order between that of a fluid and a solid. Such materials are called liquid crystals (LC). They possess many of the mechanical properties of liquids, e.g., high fluidity, formation, and coalescence of droplets [184]. At the same time they are similar to crystals in that they exhibit anisotropy in their optical, mechanical, electrical, and magnetic properties.

A.1 Classification of Liquid crystals

Liquid crystals were first discovered accidentally in 1888 by an Austrian botanist Friedrich Reinitzer. Upon heating the cholesteryl benzoate, he observed the transition from a cloudy liquid to a clear liquid, and upon cooling to blue consistency before crystallization. Further, Reinitzer had discovered and described three important features of cholesteric liquid crystals: the existence of two melting points, the reflection of circularly polarized light, and the ability to rotate the polarization direction of light. Since then, a lot of research has been done to understand and describe the properties of this material [185]. Liquid crystals have attracted interest for many reasons, some theoretical and some more practical. For mathematicians and theoretical physicists, liquid crystals are a natural laboratory for broken symmetries and the practical

application of pure mathematical disciplines such as topology and group theory to physical problems. Under the microscope liquid crystals present the most wonderful coloured patterns which provided an enormous intellectual challenge before they were understood [180, 186]. For the engineer, cheap and compact liquid crystal technology provides the most promising replacement to the bulky cathode ray tube long used in computers and TVs [58]. For the biologist, liquid crystal-like materials form the building blocks for much of the soft tissue out of which living cells and aggregations of cells are constructed [184]. Liquid crystal science is truly interdisciplinary. That is why a lot of research has been done to understand and describe the properties of this material.

Altogether, LC are classified according to the following principles [187, 188]:

1 By the method of the production: thermotropic (with a sequence of phases that change with temperature and pressure), lyotropic (with change of molecular concentration of the substance in water or other solvents), carbonized (with a change of polymerization degree during heating) and other, more rare, for example, with the formation of chain structures from inorganic substances.

2 By the shape of the molecules: rod - like or calamatic (from the greek word $\kappa\alpha\lambda\alpha\mu o\zeta$ meaning "cane") discotic, banana-shaped or bent-shaped, dendritic, etc.

3 By the optical properties: uniaxial, biaxial, optically active.

4 By chemical classes: biphenils, Schiff bases, pyrimidines, tolanes, azobezenes and many others which are not so popular.

5 By the symmetry of the phases, which determines the key properties of LC.

We will limit our discussion to thermotropic LC so far as we have worked with this type. Thermotropic LC are composed of organic molecules. The molecules usually take a rod-like or disc-like (discotic) shape [188]. Atoms in organic molecules are mainly connected by covalent bonds with characteristic energy about 1 eV per molecule. Intermolecular interactions are much weaker (0.01 - 0.1 eV), and their nature is more diverse.

There is a large number of variety of LCs phases but we will consider just few of them [186, 188, 189]. Fig. A.1 presents different phases of liquid crystals. A normal liquid is isotropic, there is no particular orientation of molecules, and the properties don't depend on direction. At high temperature the liquid crystal is in the **isotropic phase** with randomly oriented molecules. Upon cooling, the isotropic phases switch to

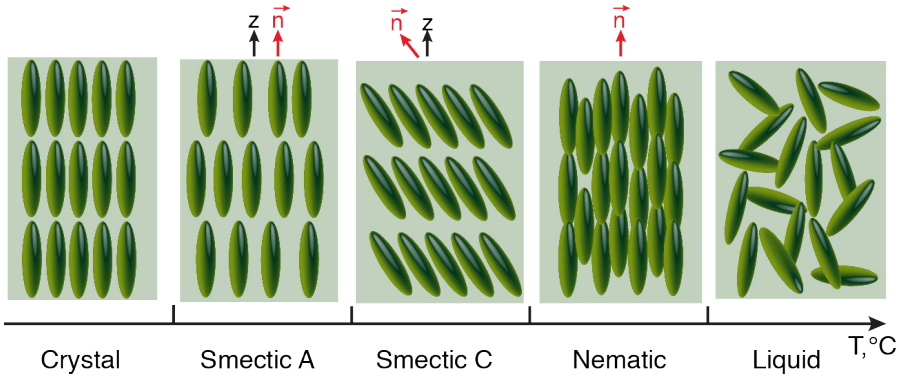

Figure A.1. The scheematic represantation of molecule arrangement in different phases. Depending on temperature, one distinguishes isotropic, nematic, smectic and crystalline phases. In isotropic liquid the molecules are randomly oriented. When the isotropic liquid is cooled down, the **nematic** phase emerges. The molecules tend to align along a particular direction $\vec{n}$, while the molecules centers of mass are still isotropically distributed. With further cooling, the nematic phase transform to smectic. The simplest smectic phase is the **smectic A**. In this phase, the average molecular orientation is perpendicular to the liquid layers. The smectis A phase can transform to **smectic C** by decreasing the temperature. It has a lower symmetry compared to the SmA phase. The tilted molecules pick a special direction in the smectic plane. And the phase with the highest order is the **crystalline** phase. Molecules are long-range ordered.

nematic phase. The nematic phase is identified by molecules without positional order but with orientational order. That means that the molecules tend to point in the same direction defined by the unit vector $\vec{n}$ (called the director). Subsequent cooling leads to the next phase transition. Nematic phase evolves into **smectic phase**. The smectic phase is another mesophase of LC with increased order compared to nematic. This phase is closer to solid - like state because the molecules show a degree of translation order and align in layers or planes. These layers can slide over one to another. There are many distinct smectic phases. For example, in the smectic A phase, the molecules are oriented along the normal of the layer, while in the smectic C phase they are tilted away from it. These phases are liquid-like within the layers.The smectic B phase (not presented on the scheme) orients with the director perpendicular to the smectic plane, but the molecules are arranged into a network of hexagons within the layer. This phase manifests as a lamellar phase having apparent similarities with traditional crystalline solids. And with further cooling, eventually the crystalline state is recovered.

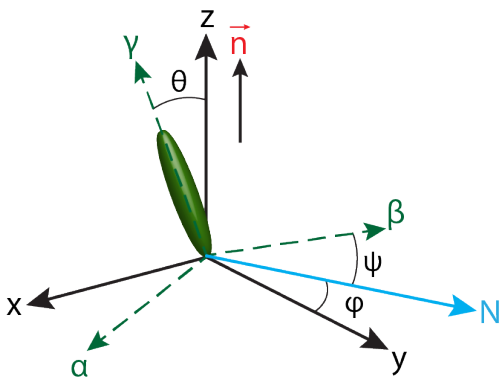

Figure A.2. Euler angles in the molecular coordinate system (α, β, γ) with respect to the laboratory system (xyz). N is the nodal line, i.e. the normal to the plane γz. The angle θ corresponds to the deviation of the longitudinal molecular axis γ from the z-axis; ψ - to the rotation of the shortest molecular axis β around the longitudinal axis γ; ϕ - to the precession of the longitudinal axis γ around the z-axis, following the conical surface.

A.2 Distribution functions of molecules by orientation and order parameter

The translational and orientational degrees of freedom affect each other, but in many cases, most often for simplicity, they can be considered separately [58, 184]. For example, in the nematic or isotropic phase, where there is no translational order, and the local densityρ is constant, for the distribution function of molecules in space P, we can put $P(r, \Omega) = \rho P(\Omega)$. In the general case, the single-particle distribution function P(r, Ω) determines the probability of finding a molecule with orientation Ω at the point r, and includes all three Euler angles ψ, ϕ and θ, as shown in Fig. A.2. For a nematic phase with a constant local density ρ, it is assumed that P(r, Ω) = ρP(Ω), and the probability P(Ω) does not depend on the positions of other molecules [190]. In the Cartesian coordinates (xyz), the z axis is chosen as the principal, which usually coincides with one of the symmetry axes of the molecular system. For the nematic phase, the rotational axis coincides with the axis of the preferred orientation of the molecules, with the director n [57]. If the nematic does not interact with the environment, the director can take any direction, and its rotation by external influences does not require any energy. The direction of the director can be fixed by a very weak magnetic or electric field or by interaction with the surfaces that limit the sample. In Fig. A.2, the direction of the director $\vec{n}$ is fixed along the z axis.

The probability to find a molecule oriented within a solid angle dΩ is given by:

$$f(\Omega, d\Omega) = f(\phi, \theta, \psi) sin(\theta) d\phi d\theta d\psi, \tag{A.1}$$

where $f(\Omega)$ is the distribution function describing the general state of molecular orientation. The probability to find a molecule in any of the orientational states is equal to 1. For the isotropic phase of LC $f(\phi, \theta, \psi)d\psi) =$ const, and after integration of Eq. (A.1) we obtain $f(\phi, \theta, \psi)d\psi)_{iso} = 1/8\pi^2$ [188, 191]. For uniaxial phases such as the nematic or smectic-A phases, according to the symmetry, the distribution of the molecules does not depend on the precession angle $\phi =$ const, but the dependence on the rotation angle ψ is retained. Below we consider uniaxial phases with molecules having axial symmetry (in the form of rods). Such molecules either have their original symmetry group with a rotational axis of infinite order or, more often, are simply considered as physical objects of the rod-like shape, which was obtained through free rotation around its γ axes [192]. In this case, $f(\Omega)$ does not depend not only on ϕ, but also on ψ: $f = f(\theta)/4\pi^2$. Additionally, $f(\theta) = f(\pi - \theta)$. From Fig. A.3 one can see, that the angles near 0 and π are equally densely populated by molecules, which illustrates the condition of nonpolar symmetry, n = -n. Angles close to $\pi/2$, on the contrary, are the least populated.

In general, $f(\theta)$ can be expanded as a sum of the Legendre polynomials [188,192] and the scalar order parameter, S is defined by the quadrupolar term:

$$\begin{aligned} S_2 &= \frac{1}{5} f_2 = \frac{1}{2} \int_{-1}^{1} (f(\theta) P_2(cos\theta) d(cos\theta) = \langle P_2(cos\theta) \rangle \\ &= \frac{1}{2} \langle 3cos^2\theta - 1 \rangle \end{aligned} \tag{A.2}$$

Here, $P_2(cos\theta)$ is the 2nd Legendre polynomial. (More detailed calculations can be found in the above-mentioned references [57, 184, 186–189, 192]) It describes the

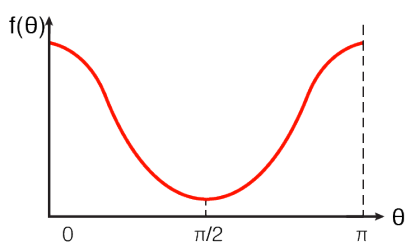

Figure A.3. Generic shape of the distribution function $f(\theta)$ in an uniaxial nematic.

quadrupole orientational order and is quite suitable for the role of the orientational order parameter of a nonpolar nematic. The scalar order parameter consequently lies within the interval -1/2$\leqslant$ S_2 $\leqslant$1. For the perfect nematic with molecular axis strictly parallel to each other (all molecules along the director) $\langle P_2(cos\theta)\rangle = 1$ and $S_2 = 1$. For completely disordered molecules in a volume $\langle P_2(cos\theta)\rangle = 1/3$, $S_2 = 0$, which corresponds to the situation of maximum symmetry of the isotropic phase with no order. The negative value of the lower bound, -1/2, signifies the theoretical ordered state along a plane perpendicular to the director.

The order parameter S_2 can be found by measuring the anisotropy of the magnetic susceptibility, optical dichroism and birefringence, as well as NMR spectra.

A.3 Phase transitions

In liquid crystals, when the temperature, pressure, or the ratio of the components in the mixture change, transitions occur between different phases [170]. Phase transitions are divided into two groups, the first and the second order, and are accompanied by interesting pre-transition phenomena. The phenomenological Landau theory or molecular statistical approaches are usually used to describe phase transitions [193]. In the following we only consider a transition as a function of temperature [194]. Thereafter, we consider phase transitions between the isotropic and nematic phases and also between the nematic and smectic A phases.

A.3.1 A. Isotropic to nematic phase transition

From the experiments few facts are known about this phase transition:

- There is a very small jump in density at the phase transition point $T = T_{NI}$, about 0.3%. Consequently, the density should be considered as a constant;
- As it was shown, the order parameter is not symmetric, its magnitude varies. Accordingly, it is the first order phase transition;
- It is necessary to take into account the tensor character of the order parameter.

Taking this features into account, the Landau-de Gennes theory for the free energy density at the phase transition to the nematic phase has the form:

$$F_N = F_{ISO} + \frac{1}{2}AQ_{\alpha\beta}Q_{\beta\alpha} - \frac{1}{3}BQ_{\alpha\beta}Q_{\beta\gamma}Q_{\gamma\alpha} + \frac{1}{4}C(Q_{\alpha\beta}Q_{\beta\alpha})^2 \qquad (A.3)$$

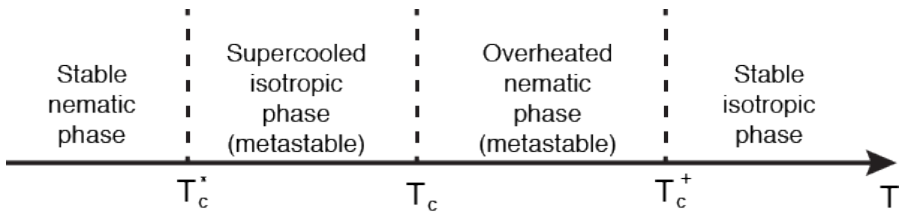

Figure A.4. The positions of the stable and metastable phases observed with a temperature change near the phase transition (N-I).

where A = a(T - T_c^*) with a temperature T_c^* only slightly below the actual transition point. It is the temperature of absolute stability loss of an isotropic phase upon cooling. The coefficient A is the fraction of molecules whose orientations lined up along n, with magnitude between 0 and 1. The coefficients B and C do not depend on T. The expression (A.3) may be further simplified in terms of the order parameter amplitude S. Omitting all intermediate calculations (see [57, 170, 192]), we finally get the solution of (A.3):

$$S_{nem} = \frac{B}{4C}\left\{1 + \left[1 - \frac{24a(T - t_c^* C}{B^2}\right]^{\frac{1}{2}}\right\} \tag{A.4}$$

From Eq. (A.4) we get an another temperature $T_c^+ = T_c^* + B^2/24aC$ ($S_c^* = B/2C$, $S_c^+ = B/4C$), below which the solution $S_{nem} > 0$ gives a local minimum of the free energy density and the nematic phase is therefore metastable. The transition temperature T_c is derived from the condition that the free energy densities of the two phases are equal, $F(S \neq 0) = F_{iso}$ and the condition of stability

$$T_c = T_c^* + \frac{B^2}{27aC} \tag{A.5}$$

with $S_c = B/3C$. When B = 0, $T_c = T_c^* = T_c^+$, this becomes a second order phase transition, in which the order parameter S is continuous at the transition point.

In general, we now have three characteristic temperatures: $T_c^* < T_c < T_c^+$. Figure A.4 illustrates the sequence of stable (metastable) phases around the NI transition.

A.3.2 B. Nematic to Smectic A phase transition

In most cases, at the time of transition to the smectic A phase, the order parameter is almost perfect S $\sim 0.6 \div 0.8$. Therefore, we can fix the free energy of

the nematic phase and assume that the order parameter in both phases is the same, $S_N = S_{SmA}$. Then we can introduce a new order parameter, taking into account the fact that in the smectic A phase, the symmetry decreases with the formation of a one-dimensional translational order [195]. We recall that in the SmA phase, the density function is modulated along the direction of the normal to the smectic layers,

$$\delta\rho(z) = \rho(z) - \rho_0 = \sum_m \rho_m \cos\left(\frac{2\pi m z}{l} + \phi_m\right) \tag{A.6}$$

Here,l is the smectic layer spacing, ρ_m and ϕ_m are the amplitudes and phases of the complex order parameters with m =1,2,3.. . In the nematic phase these amplitudes turn to zero. In the simplest approximation we can take only the term with m = 1. Therefor,

$$\delta\rho(z) = \rho_1 \cos\left(\frac{2\pi z}{l} + \phi_1\right). \tag{A.7}$$

The complex parameter $\rho_m \exp(i\phi_m)$ is the order parameter of the smectic A phase, it is used for the free energy density decomposition at the phase transition from nematic to smectic A phase. The smectic A structure is invariant with respect to the sign of ρ_1. As a consequence, the density of free energy decomposes into a series only in even powers of ρ_1. After some mathematical operations for free energy minimization (see above-mentioned references), we obtain:

$$\frac{\partial F_{SmA}}{\partial \rho_1} = \rho_1(a(T - T_{NA}) + C\rho_1^2) = 0. \tag{A.8}$$

with $a > 0$. The solution $\rho_1 = 0$ corresponds to high-temperature nematic phase. An another solution with $\rho_1 \neq 0$ determines the translation-invariant smectic A phase. Wherein, the order parameter changes continuously with the temperature from zero in transition point to some final value:

$$\rho_1 = \left[\frac{a(T_{NA} - T)}{C}\right]^{\frac{1}{2}} \tag{A.9}$$

As expected [170], the Landau theory in the form of (A.9) predicts a second-order phase transition with a root dependence of the order parameter. The temperature dependence of ρ_1, in principle, can be found with X-ray diffraction. For this, it is necessary to measure the intensity of the Bragg peak corresponding to the diffraction on a smectic structure with a period of layers l. The SmA-N phase transition has been studied for various compounds by precision calorimetry and X-ray scatter-

ing [196–198]. These studies have shown that the behavior of various thermodynamic properties at the vicinity of the transition are determined by highly developed fluctuations of the smectic order parameter. This means that near the SmA-N transition the order parameter varies in space and in time $\rho_1 = \rho_1(r, t)$. The experiments show also that the SmA-N transition can be not only of the second-order, but also of the first [176]. This difference is determined by the width of the region of existence of the intermediate nematic phase between the smectic A and isotropic phases. At a certain narrow enough temperature interval of this region, about 1 K, the line of phase transitions of the second-order SmA-N goes over into a line of phase transitions of the first-order.

A.4 Deformation and surface anchoring of nematic LC

When the LC is not affected by any external fields or influenced by confining boundaries, surfaces the equilibrium director field is uniform, determined by the internal ordering of the mesophase. Nevertheless it is ideal and very rare case [58,180,199]. Nematic LCs possess a relatively low viscosity and they can be deformed by even small external forces or presence of confining boundaries.

Considering only weak distortions, the nematic phase formally acts as an elastic medium, and the deformations can be treated by the continuum theory of nematics [58,184]. An undeformed LC is one in which the director $\vec{n}$ points in the same direction throughout the LC. A deformed LC is one in which the director changes its direction from point to point. The deformations in LCs can be described in terms of three basic

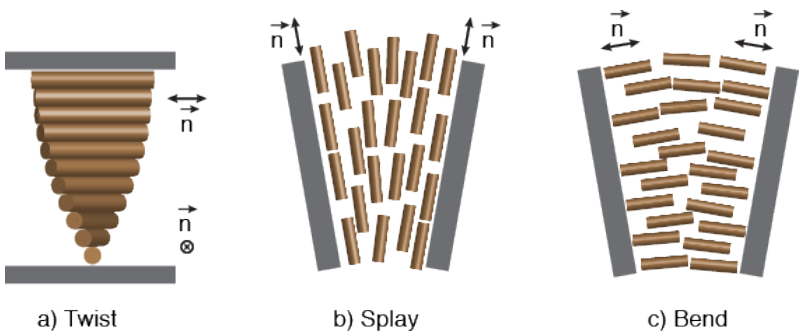

Figure A.5. Deformation in nematics. The nematic deformation falls into one or a combination of any of the basic modes: twist, splay or bend.

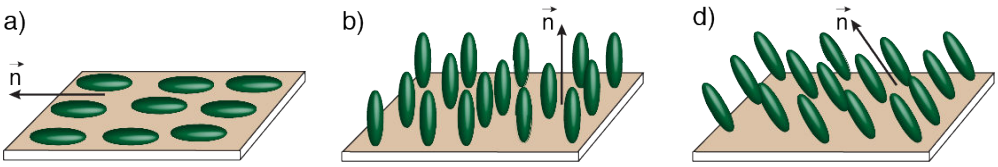

Figure A.6. Orientation of LC near a surface. (a) Uniform planar anchoring, (b) homeotropic anchoring, (c) tilted anchoring. ($\vec{n}$ is director).

types of deformation: splay, twist and band shown schematically in Fig. A.5.

In terms of the director $\vec{n}$, the free energy density of distortions can be expressed in the Frank - Oseen form:

$$F_d^{FO} = \frac{1}{2}K_1(\boldsymbol{\nabla}\cdot\vec{n})^2 + \frac{1}{2}K_1[\vec{n}\cdot(\nabla\times\vec{n})]^2 + \frac{1}{2}K_1[\vec{n}\times(\nabla\times\vec{n})]^2 \tag{A.10}$$

This equation is the basis for the theoretical treatment of defects and textures of nematic LCs [188]. For a stable distortions, the solution of the above equation have to yield a relative minima in the free energy. Distortions that do not correspond to minima of F_d are unstable and should therefore not occur in stable textures. The basic modes of nematic deformation are directly addressed by the Frank elastic constants: K_1 represents the splay deformation with $(\boldsymbol{\nabla}\cdot\vec{n})^2 \neq 0$, K_2 represents the twist deformation with $[\vec{n}\cdot(\nabla\times\vec{n})]^2 \neq 0$, K_3 corresponds to the bend deformation with $[\vec{n}\times(\nabla\times\vec{n})]^2 \neq 0$.

But for us, the most interesting is the contact of a nematic liquid crystal with a solid substrate, since in most of our experiments the LC is limited by two solid boundaries. The interaction of LCs with substrates leads to many interesting and important effects, such as a change in the long-range order parameter, the appearance of a short-range translational order, the appearance of dipole surface layers, and others. Almost any surface causes the director $\vec{n}$ to orient in a specific direction near the surface [199]. The molecules alignment at surfaces propagates over macroscopic distances.

One distinguishes 3 basic ordering types presented in Fig. A.6. These are planar, homeotropic and tilted orientations [180]. And the modifications of the basic anchoring states occur in nature. The surface, which is in a contact with the mesophase is usually considered to be flat on the microscopic scale, and the position of the director near it is determined by polar θ (between $\vec{n}$ and the substrate normal) and azimuthal ϕ angles (angle between the director projection and a reference direction on the substrate plane). In planar anchoring ($\theta = \pi/2, \phi =$ constant) the molecules are

anchored parallel to the substrate plane (see Fig. A.6 (a)). In homeotropic case ($\theta = 0$) the molecules are aligned perpendicular to the plane (Fig. A.6 (b)), and in tilted anchoring ($0 < \theta < \phi/2, \phi =$ constant) are oriented at any angle to the surface plane (Fig. A.6 (c)).

Due to the deformations of LCs there are deviations of the director from the "easy axis" (equilibrium state of $\vec{n}$) in the areas adjacent to the surfaces [58]. To orient the LC, it is necessary to treat the surface in some way. All procedures of solid substrate treatment can be roughly divided into two major groups: mechanical treatment and chemical treatment. Most often for the planar orientation of the director on the surface, a mechanical rubbing of the substrate is used. In the technology of displays, special machines with brushes rotating at a certain speed and controlled pressure are used, but for laboratory experiments the simplest way is to rub the surface manually with a clean cloth. The technique of rubbing is very simple, it provides sufficient energy of adhesion of the director to the surface. To obtain tilted orientation of the director with a given angle on the surface, a method of vacuum deposition of silicon oxide can be used. In this case it is necessary to vary the angle between the normal to the surface of the substrate and the direction to the SiO source rather finely. In addition, the director can be tilted by irradiating the photosensitive films with an oblique incident light beam, polarized or unpolarized. In order to get homeotropic orientation substrates can be washed with surfactant, lecithin for example.

Previously we have seen that the LC can be easily oriented due to surface interactions. But in addition to this, LC can be oriented by magnetic fields if the mesogen has a strong magnetic moment and LC can be easily oriented by an external electric field if the mesogen has an electric dipole moment [200]. When weak magnetic or electric field are applied to the liquid crystal, the initial effect of the field is to raise the transition temperature. For a strong enough field, no transition at all will be observed.

Appendix B

Supplementary experimental details

This appendix is devoted to describe to the readers some experimental trials, implementations and modifications of the setup that have been accomplished during this PhD thesis. Some methods presented in the following did not work for our measurements, but it will probably inspire somebody in another type of measurements with another type of problematic. We also mention some experimental tricks and techniques that could be relevant in another context.

B.1 Step-by-step procedure of sample mounting

Besides the preparation of the substrates used for the sample cell described in Chapter 3.3 (AFM measurements, cleaning of the surfaces...), the assembly of the liquid sample cell requires precision and accuracy. The photo of the whole sample holder is presented in Fig. B.1. The first step consists in mounting the linear stage and the lens holder on the three-axis positioning stage. Both should be set parallel to each other and aligned compared to the stage. After that the lens is placed in its special mount and covered by a rim to fasten the lens. During the mounting the lens, we should make sure there is no object that can tilt the parallel installation of the lens. The rim is then screwed into the lens holder by four screws, the screwing force should be distributed evenly on all four screws. Then the lens holder mechanical part remains motionless until the next measurements. This step is essential for the proper installation of the lens. The next step consists in mounting the piezo stage attached

to the aluminum square block on the linear stage. The aluminum block is centered on the piezo stage in such a way that it covers the whole surface of the moving part on which the voltage is applied. The piezo stage should be mounted parallel to the linear motor stage. Then the aluminum barrel holding the generation substrate is inserted in a hole inside the aluminum block. When all mechanical parts are fixed, we can start the rough, fine and ultrafine liquid thickness adjustment. A liquid drop is injected with a needle in between the lens and the generation substrate, right after the barrel with the generation substrate is screwed tightly from the top side of the square bloc. This barrel should be fixed in such manner that the liquid is gently squeezed and couldn't flow out, but the two substrates are not in close mechanical contact. At this stage the liquid film may be thick enough, in the hundreds of μm range. To reduce the thickness meticulously and precisely we then use the linear stage controlled by XPS. The minimal step of our stage is 0.1 μm which gives enough accuracy for this task. We approach the generation substrate to the lens in order to decrease the thickness to

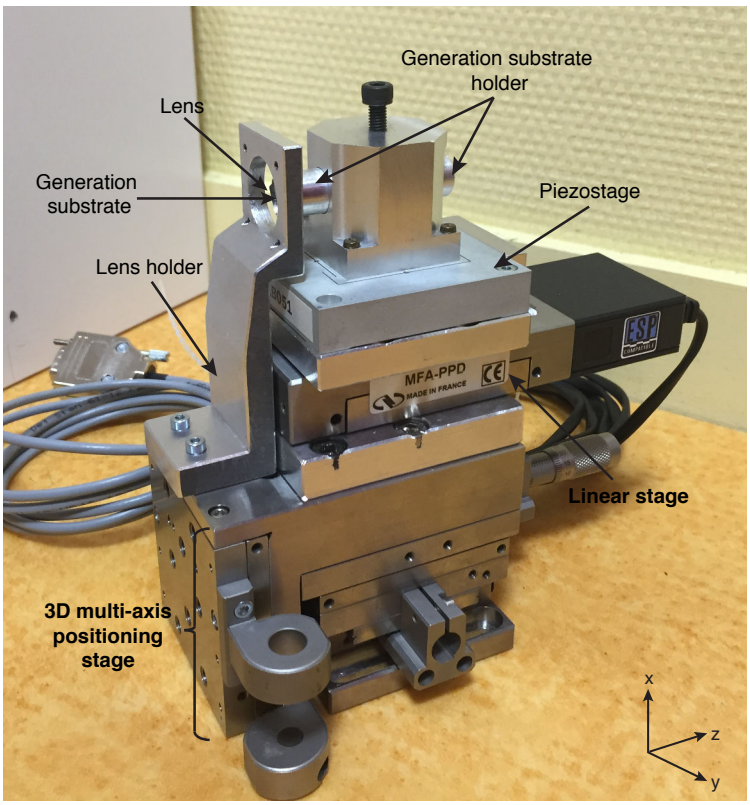

Figure B.1. Photo of the sample holder used during this work.

about less than 10 μm, since the whole range of motion of the piezo stage is 10 μm. After all these steps, the sample is then ready for the investigations.

There are several advantages of using the piezostage coupled with the motorized linear stage. After several tests of different piezo stages described in the next section, we have chosen the one that ensures an accurate minimal increment well below 1 nm to investigate confined liquids. The linear stage permits a continuous motion in a wide range of positions with great accuracy, it is computer controlled and it is implemented in our acquisition program that controls the piezo stage as well. The accuracy of the piezo displacements is high (the resolution is claimed to be $\pm$ 0.01 nm) in a 10 μm full range of displacement. The linear stage is used to tune the liquid thickness below 10 μm while the piezo stage is used to fine tune the liquid thickness below this range. So, by using this coupled displacement system, we get access to a wide range of liquid thicknesses. In addition to the piezo measurements, we have included the possibility of performing automated measurements at different lateral positions, such as in the flat-curved configuration, going from the center of the Newton ring's where the thickness is close to zero, to a desired lateral position. In fact, prior to the piezo measurements, we always perform several lateral measurements in order to precisely center the laser spot and the contact position on the lens with a micrometer resolution.

B.2 First version of sample configuration

At the beginning of this thesis, we used the sample configuration presented in Fig. B.2. In view of a couple of disadvantages this system was improved to the one described in chapter 3.3. Still, this sample system can be used for the investigations of thick liquid films that do not require nanometric precision. The sample configuration remains the same, it is based on a flat generation substrate and a curved detection substrate. The lens is attached on a lens holder which is screwed directly to the piezo actuator holder. The Piezo actuator (PI, P - 841.10 and P - 611.ZS), with a full motion range of 15 μm and a resolution of $\sim$ 0.3 nm (for P - 841.10 model), is a cylinder of 32 mm length and 12 mm of diameter. At the opposite side of the wires, into which a high voltage is applied, a threaded hole can hold a tiny screw. The generation substrate is directly glued with epoxy on this tiny screw. The piezo actuator with the generation substrate is then placed in the piezo holder. This holder is then fixed on a three-axis mechanical stage not shown in Fig. B.2.

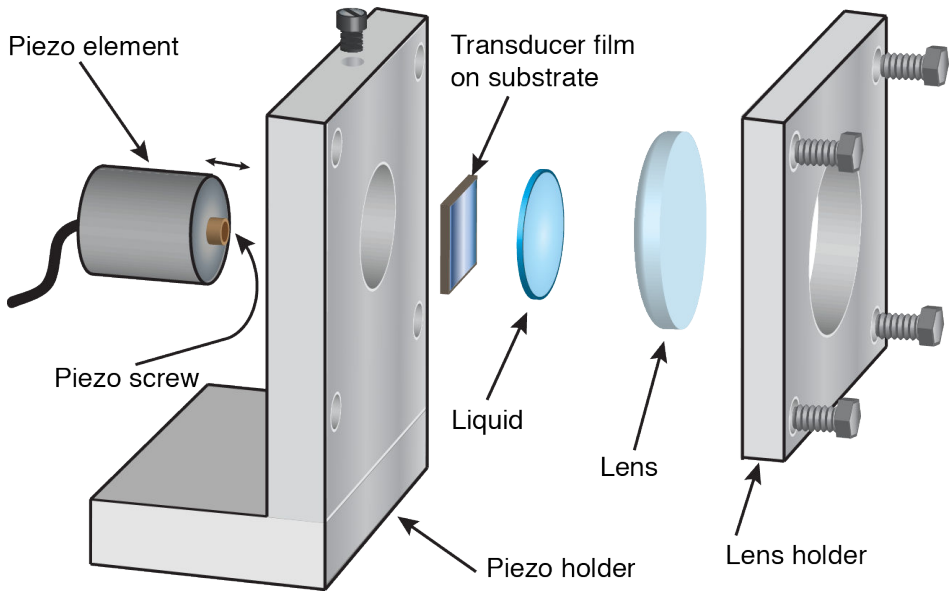

Figure B.2. Schematic representation of the first version of the sample configuration tested during this work. The Piezo actuator is a cylinder on which a screw glued with the generation substrate is attached. The liquid drop is squeezed in between the transducer film substrate and the lens.

Step-by-step sample assembly This sample geometry is more easy to install but still requires a good accuracy and precision. The first step is to fix the aluminum piezo holder on top of the three-axis manual stage. The holder should be well aligned to this stage. The flat generation substrate, small enough to fit into the hole in the holder, is glued on the piezo screw. Then the screw is fixed on the piezo cylinder. One of the main disadvantages of this piezo actuator is related to its fragility. The screw can not be fixed completely in the cylinder because it can easily break the piezo actuator. Consequently, the screw is not tight completely and can move slightly, which is completely inappropriate for our measurements with ultrathin liquids. Another disadvantage concerns the size of the screw head. The area on which the generation substrate may be glued is about 0.15 cm^2 that is extremely small. The size of the generation substrate is limited by the screw head surface but also by the diameter of the hole on the piezo holder. Afterwards the cylinder with all components is placed in the hole and screwed from the side. Then a small drop of liquid under study is injected on the transducer film and squeezed by the lens from the opposite side. The next step consists in strengthening the lens and the lens holder in such a way that the contact of the lens is aligned on the generation substrate. The lens holder is fasten

with four screws to the piezo holder in order to tune the contact surface at the center of the generation substrate. This is rather challenging and it frequently happens that when we screw the holder tightly it breaks either the generation substrate or crack the lens. It is related to the force applied to each screw which is not identical and creates a torsional force on the sample. This effect is easy to observe by movements of interference rings. Thus, the lens is not rigidly installed, and when we apply the voltage to the piezo in order to decrease the liquid film thickness, it might push the lens instead of inducing a modification of the liquid thickness. To conclude, the PI piezo actuator characteristics are disappointing and not suitable for accurate measurements requiring nanometer precision. However, this beta version of sample holder inspired the implementation of the final configuration described in Chapter 3.3.

B.3 Newton's rings visualization

An anti-reflection (AR) coating is a type of optical coating applied on the surface of the lenses and other optical elements to reduce optical reflections. In typical imaging systems, this improves the image brightness and quality since less light is lost and it avoids stray light. In general, the AR coating consists of a transparent multilayer thin film structure with alternating layers of contrasting refractive indexes. The layer thicknesses are calculated and chosen to produce destructive interferences in the beams reflected from the interfaces, and constructive interferences in the corresponding transmitted beams. The AR coating is optimized to reduce reflection losses at the air/lens interface and works in a specific wavelength range. The wavelength range of the AR lenses used in our experiments is 650 - 1050 nm. In our measurements, the AR lens is in contact with the liquid which is squeezed between the lens and the generation substrate and the AR coating is not functional anymore. Vice versa, the AR coating optimized with an air interface becomes extremely poor AR in contact with a liquid, and the AR is not anymore a good index matching medium. This is exactly the reason why we use a lens with AR coating to visualize the Newton's rings interferences. Without coating, the contrast in index of refraction between the uncoated lens and the liquid is weak and there is negligible optical reflection at the liquid-lens interface which, in turns, vanishes the optical interferences in the liquid cavity. We can't observe the Newton's rings in a situation of an uncoated lens. In order to visualize the Newton's rings, the trick consists in using AR lenses which increases the quality factor of the multiple interferences in the liquid cavity. The counterpart is that the Newton's rings interferences appear as well on the time domain signals recorded at different liquid

thicknesses which is rather troublesome. From Fig. B.3 one clearly sees the impact of the AR - coating on the Newton's ring contrast. Fig. B.3 (a) shows the sample surface image for the sample structure where an AR lens was used. The contrast in intensities from dark and bright fringes is significant and we can clearly distinguish the Newton's rings on the images so that we can conveniently set the pump and probe beams at the center of the rings with micrometric precision. In case of a liquid sample structure with an uncoated lens, we obtain a completely different image where the Newton's rings can be barely seen, it is not possible to distinguish the interferometric fringes, see Fig. B.3 (b). So, from the point of view of convenient adjustment of the pump - probe beams on the sample surface, the lens with AR coating is recommended. Nevertheless, for the pump-probe experiments where the liquid thickness is changed automatically via computer control, this AR coating plays an hazardous role. As it was already seen for the OMCTS sample, part of the data at some specific liquid thicknesses are lost because of the coating. Lately, we have only been using lenses without AR coating and aligned the pump and probe beams at the contact from lateral measurements.

Fig. B.4 demonstrates the impact of the AR coating on the recorded pump-probe signals. The top data of Fig. B.4 shows the data for a sample configuration in which an uncoated lens was used and the bottom data shows the data for sample configuration with an AR lens. The 2D plots highlights a strong difference in image quality and interpretation. Neglecting some vagueness of the recorded signals on the central part of the image in Fig. B.4 (a), the image is clear and its interpretation simple. Close to the center of the sample (X $\sim$ 0), the lens and the substrate are almost in direct contact and Brillouin signal oscillations due to acoustic propagation

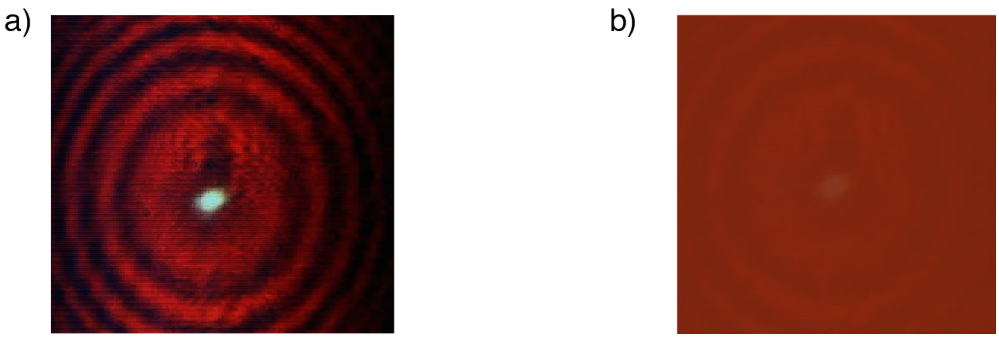

Figure B.3. Images of the sample surfaces obtained from a sample configuration with a Chromium transducer film on a flat silicon substrate, glycerol, and either a lens with antireflection coating (a) or a lens without antireflection coating (b). The Newton's rings are well contrasted in (a) and undetectable in (b).

in the substrate begin promptly. Away from the center, the signal oscillations due to acoustic wave propagation in the substrate are time delayed, and these oscillations are preceded by lower-frequency oscillations due to acoustic wave propagation in the liquid. We can even clearly see on the image the contribution of the wave reflected from the liquid/lens interface to the signal. From an image of such quality we can extract many

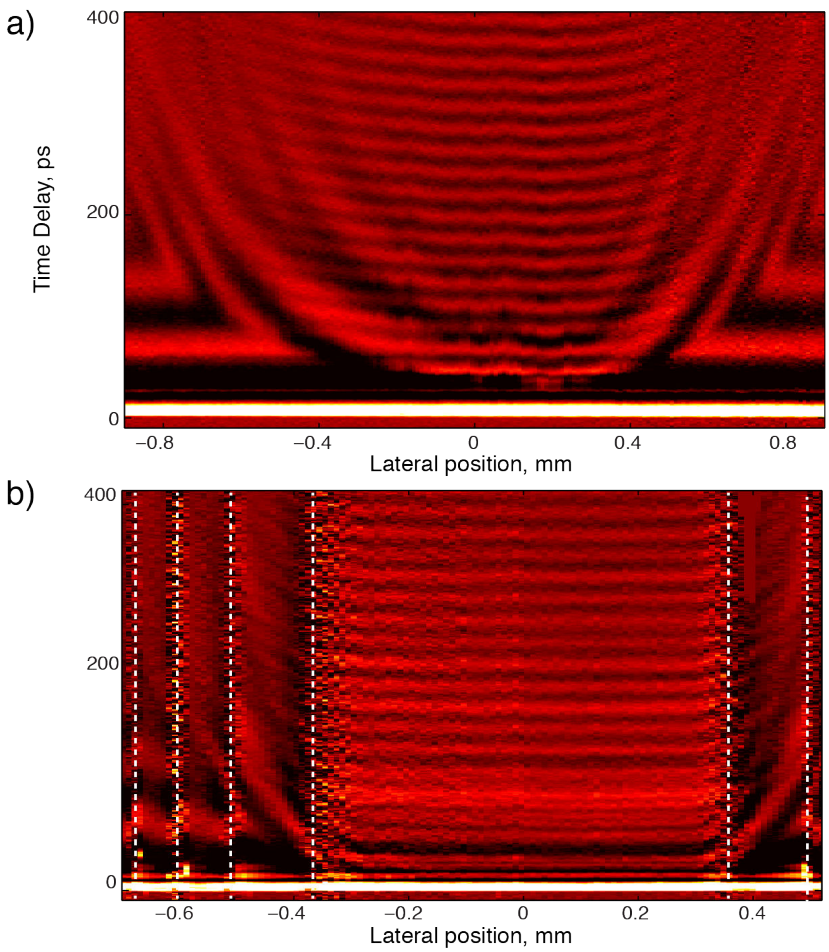

Figure B.4. Interpolated 2D plots of Brillouin data recorded at different lateral positions across a 8CB liquid sample. (a) The sample configuration consists of a Chromium transducer on a flat silicon substrate, 8 CB and an uncoated glass lens (ROC = 515.1 mm). (b) The sample configuration consists of a Chromium transducer on a flat silicon substrate, 8 CB and an AR glass lens (ROC = 500 mm). White stippled lines approximately indicate the location of the dark Newton's rings. In these areas the signal-to-noise is poor and the Brillouin signal which gather information about the acoustic waves propagating through different liquid thicknesses is lost.

useful informations on the mechanical properties of the liquid, unlike in the case of the sample configuration with an AR lens shown in Fig. B.4 (b). The wide central part with flattened dark/bright fringes corresponds to the zone where the lens is pushed into the substrate for a few tens of nanometers or even several hundreds of nanometers. Away from the center, we can observe some regions, highlighted on the image with white stippled lines, with pronounced noise level that correspond to the dark Newton's rings position. Apparently, the intensity of the probe beam reflected from such dark regions is weak and thereafter the current detected on the photodiode gets significantly noisy. Since we are using two photodiodes in our experimental configuration, we need to make sure that the signals on both photodiodes remains well balanced, even in case of dark fringes, which is not an easy task. The use of an AR lens hinder the possibility of balancing the photodiodes for better signal-to-noise ratio on the signals. Additionally, the most important zone for the investigation of interfacial effects and liquid confinement effects is precisely located at close vicinity of the lens/substrate contact region, that is exactly at the dark fringe location, where we can't profit of the useful scheme of balanced photodiodes.

B.4 Interferometric determination of the contact zone from the fs probe reflectivity

Another problem that we encountered during this work was the determination of the accurate position when the lens and the flat silicon substrate holding the Chromium film are in direct contact, right when the lens slightly approaches the flat substrate without pushing into it. This is the starting point of the measurements, the zero thickness determination of the liquid. In order to optically detect the contact position, we have implemented a method based on the measurement of the DC reflectivity intensity change of the femtosecond probe beam for different thicknesses. This method is valid only in case of AR lenses since it uses the interferences effect produces in the liquid cavity. These measurements enable the estimate of the refractive index of the material at a specific wave length, considering that the liquid thickness is well determined. The result of this measurement is presented in Fig. B.5. The DC change in intensity of the reflected probe beam was measured for a sample composed of a silicon flat substrate holding a 50 nm thick Chromium film, a glycerol liquid layer at room temperature and an AR plano-convex lens. The DC reflectivity change of the probe light reflected from different liquid thicknesses is plotted against the relative piezo displacement (in this case we went from thick to thin liquid layers). One sees that

the current measured on the photodiode oscillates and stops varying when it reaches 5.3 μm approximately, it indicates that the lens touches the flat silicon substrate. If the piezo moves even further, the deeper the lens goes into the substrate. This method is quite reliable for the determination of the contact zone. Nonetheless it has more disadvantages than advantages. First of all, to be sure that the reflectivity does not change anymore the piezo stage is moved forward deeply in the substrate which leads to substrate deformation. Secondly, the piezo stage displacement is hysteretic. When the piezo is moved backward, the starting point of zero liquid thickness is not reliable anymore. As long as the idea is to investigate ultrathin liquid layers, this hysteric behavior is inappropriate. In particular, since empirically we understood that such ultra thin liquid measurements need to be performed while reducing the liquid thickness always, to avoid the nucleation or cavitation of bubbles if the liquid thickness is increased from solid - solid contact to thicker liquids. Indeed, we have experimentally observed several times bubble nucleation that forms in liquid layers, which needs to be avoided.

Nevertheless, this experimental method is advantageous for the determination of the refractive index of different liquids at the probe wavelength. In Fig. B.5 we can notice that the intensity of the reflected probe beam changes periodically, varying from a minimum to a maximum intensity with at a well defined increment of the liquid

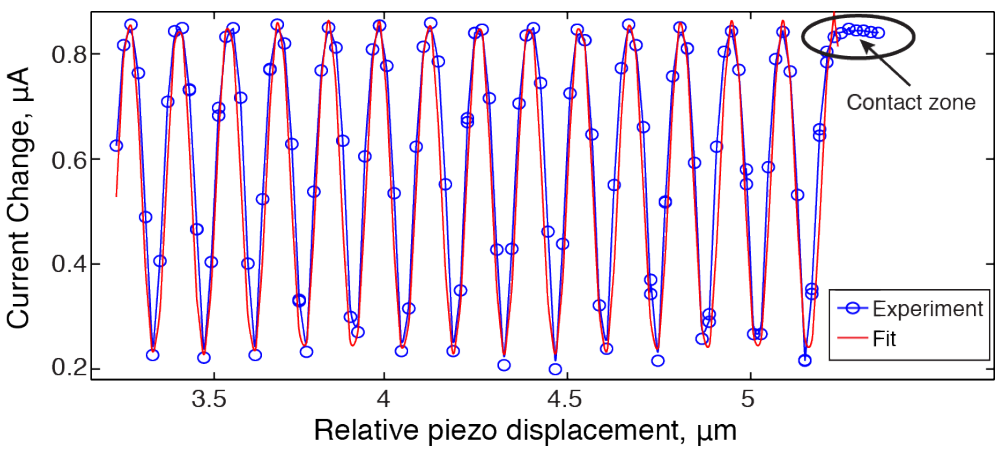

Figure B.5. Change of the reflected probe intensity from different thicknesses of glycerol. The sample configuration consists of a silicon substrate holding a 50 nm thick Chromium film, glycerol, and an AR plano - convex lens. This sort of measurement allows to optically determine the zone where lens is in direct contact with the flat generation substrate (black ellipse). From the spatial period of the oscillations, the refractive index of the liquid may be calculated.

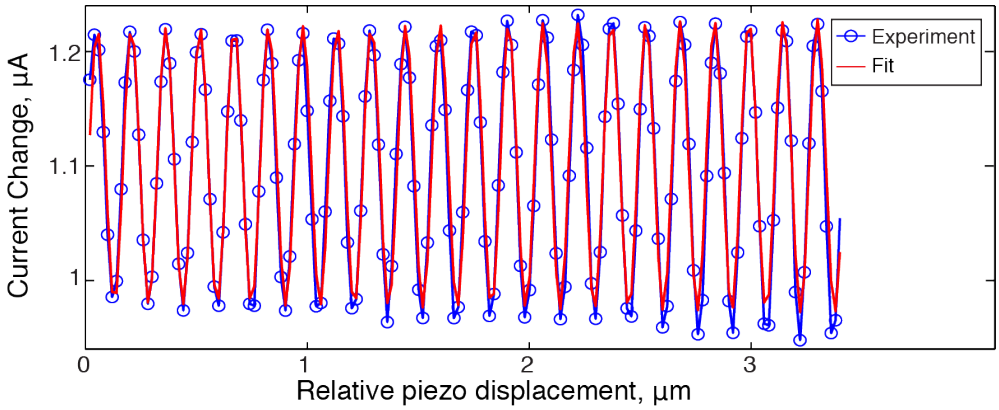

Figure B.6. Change of the reflected probe intensity from different thicknesses of OMCTS. The sample configuration consists of a silicon substrate holding a 50 nm thick Chromium film, OMCTS, and an uncoated plano-convex lens. From the spatial period of the oscillations, the refractive index n of OMCTS at the probe wave length is extracted.

thickness. This spatial period corresponds to the period between two successive dark or bright Newton's rings. By fitting the experimental data with a sinusoidal function, we can extract the spatial period of the oscillations, correspondingly. The spatial period of the oscillations matches the optical path difference δ for the probe beam reflected from different liquid thicknesses. Let us calculate the index of refraction of glycerol from Fig. B.5, and compare this value with the literature value. The experimental data were fitted with the equation $y = A \cdot cos(2\pi \cdot d/\delta + \phi)$, where A is the amplitude, ϕ is an arbitrary constant phase, d is the piezo displacement, and δ is the spatial period which follows the relationship $\delta = \lambda/2n$ with λ the probe wavelength in air and n the index of refraction. From the extracted value of $\delta = 134$ nm, we obtain $n = 1.475$ at the probe wavelength. This value is very close to the literature value at room temperature [101, 201].

This method was used for the determination of the refractive index of OMCTS at 395 nm probe wavelength and at room temperature. This data is not available in the literature. The experimental results are presented in Fig. B.6. The data were fitted from the equation $y = A \cdot cos(2\pi \cdot d/\delta + \phi)$, where we varied δ to get the best fit. From the extracted value of δ that best match the experimental data, we have calculated the refractive index of OMCTS at the probe wave length and at room temperature,

$$n_{400}(OMCTS) = \frac{\lambda}{2 \cdot \delta} = 1.37 \cdot \tag{B.1}$$

To conclude, the method of measuring the change in the reflected probe intensity from different liquid thicknesses can be used firstly for an accurate determination of the refractive index of the liquids, and for the determination of the solid-solid contact in situations when the liquid thickness determination does not need high accuracy.

B.5 Measurements with the Death Star pulse shaper

As we have already seen in Chapter 4, laser mediated cumulative heating effect can be observed in our measurements. This effect is directly linked to the laser itself that governs the cumulative sample heating. In this section, the so called Death Star pulse shaper was used in order to monitor the sample heating under the experimental conditions of a train of several pump pulses separated in time. The main role of the pulse shaper is the excitation of narrowband acoustic wavepackets for the selection of a well defined frequency component in the propagating acoustic waves. In our case, the shaper was fixed at a repetition frequency of $\nu_{B,liq} = 21$ GHz that matches the Brillouin frequency in glycerol. A more detailed description of the pulse shaper can be found in Section 2.2.1. The intuitive idea was to use the pulse shaper in order to decrease the cumulative effect without altering the Brillouin signal. Splitting at the incoming single pulse, which is introduced in the Death Star shaper, into seven pulses slightly time delayed, entails that the energy carried by the incoming single pulse is split in seven pulses and that the overall heating of the metal transducer film caused by the laser light absorption of the train of pulses could be decreased assuming that the sample would cool down in between each of the seven pulses. This cumulative heating is afterwards transmitted to the adjacent liquid layer and could be less than in case of a single pulse of equivalent laser energy. In fact, we have evidenced a counterintuitive effect. Data for a sample with 40 nm thick Chromium film on a silicon flat substrate, glycerol and an uncoated plano-convex lens (LA 1172, Thorlabs) were recorded at a fixed temperature of about 300 K for several laser powers of the pump pulse for two positions of the pulse shaper, at "zero" position when all of the five pulses hit the sample surface without any temporal separation (Δt = 0 ps), and adjusted to "21 GHz" position (the temporal separation between all of the five pulses is changed evenly and is equal to Δt $\approx$ 47 ps). An example of the recorded signals is shown in Fig. B.7 (a). The excitation pulse sequence was adjusted to match the Brillouin scattering frequency in glycerol at 21 GHz in order to enhance the acoustic spectral brightness at this specific frequency. This excitation feature is visible in the signal of Fig. B.7 (a) until about 210 ps (green curve). The data were normalized

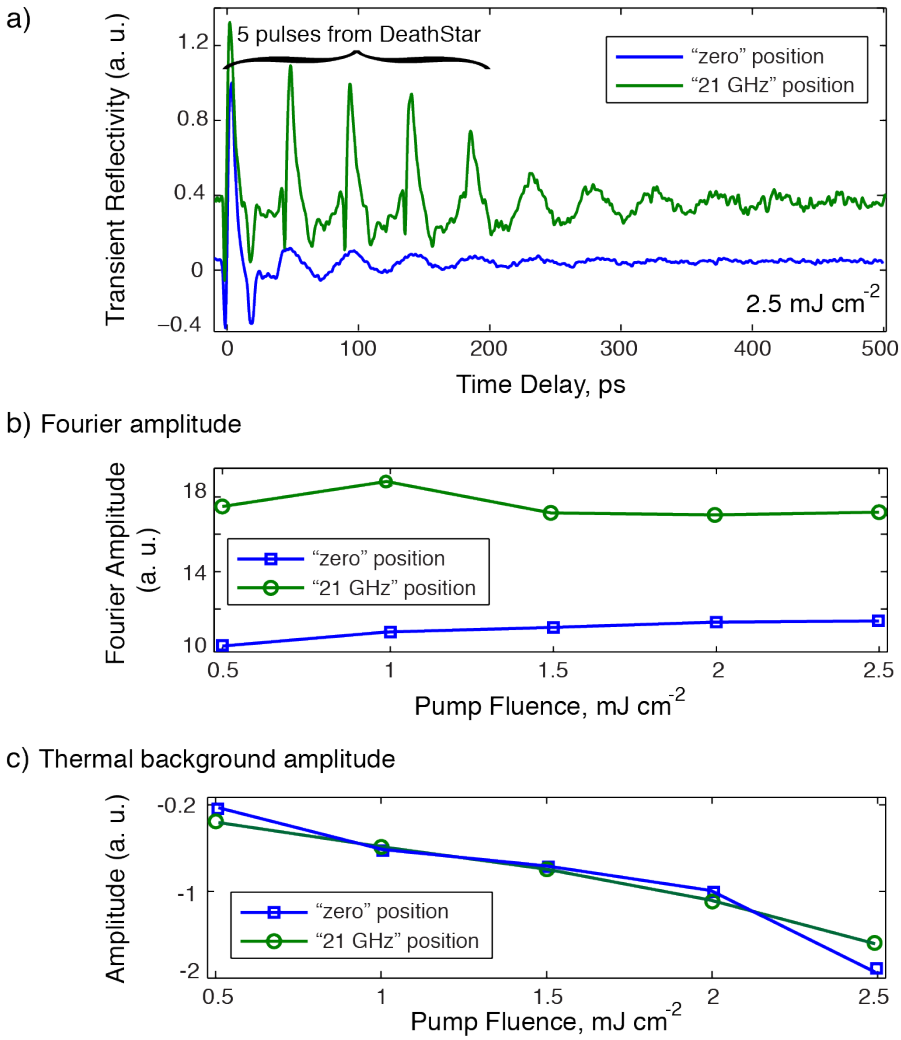

Figure B.7. (a) Time derivative of the measured signal intensity for two distinct positions of the Death Star pulse shaper (with $\Delta t = 0$ ps and $\Delta t \approx 47$ ps of time delay between pulses) for a sample composed of a 40 nm thick Chromium film on a silicon flat substrate, glycerol and an uncoated plano - convex lens at 300 K and at overall pump fluence of 2.5 mJ·cm^{-2}. (b) Brillouin acoustic amplitude spectrum of both signals at several pump fluences. (c) Amplitude of the thermal background extracted from the normalized data.

by the electronic peak intensities of this excitation sequence before taking the time derivatives of the signals. The two curves in Fig. B.7 (a) are slightly offset for better display. In the time interval between $\sim$ 210 to 500 ps ("21 GHz" position) and between 40 ps to 500 ps ("zero" position), Brillouin oscillations due to coherent longitudinal

waves in the glycerol can be observed. Their corresponding Fourier amplitudes are shown in Fig. B.7 (b). From these data one notices that the acoustic wave excitation at this particular frequency is enhanced almost twofold. The analysis of the thermal background which is intimately related to the cumulative heating and temperature gradient in the sample is displayed in Fig. B.7 (c). From these data one remarks that the result is opposite to intuition. If we take the absolute value of the thermal background amplitude, the background at "21 GHz" position is as high as that for "zero" position of the pulse shaper. This amplitude reflects the cumulative heating effect in the sample.

This surprising result may be interpreted based on the arrival time of each pulse. When one pump pulse with certain energy arrives at the metal transducer film, this optical energy gets absorbed by this transducer film. The pump pulse is modulated at some frequency which is sufficiently high to give the time for the liquid to cool down a little bit (f_{pump} = 260 kHz). In case of optical pulse sequence, one pump pulse is split into 5 pulses with some time delay between them. When one pulse from pulse sequence arrives to the transducer film it heats it up, then arrives second pulse and so on and some heat is deposited into the transducer film surface which afterwards is transferred to liquid. The time between pulses is excessively low and unsufficient for adequate liquid cooling. When the second pump pulse arrives the liquid is already heated as much as in case of shot-by-shot heating. It means that most probably the heat cumulates nonlinearly with the use of the optical pulse sequence.

B.6 Optical derivative

Another puzzle that we faced during this project is related to the unwanted presence of a slow decaying thermal background in the recorded signals that depends on the liquid thickness as well. This slow thermal background increases the complexity of the data analysis and can reduce the accuracy of the acoustic measurements. In Chapter 2, the analysis of the Brillouin signal is reduced to fitting the experimental data with the simplified functional form of equation Eq. (2.20) that reads,

$$\triangle R = A_0 \exp(-\Gamma t) \cos(2\pi f t + \phi). \tag{B.2}$$

This simplified equation gives access to two relevant parameters related to the acoustic waves propagating through some medium, the attenuation rate and the Brillouin frequency which is related to the speed of sound. It does not account for the thermal background that influences the reflectivity measurement and Eq. (2.20) is inappro-

priate as it is. A better approach is to use the functional form of Eq. (2.23) that reads,

$$\triangle R = A_0 \exp(-\Gamma t) \cos(2\pi f t + \phi) + B_0 \exp\left(-\frac{t}{\mu}\right) + \delta. \tag{B.3}$$

In this equation, there are plenty of parameters that one should vary during the fitting procedure of the acoustic signal and of the thermal background. In this case, the fitting procedure is complicated and it increases the uncertainties in the two parameters of interest Γ and ν_B. Instead, it is often preferred to perform the time derivative prior of the fitting of the experimental data to vanish the slow varying thermal background. The time derivative almost suppresses the slow thermal background and only the acoustic term remains and we can use the simplified functional form of Eq. (2.20) with high accuracy. However, the counterpart is that the procedure of taking the numerical time derivative of the recorded signal increases the shot noise of the data that becomes sometimes impossible to process. Therefor, we have made some attempts in order to improve our experimental setup and overcome the limitations of the time derivative routine for data analysis. Some modifications were made to our setup to perform the optical derivative, not numerically but rather optically. The derivative of any function represents an infinitesimal change in the function upon a slight modification of a variable. The time derivative of the reflectivity function R with respect to the variable t can be written as,

$$dR = \frac{R(t + \Delta t) - R(t)}{\Delta t}. \tag{B.4}$$

This is valid for both numerical or optical signal derivate. In case of the numerical derivative, Δtrepresents the temporal resolution of the recorded signals. In case of the optical derivative, this infinitesimal change Δt can be produced artificially by using two probe pulses instead of one with an optical temporal delay Δt. The main advantage of the optical derivative compared with the numerical derivative is that both femtosecond probes gather the same noise and the optical derivative is compatible with the use of balanced photodiodes.

In the following, we will describe several techniques to perform the optical derivative, either by use of piece of glass or by use of a shaker.

Optical derivation by means of probe pulse splitting

The first configuration, that was tested on our set up is presented in Fig. B.8 (a) and is based on the probe beam splitting into two probe beams slightly time delayed between each other. Half of the pump beam passes through a piece of glass of some

thickness e, another half goes through air without any deviation. We obtain two sub-beams time delayed between each other. The piece of glass creates an optical path difference δ between both beams,

$$\delta = e(n-1), \tag{B.5}$$

where n is the glass refractive index (n = 1.5) that entails a time delay between both sub-beams of $\tau = \delta/c$ where c is the light velocity in air. In practice, we used a microscope glass coverslip of 300 μm thickness that gives a time delay of $\tau = e(n-1)/c$ = 0.5 ps relative to the second part of the sub-beam. After reflection from the sample surface these two pulses are separated by a wedge mirror, one sub-beam goes to one photodiode (P1), another goes to the second photodiode (P2). These two photodiodes are balanced -i.e. subtracted- and the output is sent to the Lock-in amplifier.

The trick of this configuration is that the two signals from P1 and P2 are subtracted electronically prior to the Lock-In amplifier and we obtain the signal derivative with a resolution of τ as in Eq. (B.4). Results obtained from a sample similar to previous measurements with or without optical derivation are presented in Fig. B.8 (b) and (c). Both signals are very much alike. The decaying rates are equivalent. Nonetheless, the dissimilarity, not visible at first glance, is in the noise level. Upon careful examination, one can notice that the signal obtained from the experimental configuration without optical derivative is much noisier than from the configuration with optical derivative. From further numerical derivation of signals, the noise level increases in twofold. So, this configuration is beneficial and profitable for noise level reduction of the recorded signals. The fact that it does not perform properly the derivative of the signal comes from the fact that the spot sizes of the pump and of the two sub-beams that do not overlap on the sample surface have to be carefully adjusted. In fact the pump spot size should be large enough so that each sub-probe beams measures the same amount of signal. It was probably not the case at the time that we recorded these data. Another configuration such as described in [202] that uses a thick piece of calcite to create two delayed probe beams was tested too and give more accurate time derivative (the results are not presented in this work).

Note that, in a similar manner, a piece of glass can be used for trivial coherent control. It is a cheap version of a pulse shaper. For that purpose, the glass thickness should be carefully selected in order to selectively enhance or cancel a specific frequency in the signal. An example of coherent control from a piece of glass of the Brillouin signal is presented in Fig. B.9. The sample structure is replicated from the sample cell used for the investigation of ultrathin liquids, a Chromium film on a flat Silicon substrate,

glycerol and a plano-convex lens. Fig. B.9 (b) displays the Brillouin signal with a single pump pulse. The detected Brillouin signal corresponds to the signal detected in the plano-convex glass lens in contact with the Chromium film on its substrate. The signal displayed in Fig. B.9 (c) corresponds to the configuration with a piece of glass as a pulse shaper. One part of the pump beam goes through a glass plate of 6 mm thickness which creates a delay of 15 picoseconds between pulses. By comparing the normalized reflectivity signals displayed in Fig. B.9 (b) and (c), we can notice that the amplitude of the Brillouin oscillations in the glass substrate is significantly low in case

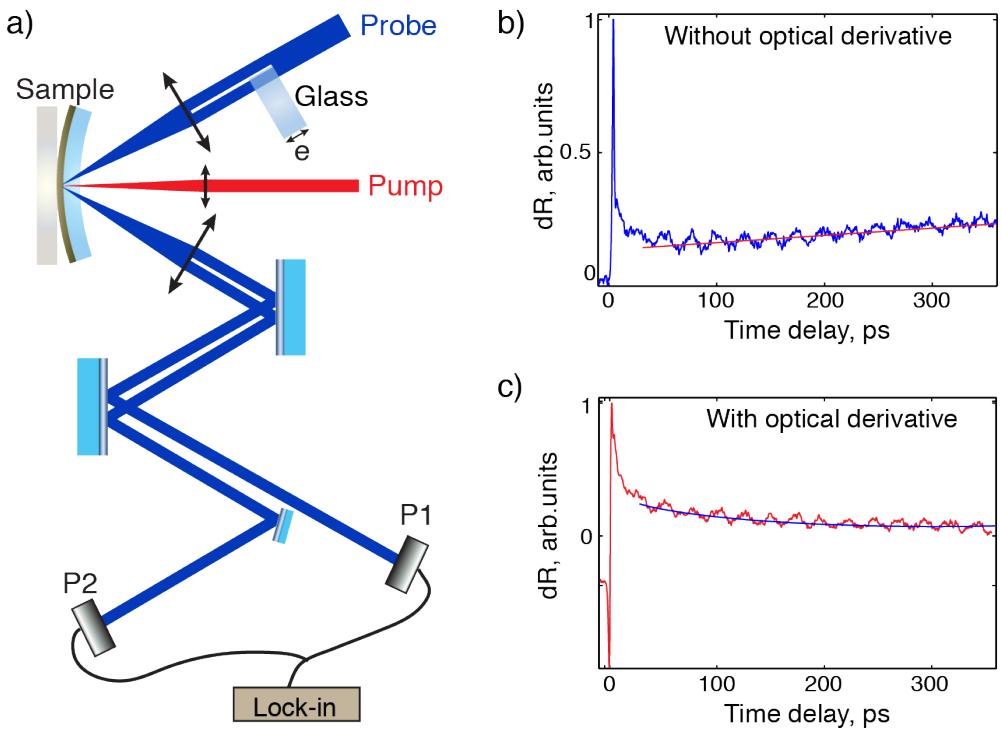

Figure B.8. (a) Sketch of the experimental setup configuration performing the optical derivative by means of probe beam splitting. Half of the probe beam passes through a glass plate of 300 μm thickness. Whereupon this part becomes delayed by $\tau = e(n-1)/c = 0.5$ ps relative to the second part. After reflection from the sample surface these two pulses are separated, one goes to one photodiode P1, another goes to the second photodiode P2, afterwards both are subtracted/balanced and the output is sent to the Lock-in amplifier. (b) Recorded transient reflectivity signal from a sample with a Chromium film deposited on a flat Silicon substrate, glycerol and plano-convex lens in contact the the transducer substrate. The Brillouin oscillations at $\nu_B \simeq 45$ GHz correspond to the acoustic waves detected in the glass lens. (c) Recorded optical derivative of the transient reflectivity signal displayed in (b).

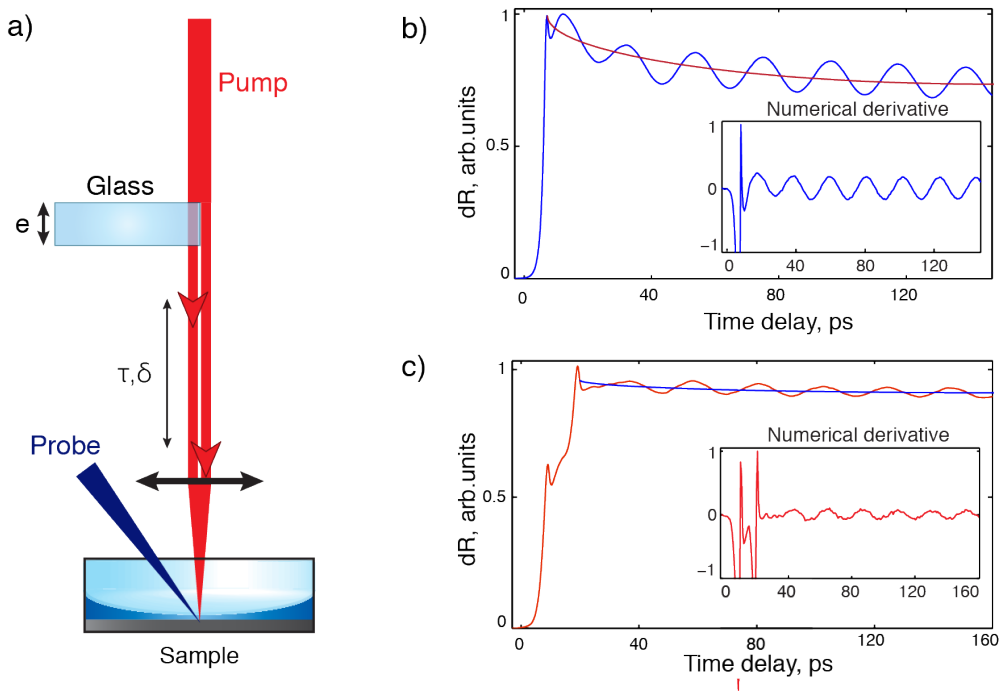

Figure B.9. (a) Schematic representation of the glass pulse shaper. The pump beam is split into two sub-beams. Half part of the pump beam passes through a glass plate of e = 6 mm thickness that leads to a time delay between both sub-beams τ = 15 ps. (b) Transient reflectivity signal recorded from a sample with a Chromium film deposited on flat Silicon substrate, glycerol and a plano-convex lens in contact with the transducer substrate. The Brillouin oscillations at $\nu_B \simeq 45$ GHz correspond to the acoustic waves detected in the glass lens. (c) Recoded transient reflectivity signal in case of a piece of glass on the pump path. The almost cancellation of the Brillouin oscillations is related to the antiphase propagation of the two acoustic wavepackets from the two delayed pump pulses.

of coherent control by a piece of glass. The decrease in amplitude is due to the fact that the delay between two separated pump pulses is quite close to the half period of the Brillouin oscillations ($\nu_B \approx 45$ GHz $\rightarrow$ $T_B = 22$ ps). This leads to the fact that the two acoustic wave packets generated by the two pump pulses propagate in almost antiphase. That is why the amplitude of the Brillouin oscillations have vanished with the piece of glass.

Optical derivative by means of a pulse shaker

In order to perform the optical derivative in a proper manner, several modifications of the current experimental setup described in the previous Chapters were

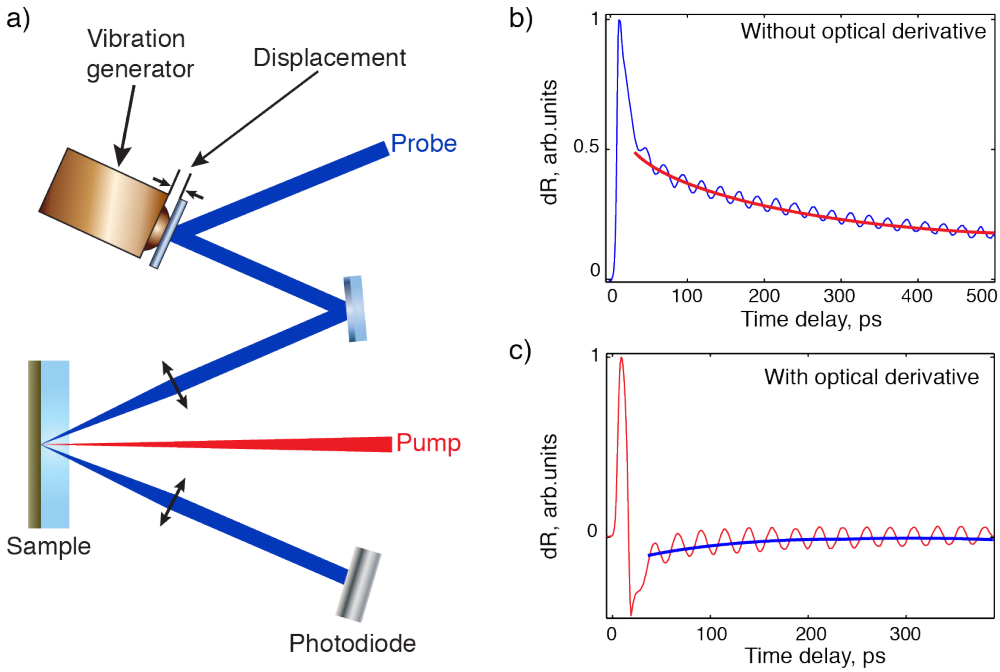

Figure B.10. (a) Illustration of the optical derivative experimental setup based a pulse shaper. The probe beam is reflected from a mirror placed on the pulse shaker. The amplitude and the frequency of the mirror displacements are controllable by a function generator. (b) Recorded signal without the use of the pulse shaker. (c) Recorded signal using the pulse shaper. The slow decaying rate of the recorded signal is negligible, the amplitude of the Brillouin oscillations is higher than in case of (b), the noise level is not bothering for further data analysis, and the recorded data do not need further numeric processing.

made. For this purpose, a pulse shaker (vibration generator) was used as depicted in Fig. B.10 (a). A mirror was placed on the vibration generator to create a cycling time delay Δt of the probe beam. The displacement amplitude, that governs the maximum time delay of the pulse shaker, and the frequency ν_s of the pulse shaker displacements are tuneable by a function generator. The frequency of the pulse shaper is set that the motion of the delay line is negligible during several cycles of the shaker and the amplitude of the pulse shaker is set to add a cycling time delay in the range of few picoseconds or less. The pulse shaper frequency is sent to a second lock-in amplifier that demodulates the signal from the first lock-in, set at the pump modulation frequency. The output of the second lock-in is proportional to the tiny change of the reflectivity dR upon a slight modification of the time delay Δt produced by the shaker, as in Eq. B.4. The only disadvantage of this experimental scheme that accomplishes the

optical derivative is that it requires a pulse shaker and a second lock-in, that adds more complexity and expensive electronic equipments on the actual setup. An example of the optical derivative obtained with this setup, conducted on a sample consisting of a Chromium film of 60 nm thickness on a flat glass substrate, is presented in Fig. B.10. The frequency of the pulse shaker was set to 30.0 Hz and the displacement in the range of 100 μm. First of all, the decay rate is clearly different with or without the optical derivative obtained with the pulse shaker, as evidenced in the data displayed in Fig. B.10 (b) and (c). Fig. B.10 (c) demonstrates the result of the optical derivative to which we aspired. The decaying rate of the recorded signal with the optical derivative is negligible, the brightness of the Brillouin oscillations is higher, the noise level is not bothering for further data analysis, and the recorded data do not need additional numeric processing. Indeed, this experimental setup may be exquisite for the studies of thin films on different substrates, to get rid of unwanted thermal background in the recorded data. In our case, since we were interested in continuous liquid film thickness change for analysis of the phase of the Brillouin oscillations, the generated acoustic waves can be detected free of the thermal background. In fact, in the case of the study of liquid films, we could even envision an experiment based on the optical derivative, that removes the thermal background, free of a delay line. We could simply measure the phase modification of the Brillouin signal by varying the liquid thickness, at a fixed pump-probe time delay. We would not need anymore a delay line, only a pulse shaker.

Appendix C

Physical properties of materials

C.1 Thermal properties

Thermal properties (T = 300 K)					
	ρ, kg/m^3	K, W/m·K	C$_p$, J/kg·K	α, m^2/s	e·10^3, J/K·m^2· $s^{\frac{1}{2}}$
Si	2329	124	712	0.8·10^{-4}	14.4
Cr	7150	93.7	449	0.29·10^{-4}	17.3
Glycerol	1261	0.285	2377	95.1·10^{-9}	0.92
Glass, [201] (N-BK7)	2196	1.114	858	5.9·10^{-7}	1.5
OMCTS, [203, 204]	956	0.104-0.113	1731	6.3· 10^{-8}	0.41
8 CB, [205–208]	990	0.26	$\sim$ 1900	14 · 10^{-8}	0.7

$$\alpha = \frac{K}{\rho \cdot C_p} \tag{C.1}$$

$$e = \sqrt{\rho \cdot K \cdot C_p} \tag{C.2}$$

C.2 Acoustic properties

Acoustic properties (T = 300K)			
	ρ, kg/m^3	v$_l$, m/s	Z$_{ac}$, MRayl
Si	2329	7880	19.7
Cr	7150	5940	43
Glycerol	1261	2800	2.34
Glass, (N-BK7)	2196	5968	8.83
OMCTS	956	911 - 1050 [209]	0.87 - 1
8 CB	990	$\sim$ 1750 [210, 211]	1.7

$$Z_{ac} = \rho \cdot v_l \tag{C.3}$$

C.3 Refractive index of studied materials

Refractive index (T = 300K)									
λ, **nm**	400	450	500	550	600	650	700	750	800
Si, [212]	5.56	4.67	4.29	4.08	3.95	3.85	3.78	3.73	3.69
Cr, [213]	2.015	2.32	2.78	3.18	3.19	3.1	3.05	3.07	3.16
Glycerol, [214]	1.48	1.479	1.476	1.474	1.472	1.47	1.469	1.468	1.466
Glass, [201] (N-BK7)	1.531	1.525	1.521	1.518	1.516	1.514	1.513	1.512	1.511
OMCTS	1.37*	1.396 [203, 215]							
8 CB	n$_o$ = 1.51; n$_e$ = 1.67 (at 632.8 nm) [216] n$_o$ = 1.46, n$_e$ = 1.59 (at 600 nm, confined) [62]								

* - this work.

The penetration depth of Cr for the laser light with a wavelength of 790 nm was estimated to be $\delta = 18$ nm based on the absorption coefficient of $\alpha = 5.49 \cdot 10^5 \cdot \text{cm}^{-1}$ [213].

C.4 Temperature dependent parameters of glycerol

Temperature dependent density:

$$\rho(T > T_g) = 1272 - 0.655 \cdot (T(K) - 273K) \tag{C.4}$$

$$\rho(T < T_g) = 1332 - 0.32 \cdot (T(K) - 187K) \tag{C.5}$$

Temperature dependent refractive index:

$$n_{395}(T > T_g) = 1.675 - 6.5 \cdot 10^{-4} \cdot T(K) \tag{C.6}$$

$$n_{395}(T < T_g) = 1.583 - 1.6 \cdot 10^{-4} \cdot T(K) \tag{C.7}$$

Bibliography

1. "There is plenty romm at the bottom", R. Feynman, (1959)

   `http://web.pa.msu.edu/people/yang/RFeynman_plentySpace.pdf`

2. J. N. Israelachvili and S. J. Kott, J. Chem. Phys., **88**, 7162 (1988)

3. S. J. O'Shea and M. E. Welland, Langmuir, **14**, 4186 (1998)

4. K. Kurihara, Progr. Colloid. Polym. Sci, **121**, 49 (2002)

5. M. He, A. S. Blum, G. Overney, R. M. Overney, Phys. Rev. Lett., **88**, 154302 (2002)

6. S. P. Jarvis, G. Kaggwa, and K. Sheikh, Liquid structuring at the Solid-liquid interface. In Nanoscale Liquid Interfaces: Wetting, Patterning, and Force Microscopy at the Molecular Scale, eds. T. Ondarçuhu and J.-P. Aimé, Pan Stanford Publishing Pte Ltd., Singapore, 1 - 27 (2013)

7. H. Han, S. Mérabia, and F. Müller-Plathe, J. Phys. Chem. Lett., **8**, 1946 (2017)

8. M. C. Messmer, J. C. Conboy, and G. L. Richmond, J. Am. Chem. Soc., **117**, 8039 (1995)

9. J. N. Israelachvili, Intermolecular and Surface Forces. 2nd ed. London: Academic Press. 260-282 (1991)

10. G. Evmenenko, S. W. Dugan, J. Kmetko, and P. Dutta, Langmuir , **17**, 4021 (2001)

11. H. Mingyan, A. Szuchmacher Blum, G. Overney, and R. M. Overney, Phys. Rev. Lett., **88**, 154302 (2002)

12. M. Alcoutlabi, G. B. McKenna, J. Phys.: Condens. Matter, **17**, R461 (2005)

13. L. Cheng, P. Fenter, K. L. Nagy, M. L. Schlegel, N.C. Sturchio, Phys. Rev. Lett., **87**, 156103 (2001)

14. J. N. Israelachvili and H. Wennerström, Nature, **379**, 219 (1996)

15. A. Weinstein and S. A. Safran, EPL, **42**, 61 (1998)

16. J. W. M. Frenken, and T. H. Oosterkamp, Nature, **464**, 38 (2010)

17. S. H. Khan, G. Matei, S. Patil, and P. M. Hoffmann, Phys. Rev. Lett., **105**, 106101 (2010)

18. A. Maali, T. Cohen-Bouhacina, G. Couturier, and J.-P; Aime, Phys. Rev. Lett, **96**, 086105 (2006)

19. H. K. Christenson, D. W. R. Gruen, R. G. Horn, and J. N. Israelachvili, J. Chem. Phys., **87**, 1834 (1987)

20. J. Gao, W. D. Luedtke, Uzi Mandman, Phys. Rev. Lett., **79**, 705 (1997)

21. J. N. Israelachvili and G. E. Adams, J. Chem. Soc. Faraday Trans. 1, **4**, 975 (1978)

22. R. G. Horn, J. N. Israelachvili, J. Chem. Phys., **75**, 1400 (1981)

23. J. Israelachvili and D. Gourdon, Science, **292**, 867 (2001)

24. G. B. McKenna, Eur. Phys. J. Special Topics, **141**, 291 (2007)

25. S. W. Coles, A. M. Smith, M. V. Fedorov, F. Hausen, and S. Perkin, Faraday Discuss., 2017, DOI: 10.1039/C7FD00168A

26. J.-M. Zanotti and D. Morineau, V. Garciía Sakai et al. (eds.), Dynamics of Soft Matter: Neutron Applications, Chap. 14, pp. 367-409, Springer Science - Business Media (2012)

27. S. Granick, Science, **253**, 1374 (1991)

28. J. M. Rickman, Phys. Rev. E, **86**, 062501 (2012)

29. C. Alba-Simionesco, G. Dosseh, E. Dumont, B. Frick, B. Geil, D. Morineau, V. Teboul, and Y. Xia, Eur. Phys. J. E, **12**, 19 (2003)

30. C. Y. Lee, J. A. McCammon, P. J. Rossky, J. Chem. Phys., **80**, 4448 (1984)

31. C. Alba-Simionesco, B. Coasne, G. Dosseh, G. Dudziak, K. E. Gubbins, R. Radhakrishman, and M. Sliwinska-Bartkowiak, J. Phys.: Condens. Matter, **18**, R15 (2006)

32. R. Mancinelli, J. Phys. Condens. Mat., **22**, 404213 (2010)

33. H. K. Christenson, J. Phys.: Condens. Matter, **13**, R95 (2001)

34. K. Dalnoki-Veress, J.A. Forrest, C. Murray, C. Gigault, J.R. Dutcher, Phys. Rev. E, **63**, 031801 (2001)

35. C.B. Roth, J.R. Dutcher, J. Polym. Sci. Part B. Polym. Phys., **44**, 3011 (2006)

36. `https://en.wikipedia.org/wiki/DLVO_theory`

37. H. K. Christenson, R. G. Horn and J. N. Israelachvili, J. Colloid Interface Sci, **88**, 79 (1982)

38. M. Heuberger, M. Zäch, N. D. Spencer, Science, **292**, 905 (2001)

39. I. K. Snook and W. van Megen, J. Chem. Phys., **72**, 2907 (1980)

40. W. J. van Megen and I. K. Snook, J. Chem. Phys., **74**, 1409 (1981)

41. J. N. Israelachvili, Intermolecular and Surface Forces: With Applications to Colloid and Biological Systems, 2nd ed. London: Academic Press, 260-281 (1985)

42. T. R. Jensen, M. Ø. Jensen, N. Reitzel, K. Balashev, G. H. Peters, K. Kjaer, and T. Bjørnholm, Phys. Rev. Lett., **90**, 086101 (2003)

43. H. K. Christenson, J. Phys. Chem., **90**, 4(1986)

44. L. J. Douglas Frink and F. van Swol, J. Chem. Phys., **108**, 5588 (1998)

45. C. Ghatak and K. G. Ayappa, J. Chem.Phys., **120**, 9703 (2004)

46. R. M. Pashley, P. M. McGuiggan, B.W. Ninham, and D.F. Evans, Science, **229**, 1088 (1985)

47. T-D. Li, J. Gao, R Szoszkiewicz, U. Landman, and E. Riedo, Phys. Rev. B, **75** 115415 (2007)

48. H-W. Hu, G. A. Carson, and S. Granick, Phys. Rev. Lett, **66**, 2758 (1991)

49. J. Klein and E. Kumacheva, Science, **269**, 816 (1995)

50. S. Xu, G. C. Simmons, T. S. Mahadevan, G. W. Scherer, S. H. Garofalini, and C. Pacheco, Langmuir, **25**, 5084 (2009)

51. S. Xu, G. W. Scherer, T. S. Mahadevan, and S. H. Garofalini, Langmuir, **25**, 5076 (2009)

52. E. Courtens, M. Foret, B. Hehlen, R. Vacher, Solid State Communications, **117**, 187 (2001)

53. R. Busselez, R. Lefort, Q. Ji, F. Affouard and D. Morineau, Phys. Chem. Chem. Phys., **11**,11127 (2009)

54. G. Monaco and S. Mossa, PNAS, **106**, 16907 (2009)

55. H. Matsubara, F. Pichierri, K. Kurihara, J. Chem. Theory Comput., **6**, 1334 (2010)

56. H. Matsubara, F. Pichierri, K. Kurihara, Phys. Rev. Let., **109**, 197801 (2012)

57. P. G. de Gennes, J. Prost, The Physics of Liquid Crystals, Oxford University Press, (1995)

58. D. K. Yang, S. T. Wu, Fundamentals of Liquid Crystal Devices, Wiley, West Sussex, (2006)

59. O. Lehmann, , Flüssige Kristalle und ihr scheinbares Leben, Leipzig 1921

60. L. Radzinovsky and J. Toner, Phys. Rev. B, **60**, 206 (1999)

61. T. Bellini,L. Radzinovsky, J. Toner, N. A. Clark , Science, **294**, 1074 (2001)

62. R. Guégan, PhD Thesis, Université de Rennes I, 2008 (https://tel.archives-ouvertes.fr/tel-00264429)

63. G. Chanine, PhD Thesis, Université de Rennes I, 2010

64. T. Araki, M. Buscaglia, T. Bellini and H. Tanaka, Nature Materials, **10**, 303 (2011)

65. S. H. Ryu and D. K. Yoon, Liquid crystals, **43**, 1951 (2016)

66. D. de las Heras, E. Velasco, L. Mederos, J. Chem. Phys., **120**, 4949 (2004)

67. M. Vilfan, I. D. Olenik, M. Čopič, **Chapter** Dynamical Processes in Confined Liquid Crystals in "Time-Resolved Spectroscopy in Complex Liquids", pp. 185 - 216 (2008)

68. S. Stallinga, M. M. Wittebrood, D. H. Luijendijk, and Th. Rasing, Phys. Rev. E, **53**, 6085 (1996)

69. M. M. Wittebrood, TH. Rasing, S. Stallinga, and I. Muševič, Phys. Rev. Lett., **80**, 1232 (1998)

70. C R Safinya, E B Sirota, R Planoi and R F Bruinsma, J. Phys.: Condens. Matter, **2**, SA365 (1990)

71. C. R. Safinya, E. B. Sirota, and R. J. Piano, Phys. Rev. Lett., **66**, 1986 (1991)

72. S. H. J. Idziak, C. R. Safinya, R. S. Hill, K. E. Kreiser, M. Ruths, H. E. Warriner, S. Steinberg, K. S. Liang, J. N. Israelachvili, Science, **264**, 1915 (1994)

73. S. H. J. Idziak, I. Koltover, K. S. Liang, J. N. Israelachvili and C. R. Safinya, Int. J. Thermophys, **16**, 299 (1995)

74. S. H. J. Idziak, I. Koltover, J. N. Israelachvili, and C. R. Safinya , Phys. Rev. Let, **76**, 1477 (1996)

75. A. Centrone, E. Penzo, M. Sharma, J. W. Jackson, N. Marzari, F. Stellacci, Proc. Natl. Acad. Sci. USA, **105**, 9886 (2008)

76. T. Fukuma, Y. Ueda, S. Yoshioka, and N.Asakawa, Phys. Rev. Lett., **104**, 016101 (2010)

77. Q. Du, E. Freysz, and Y. R. Shen, Science, **264**, 826 (1994)

78. C.-Y. Ruan, V. A. Lobastov, F. Vigliotti, S. Chen, and A. H. Zewail, Science, **304**, 80 (2004).

79. G. Held and D. Menzel, Phys. Rev. Lett., **74**, 4221 (1995)

80. T. Mitsui, M. K. Rose, E. Fomin, D. F. Ogletree, and M. Salmeron, Science, **297**, 1850 (2002)

81. S. H. Lee, P. J. Rossky, J. Chem. Phys., **100**, 3334 (1994)

82. Y. Leng, P. T. Cummings, J. Chem. Phys., **124**, 074711 (2006)

83. D. Argyris, T. Ho, D. R. Cole, A. Striolo, J. Phys. Chem., **115**, 2038 (2011)

84. P.-A. Mante, C.-C. Chen, Y.-C. Wen, H.-Y. Chen, S.-C. Yang, Y.-R. Huang, I.-J. Chen, Y.-W. Chen, V. Gusev, M.-J. Chen, J.-L. Kuo, J.-K. Sheu, and C.-K. Sun, Sci. Reports, **4**, 6249 (2014)

85. C. Klieber, T. Pezeril, V. Gusev, K. A. Nelson, Phys. Rev. Lett. **114**, 065701 (2015)

86. C. Klieber, T. Pezeril, S. Andrieu, K. A. Nelson, J. Appl. Phys. **112**, 013502 (2012)

87. C. Klieber, Ph.D. Thesis, `http://hdl.handle.net/1721.1/57801`, MIT (2010)

88. C. Thomsen, H. T. Grahn, H. J. Maris, and J. Tauc, Phys. Rev. B, **34**, 4129 (1986)

89. H. T. Grahn, H. J. Maris, and J. Tauc, IEEE Quantum Electronics, **25**, 2562 (1989)

90. S. A. Akhmanov and V. E. Gusev, Sov. Phys. Usp., **35**, 153 (1992)

91. R. M. White, J. Appl. Phys. **34**, 3359 (1963)

92. T. Pezeril, P. Ruello, S. Gougeon, N. Chigarev, D. Mounier, J.-M. Breteau, P. Picart, V. Gusev, Phys. Rev. B, **75**, 174307 (2007)

93. T. Pezeril, F. Leon, D. Chateigner, S. Kooi, and K. A. Nelson, Appl. Phys. Lett., **92**, 061908 (2008)

94. T. Pezeril, Opt. & Laser Tech. **83**, 177 (2016)

95. T. Saito, O. Matsuda, and O. B. Wright, Phys. Rev. B, **67**, 205421 (2003)

96. G. L. Eesley, B. M. Clemens, and C. A. Paddock, Appl. Phys. Lett., **50**, 717 (1987)

97. R. Y. Chiao, C. H. Townes, and B. P. Stoicheff, Phys. Rev. Lett., **12**, 592 (1964)

98. B.Ya. Zel'dovich, V.I.Popovichev, V.V.Ragulskii and F.S.Faisullov, Sov. Phys. JETP, **15**, 109 (1972)

99. H.N. Lin, R.J. Stoner, H.J. Maris and J. Tauc, J. Appl. Phys., **69**, 3816 (1991)

100. M. E. Msall, O. B. Wright, and O. Matsuda, J. of Phys.: conference Series, **92**, 012026 (2007)

101. C. Klieber, D. Torchinsky, T. Pezeril, K. Manke, S. Andrieu, and K. A. Nelson, J. of Phys.: conference Series, **214**, 012033 (2010)

102. G. Tas and H.J. Maris, Phys. Rev. B, **49**, 15046 (1994)

103. O. B. Wright and V. Gusev, IEEE Transactions on Ultrasonics, Ferroelectrics and Frequency Control, **42**, 331 (1995)

104. O. Matsuda, M. C. Larciprete, R. Li Voti, O. B. Wright, Ultrasonics, **56**, 3 (2014)

105. L. D. Landau and E. M. Lifshitz, Mechanics, Elsevier, New York, (1982)

106. W. Nowacki, Thermoelasticity, Pergamon Press, Oxford, London, New York, Paris, (1962)

107. J. D. Beers, M. Yamaguchi, T. Feurer, B. J. Paxto, and K. A. Nelson, "Ultrafast Phenomena XIV", vol. 79, Springer, pp. 236-238 (2005)

108. Photoacoustic Imaging and Spectroscopy, ed. L. V. Wang, Taylor&Francis, New York,(2013)

109. C. A. Angell, K. L. Ngai, G. B. McKenna, P. F. McMillan and S. W. Martin, J. Appl. Phys, **88**, 3113 (2000)

110. Ya. E. Ryabov, Y. Hayashi, A. Gutina, and Y. Feldman, Phys. Rev. B, **67**, 132202 (2003)

111. M. E. Möbius, T. Xia, W. van Saarloos, M. Orrit, and M. van Hecke, J. Phys. Chem., **114**, 7439 (2010)

112. S. Samanta and R. Richert, J. Chem. Phys., **142**, 044504 (2015)

113. C. A. Angell, J. Non-Cryst. Solids, **131-133**, 13 (1991)

114. H. van Koningsveld, Recl. Trav. Chim. Pays-Bas, **87**, 243 (1968)

115. `https://en.wikipedia.org/wiki/Newton\%27s_rings`

116. D. Slayton, PhD Thesis, Harvard University, (2002)

117. T. Hecksher, Mester thesis, IMFUFA, RUC, (2006)

118. S. I. Anisimov, B. L. Kapelioivich, and T. L. Perel'man, Sov. Phys. JETP, **39**, 375 (1974)

119. V. E. Gusev, O. B. Wright, Phys. Rev. B, **57**, 57 (1998)

120. M. N. Libenson, Proceeding of SPIE, **4423**, 1 (2001)

121. B. Rethfeld, A. Kaiser, M. Vicanek and G. Simon, Phys. Rev. B, **65**, 214303 (2002)

122. I. H. Chowdhury and X. Xu, Numerical Heat Transfer, Part A, 44, 219 (2003)

123. A. T. Karim, Z. Lin, L. V. Zhigilei, AIP Conf. Proc., **1464**, 280 (2012)

124. J. G. Fujimoto, J. M. Liu, and E. P. Ippen, Phys. Rev. Lett., **53**, 1837 (1984)

125. R. W. Schoenlein, W. Z. Lin, and J. G. Fujimoto, Phys. Rev. Let., **58**, 1680 (1987)

126. N. Del Fatti, R. Bouffanais, F. Vallée, and C. Flytzanis, Phys. Rev. Lett., **81**, 922 (1998)

127. J. Hohlfeld, S.-S. Wellershoff, J. Güdde, U. Conrad, V. Jühnke, E. Matthias, Chem. Phys., **251**, 237 (200)

128. C. Voisin, N. Del Fatti, D. Christofilos, and F. Valleé, J. Phys. Chem. B, **105**, 2264 (2001)

129. W. Wu and Y. Wang, Opt. Lett., **40**, 64 (2015)

130. T. Q. Qiu, C. L. Tien, J. Heat Transf., **115**, 835 (1993)

131. M. I. Kaganov, I. M. Lifshitz and L. V. Tanatarov, Sov. Phys. JETP, **4**,173 (1957)

132. M. Hase, K. Ishioka, J. Demsar, K. Ushida, and M. Kitajima, Phys. Rev. B, **71**, 184301 (2005)

133. L. Foglia, PhD Thesis, Freie Universität Berlin, 2011

134. D. Cahill, Rev. Sci. Instrum. **75**, 5119 (2004)

135. A. Schmidt, M. Chiesa, X. Chen, G. Chen, Rev. Sci. Instrum. **79**, 064902 (2008)

136. A. Schmidt, X. Chen, G. Chen, Rev. Sci. Instrum. **79**, 114902 (2008)

137. D. Cahill, P. Braun, G. Chen, D. R. Clarke, S. Fan, K. Goodson, P. Keblinski, W. King, G. Mahan, A. Majumdar, H. Maris, S. Phillpot, E. Pop, L. Shi, Appl. Phys. Rev. **1**, 011305 (2014)

138. A. Schmidt, R. Cheaito, M. Chiesa, Rev. Sci. Instrum. **80**, 094901 (2009)

139. C. Mechri, P. Ruello, J.-M. Breteau, M. Baklanov, P. Verdonck, V. Gusev, Appl. Phys. Lett. **95**, 091907 (2009)

140. A. Steigerwald, Y. Xu, J. Qi, J. Gregory, X. Liu, J.K. Furdyna, K. Varga, A.B. Hmelo, G. Lüpke, L.C. Feldman, N. Tolk, Appl. Phys. Lett. **94**, 111910 (2009)

141. A. M. Lomonosov, A. Ayouch, P. Ruello, G. Vaudel, M. R. Baklanov, P. Verdonck, L. Zhao, V. E. Gusev, ACS Nano **6**, 1410 (2012).

142. S. Nikitin, N. Chigarev, V. Tournat, A. Bulou, D. Gasteau, B. Castagnede, A. Zerr, V. Gusev, Scientific reports, **5**, 9352 (2015)

143. T. Dehoux, M. Ghanem, O. Zouani, M. Ducousso, N. Chigarev, C. Rossignol, N. Tsapis, M.-C. Durrieu, B. Audoin, Ultrasonics **56**, 160 (2015)

144. S. Danworaphong, M. Tomoda, Y. Matsumoto, O Matsuda, T. Ohashi, H. Watanabe, M. Nagayama, K. Gohara, P. H. Otsuka, O. B. Wright, Appl. Phys. Lett. **106**, 163701 (2015)

145. F. Pérez-Cota, R. J. Smith, E. Moradi, L. Marques, K. F. Webb, M. Clark, Appl. Opt. **54**, 8388 (2015)

146. A. Bojahr, M. Herzog, D. Schick, I. Vrejoiu, and M. Bargheer, Phys. Rev. B **86**, 144306 (2012)

147. T. Pezeril, C. Klieber, S. Andrieu, K. A. Nelson, Phys. Rev. Lett. **102**, 107402 (2009)

148. C. Klieber, T. Hecksher, T. Pezeril, D. H. Torchinsky, J. C. Dyre, and K. A. Nelson, J. Chem. Phys. **138**,12A544 (2013)

149. I. Chaban, H. D. Shin, C. Klieber, R. Busselez, V. E. Gusev, K. A. Nelson, and T. Pezeril, Rev. Sci. Instrum., **88**, 074904 (2017)

150. L. Shelton, F. Yang, W. K. Ford, and H. J. Maris, Phys. Stat. Sol. (b) **242**, 1379 (2005)

151. J. D. Hoffman, J. Am. Chem. Soc. **75**, 6313 (1953)

152. R. Niepmann, U. Schmidt, J. Chem. Thermodynamics **12**,1133 (1980)

153. A. Sterczyńska, A. Derylo-Marczewska, M. Śliwińska-Bartkowiak, J. Z. Piotrowska, M. Jarek, K. Domin, J. Therm. Anal. Calorim. **118**, 263 (2014)

154. L. Comez, D. Fioretto, F. Scarponi, J. Chem. Phys. **119**, 6032 (2003)

155. C. v. Korff Schmising, M. Bargheer, M. Kiel, N. Zhavoronkov, M. Woerner, T. Elsaesser, I. Vrejoiu, D. Hesse, M. Alexe, Phys. Rev. Lett. **98**, 257601 (2007)

156. A. Maznev, K. Manke, C. Klieber, K. A. Nelson, S. Baek, C. Eom, Opt. Lett. **36**, 2925 (2011)

157. S. Perkin, Phys. Chem. Chem. Phys. **14**, 5052 (2012)

158. F. P. Incropera and D. P. De Witt, Introduction to heat transfer, 3rd ed. (Wiley, New York, 1985, 1996 reissue)

159. A. Mandelis, Diffusion-wave fields: mathematical methods and green functions, (Springer-Verlag, New York, 2001)

160. D. Cahill, W. Ford, K. Goodson, G. Mahan, A. Majumdar, H. Maris, R. Merlin, J. Appl. Phys. **93**, 793 (2003)

161. S. Volz et al., Eur. Phys. J. B **89**, 15 (2016)

162. J. N. Israelachvili, Intermolecular and surface forces, Academic Press, New York, (1992)

163. S. J. O'Shea, M.E. Welland, and T. Rayment, Appl. Phys. Lett., **60**, 2356 (1992)

164. K. Koga and X. C. Zeng, Phys. Rev. Lett., **79**, 853 (1997)

165. T. Uchihashi, M. J. Higgins, S. Yasude, S. P. Jarvis, S. Akita, Y. Nakayama, J. E. Sader, Appl. Phys. Lett., **85**, 16 (2004)

166. S. De Beer, W. K. Den Otter, D. Van Den Ende, W. J. Briels and F. Mugele, EPL, **97**, 46001 (2012)

167. R.-G. Xu and Y. Leng, J. of Chem. Phys., **140**, 214702 (2014)

168. H. Matsubara, F. Pichierri, and K. Kurihara, J. of Chem. Phys., **134**, 044536 (2011)

169. S. Singh, D. A. Dunmur, Liquid Crystals: Fundamentals, World Scientific Co Pte. Ltd., New Jersey, London, Singapore, Hong Kong, (2002)

170. S. Singh, Phys. Reports, **324**, 107 (2000)

171. M. Marinelli, F. Mercuri, S. Foglietta, U. Zammit, and F. Scudieri, Phys. Rev. E, **54**, 1604 (1996)

172. Physical Properties of Liquid Crystals, ed. by D. Demus, J. Goodby, G. W. Gray, H.-W. Spiess, V. Vill, - Weinheim; New York; Chichester; Brisbane; Singapore; Toronto: Wiley - VCH, 1999

173. A. Zidanšek, G. Lahajnar, and S. Kralj, Appl. Magn. Reson., **27**, 311 (2004)

174. D. Sharma, J. C. MacDonald, and G. S. Iannacchionne, J. Phys. Chem, **110**, 16679 (2006)

175. O. Oltutu, F. Cakirtas, N. Yorulmaz, and S. Yilmaz, Phase Transitions, **89**, 242 (2016)

176. R. L. McMillan, Phys. Rev. A, **7**, 1673 (1973)

177. L. Wu, M. J. Young, Y. Shao, C. W. Garland, R.J. Birgencau, Phys. Rev. Lett., **72**, 376 (1994)

178. G. W. Bradberry and J. M. Vaughan, J. Phys. C: Solid state Physics, **9**, 3905 (1976)

179. M. Lejman, I. C. Infante, G. Vaudel, I. Chaban,M. Edely, P. Gemeiner, G. Nataf, J. Kreiser, V. E. Gusev, B. Dkhil, P. Ruello, Nat. Commun. **7**, 12345 (2016)

180. I. Dierking, Textures of Liquid Crystals, Wiley, Weinheim, (2003)

181. T.-C. Chung, Thermotropic Liquid Crystal Polymers, Technomic Publishing Company, Pennsylvania, 2001

182. S. Shojaei-Zadeh and S. L. Anna, Langmuir, **22**, 9986 (2006)

183. B. Zappone and E. Lacaze, Phys. Rev. E, **78**, 061704 (2008)

184. G. H. Brown, J. J. Wolken, Liquid Crystals and Biological Structures, Academic Press, (1979)

185. `https://en.wikipedia.org/wiki/Liquid_crystal`

186. S. Chandrasekhar, Liquid Crystals, Cambridge University Press, Cambridge, 1992

187. T.J. Sluckin, D.A. Dunmur, H. Stegemeyer, Crystals That Flow: Classic Papers from the History of Liquid Crystals, Taylor&Francis, London, (2004)

188. L. M. Blinov, Structure and Properties of Liquid Crystals, Springer, (2011)

189. I. C. Khoo, Liquid Crystals, Wiley, New Jersey, (2007)

190. P. Oswald, P. Pieranski, Nematic and Cholesteric Liquid Crystals: Concepts and Physical Properties Illustrated by Experiments, Chap. B. V, Taylor&Francis, Boca Raton, (2005)

191. I. W. Stewart, The Static and Dynamic Continuum Theory of Liquid Crystals, Taylor&Francis, London, (2004)

192. A. Sengupta, Topological Microfluidics, Springer Theses, Chap. 2, Springer International Publishing Switzerland, (2013)

193. J. C. Toledano, P. Toledano, The Landau Theory of Phase Transitions, World Scientific, Singapore, (1987)

194. G. W. Gray, Thermotropic Liquid Crystals, Wiley, New York, (1987)

195. P. Barois, Phase Transitions in Liquid Crystals, eds. S. Martellucci and A. N. Chester, Plenum Press, New York, Ch. 4, pp. 41-66 (1992)

196. A. Caillé, Remarques sur la diffraction des rayons X dans les smectiques, Acad. C. R. Sci. B, **247**, 891 (1972)

197. M. A. Osipov, B. I. Ostrovskii, Cryst. Rev., **3**, 113 (1992)

198. M. De. Santo, R. Barberi, L. M. Blinov, eds. Th. Rasing and I. Muševič, Springer, Berlin, pp. 194 - 210 (2004) (2004)

199. A. A. Sonin, The Surface Physics of Liquid Crystals, Gordon and Breach, Luxembourg, (1995)

200. C. Fan and M. J. Stephen, Phys. Rev. Lett., **25**, 500 (1970)

201. SCHOTT optical glass data sheets, (2015)

202. J. Chandezon, J.-M. Rampnoux, S. Dilhaire, B. Audoin, and Y. Guillet, Opt. Express, **23**, Issue 21, 27011 (2015)

203. J. A. Dean Lange's handbook of chemistry, (1999)

204. CRS Handbook of Chemistry and Physics, 90 ed. - CRC Press (2010)

205. A. J. Leadbetter, J. L. A. Durrant, and M. Rugman, Mol. Cryst. Liq. Cryst., **34**, 231 (1977)

206. G. A. Oweimreen, J. Phys. Chem., **105**, 8417 (2001)

207. Heat Capacities: Liquids, Solutions and Vapours, Published by The Royal Society of Chemistry, (2010)

208. S. Paoloni, F. Mercuri, and U. Zammit, J. Chem. Phys., **145**, 124506 (2016)

209. R. Niepman and U. Schmidt, J. Chem. Thermodynamics, **12**, 1133 (1980)

210. G. W. Bradberry and J. M. Vaughan, Phys. Lett., **62A**, 225 (1977)

211. G. W. Bradberry and C. F. Clarke, Phys. Lett., **95A**, 3055 (1983)

212. D. E. Aspnes and A. A. Studna, Phys. Rev. B., **27**, 985 (1983)

213. P. B. Johnson, and R. W. Christly, Phys. Rev. B, **9**, 5056 (1974)

214. J. Rheims, J. Köser and T. (Wriedt, Meas. Sci. Technol., **8**, 601 (1997)

215. H. L. Clever, M.L. Taylor, J. Chem. Eng. Data, **16**, 91 (1971)

216. R. G. Horn, J. de Phys., **39**, 105 (1977)

UNIVERSITE BRETAGNE LOIRE

Le Mans Université

Thèse de Doctorat

Ievgeniia CHABAN

Investigation des propriétés thermiques et mécaniques de liquides ultra-minces aux fréquences GHz

Investigation of thermal and mechanical behavior of ultra-thin liquids at GHz frequencies

Résumé

La structuration des liquides près d'interfaces est liée aux forces d'interactions liquide/interface à des distances de quelques dimensions moléculaires. Cet effet de structuration universel joue un rôle primordial dans divers domaines tels que le transport de chaleur, le transport de particules à travers les membranes biologiques, la nanofluidique, la microbiologie et la nanorhéologie.
Le but principal de cette thèse est de réaliser l'échographie par laser de liquides nanostructurés près d'une interface, afin de mieux comprendre les propriétés physiques de liquides confinés à des échelles moléculaires. La méthode expérimentale utilisée est la technique d'acoustique picoseconde, qui est une technique tout optique impliquant des lasers impulsionnels pour la génération et la détection d'ultrasons picosecondes. Nous avons adapté la technique expérimentale afin d'étudier les propriétés acoustiques longitudinales à hautes fréquences des liquides ultra-minces (glycérol, OMCTS, cristaux liquides) confinés dans différentes configurations. Les résultats de la diffusion Brillouin dans le domaine temporel sont utilisés pour déterminer le profil de distribution de la température dans le volume de liquide étudié qui peut être extrapolé aux dimensions nanométriques. Les résultats sur le changement de la fréquence Brillouin aussi bien que sur l'atténuation acoustique en fonction de la puissance du laser donnent un aperçu de la relation entre les propriétés thermiques et mécaniques des liquides. L'analyse de Fourier des résultats expérimentaux pour différentes épaisseurs de liquide donne l'information sur la vitesse du son et l'atténuation aux fréquences GHz. Ceux-ci sont comparés aux résultats des mesures pour des liquides épais à température ambiante. Ce nouveau schéma expérimental est une première étape vers la compréhension des liquides confinés mesurés par échographie d'ultrasons aux fréquences GHz.

Mots clés
Phénomènes ultra-rapides, acoustique picoseconde, liquides confinés, diffusion Brillouin, effets interfaciaux, structuration moléculaire, chauffage cumulatif de liquides, couches minces fluidiques

Abstract

The phenomenon of liquid structuring near interfaces is related to the liquid/interface interaction forces at distances of some molecular dimensions. Despite the fact that this universal structuring effect plays a key role in various fields such as heat transport, particle transport through biological membranes, nanofluidics, microbiology and nanorheology, the experimental investigation of liquid structuring remains challenging. The aim of this PhD thesis is the experimental study of the structuring/ordering of liquids at nanoscale distances from their interfaces with solids. In this context, we have adapted the experimental technique of picosecond laser ultrasonics to investigate high-frequency longitudinal acoustic properties of ultrathin liquids (glycerol, OMCTS, liquid crystals) confined between solid surfaces of different types. At first, we will present results of time-domain Brillouin scattering (TDBS) used to determine the temperature distribution profile in the investigated liquid volume which can be extrapolated to nanometer dimensions. Results for the evolution of the extracted Brillouin scattering frequencies and attenuation rates recorded at different laser powers give insight to the intrinsic relationship between thermal and mechanical properties of liquids. Second, we will describe our results for the measurements of mechanical properties of ultrathin liquids with nanometric resolution. Fourier analysis of the recorded TDBS signals for different liquid thicknesses yield the value of the longitudinal speed of sound and attenuation at GHz frequencies. These are compared to the results of separate measurements of bulk liquids at ambient temperature. This novel TDBS experimental scheme is a first step towards the understanding of confined liquids measured by GHz ultrasonic probing.

Key Words
Ultrafast phenomena, picosecond laser ultrasonics, liquid confinement, time-resolved spectroscopy, interfacial effects, cumulative heating of liquids

L'Université Bretagne Loire